Quantum correlations measured with multi-pixel detectors

Frauke Izdebski

Dipl.-Ing. (FH)

Submitted for the degree of Doctor of Philosophy

Heriot-Watt University

Institute of Photonics and Quantum Sciences

School of Engineering and Physical Sciences

August 2013

ABSTRACT

This thesis investigates the measurement of spatial correlations of photon pairs generated through spontaneous parametric down-conversion with single-photon sensitive multi-pixel detectors.

A custom designed and fabricated 8×1 fibre array detector for time to position multiplexing was characterised. This detector was then commissioned in an experiment measuring the spatial correlations of photon pairs in position, momentum and intermediate bases. The fibre array measured eight positions simultaneously with one Single-Photon Avalanche Diode, which led to an eight-fold increase in the data acquisition rate compared to traditional experiments, where a single SPAD was scanned across the detection plane.

To capture all of the emitted light, an electron-multiplying CCD (EMCCD) camera was used. The spatial correlations were measured for the first time in momentum *and* position bases with a single-photon sensitive camera. Additionally, over 2500 spatial states were accessed, which, to date, is the highest number of accessed states, using the transverse positions of correlated photon pairs.

The detected photon pairs were tested, if they fulfil the requirements of entanglement. The calculated variance product was 1 order of magnitude and almost three orders of magnitude below the classical limit of separability for the fibre array and the EMCCD camera respectively.

Finally the image enhancement of using a correlated light source with a noise rejection algorithm was investigated experimentally and theoretically.

ACKNOWLEDGEMENTS

This thesis would not have come into being, if it were not for the help and support of many wonderful people. Firstly I would like to thank my supervisor, Prof. Gerald Buller for giving me the opportunity to pursue a PhD in his research group, for his support, and for signing an *almost* endless pile of travel expense claims for my work at the University of Glasgow. I would like to thank Dr. Ryan Warburton for teaching me SPAD characterisation techniques and for being the chief proofreader. Furthermore I would like to thank Dr. Aongus McCarthy for helpful discussions about the optical design for one of the experiments, and Dr. Robert Collins for taking out time, in order to teach me how to operate the fibre splicer. For valuable discussions, general entertainment and team-building exercises, like ice skating, rugby and trips to the nearest local, I would like to thank the current and past group members: Silvia Butera, Patrick Clarke, Ross Donaldson, Nathan Gemmel, Giuseppe Intermite, Nils Krichel, Aurora Maccarone, Agata Pawlikowska, Christian Reimer, Ximing Ren, and Dr. Peter Vines. I am also indebted to Prof. Robert Hadfield and Dr. Chandra Natarajan for giving me access to their Superconducting Nanowire Single-Photon Detector.

I would like to thank the Optics group at the University of Glasgow for welcoming and integrating me in their group. I will never forget the lunch hours, the (power-tool) tea breaks, and social outings with the whole group. Being part of such a great group proved very valuable, when pinching desperately needed optics and learning new LabView tips & tricks. I am not attempting to write down a list of all past and present members of the group, as I am sure that I will forget someone and therefore I will only mention the people I have spent most of the days in the lab: I would like to thank Prof. Miles Padgett for his guidance and support throughout my PhD. Although, I was not one of his PhD students, he treated me as one of his own. I am also indebted to Dr. Matt Edgar for spending many hours in the dark lab with me. The long days in the lab just flew by, while chatting and listening to music. His out-of-office hours introductory lessons in MATLAB and LaTeX were really appreciated and of great help when preparing various scientific documents. I am also indebted to Dr. Daniel Tasca for his explanations of the theoretical aspects of the experiments, and for lending me an additional pair of hands whenever needed. I would like to thank Alexis Pennes for working with me on the contrast enhancement experiment and Reuben Aspden for his excellent choice of music. I must not forget to thank Dr. Jonathan Leach, who was in a superposition of being one

of my post-docs in Glasgow, a collaborator in Canada and finally my second supervisor at Heriot-Watt.

There are a few collaborators with whom I have worked particularly closely, and who have contributed to the work set out in the forthcoming chapters, and therefore I would like to thank the following persons: Prof. David Ireland from the University of Glasgow for programming the coincidence circuit program in LabView, Dr. Alison Yao and Prof. Stephen Barnett from the University of Strathclyde for helpful discussion concerning the theory for the correlations measured with the fibre array detector, and from the University of Ottawa (Canada) I would like to thank Megan Agnew for programming the EMCCD camera control vi, and Prof. Robert Boyd for his valuable discussions about the correlation measurements with the EMCCD camera.

Although not directly involved in any of the experiments, I would like to thank my family and friends for their constant support and encouragement.

Special thanks go out to my office mates Tunmise Dada, Chaitanya Joshi, and Akhil Rajan for putting up with me over the last 3.5 years, and for keeping me entertained, while I was writing-up my thesis. I will never forget the legendary whiteboard discussions about theoretical physics between Tunmise and Joshi in our old office.

I would like to thank Thomas Schratwieser, Dave MacLachlan, Jonathan Morton, Rose Mary, and Ashleigh Barron, for proving to me, that there is life outside the lab and my office desk. It was a pleasure to run the OSA student chapter with them, and I am wishing the new committee best of luck in their future endeavours.

A special thanks goes to Malcolm McWilliams, who never failed to put a smile on my face, for lending me an ear during difficult times and for telling me to: “Hang in there.”

I would also like to thank my friends from home and abroad for all of their support, the good times we have spent together and all the laughter we have shared: Simone Adam, Manuela Göbelt, Sarah Heinen, Stephen Kilbride, Norbert Lorenz, Suzanne McEndoo, and Milena Müller.

Last, but not least, I would to thank my parents for their constant support, both moral and financial, and for their encouragement throughout my PhD.

ACADEMIC REGISTRY
Research Thesis Submission

Name*:*			
School/PGI:			
Version: *(i.e. First, Resubmission, Final)*		Degree Sought (Award **and** Subject area)	

Declaration

In accordance with the appropriate regulations I hereby submit my thesis and I declare that:

1) the thesis embodies the results of my own work and has been composed by myself
2) where appropriate, I have made acknowledgement of the work of others and have made reference to work carried out in collaboration with other persons
3) the thesis is the correct version of the thesis for submission and is the same version as any electronic versions submitted*.
4) my thesis for the award referred to, deposited in the Heriot-Watt University Library, should be made available for loan or photocopying and be available via the Institutional Repository, subject to such conditions as the Librarian may require
5) I understand that as a student of the University I am required to abide by the Regulations of the University and to conform to its discipline.

* *Please note that it is the responsibility of the candidate to ensure that the correct version of the thesis is submitted.*

Signature of Candidate*:*		Date:	

Submission

Submitted By *(name in capitals):*	
Signature of Individual Submitting:	
Date Submitted:	

For Completion in the Student Service Centre (SSC)

Received in the SSC by *(name in capitals):*			
Method of Submission *(Handed in to SSC; posted through internal/external mail):*			
*E-thesis Submitted (**mandatory for final theses)***			
Signature:		Date:	

CONTENTS

LIST OF FIGURES

LIST OF TABLES

LIST OF ABBREVATIONS

ADC ..... Analogue to Digital Converter

APD ..... Avalanche Photodiode

BBO ..... β-Barium metaborate

C ..... Contrast

CCD ..... Charge Coupled Device

CCR ..... Classical Count Rate

CFD ..... Constant Fraction Discriminator

CIC ..... Clock Induced Charge

CMOS ..... Complementary Metal Oxide Semiconductor

cps ..... Counts Per Second

CTE ..... Charge Transfer Efficiency

CV ..... Continuous Variables

DCR ..... Dark Count Rate

EMCCD ..... Electron-Multiplying Charge Coupled Device

ENF ..... Excess Noise Factor

EPR ..... Einstein-Podolsky-Rosen

FC/PC ..... Ferrule Connector/ Physical Contact

FF ..... Far-Field

FLIM ..... Fluorescence Lifetime Imaging Microscopy

FT ..... Frame-Transfer

FW1/100M ..... Full Width at 1/100 Maximum

FW1/10M ..... Full Width at 1/10 Maximum

FW1/eM ..... Full Width at 1/e (36.6%) Maximum

FWHM ..... Full Width at Half Maximum

Ge ..... Germanium

ICCD ..... Intensified Charge Coupled Device

IDQ ..... ID Quantique

IP ..... Image Plane

KTP ..... Potassium Titanyl Phosphate

LBO ..... Lithium Triborate

LC ..... Laser Components

LCOS ..... Liquid Crystal On Silicon

mom ..... momentum
MOS ..... Metal Oxide Semiconductor
MPD ..... Micro-Photon Devices
NbN ..... Niobium Nitride
ND ..... Neutral Density
NEP ..... Noise Equivalent Power
P ..... Phosphor
PE ..... Perkin Elmer
pos ..... position
PPLN ..... Periodically Poled Lithium Niobate
QKD ..... Quantum Key Distribution
RC ..... Resonant Cavity
rms ..... Root Mean Square
ROI ..... Region Of Intrest
SBR ..... Signal to Background Ratio
Si ..... Silicon
SLM ..... Spatial Light Modulator
SNR ..... Signal to Noise Ratio
SNSPD ..... Superconducting Nanowire Single Photon Detector
SPAD ..... Single-Photon Avalanche Diode
SPDC ..... Spontaneous Parametric Down-Conversion
SPDE ..... Single-Photon Detection Efficiency
TAC ..... Time to Amplitude Converter
TCSPC ..... Time-Correlated Single-Photon Counting
TDC ..... Time to Digital Converter
TOF ..... Time Of Flight
vi ..... Virtual Instrument
$\eta_{coupling}$ ..... Coupling efficiency
$\hbar$ ..... Planck's constant
λ ..... Wavelength
ω ..... Frequency of photon
Ψ ..... Transverse wave function of the post-selected two photon field
ρ_i ..... Transverse position of the photon
σ_{mom} ..... Length of momentum correlations

σ_{noise} ..... Standard deviation of camera noise

σ_{pos} ..... Length of position correlations

τ ..... Recharge time of a diode

°C ..... Degree Celsius

Hz ..... Hertz

MHz ..... Megahertz

µm ..... Micrometre

nm ..... Nanometre

ns ..... Nanosecond

Ω ..... Ohm

ps ..... Picosecond

c ..... Speed of light

δ ..... Phase modulation

ϕ ..... Electrical potential

k ..... Wave vector

C ..... Capacitance of diode

D^{max} ..... Maximum number of joint detections

e^- ..... Electron

E_C ..... Conduction band energy

E_F ..... Fermi energy

E_G ..... Band gap energy

E_V ..... Valence band energy

f ..... Focal length

K ..... Kelvin

n_o ..... Refractive index for the ordinary beam

n_{eo} ..... Refractive index for the extra-ordinary beam

R ..... Resistance of resistor

T ..... Temperature

LIST OF PUBLICATIONS BY THE CANDIDIATE

1. Daniel S. Tasca, Matthew P. Edgar, **Frauke Izdebski**, Gerald S. Buller and Miles J. Padgett. 'Optimizing the use of detector arrays for measuring intensity correlations of photon pairs.' *Phys. Rev. A*, 88(1):013816, 2013

2. Daniel S. Tasca, Matthew P. Edgar, **Frauke Izdebski**, Ryan E. Warburton, Jonathan Leach, Megan Agnew, Gerald S. Buller, Robert W. Boyd, and Miles J. Padgett. 'High-dimensional spatial entanglement observed with an electron multiplying CCD.' *Proc. SPIE 8542, Electro-Optical Remote Sensing, Photonic Technologies, and Applications VI*, 85421T, 2012.

3. Matthew P. Edgar, Daniel S. Tasca, **Frauke Izdebski**, Ryan E. Warburton, Jonathan Leach, Megan Agnew, Gerald S. Buller, Robert W. Boyd, and Miles J. Padgett. 'Imaging high-dimensional spatial entanglement with a camera'. *Nature Communications*, 3: 984 - 6 , 2012.

4. **Frauke Izdebski**, Jonathan Leach, Ryan E. Warburton, David. G. Ireland, Stephen M. Barnett, Alison M. Yao, Gerald S. Buller, and Miles J. Padgett. 'Quantum correlations in position, momentum and intermediate bases, measured using fiber arrays'. *Proc. SPIE 8274, Complex Light and Optical Forces VI.*, 82740E, 2012.

5. Jonathan Leach, Ryan E. Warburton, David G. Ireland, **Frauke Izdebski**, Stephen M. Barnett, Alison M. Yao, Gerald S. Buller, and Miles J. Padgett. 'Quantum correlations in position, momentum, and intermediate bases for a full optical field of view'. *Phys. Rev. A*, 85(1):013827, 2012.

6. Ryan E. Warburton, **Frauke Izdebski**, Christian Reimer, Jonathan Leach, David G. Ireland, Miles Padgett, and Gerald S. Buller. 'Single-photon position to time multiplexing using a fiber array'. *Opt Express*, 19(3):2670–2675, 2011.

CHAPTER 1

INTRODUCTION

In this chapter, a short overview of the work previously done in multi-pixel detectors, detecting spatial correlations of photon pairs, and low-light level imaging will be given. Additionally, the different thesis chapters will be outlined.

1.1 Multi-pixel detectors

There is a rising demand for multi-pixel detectors with single-photon sensitivity and which are able to perform time resolved measurements in the ns and ps regime. Applications which would benefit from detectors with time and spatial resolution include but are not limited to: biophotonics [1.1, 1.2], ranging [1.3, 1.4], and quantum optics [1.5, 1.6]. The ideal detector would have a high spatial resolution with a 100 % fill factor, 100 % single-photon detection efficiency, no noise present, each pixel would have uniform characteristics, and the time resolution should be at least in the ps regime. Unfortunately, such a detector does not exist and there is always a trade-off between the different detector characteristics.

While electron-multiplying CCD (EMCCD) cameras offer a high spatial resolution with a pixel size in the region of $\approx 16\,\mu m \times 16\,\mu m$, a fill factor of 100 % and high single-photon detection efficiencies in excess of 75 % [1.7], these multi-pixel detectors are lacking the ability to perform time resolved measurements in the sub-microsecond regime, needed for applications like ranging [1.3] or time resolved fluorescence spectroscopy [1.8].

Single Photon Avalanche Diode (SPAD) arrays [1.9, 1.10] are capable of performing position and time resolved measurements in the picosecond-regime. However, these detectors currently have a low fill factor of $< 5\,\%$ [1.11, p. 155], as typically the photo-

sensitive area of the 100 µm × 100 µm pixel measures only 20 µm in diameter. Using a carefully aligned micro-lens array might increase the fill factor to 90 %, however, due to the pixel size, the spatial resolution is relatively low. Also detector non-uniformities in detection efficiency, timing jitter, and dark count rate must be taken into account.

Instead of using a detector array, a single detector can be scanned across the desired positions. The scanning process may result in position errors during the movement of the detector and only data from one position at a time can be recorded, which leads to a greatly increased acquisition time.

An alternative approach would be to use a single SPAD connected to an array of fibres and a fibre combiner. The fibres have different pre-determined lengths, resulting in well defined arrival times at the detector. This approach combines the ability to measure multiple spatial positions simultaneously by correlating the temporal information of the photons with their spatial position. Another advantage is the cost efficiency and performance enhancement of using only one optimised detector. This makes it possible to observe differences in temporal response from different areas of the sample under test as well. The possibility to measure different positions simultaneously leads to an increased data acquisition rate. Therefore, applications where the time range for taking data is limited will benefit from this receiver system. Applications include fluorescence lifetime imaging microscopy (FLIM), ranging, and quantum imaging.

In this thesis, a multi-pixel detector was developed, using a fibre array with different pre-determined fibre lengths. The detector was specifically designed for an experiment measuring the spatial correlations of photon pairs, generated through spontaneous parametric down-conversion, in position and momentum bases.

1.2 Measuring spatial correlations of photon pairs

Photon pairs generated through spontaneous parametric down-conversion, a nonlinear process, which splits up a high-energy pump photon into two low-energy daughter photons, can possess very tight correlations. These tight correlations cannot be reproduced classically. Erwin Schrödinger [1.12] used the term *Entanglement* as a response to the famous *Gedankenexperiment* by Albert Einstein, Boris Podolsky, and Nathan Rosen (EPR) [1.13] to describe this kind of tightly correlated particles. En-

tangled particles can no longer be seen as separate systems as they are in the quantum mechanical state called *superposition*. The spatial position of the entangled particles has no effect on the entangled state and a measurement on one particle will instantaneously reveal information of the second particle. Einstein refers to this phenomenon as a "spooky action at a distance" [1.14, p. 158]. Different types of entanglement exist, for example the nucleus can be entangled in spin, while photons can be entangled in polarisation and/or position and momentum.

Historically, photon correlations in position and momentum were measured by scanning a single SPAD across the detection plane [1.15–1.18]. Correlated photons have also been measured with intensified CCD cameras in the momentum basis [1.7, 1.19–1.21]. However, these publications did not include the measurement of position correlations for the photon pairs.

In this thesis the transverse spatial correlatated photon pairs generated through spontaneous parametric down-conversion were measured with multi-pixel detectors in momentum *and* position bases. The detectors used in the experiments were a fibre array detector consisting of 8 fibres with different pre-determined lengths coupled into a single SPAD and an EMCCD camera, with a user-defined region of interest measuring 201 pixels × 201 pixels. The detected photon pairs in position and momentum bases were tested, to see if they fulfil the requirements for spatial entanglement.

1.3 Low-light level imaging

Multi-pixel arrays like EMCCD cameras have been used for a wide range of different low light level imaging applications like Astronomy [1.22, 1.23], Surveillance [1.24], Life Sciences Imaging [1.25–1.27], and Quantum Optics [1.28, 1.29]. EMCCD cameras offer single-photon sensitivity with a wavelength-dependent single-photon detection efficiencies of up to 90 %, combined with a good resolution due to their small pixel size of the order of 16 µm × 16 µm. Due to these characteristics, such camera technology is a useful resource for advanced imaging applications. However, the camera suffers from noise, which is prominent in extreme low-light level imaging applications. Therefore noise cancelling techniques must be developed in order to improve the quality of the recorded images with the EMCCD camera.

For this thesis, images with a low photon flux were recorded with an EMCCD camera. The image enhancement of using a noise reduction algorithm in combination with a correlated light source was investigated.

1.4 Overview of thesis

This thesis investigates the measurement of spatial correlations of photon pairs using different multi-pixel detectors and is organised as follows.

In Chapter 2, the theoretical background concerning SPADs and Time-Correlated Single-Photon Counting is outlined. An 8×1 pixel detector using position to time multiplexing is designed, built, and characterised. The full detection system is characterised with different types of single photon detectors in terms of single-photon detection efficiency and timing jitter. Additionally, the channel capacity is calculated for a thick and thin junction SPAD.

Chapter 3 outlines the theoretical background for the generation of correlated photon pairs through spontaneous parametric down-conversion, nonlinear crystals, and the requirements for spatial entanglement of photon pairs in position and momentum bases. The operational principle of spatial light modulators is described as well. Further full-system detector characterisation are performed. Spatial correlations of photons are measured in position and momentum in 8 positions simultaneously and calculations to verify quantum behaviour of the photon pairs are performed.

Quantum correlations over the full-field of view are measured with an EMCCD camera in Chapter 4. This chapter includes the theoretical background for EMCCD cameras. The EMCCD camera is characterised in terms of noise, and techniques to minimise the camera noise are explained, as well. The marginal, and joint correlations, as well as the dimensionality of the photon pairs are calculated.

In Chapter 5 the camera noise is reviewed and an algorithm to minimise the number of recorded noise events is introduced. The image enhancement of using a correlated light source with the algorithm applied to the data is investigated experimentally and with numerical simulations.

Finally, Chapter 6 summarises the conclusions of each chapter and reports the possibilities for future work in the fields studied within this thesis.

1.5 References

[1.1] Y. Hiraoka, T. Shimi and T. Haraguchi. 'Multispectral imaging fluorescence microscopy for living cells.' Cell. Struct. Funct., Vol. 27, (2002), pp. 367–374 (cited on page: 1).

[1.2] J. J. Field, R. Carriles and J. A. Squier. 'Photon-counting photobleaching measurements and the effect of dispersion in two-photon microscopy'. *Conference on Lasers and Electro-Optics, 2009 and 2009 Conference on Quantum electronics and Laser Science Conference. CLEO/QELS 2009.* (2009) (cited on page: 1).

[1.3] A. McCarthy, N. J. Krichel, N. R. Gemmel, X. Ren, M. G. Tanner, S. N. Dorenbos, V. Zwiller, R. H. Hadfield and G. S. Buller. 'Kilometer-range, high resolution depth imaging via 1560 nm wavelength single-photon detection'. Opt. Express, Vol. 21, (2013), pp. 8904–8915 (cited on page: 1).

[1.4] S. Bellisai, F. Guerrieri and S. Tisa. '3D ranging with a high speed imaging array'. *Conference on PhD Research in Microelectronics and Electronics (PRIME), 2010.* (2010) (cited on page: 1).

[1.5] A. R. Altman, K. G. Köprülü, E. Corndorf, P. Kumar and G. A. Barbosa. 'Quantum imaging of nonlocal spatial correlations induced by orbital angular momentum'. Phys. Rev. Lett., Vol. 94, (2005), p. 123601 (cited on page: 1).

[1.6] M. N. O'Sullivan-Hale, I. A. Khan, R. W. Boyd and J. C. Howell. 'Pixel entanglement: Experimental realization of optically entangled d=3 and d=6 qudits'. Phys. Rev. Lett., Vol. 94, (2005), p. 220501 (cited on page: 1).

[1.7] L. Zhang, L. Neves, J. S. Lundeen and I. A. Walmsley. 'A characterization of the single-photon sensitivity of an electron multiplying charge-coupled device'. J. Phys. B: At. Mol. Opt. Phys., Vol. 42, (2009), p. 114011 (cited on pages: 1, 3).

[1.8] D. P. Millar. 'Time-resolved fluorescence spectroscopy'. Curr. Opin. Struct. Biol., Vol. 6, (1996), pp. 637–642 (cited on page: 1).

[1.9] F. Guerrieri, S. Tisa, A. Tosi and F. Zappa. 'Two-dimensional SPAD imaging camera for photon counting'. IEEE Photonics J., Vol. 2, (2010), pp. 759–774 (cited on page: 1).

[1.10] S. Tisa, F. Guerrieri and F. Zappa. 'Monolithic array of 32 SPAD pixels for single-photon imaging at high frame rates'. Nucl. Instrum. Methods Phys. Res., Sect. A, Vol. 610, (2009), pp. 24–27 (cited on page: 1).

[1.11] F. Guerrieri. 'High-speed single-photon camera'. PhD thesis. Milano, Italy: Dipartimento di Elettronica e Informazione, Politecnico di Milano, 2010 (cited on page: 1).

[1.12] E. Schrödinger. 'Die gegenwärtige Situation in der Quantenmechanik'. Die Naturwissenschaften, Vol. 50, (1935), pp. 844–849 (cited on page: 2).

[1.13] A. Einstein, B. Podolsky and N. Rosen. 'Can quantum-mechanical description of physical reality be considered complete?' Physical review, Vol. 47, (1935), pp. 777–780 (cited on page: 2).

[1.14] A. Einstein, M. Born and H. Born. *The Born-Einstein letters: correspondence between Albert Einstein and Max and Hedwig Born from 1916-1955, with commentaries by Max Born*. Macmillan, 1971 (cited on page: 3).

[1.15] J. C. Howell, R. S. Bennink, S. J. Bentley and R. W. Boyd. 'Realization of the Einstein-Podolsky-Rosen paradox using momentum- and position-entangled photons from spontaneous parametric down conversion'. Phys. Rev. Lett., Vol. 92, (2004), p. 210403 (cited on page: 3).

[1.16] M. D'Angelo, Y.-H. Kim, S. P. Kulik and Y. Shih. 'Identifying entanglement using quantum ghost interference and imaging'. Phys. Rev. Lett., Vol. 92, (2004), p. 233601 (cited on page: 3).

[1.17] L. Neves, G. Lima, J. G. Aguirre-Gómez, C. H. Monken, C. Saavedra and S. Pádua. 'Generation of entangled states of qudits using twin photons'. Phys. Rev. Lett., Vol. 94, (2005), p. 100501 (cited on page: 3).

[1.18] M. P. Almeida, S. P. Walborn and P. H. Souto Ribeiro. 'Experimental investigation of quantum key distribution with position and momentum of photon pairs'. Phys. Rev. A, Vol. 72, (2005), p. 022313 (cited on page: 3).

[1.19] S. S. R. Oemrawsingh, W. J. van Drunen, E. R. Eliel and J. P. Woerdman. 'Two-dimensional wave-vector correlations in spontaneous parametric downconversion explored with an intensified CCD camera'. J. Opt. Soc. Am. B: Opt. Phys., Vol. 19, (2002), pp. 2391–2395 (cited on page: 3).

[1.20] G. Brida, I. P. Degiovanni, M. Genovese, M. L. Rastello and I. Ruo-Berchera. 'Detection of multimode spatial correlation in PDC and application to the absolute calibration of a CCD camera'. Opt. Express, Vol. 18, (2010), pp. 20572–20584 (cited on page: 3).

[1.21] B. M. Jost, A. V. Sergienko, A. F. Abouraddy, B. E. A. Saleh and M. C. Teich. 'Spatial correlations of spontaneously down-converted photon pairs detected with a single-photon-sensitive CCD camera'. Opt. Express, Vol. 3, (1998), pp. 81–88 (cited on page: 3).

[1.22] N. M. Law, C. D. Mackay and J. E. Baldwin. 'Lucky imaging: high angular resolution imaging in the visible from the ground'. A & A, Vol. 446, (2006), pp. 739–745 (cited on page: 3).

[1.23] C. Mackay, K. Weller and F. Suess. 'Photon counting EMCCDs: New opportunities for high time resolution astrophysics'. *Proc. SPIE 8453, High Energy, Optical, and Infrared Detectors for Astronomy V.* (2012), p. 845302 (cited on page: 3).

[1.24] United Vision Solutions. *EV3000-D-IR-750 - data sheet.* online, last accessed 2013-04-30. (2011). URL: `http://www.longrangecamera.com` (cited on page: 3).

[1.25] H. R. Petty. 'Fluorescence microscopy: Established and emerging methods, experimental strategies, and applications in immunology'. Micros. Res. Tech., Vol. 70, (2007), pp. 687–709 (cited on page: 3).

[1.26] G. Rong, H. Wang, L. R. Skewis and B. M. Reinhard. 'Resolving sub-diffraction limit encounters in nanoparticle tracking using live cell plasmon coupling microscopy'. Nano Lett, Vol. 8, (2008), pp. 3386–3393 (cited on page: 3).

[1.27] M. Burkhardt and P. Schwille. 'Electron multiplying CCD based detection for spatially resolved fluorescence correlation spectroscopy'. Opt. Express, Vol. 14, (2006), pp. 5013–5020 (cited on page: 3).

[1.28] M. P. Edgar, D. S. Tasca, F. Izdebski, R. E. Warburton, J. Leach, M. Agnew, G. S. Buller, R. W. Boyd and M. J. Padgett. 'Imaging high-dimensional spatial entanglement with a camera'. Nat. Commun., Vol. 3, (2012), p. 984 (cited on page: 3).

[1.29] J.-L. Blanchet, F. Devaux, L. Furfaro and E. Lantz. 'Purely spatial coincidences of twin photons in parametric spontaneous down-conversion'. Phys. Rev. A, Vol. 81, (2010), p. 043825 (cited on page: 3).

CHAPTER 2

SINGLE-PHOTON POSITION TO TIME MULTIPLEXING USING A FIBRE ARRAY

For this chapter, the aim was to design, to build, and to characterise a receiver system capable of detecting multiple spatial positions with a single detector. This was accomplished by converting the spatial information from single-photons into a temporal signature. In this chapter, the operating principles for Single-Photon Avalanche Diodes (SPADs), Superconducting Nanowire Single-Photon Detectors (SNSPDs) and noise associated with the detection process are discussed. The receiver system was characterised in terms of single-photon detection efficiency and timing jitter with different types of detectors, namely: thick junction SPAD, thin junction SPADs, a thin junction SPAD with enhanced detection efficiency due to a resonant cavity, and a SNSPD. The channel capacity of the receiver system was determined with a thick and a thin junction SPAD.

2.1 Theoretical Background

The following section details the operating principle of SPADs and SNSPDs. Furthermore the origin of noise in detector systems is explained and a short introduction to Time-Correlated Single-Photon Counting (TCSPC) is given.

2.1.1 *Avalanche Photodiodes*

Avalanche Photodiodes (APD) are optical detectors made from semiconductor diodes. Materials with an electrical resistivity ranging from $1 \times 10^{-2}\,\Omega\,\mathrm{cm}$ to $1 \times 10^{9}\,\Omega\,\mathrm{cm}$ [2.1, p. 207] and a band gap energy between 0 eV and 5 eV at room temperature are classified as semiconductors. The properties of a semiconductor can be manipulated by,

for example, the introduction of dopants and by band structure engineering. Due to the temperature dependency of semiconductors, changing the ambient temperature can also alter their properties. Semiconductors can be divided into elemental semiconductors, which consist of group IV elements like silicon (Si) and germanium (Ge), and compound semiconductors, which are formed from elements of different groups. Binary compounds for example can be formed from the following groups: III-V (e.g. GaAs), I-VII and II-VI (e.g. ZnSe). Semiconductor materials suitable for single-photon detection include Si, Ge and various III-V compound semiconductors.

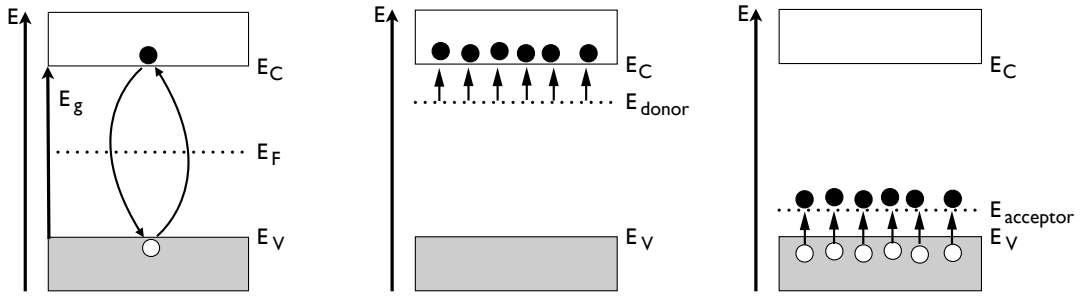

(a) Intrinsic (b) Extrinsic with n-type doping (c) Extrinsic with p-type doping

Figure 2.1: *Schematic illustration of intrinsic and extrinsic semiconductors at temperatures above* 0 K. *(a) depicts an intrinsic semiconductor without any impurities. The Fermi level lies within the forbidden gap between the valence and conduction bands. (b) shows an extrinsic semiconductor with n-type doping. The donor level is located close to the conduction band. At* 0 K *this donor level is filled with electrons and at higher temperatures these electrons are thermally excited and promoted to the conduction band. (c) is an extrinsic semiconductor with p-type doping. Here the acceptor level lies close to the valence band. At* 0 K *the valence band is empty, but at higher temperatures, electrons from the valence band are promoted to the acceptor level, leaving behind holes in the valence band.*

Intrinsic semiconductors possess no impurities and lattice defects. At a temperature of 0 K the conduction band is empty and only the valance band is filled, as shown in Figure 2.1(a). The valence and conduction band are separated by the band gap energy E_g. The band gap energy is the difference of the minimum conduction band energy E_C and the maximum energy of the valence band E_V. The Fermi energy E_F lies within the forbidden gap between the conduction and the valence bands and is, in semiconductors, determined by the carrier concentration. For an intrinsic material, the concentration of electrons in the conduction band is equal to the concentration of holes in the valence band and therefore E_F is located approximately in the middle of the band gap energy. At higher temperatures the conduction band starts to fill up, as electron- hole pairs are created through thermal excitation. For an intrinsic semiconductor the gen-

eration rate for the electron- hole pairs equals the recombination rate of the electron-hole pair.

In contrast, extrinsic semiconductors possess impurities like dopants. The Fermi energy of the doped semiconductor lies close in energy to the impurity levels arising from the donor or acceptor levels. In the case of a semiconductor with n-type doping, electrons stored in the donor level are thermally excited and fill up the conduction band, as shown in Figure 2.1(b). The Fermi energy lies close to the donor energy levels, as the the concentration of electrons in the conduction band is higher than the concentration of holes in the valence band.

For p-type doping the acceptor-level is empty for 0 K. At higher temperatures the acceptor level fills up with electrons from the valence band, leaving holes behind, as shown in Figure 2.1(c). Due to the high concentration of holes in the valence band, the Fermi energy approximately coincidences with the acceptor energy levels. Each impurity atom can accept one electron from the valence band leaving behind holes.

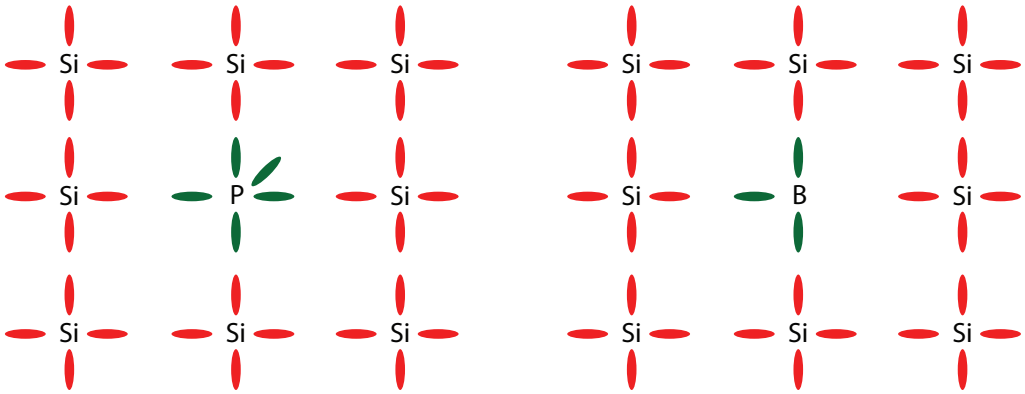

(a) n-type doping (b) p-type doping

Figure 2.2: *Schematic illustration of valence electrons for different semiconductor materials. The material to be doped is Si. (a) shows n-type doping as because P has five valence-electrons compared to the four valence-electrons provided by Si. The n-doped material is now negatively charged. (b) depicts p-type doping of Si with B. As Boron possesses only three valence electrons, the doped material is now positively charged.*

The diode is formed by a junction between a p-type semiconductor, where excess holes are predominant and a n-type semiconductor, where electrons are predominant. The predominance of either holes or electrons is caused by doping the semiconductor material. Si is a tetravalent element with four valence electrons in the outer-shell. Doping the Si-semiconductor with, for example, phosphorus (P), a pentavalent element, would lead to a n-type semiconductor layer because phosphorus has five valence- electrons,

which is one more valence-electron compared to Si. In order to produce a p-type semiconductor, silicon can be doped with boron (B), as boron, a trivalent element, has only three valence-electrons as shown in Figure 2.2 for clarity.

At the pn-junction of the photodiode the depletion region is formed, which is free from all carriers. The junction is reversed biased when the n-type semiconductor is at a higher potential than the p-type semiconductor as shown in Figure 2.3. At the barrier of the n-type and the p-type semiconductor layers the electrons and holes diffuse into the region, leading to recombination of electrons and holes. Stationary charges caused by donor and acceptor ions are still present and cause a depletion area with an internal electric field across it. If a photon gets absorbed within this region and an electron-hole pair is generated then the electric field separates the electron and the hole.

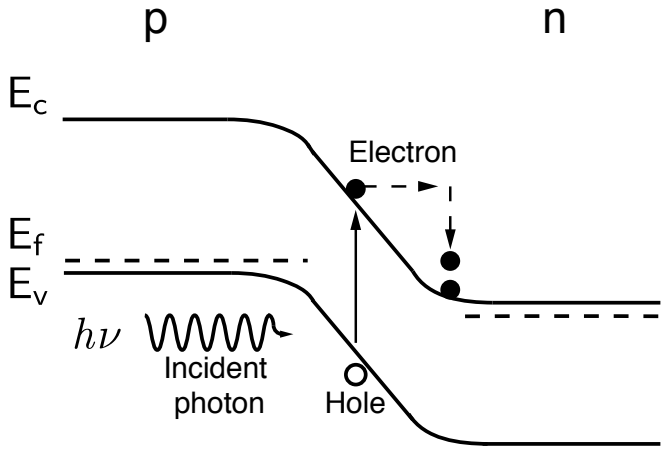

Figure 2.3: *An incident photon is absorbed in the depletion region of the pn- junction. In this process, an electron is promoted from the valence band to the conduction band, leaving behind a hole. In the depletion area there is a high internal electric field, accelerating the electron. If the kinetic energy of the accelerated electron is sufficiently high impact ionisation occurs after the electron collides with an atom in the lattice. The secondary electrons will be accelerated in the electric field as well and knock out further electrons, starting a self-sustaining avalanche when the device is operated in bias region IV see Figure 2.4.*

If the electric field is high enough then a drifting electron or hole will be accelerated and gains enough kinetic energy to excite further electrons or holes after a collision with an atom in the semiconductor lattice (see Figure 2.3). This process is known as impact ionisation. The secondary electrons will be accelerated in the electric field as well and knock out further electrons, starting an avalanche. The same process occurs for the holes accelerated in the opposite direction. The probability of this ionisation event to happen depends on the impact ionisation coefficient, which is dependent on the electric field and the temperature.

For Si- the ionisation coefficient k is greater for electrons than for holes, so that ionisation events are more like to be caused by electrons than by holes. The electrons generated by impact ionisation lead to an internal amplification of the photocurrent within the APD. When the APD is operated in linear mode (region III in Figure 2.4) then current gain in excess of 10 to 1000 [2.2] is readily achievable. The current gain depends on the bias voltage.

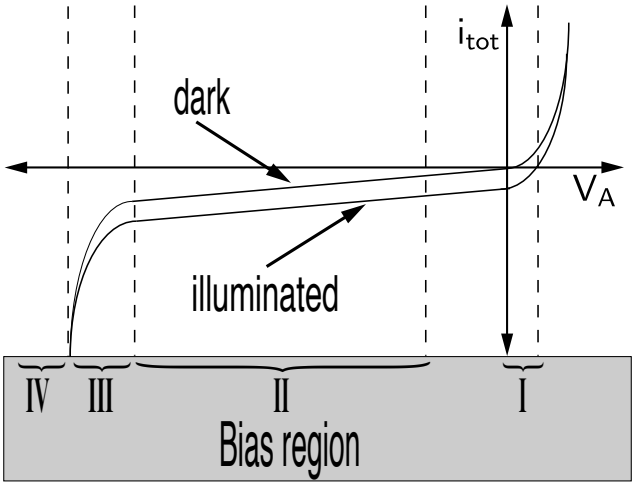

Figure 2.4: *Current-Voltage characteristic of an avalanche photodiode [2.3]. Single-photon avalanche diodes are operated in bias region IV, which is for dark and illuminated detectors above the reverse breakdown voltage.*

Single-Photon Avalanche Diodes are operated above the reverse breakdown voltage (in the so-called Geiger Mode) and their operating principle will be detailed in the following section.

2.1.2 *Single-Photon Avalanche Photodiodes*

The high electric field region is free of conducting carriers, when it is biased above the reverse bias avalanche breakdown voltage (Region IV in Figure 2.4), so that no current flows or an avalanche can occur. When a single carrier is injected into the high electric field region, it can give rise to an exponentially growing avalanche current. The avalanche current is self-sustaining and must be quenched in order to reset the device. The current must be quenched in order to prevent overheating and damage to the diode. Additionally, carriers must be given sufficient time to leave the high electric field region and the bias must be restored above the breakdown value, before another photon can be detected.

The dead time of the detector, in which no further photon can be detected, depends on the type of quenching circuit. A passive quenching circuit includes a large series resistor, which is responsible for the self-quenching. The recharge time (τ = RC) of the diode is limited by the resistance of the large series resistor R and the capacitance of the diode C. The long recharge time of the diode limits the maximum count rate. For a Si- detector with a detection area of 1 mm^2 at room temperature, typical values for the large load resistance are 200 kΩ up to 2.5 MΩ for a thick junction SPAD and a typical value for the capacitance of the diode is 1 pF [2.4]. This leads to a recharge time of more than 2.5 µs for a load resistance of 2.5 MΩ.

An active quenching circuit includes external circuitry, which reduces the diode voltage as quickly as possible to several volts below the breakdown voltage. The diode is recharged as fast as possible, reducing the dead time to less than 50 ns [2.5] and therefore enabling count rates in the order of 10 Mcps. This is accomplished by a fast comparator in the external circuitry. After a photon is absorbed and the avalanche current rises, the comparator senses the rising avalanche current and subsequently switches the bias voltage source to a value well below the breakdown voltage and the avalanche is quenched. The voltage is kept below the breakdown voltage in order to allow the release of any trapped carriers and therefore to avoid the effects of afterpulsing. Afterpulsing is a phenomenon where trapped carriers are later released and initiate an unwanted avalanche event.

2.1.3 *SPAD Designs*

The two main types of Si-SPAD designs described in this chapter are thick junction and thin junction SPADs. The difference between those types of SPADs is the thickness of the depletion region, where the absorption of the photons takes place, as depicted in Figure 2.5. Thick junction SPADs have a depletion thickness of several 10's µm, leading to high Single-Photon Detection Efficiencies (SPDE) of up to 65% at 650 nm [2.6]. However, the detector jitter in thick junction SPADs is relatively high. In recent commercially available thick junction SPADs the jitter is in the order of 400 ps [2.7]. In contrast thin junction SPADs possess a depletion layer thickness of a couple of micrometers, resulting in a timing jitter in the order of 35 ps [2.8]. Due to the thinness of the depletion region fewer photons are absorbed and contribute to the photocurrent,

leading to a lower SPDE of approximately 37% at 650 nm [2.8]. For thin junction SPADs based on CMOS technology the SPDE is even lower. For λ = 650 nm the SPDE is ≈ 23 % [2.9]. At higher wavelengths the difference in SPDE between the thick and thin junction SPADs increases even further. For example at 800 nm the SPDE for a thick junction SPAD is of the order of 70 %, while the thin junction SPAD possesses an SPDE of 15 % [2.10] and the thin junction SPAD based on CMOS technology has a SPDE of merely 5 %.

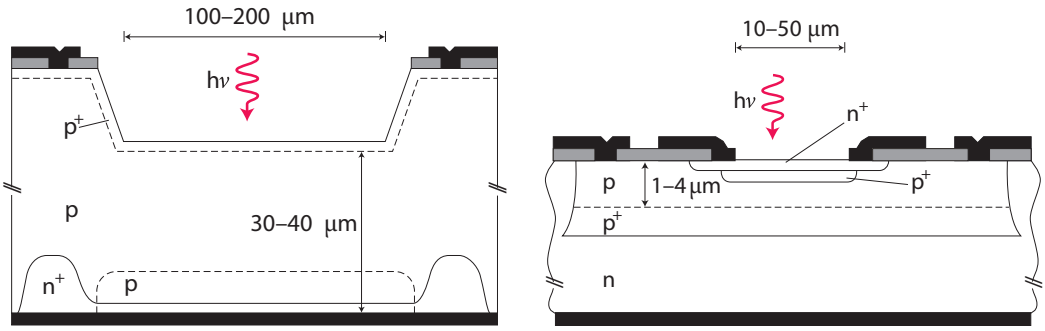

(a) Thick junction (b) Thin junction

Figure 2.5: *Comparison of (a) thick and (b) thin junction Si-SPAD designs. The characteristics of the SPAD in terms of SPDE and timing jitter depend in the thickness of the depletion region. A thick depletion region will result in a higher SPDE at the cost of a high timing jitter. Figure taken from Ref. [2.11, 2.12].*

Evidently, there is a relationship between the thickness of the junction and the resulting characteristics of the device. A thick junction SPAD will have a higher SPDE than a thin junction SPAD, but the thick junction SPAD has a considerably higher jitter compared to the thin junction SPAD leading to a trade off between SPDE and jitter. The lower SPDE of thin junction SPADs can be improved by incorporating a resonant cavity. This way the detection efficiency of the thin junction can be increased from 10% at 850 nm to 34%, while keeping the jitter at a low level [2.13]. In order to manufacture a resonant cavity-enhanced detector, a thin junction SPAD is fabricated on top of a reflecting silicon on insulator substrate. The substrate contains a two period distributed Bragg reflector, which is designed to have a reflectivity in excess of 90% over a wavelength range of 750 nm to 950 nm. A Fabry-Pérot cavity is formed between the distributed Bragg reflector and the semiconductor/air top interface, which enhances the optical field in the SPAD at resonant wavelengths. With this approach the SPDE of the SPAD can be improved without increasing the timing jitter.

2.1.4 *Wavelength Dependency*

The absorption of light in semiconductor materials is wavelength dependent, which means that the detector can only absorb photons within a certain wavelength range. Each semiconductor has a certain cut-off wavelength $\lambda_{\text{cut-off}}$ after which it cannot register any incoming photons as shown in Figure 2.6. For wavelengths longer than $\lambda_{\text{cut-off}}$ the photon energy is too small to excite electrons and therefore the detector response drops to zero.

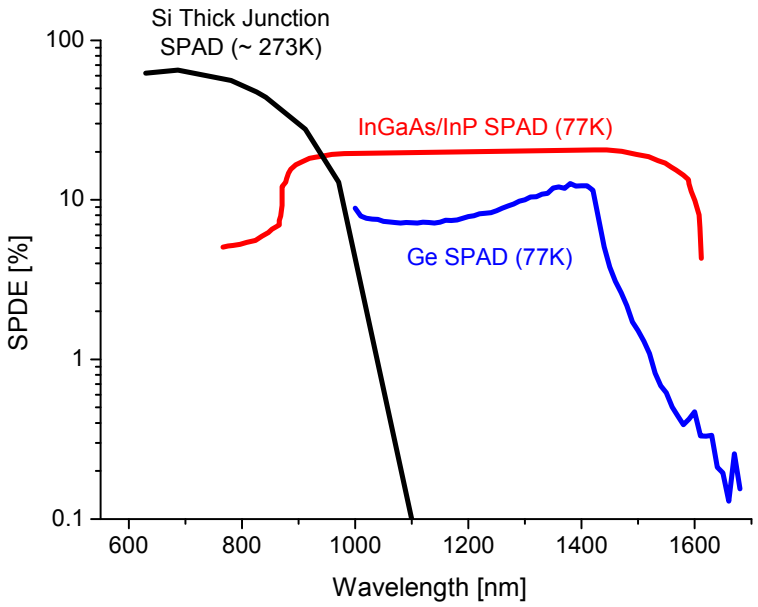

Figure 2.6: *Single-photon detection efficiencies as a function of wavelength for Si, InGaAs and Ge SPADs at different temperatures [2.10].*

The cut-off wavelength $\lambda_{\text{cut-off}}$ is defined as the maximum wavelength at which the detector can detect incident photons and depends on the band gap energy E_g (in eV) of the respective semiconductor, where $\lambda_{\text{cut-off}} = 1.24\,\mu\text{m eV}/E_g$.

The band gap energy E_g is mostly given for either 0 K or 300 K. For calculating the band gap energy at different temperatures the Varshni equation [2.14] is a good approximation.

$$E_g(T) = E_g(0) - \frac{\alpha \cdot T^2}{T + \beta} \tag{2.1}$$

$E_g(0)$ is the band gap energy at absolute zero, α and β are fitting parameters. α is related to the electron-phonon interaction, while β is related to the temperature. For higher temperatures, the band gap energy shifts to lower energies.

Si photon detectors can be used in the visible and near infrared wavelength range. Al-

though silicon is an indirect band gap material and therefore the absorption is less efficient than for a direct band gap semiconductor, due to the advanced silicon semiconductor technology Si detectors are extensively used in many applications. Ge detectors can be used in the infrared. Germanium APDs have a comparatively high excess noise factor (ENF), which limits the performance of the detector. The ENF's origin is the stochastic process of the electron multiplication for APDs. Only the mean value of the multiplication can be determined, but it is impossible to know the gain for each primary charge. An alternative to using Ge- detectors in the 1.0 µm to 1.6 µm region are InGaAs- detectors. InGaAs is a direct band gap semiconductor compound material, which has a much higher absorption coefficient and therefore a higher detection efficiency than Ge. InGaAs APDs also possess a lower excess noise factor, which makes these detectors fast enough for high speed telecommunication applications.

2.1.5 *Superconducting Nanowire Single-Photon Detectors*

Superconducting Nanowire Single-Photon Detectors (SNSPD) can detect single-photons in the visible and near-infrared wavelength region. The advantages of SNSPDs are their low dark count rates below 100 Hz [2.15], their short recovery time of approximately 20 ns for large area detectors and a low symmetric timing jitter of less than 30 ps in a multi-element detector [2.16] or less than 60 ps for a single large area Niobium Nitride (NbN) nanowire covering an area of 20 µm × 20 µm [2.17]. The detector response of an SNSPD possesses a near- Gaussian shape without a slowly decaying tail, which is present in Si-SPADS, as shown in Figure 2.7.

The detector used in this experiment consists of a 100 nm-wide NbN nanowire, which was patterned by electron beam lithography in an ultra-thin niobium nitride superconducting film. The film is approximately 5 nm thick. For a high SPDE and a high probability of photon absorption the nanowire is arranged in a meander style, covering an area of 20 µm × 20 µm with a fill factor of 50% [2.11]. The meandering wire must be uniform along its length otherwise the detector will suffer from different hotspot resistances resulting in different pulse rise times, which will broaden the overall timing jitter [2.19]. The use of wider nanowires is not feasible, as the nanowire would not be sufficiently resistive. The nanowire, used for the experiments in this thesis, is cooled down to temperatures below 4 K (range of 1.8 K to 4 K) with a closed cycle refri-

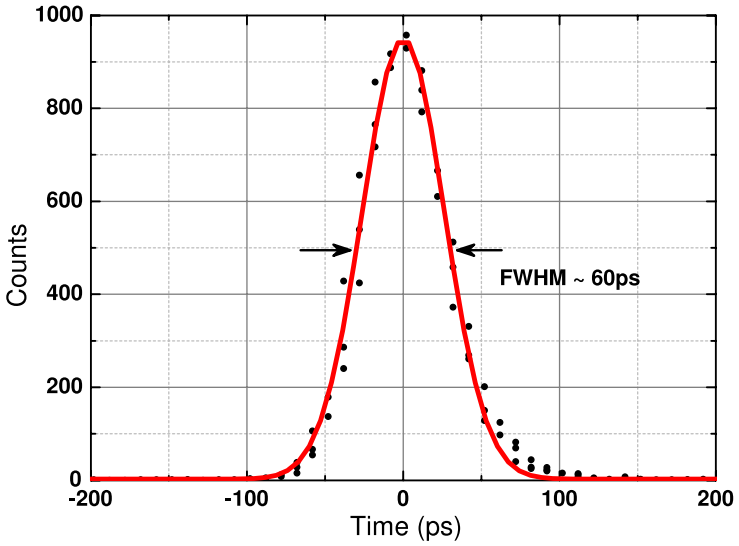

Figure 2.7: *Detector response from a large area SNSPD [2.18].*

gerator. This temperature is below the superconducting transition temperature of the NbN film. The transition temperature depends on the layer thickness and for a 5 nm thick wire, the typical transitions temperature is 7 K [2.20, p. 167]

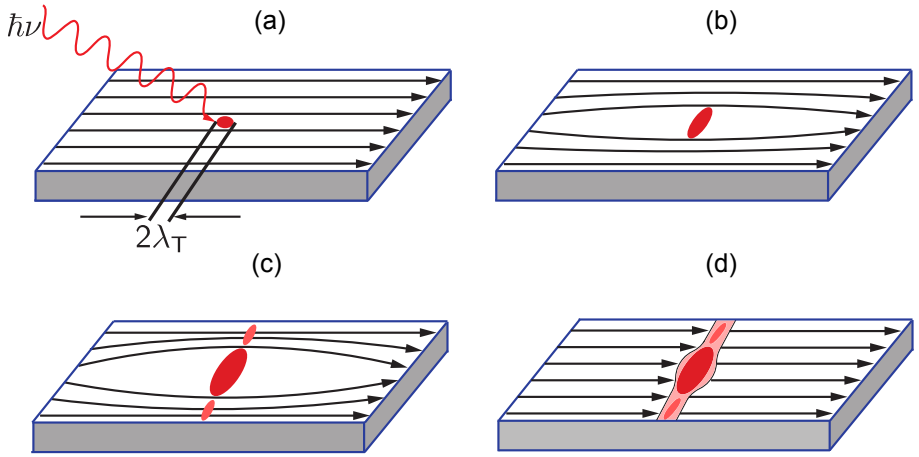

Figure 2.8: *Schematic illustration of the working principle of a superconducting nanowire detector [2.21].*

The nanowire is biased just below its critical current as at higher currents the nanowire becomes resistive. When a photon gets absorbed by the nanowire, the absorbed photon splits up Cooper pairs [2.22] and therefore reduces the local critical current below that of the bias current and a localised hotspot is formed as illustrated in Figure 2.8(a). The hotspot is a local non-superconducting region with a thermalisation length of $2\lambda_T$. In Figure 2.8(b) the hotspot redirects the current around itself. In Figure 2.8(c) the excited electrons spread from the initial point where the photon had been absorbed forcing the current to be diverted through the edge region of the nanowire. In Figure 2.8(d) these edge regions for the current density exceed the critical current

density and cause a resistive stripe across the width of the nanowire. The resistive stripe triggers a fast measurable voltage pulse across an external lead resistance. As the nanowire cools down to its operating temperature, the hot spot shrinks and the nanowire returns to its superconducting state and is reset. Typically the reset time is 10's ns.

2.1.6 *Origin of noise in detectors*

In each detector, noise is inevitably present. The Dark Count Rate (DCR) is the number of counts per second for dark events, which triggered the detector. An example for such a dark event is the thermal excitation of carriers. The Noise Equivalent Power (NEP) gives information about the sensitivity of the detector. The minimal detectable signal, where the Signal to Noise ratio (SNR) is unity, is given by the NEP, which means, the lower the NEP is, the higher is the sensitivity of the detector. The NEP can be expressed as $NEP = \mathrm{h}\nu/\mathrm{SPDE} \cdot \sqrt{2\,\mathrm{DCR}}$, where $\mathrm{h}\nu$ is the energy of the incident photon and SPDE is the Single-Photon Detection Efficiency [2.23]. The NEP represents the least measurable optical power with 1 Hz bandpass noise filtering, which represents a total counting time of 1 s in single-photon counting.

2.2 Time-Correlated Single-Photon Counting

Time-Correlated Single-Photon Counting (TCSPC) is based on the detection of single-photons from a pulsed light source. A basic TCSPC setup is depicted in Figure 2.9. A master clock sends out an electrical pulse to the pulsed light source, and to the photon counting card in order to start the timing process. The laser emits a single pulse, which eventually gets detected by the single-photon detector. Once the detector registered an event (either a photon or a dark count), it sends an electronic signal to the photon counting card to stop the measurement.

The waveform of the optical pulse is reconstructed from individually detected single-photons in many measurements. The light intensity must be very low to avoid pulse pile-up, which can lead to significant signal distortion, when more than one signal is present in one signal period. In this case only the photons at the beginning of the

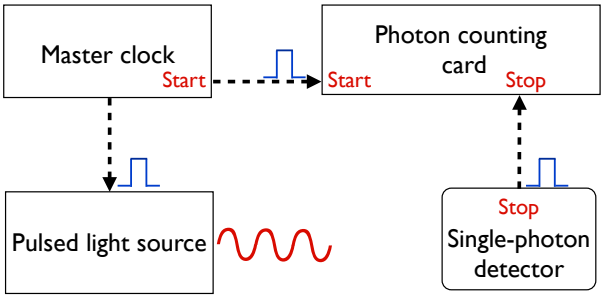

Figure 2.9: *Principle experimental setup for TCSPC.*

signal period will be recorded, while the chance to measure a photon in the latter part of the signal period is greatly reduced. In order to avoid pulse pile up the stop rate must be smaller than 10% of the start rate. State of the art TCSPC devices are now able to operate at count rates of several million counts per second. The individual signal pulses are randomly distributed and when one photon or dark count gets detected, its time within the signal period is measured and a logic “1” is added to the memory with an address proportional to the detection time. This measurement is repeated and waveform of the optical pulse builds up in the histogram as shown in Figure 2.10.

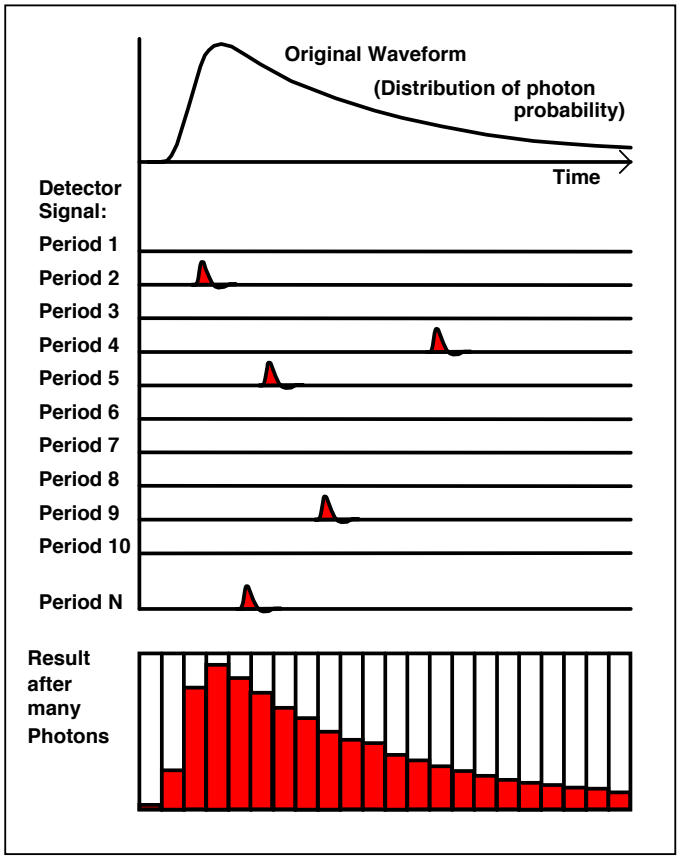

Figure 2.10: *Principle of Time Correlated Single-Photon Counting [2.24, p. 16]. The bottom graph depicts a histogram after many photons were detected. For each detected photon, the detection time within the signal period is measured and a logic "1" is added to the memory to an address proportional to the detection time.*

In TCSPC there are a number of contributors to jitter. One major contributor is detector jitter, caused by statistical variations in the rise time. This effect can depend on the the wavelength of the light sources as well as the material of the detector is wavelength dependent. In addition to detector jitter, the timing jitter in the discriminator at the input of the photon counter increases the overall timing jitter. The amplitude of the single-photon pulse varies, which causes a variable delay in the trigger circuit. Although the timing jitter due to amplitude fluctuations can be limited with a Constant Fraction Discriminator (CFD), it can not be fully avoided. The amplitude jitter is caused by the random amplification mechanisms in the detector. If a simple leading edge discriminator is used, it would trigger when the leading edge of the input pulse reaches the predefined threshold. Even if the leading edge discriminator would be infinitely fast, the amplitude jitter would introduce a timing jitter in the order of the pulse rise time (see Figure 2.11).

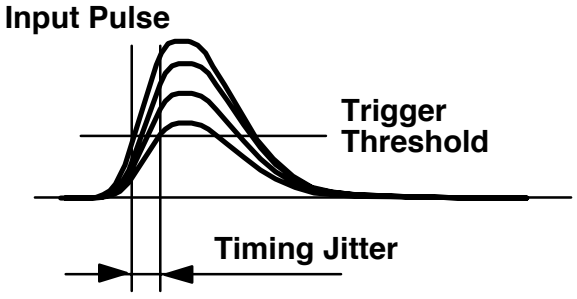

Figure 2.11: *Example for leading edge triggering and the resulting timing jitter. [2.24, p. 35] By just setting a trigger threshold in pulse amplitude, the timing jitter introduced by a leading edge discriminator would be at least of the order of the pulse rise time.*

A CFD triggers at a constant fraction of the pulse amplitude and therefore avoids the pulse amplitude induced timing jitter. The CFD triggers at the zero- cross point of the sum of the input pulse and the inverted and delayed input pulse.

The temporal position of the cross over point is independent of the pulse height and therefore minimises the timing jitter caused by amplitude jitter (see Figure 2.12). The threshold or amplitude window (depending on the discriminator) can be adjusted to reject noise like pre-amplifier or small background pulses from the detector.

The Time to Amplitude Converter (TAC) measures the time between the detected photons at the detector input and the next pulse from the reference input. This measurement technique is called the reversed start-stop method. The advantage of this method is that the speed requirement for the TAC is reduced as the working cycle

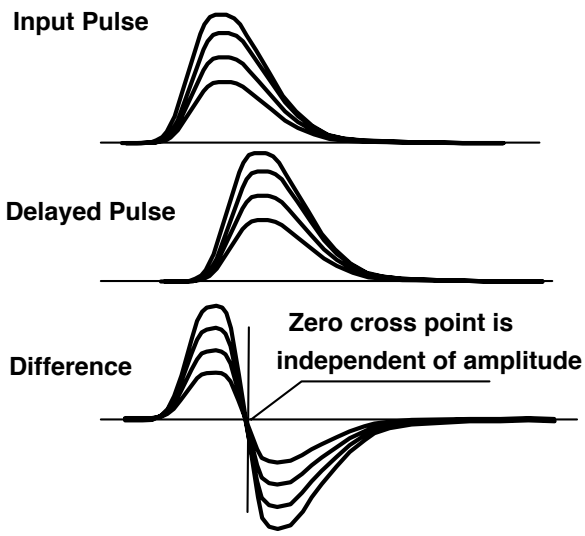

Figure 2.12: *Principle of Constant Fraction Triggering [2.24, p. 35]. The CFD triggers at a constant fraction of the pulse amplitude and therefore avoids the pulse amplitude induced timing jitter, which is present in leading edge triggers. The CFD triggers at the zero-cross point of the input pulse and the delayed and inverted input pulse.*

(start-stop-reset) has to be performed at the photon detection rate, which is considerably lower than the pulse repetition rate. When the TAC is started by a pulse at the start input, a linear ramp voltage is generated until stopped by a pulse arriving at the stop input. The TAC generates an output voltage which is dependent on the temporal position of the photon. The minimum time resolution of the TAC used in the Becker & Hickl photon counting card SPC 600 is roughly 13 ps [2.24, p. 355]. The TAC range can be set from 50 ns to 2 µs and the TAC range can be divided into up to 4096 time channels.

The Analogue to Digital Converter (ADC) converts the amplified TAC signal into the address of the memory. The ADC resolves the TAC signal into up to 4096 bins (time channels) depending on the histogram settings. The maximum number of time bins depends also on the max. number of curves in memory and the max. number of detector channels. Each bin width must be equal within 1% or better and therefore the ADC must be extremely accurate [2.24, p. 355]. The TAC signal is converted into the different time channels with a channel uniformity of 1%. Instead of using a TAC and an ADC, these can be replaced with a single digital circuit also known as Time to Digital Converter (TDC). These circuits can measure time differences based on the delay times of signal in semiconductor logic gates or the conductor stripes between them, leading to resolutions below the actual gate delay [2.25, p. 6]. PicoQuant's PicoHarp 300 and HydraHarp 400 offer an electrical time resolution of < 12 ps rms [2.26, 2.27].

2.3 Experiments

For single-photon counting experiments, position to time multiplexing, where different positions can be measured simultaneously, leads to numerous advantages like rapid data acquisition and a reduced loss of counted photons compared to a single detector. Single-photon detectors can be scanned over an area, but the single detector can only measure one spatial position at a time. The conversion of timing to position information for using the V-Groove fibre array is accomplished by the use of fibres differing in length by a pre-determined distance for equally stepped arrival times of each channel at the detector. Using a fibre combiner it is possible to combine the signals from the V-Groove fibre array to a single output fibre. The single output fibre can then be coupled to an individual detector. The receiver system has been characterised in terms of efficiency and timing jitter for different single-photon detectors.

2.3.1 *Single-Photon Detector Characterisation*

In this section different single-photon detectors are characterised in terms of efficiency and timing jitter without any additional components, namely the V-Groove fibre array and the fibre combiner. The full receiver setup with all components is characterised in Sections 2.3.3 and 2.3.4.

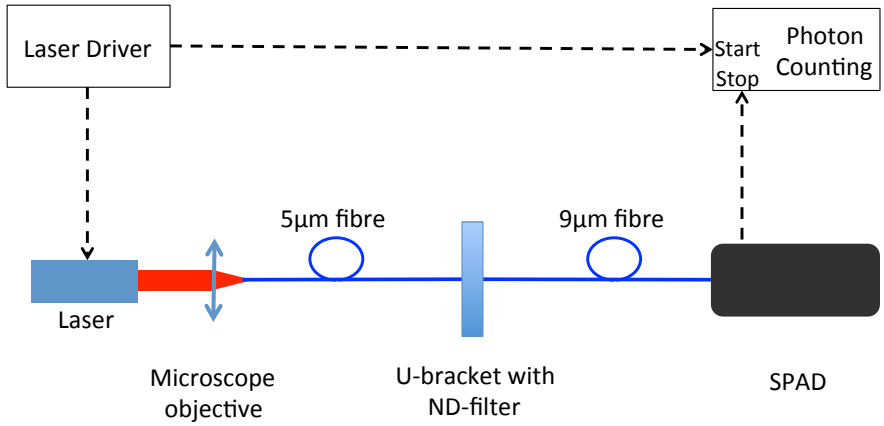

Figure 2.13: *Experimental TCSPC setup for detector characterisation. The single-photon detectors were characterised with a photon counting card from Becker and Hickl (SPC 600) The laser driver provided the start signal for the measurement on the photon counting card and provided a short pulse to enable the laser. Once the SPAD detected a photon an electronic output pulse was sent to the photon counting card to stop the measurement. The ND-filters were used to reduce the photon flux to the detector and to ensure safe and statistically correct operating conditions.*

The setup for the timing jitter and detection efficiency measurements is shown in Figure 2.13. A pulsed laser diode with a repetition rate of 20 MHz and an emission wavelength of λ = 850 nm is coupled into a singlemode fibre with a core diameter of 5 µm. The incident light is then attenuated by Neutral Density (ND) filters. This ensures a low photon flux arriving at the single-photon detector under test and avoids pulse pile-up. After the U-bracket the light its coupled into a 9 µm fibre. This fibre was chosen, as it can be used more easily with fibre-coupled detectors particularly the Resonant Cavity (RC) SPAD. The electronic output from the detector was connected to the CFD input of the Photon Counting Card SPC 600 from Becker and Hickl. Each measurement lasted for 100 s.

Ideally the SPADs should have been characterised at a wavelength close to λ = 710 nm because this was the operational wavelength for the follow up experiment (see Chapter 3). Unfortunately, no calibrated attenuation was available at this wavelength. The only calibrated attenuator available was for λ = 850 nm.

The following detectors were characterised:

Perkin Elmer SPAD: The Perkin Elmer single-photon detector is a commercially available thick junction Si-SPAD. The photosensitive area has a diameter of 180 µm. Typical values for the detection efficiency at λ = 850 nm is 43% and typical values for the timing jitter at FWHM are 350 ps [2.6].

MPD: The detector from MPD (Micro-Photon-Devices) is a thin junction Si-SPAD. This detector possesses a pigtailed 62.5 µm graded index fibre. The fibre is directly coupled onto a detector with a diameter of 62.5 µm. Typical values for the detection efficiency at λ = 850 nm is 10% and typical values for the timing jitter at FWHM are 50 ps [2.8].

ID Quantique: The ID Quantique is another commerically available thin junction SPAD, fabricated using CMOS processes, but unlike the MPD does not possess a pigtailed fibre. The sensor has a diameter of 50 µm. A typical value for the detection efficiency at λ = 850 nm is 4% and the FWHM timing resolution is 40 ps [2.9].

Resonant Cavity: The RC detector was a prototype thin junction device developed by the Politecnico di Milano [2.28]. A resonant-cavity-enhanced single-photon

avalanche diode was fabricated by growth on a silicon-on-insulator (SOI) substrate. This SOI substrate incorporated a two period Bragg-reflector, forming a Fabry-Pérot cavity with the mirror formed at the air/semiconductor interface. The distributed Bragg reflector was designed to have high reflectivities in the near-infrared. A typical value for the detection efficiency at λ = 850 nm is 34% at a dark count rate of 50 cps [2.29] and the timing jitter at FWHM is 50 ps.

The different SPADs were characterised in terms of their timing jitter at Full-Width- at Half- Maximum (FWHM), Full Width 1/10 Maximum (FW1/10M) and Full Width 1/100 Maximum (FW1/100M).

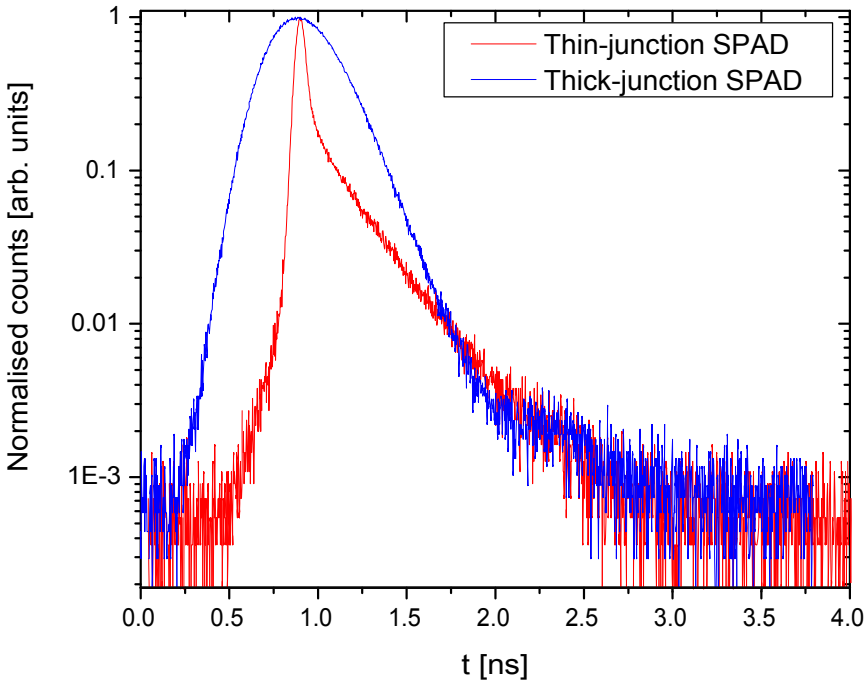

Figure 2.14: *Experimental results for detector timing jitter characterisation. The number of counts was normalised for each detector to allow easy comparison of the timing jitter. As expected the thick junction SPAD possesses a higher timing jitter than the thin junction SPAD. The FWHM is over* 320 ps *for the thick junction SPAD, while the FWHM for the thin junction SPAD is* 70 ps. *The long tail is caused by carrier diffusion. See Table 2.1 for reference.*

The time response of the detector consists of two different components: (1) a narrow distribution and (2) a decaying tail. The timing jitter is usually defined as the FWHM of the photon arrival time distribution [2.30, p. 45]. It is a statistical spread of the timing interval of the photon arrival at the actual detection time marked by detection of the leading edge of the output pulse [2.31]. The shape of this statistical spread is near-Gaussian and caused by the photons absorbed in the depletion region. The lower limit for the timing jitter depends on the drift transit time, which is related to the size of the

depletion layer and the absorption point of the photon in the depletion layer. The drift transit time is defined as the time the carriers need to drift across the depletion region, until they can be swept out of the device. The theoretical value for the drift velocity in the depletion region of a Si SPAD is $0.1\,\mu m\,ps^{-1}$ [2.32]. Thin junction SPADs have a shorter drift transit time than thick junction SPADs.

In SPADs a low amplitude tail consisting of one or more exponential decay components is present as well [2.33, p. 260]. This tail is caused by photons, which were absorbed in the quasi-neutral regions of the pn- junction and generated carriers outside the depletion region [2.34]. These carriers slowly diffuse into the high-electric field depletion region. The longer the distance from the origin of the carriers the longer is the mean value and the fluctuation of the diffusion delay. Due to the slow diffusion the timing resolution tail is orders of magnitude longer, than the narrow distribution caused by the carriers in the depletion region.

The results of the detector timing jitter characterisations are summarised in Table 2.1. Figure 2.14 visualises the different timing jitter characterisations for a thick and a thin junction Si-SPAD. As expected the thin junction SPAD possesses less jitter than the thick junction SPAD. The long tail is caused by carrier diffusion. After characterising

Detector	FWHM [ps]	FW1/10M [ps]	FW1/100M [ps]
PE	322.8	629.8	1041.3
MPD	70.8	275.7	898.0
IDQ	63.5	193.3	1244.5
RC	57.0	271.2	1082.3

Table 2.1: *Measured timing jitter of the SPADs. The PE was the only thick junction SPAD under test. The MPD, IDQ and RC were all thin junction SPADs.*

the detectors in terms of jitter, their single-photon detection efficiency was calculated. The theoretical number of photons n_{total} emitted from an attenuated pulsed laser with a repetition rate of f_{laser} and acquisition time t was calculated and compared to the number of photons measured with the SPADs.

An example for the characterisation, and a typical calculation are shown below. The following experimental parameters were used to characterise the detector: The operational wavelength of the laser was λ = 850 nm with a laser repetition rate of f_{laser} = 20 MHz, providing a pulse length of t_{pulse} = 50 ns. The average laser power of the unattenuated beam measured with the power meter was $P_{\text{laser}} = 31 \times 10^{-9}$ W. The laser

power was attenuated with a calibrated attenuator by 50 dB to reduce the average number of photons per pulse to less than 1 photon per pulse. The acquisition time was t = 10 s.

In order to calculate the number of photons in a laser pulse the following equation can be used:

$$n_{\text{pulse}} = \frac{\text{P}_{\text{laser}} \cdot \text{t}_{\text{pulse}}}{h \cdot c/\lambda} \tag{2.2}$$

Inserting the above specifications into Equation (2.2) gives the number of photons per pulse for the unattenuated laser $\text{n}_{\text{pulse}} = 6.63 \times 10^3$. For an additional attenuation of 50 dB, the laser power was attenuated to 31×10^{-14} W. Inserting the new value for the laser power in Equation (2.2), gives the value for the number of photons per pulse for the attenuated laser beam. The calculated average number of photons per pulse after attenuation is $\text{n}_{\text{pulse}} = 0.066$. For a measurement duration of t = 10 s the number of the total generated photons can be calculated with Equation (2.3):

$$\text{n}_{\text{total}} = \text{n}_{\text{pulse}} \cdot \text{f}_{\text{laser}} \cdot \text{t} \tag{2.3}$$

The total number of generated photons in the 10 second time frame is $\text{n}_{\text{total}} = 13.2 \times 10^6$. The measured number of photons with the PE SPAD in combination with the Becker and Hickl photon counting card is $\text{n}_{\text{detected}} = 4431091$. In order to get the number of detected photons, the area underneath the peak was integrated and the number of background counts was subtracted. The background counts were summed outside of the peak region and averaged over a 10 ns window. The interval for the background counts and the peak were of the same size.

The detection efficiency is the ratio of the number of generated photons and the number of detected photons, see Equation (2.4)

$$\text{SPDE}[\%] = \frac{\text{n}_{\text{detected}}}{\text{n}_{\text{total}}} \cdot 100[\%] \tag{2.4}$$

This lead to an overall detection efficiency of 33.6% for the PE detector.

Table 2.2 shows the measured detection efficiencies for λ = 850 nm. The detection efficiencies for λ = 686 nm are included as well, however these values have been taken from the data sheets provided by the manufacturers [2.6, 2.8, 2.9, 2.28]. For λ = 686 nm

only the relative efficiencies were measured as the exact value of the attenuation with the ND filters was unknown.

Detector	SPDE at λ = 686 nm [%]	SPDE at λ = 850 nm [%]
PE	72.0	33.6
MPD	33.1	8.4
IDQ	18.8	1.6
RC	44.0	15.2

Table 2.2: *Measured detection efficiency of the SPADs at two different wavelengths.*

As expected the Perkin Elmer SPADs have the highest detection efficiency, but also the highest timing jitter. The thin junction SPADs have a lower detection efficiency but a low timing jitter of approximately 70 ps at FWHM.

2.3.2 *Characterisation of V-Groove Fibre Array and Fibre Combiner*

In this section, the V-Groove fibre array and the fibre combiner are characterised in terms of relative efficiency, time delay between neighbouring channels, and overall timing jitter.

V-Groove Fibre Array

The V-Groove fibre array consists of eight optical fibres. Each fibre is placed in a single V-Groove, which had been anisotropically etched into a silicon substrate. Several different anisotropical etch techniques exist for silicon including KOH [2.35], ethylene-diamine, pyrocatheol, deionised water (EDA) [2.36] and hydrazine-deionised water [2.37]. What these etch techniques have in common is, that they preferentially etch one crystal plane faster than the others, resulting in a triangular etch shape in the etched substrate. In this experiment eight V-Grooves have been etched into a silicon substrate. As shown in Figure 2.15 the pitch of the neighbouring grooves is 127 µm. In each V-Groove a multi-mode fibre with a core diameter of 50 µm and a cladding of 125 µm is located. Each optical fibre possesses a different pre-determined length, resulting in different optical path lengths. The different optical lengths give a unique timing signature and from this timing signature the fibre, into which the photon has entered can be determined.

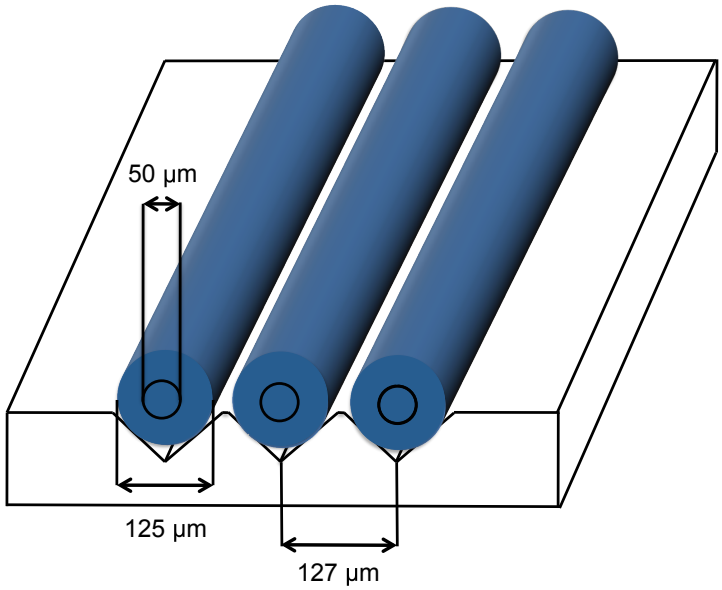

Figure 2.15: *Schematic illustration of V-Groove Fibre Array showing the fibre pitch, the fibre core size and the diameter of the fibre cladding. For clarity only three V-Grooves with fibres are shown.*

Two different V-Groove fibre arrays were procured from Oz Optics. Each fibre array had a bespoke specification for the fibre lengths, see Table 2.3 for details. The refractive index of the V-Groove fibres is 1.481.

	"Short" arm			"Long" Arm		
V-Groove Channel	Fibre length [m]	TOF [ns]	Time delay [ns]	Fibre length [m]	TOF [ns]	Time delay [ns]
1	0.43	2.12	–	0.23	1.13	–
2	0.68	3.37	1.25	0.48	2.38	1.25
3	0.94	4.62	1.25	0.74	3.63	1.25
4	1.19	5.87	1.25	0.99	4.88	1.25
5	1.44	7.12	1.25	1.24	6.13	1.25
6	1.69	8.37	1.25	1.49	7.38	1.25
7	1.95	9.62	1.25	1.75	8.63	1.25
8	2.20	10.87	1.25	2.00	9.88	1.25

Table 2.3: *Specifications for short and long V-Groove fibre array. The fibre lengths were chosen to have a time delay of* 1.25 ns *between neighbouring channels.*

The time of flight (TOF) of the fibres in the V-Groove fibre array was measured with the setup illustrated in Figure 2.16.

For the prospective experimental quantum correlations measurement setup, the combination of the short and long V-Groove fibre arrays must be able to resolve 64 peak positions, as there are 8×8 different combinations that the two entangled photons can enter the two fibre arrays (see Section 3.2.7). The spacing used in these measurements

was aimed at measuring 8 different positions in a 10 ns window for compatibility with a 100 MHz repetition rate source [2.38]. In the short arm, a small time delay of 1.25 ns between adjacent fibres was chosen. Overall eight fibres, in the start arm, the total delay was 10 ns. The time delay in the long arm must exceed this value. In order to avoid overlap between adjacent channels a time delay of 12 ns was chosen. The additional delay was generated by additional fibres of increasing length. Table 2.4 shows the calculations for the needed delay fibres. The refractive index of the delay fibres was measured to be 1.466.

	V-Groove			Delay fibre			
V-Groove Channel	Fibre length [m]	TOF [ns]	Time delay [ns]	Fibre length [m]	TOF [ns]	Time delay [ns]	Delay [ns]
1	0.23	1.13	–	2.40	11.73	–	–
2	0.48	2.38	1.25	4.60	22.48	10.75	12.00
3	0.74	3.63	1.25	6.80	33.23	10.75	12.00
4	0.99	4.88	1.25	9.00	43.99	10.76	12.01
5	1.24	6.13	1.25	11.20	54.73	10.74	11.99
6	1.49	7.38	1.25	13.40	65.48	10.75	12.00
7	1.75	8.63	1.25	15.60	76.23	10.75	12.00
8	2.00	9.88	1.25	17.80	86.98	10.75	12.00

Table 2.4: *Calculations for delay fibres used with the long V-Groove fibre array. The combination of V-Groove fibre and delay fibre was chosen to give a time delay of* 12.00 ns *between consecutive fibres.*

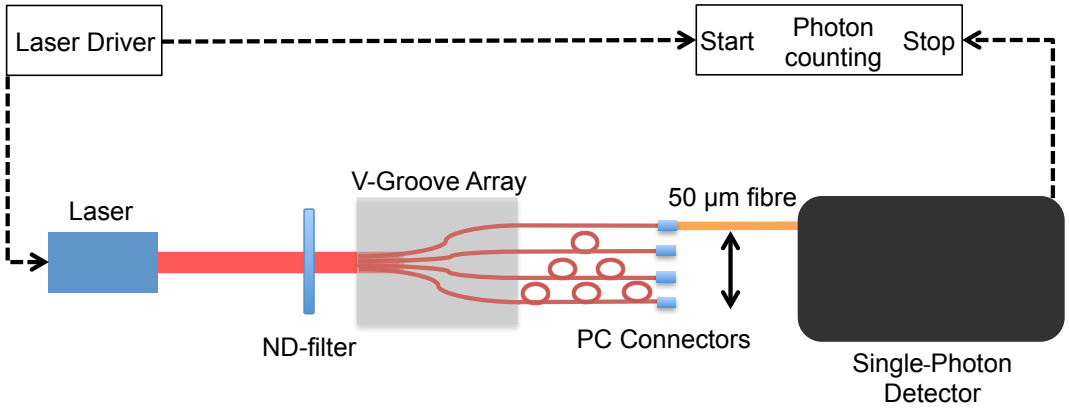

Figure 2.16: *Schematic illustration of V-Groove Fibre Array time of flight measurement. For clarity only four V-Grooves with fibres are shown. Each fibres was characterised individually.*

The V-Groove was uniformly illuminated with a λ = 780 nm pulsed laser diode from PicoQuant. The sync output from this laser driver was connected to sync input of the Becker and Hickl photon counting card SPC 600, providing the start signal. In order to protect the SPADs, the laser power was attenuated with ND-filters, which were placed

in the free space between the laser diode and the V-Groove array. Each channel of the V-Groove fibre array was individually connected via a 50 µm fibre to the SPAD. The electrical output from the SPAD was connected to the CFD of the photon counting card, giving the stop signal.

The measurement for each channel lasted 10 s. The theoretical values in Table 2.4 were then compared with the experimental data illustrated in Figure 2.17 and summarised in Table 2.5.

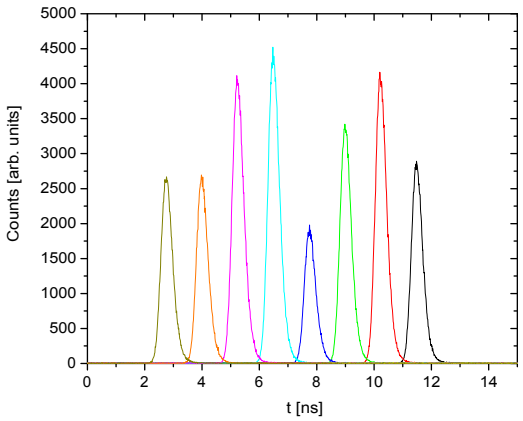

(a) TOF-measurement for the short V-Groove fibre array.

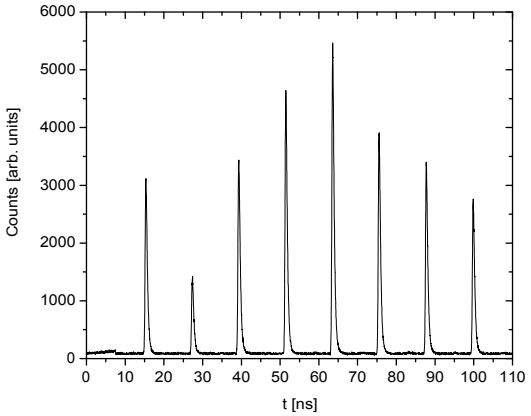

(b) TOF-measurement for the long V-Groove fibre array in conjunction with the delay fibres.

Figure 2.17: *TOF measurements for the Start- V-Groove (a) and the Stop V-Groove with delay fibres (b)*

The measured average time delay between adjacent V-Groove channels is $\Delta t_{V-Groove}$ = 1.26 ns ± 0.02 ns. The maximum deviation from the theoretical value is 2.4%. For the V-Groove with the additional delay fibres the measured average time delay between adjacent channels is Δt_{Delay} = 12.07 ns ± 0.09 ns. The maximum deviation from the specified time delay in this case is 1.3%.

Overall the measured results are in good agreement with the theoretical values. The source for the small deviations are the slightly offset fibre lengths, which originate from the manufacturing process. For example a fibre which is 5 mm too long would result in an additional time delay of 0.02 ns. For the V-Groove with the delay fibres this effect is even bigger, as there are two fibres in each channel, which can result in higher inaccuracies, if both fibres do not match the specified length.

	V-Groove		V-Groove + Delay fibre	
V-Groove Channel	TOF [ns]	Δt [ns]	TOF [ns]	Δt [ns]
1	3.68	–	15.41	–
2	4.95	1.27	27.41	12.01
3	6.18	1.23	39.40	11.98
4	7.44	1.26	51.55	12.15
5	8.71	1.27	63.65	12.10
6	9.98	1.27	75.62	11.97
7	11.22	1.24	87.82	12.20
8	12.50	1.28	99.93	12.11
Total	$\Delta t_{V-Groove}$ = 1.26 ns ± 0.02 ns		Δt_{Delay} = 12.07 ns ± 0.09 ns	

Table 2.5: *Measured TOF in V-Groove fibre arrays and delay fibres. The measured TOFs were slightly longer than specified due to longer fibre lengths caused by inaccuracies in the manufacturing process.*

Fibre combiner

The fibre combiner consists of eight input fibres with a 50 µm core diameter and a 125 µm cladding, matching the specifications of the V-Groove fibres. The input fibres were tapered and fusion spliced onto the output fibre. The output fibre has a core diameter of 105 µm and a cladding of 125 µm. In conjunction with the V-Groove fibre array, eight positions can be detected on the same SPAD simultaneously due to position to time multiplexing. In the following section the fibre combiner was characterised in terms of efficiency, time of flight, and jitter.

The V-Groove fibre array was uniformly illuminated with laser diode emitting at λ_{Laser} = 780 nm and for in a second experiment at λ = 686 nm. Ideally the V-Groove and the fibre combiner should have been characterised at λ = 710 nm, as this is the wavelength of the down-converted photons used in the quantum correlations experiments (see Chapters 3 and 4). The laser diodes emitting at λ = 780 nm and λ = 686 nm were the only available laser sources near the wavelength of the down-converted photons. The V-Groove fibres were coupled to the fibre combiner's input fibres, using Physical Contact (PC) connectors. The output fibre of the fibre combiner was connected to a fibre-coupled power meter. Figure 2.18 shows the experimental setup for the efficiency measurement.

The overall efficiency (see Table 2.6) of the fibre combiner is 68.7% at λ = 780 nm and 71.7% for λ = 686 nm respectively. Losses could have been introduced by coupling the

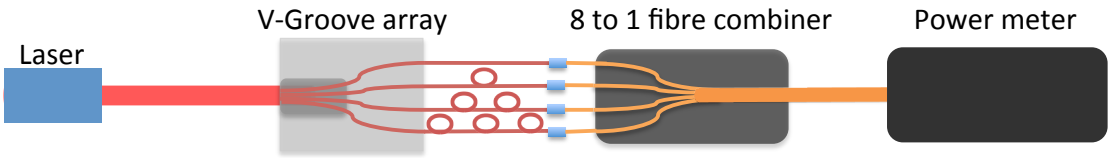

Figure 2.18: *Schematic illustration of the fibre combiner efficiency measurement. For clarity, only four V-Grooves with fibres are shown.*

	$\lambda = 780$ nm			$\lambda = 686$ nm		
V-Groove Channel	$P_{V-Groove}$ [µW]	$P_{Combiner}$ [µW]	Eff. [%]	$P_{V-Groove}$ [µW]	$P_{Combiner}$ [µW]	Eff. [%]
1	0.76	0.47	61.8	0.19	0.13	68.4
2	0.96	0.68	70.8	0.28	0.20	71.4
3	0.89	0.62	69.7	0.24	0.20	83.3
4	1.11	0.80	72.1	0.31	0.23	74.2
5	1.11	0.75	67.6	0.39	0.29	74.4
6	1.00	0.72	72.0	0.37	0.26	70.3
7	0.89	0.56	62.9	0.26	0.18	69.2
8	0.62	0.44	71.0	0.23	0.15	65.2
Total	7.34	5.04	68.7	2.26	1.62	71.7

Table 2.6: *Comparison of output power from an individual V-Groove fibre and the output power from the V-Groove fibre array connected to the fibre combiner. The efficiencies were measured with laser sources emitting at* $\lambda = 780$ nm *and* $\lambda = 686$ nm *respectively.*

V-Groove fibre array to the fibre combiner, where typical coupling losses are 0.5 dB per FC/PC (Ferrule Connector/ Physical Contact) connector [2.39], and by coupling the tapered input fibres to the output fibre.

Additional to the power measurement, the fibre combiner was characterised in terms of its time of flight. The experimental setup is outlined in Figure 2.19. A set of ND-filters was used to reduce the power of the laser light to a safe level for the SPAD. The ND-filters were placed in a U-Bracket and each side of the U-bracket had a fibre connector to allow easy coupling. In the first experiment (Figure 2.19(a)) the time of flight in each V-Groove fibre was characterised. After measuring the peak position for each V-Groove channel individually, the V-Groove channels were connected to the input fibres of the fibre combiner. The output of the fibre combiner was attenuated with the same set of ND-filters, see Figure 2.19(b). Due to the additional delay introduced by the fibre combiner, the last peak in the histogram of the fibre combiner measurement was aligned with the last peak of the V-Groove measurement for the data analysis. Table 2.7 and Figure 2.20 show the results.

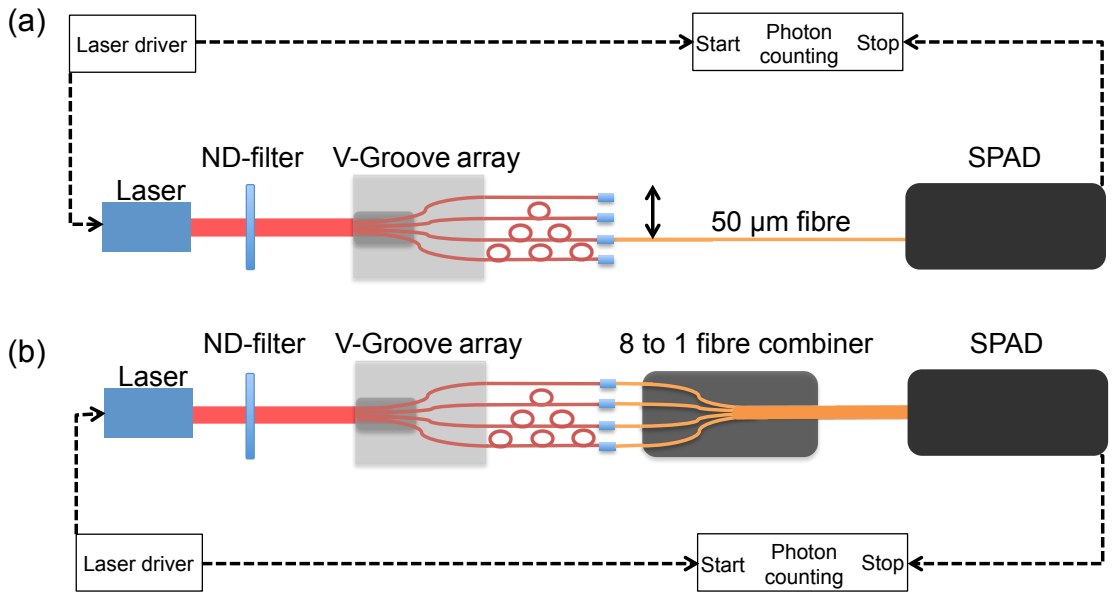

Figure 2.19: *Schematic illustration of fibre combiner jitter measurement. (a) shows the single channel measurement with a* 50 µm *multi-mode fibre connected to a SPAD. (b) shows the fibre combiner placed in between the V-Groove fibre array and the SPAD. Here all channels were connected to the SPAD at the same time.*

$Peak_{Histogram}$	$t_{V-Groove}$ [ns]	$t_{fibre\,combiner}$ [ns]	Δt [ns]
1	2.77	2.76	0.01
2	4.01	3.96	0.05
3	5.26	5.22	0.04
4	6.50	6.41	0.09
5	7.77	7.57	0.20
6	9.01	8.96	0.05
7	10.24	10.27	0.03
8	11.50	11.50	0.00

Table 2.7: *Comparison of time of flight from an individual V-Groove fibre and the time of flight from the V-Groove fibre array connected to the fibre combiner. Δt is not the same for all fibres indicating that the length of the fibre combiner fibres varies.*

In Figure 2.20 one can see that peak no. 5 is offset by 0.20 ns, while for the other peaks the additional time of flight ranges from 0.01 ns to 0.09 ns. These small variations are due to the slightly different fibre length and were caused during the production of the fibre combiner.

In contrast to the V-Groove-only measurement, the peaks in the fibre combiner measurement were broader. The broader peaks could have been caused by dispersion effects within the fibre combiner due to the large output core, which increased the total timing jitter. In order to characterise the timing jitter in each channel of the fibre combiners the same setup as in Figure 2.19(a) plus the fibre combiner was used. Here each

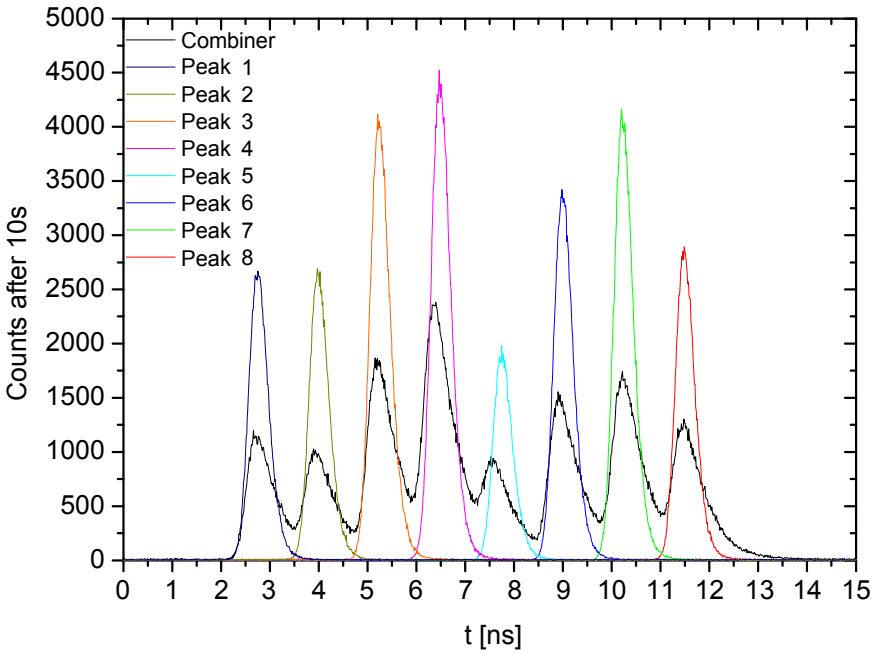

Figure 2.20: *Coupling V-Groove fibre array to a single* 50 µm *multi-mode fibre vs coupling the V-Groove fibre array to the fibre combiner. Changes of peak position are evident. These could have been caused by different fibre lengths of the fibre combiner fibres. Overall, the coupling efficiency reduces, when the fibre combiner is used.*

measurement lasted for 60 seconds. One fibre combiner has a orange coating and is referred to as "combiner # 1", the other combiner has a yellow coating is referred to as "combiner # 2"

Figure 2.21 and the Table 2.8 summarise the results of the jitter measurements.

Channel	Jitter$_{\#1}$ [ps]	Jitter$_{\#2}$ [ps]
1	616	644
2	612	628
3	612	644
4	634	628
5	588	648
6	608	632
7	616	628
8	596	664
Total	$\Delta t = 610.0 \pm 13.4$	$\Delta t = 639.5 \pm 12.9$

Table 2.8: *Comparison of timing jitter in the fibre combiners. The fibre combiner # 1 possesses a lower timing jitter of* 610 ps, *while the combiner # 2 possesses a timing jitter of almost* 640 ps

The average jitter measured at the output of the combiner # 2 is 639.5 ps ± 12.9 ps, while the jitter of the combiner # 1 is 610.0 ps ± 13.4 ps. For the following timing jitter experiments only the combiner # 1 was used.

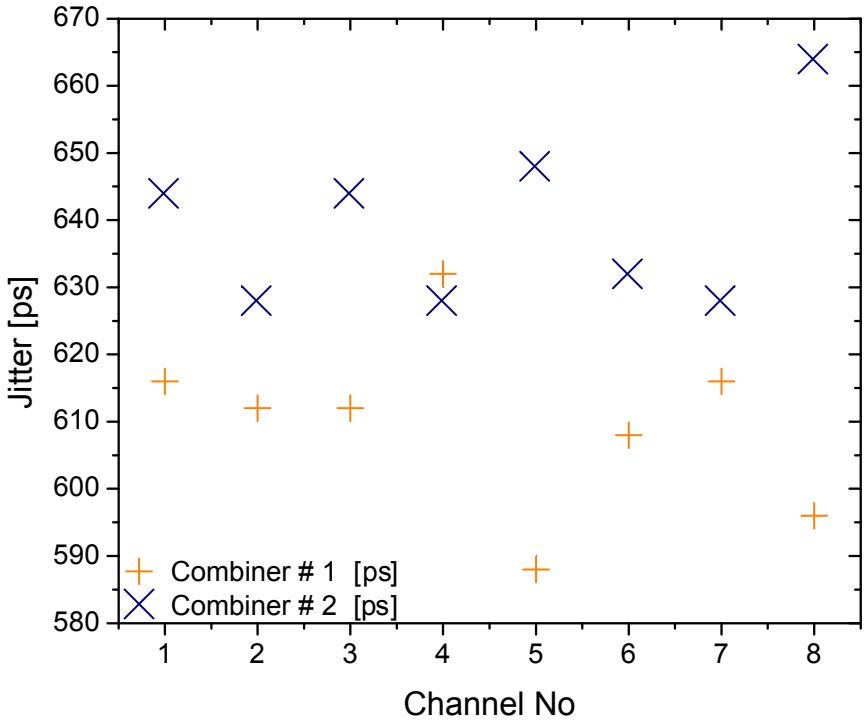

Figure 2.21: *The fibre combiner with the yellow coating (# 2) possesses an overall higher timing jitter than the fibre combiner with the orange coating (# 1).*

Also the effect of having delay fibres in the experimental setup was characterised. Here for each channel three different measurements were performed. For the first series of measurements a single 2 m long multimode fibre was connected to the V-Groove fibre array and the SPAD. For the second series, the multi-mode fibre was replaced by the fibre combiner and finally in the third measurement series the fibre combiner and the multimode fibre were used.

Peak No.	A $FWHM_{Delay+Combiner}$ [ps]	B $FWHM_{Combiner}$ [ps]	C A - B [ps]	D B - 410 ps [ps]
1	646	616	30	206
2	634	612	22	202
3	665	612	53	202
4	680	632	48	222
5	619	588	31	178
6	676	608	68	198
7	663	616	47	206
8	700	596	104	186
Total	660 ± 26	610 ± 13	50 ± 26	200 ± 13

Table 2.9: *Measured timing jitter caused by the delay fibres and the fibre combiner. The fibre combiner adds another* 200 ps *of timing jitter, while the delay fibres contribute with* 50 ps *to the total timing jitter.*

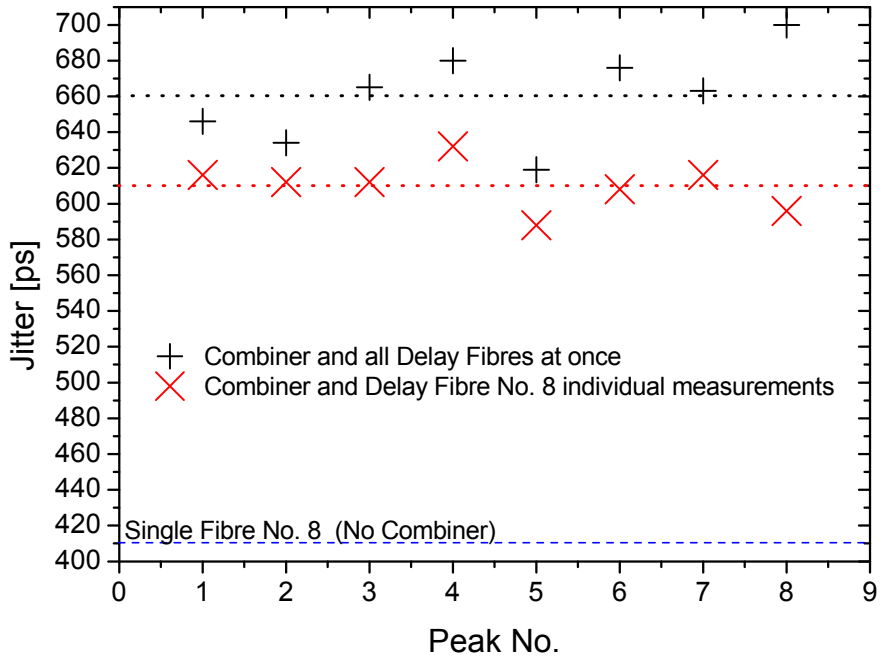

Figure 2.22: *Jitter measured at the output of the fibre combiner with and without delay fibres compared to the jitter of a single* 2 m *long* 50 µm *multi-mode fibre.*

Figure 2.22 and Table 2.9 show the timing jitter for the three different measurements. The measurement where only the multi-mode fibre was used possesses the smallest jitter of only 410 ps. Once the fibre combiner was added to the setup, the measured jitter increased by almost 200 ps through all channels. Using the additional delay fibres added another 50 ps to the total timing jitter due to dispersion in the fibre.

2.3.3 *Full-system timing jitter measurements*

In order to characterise the receiver system in terms of timing jitter, the setup shown in Figure 2.23 was used. A pulsed laser diode operating at a laser repetition rate of 10 MHz and an emission wavelength of λ = 686 nm was used. The laser light was coupled with a microscope objective into a 5 µm fibre. A second microscope objective coupled the light out of the fibre and expanded the beam. Neutral density filters attenuated the emerging light beam to reduce the photon flux at the detectors. The expanded beam fully illuminated the V-Groove fibre array. The V-Groove array consisted of eight grooves, which were anisotropically etched into a silicon substrate. The V-Groove pitch was 127 µm and each V-Groove held one bare fibre with a core diameter of 50 µm and a 125 µm cladding. The bare fibres were evenly stepped in differing lengths, resulting in different pre-determined arrival times at the detector. The differ-

ence in arrival time between two neighbouring fibres had been chosen to be 1.25 ns to match an overall laser pulse repetition frequency of 100 MHz used in the eventual quantum imaging demonstration. The V-Groove fibres were FC/PC connectorised and were connected to the eight input fibres of the fibre combiner. The fibre combiner consisted of eight input fibres with a core diameter of 50 µm and a cladding of 125 µm. The core diameter of 50 µm was chosen, to match the core diameter of the V-Groove fibres and therefore enabled efficient fibre to fibre coupling. The input fibres were first stretched and tapered and then fusion spliced onto the output fibre which had a core diameter of 105 µm. The output fibre was coupled onto a large active area SPAD.

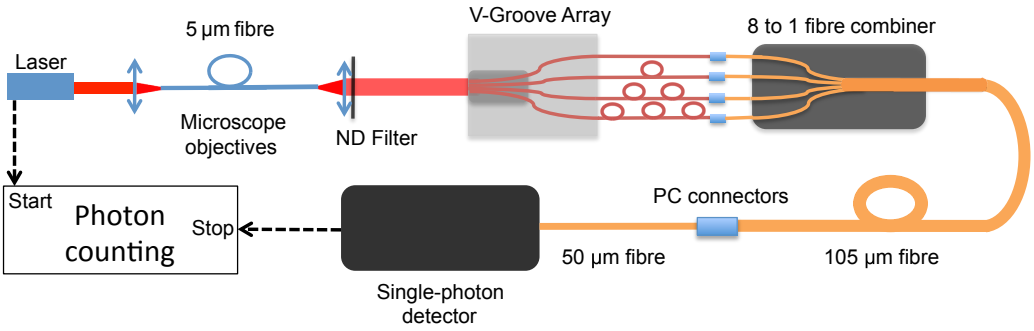

Figure 2.23: *Experimental setup for timing jitter measurement. For clarity only four V-Groove fibres are shown.*

The detectors used in this timing jitter measurement experiment were the following:

- **Perkin Elmer** (PE), model number: SPCM-CD2882. The PE is a commercially available thick junction Si-SPAD. The thickness of the junction was in the order of 30 µm and the diameter of the detection area was 180 µm, which leads to a high detection efficiency. The SPDE of the PE was 59.9% at 686 nm. The timing jitter of the detector was 350 ps [2.6].

- **MPD**, model number: PDF series with a 62.5 µm graded index fibre. The MPD detector is a commercially available thin junction Si-SPAD. The detector diameter was 62.5 µm and the thickness of the junction was in the order of a few micrometres. The SPDE at a wavelength of λ = 686 nm was 30.8%. The timing jitter at FWHM of the thin junction detector was 35 ps. The PDF series detector was pigtailed with a 62.5 µm graded index fibre which was directly coupled to the sensor, without the use of free space optics [2.8].

- **Resonant Cavity** (RC) SPAD with a 20 µm diameter active area. The Resonant

Cavity detector is not commercially available. During the production process of the thin junction Si-SPAD a silicon on insulator substrate was fabricated on the bottom of the SPAD. The silicon on insulator substrate incorporated a two period Bragg reflector. This buried reflector formed the bottom mirror and the air/semiconductor interface formed the top mirror to form a Fabry-Pérot cavity. The distributed Bragg reflector was designed for a high reflectivity in excess of 90% in the near infrared ranging from 750 nm to 950 nm. Although the SPDE in the near infrared improved from 9.3% to 17.5% at 850 nm, the SPDE at 686 nm only slightly improved from 30.8% to 32.2% [2.28].

- **ID Quantique** (IDQ), model number: id100-MMF50. The ID Quantique is another commercially available thin junction Si-SPAD fabricated using a CMOS process. A 50 µm fibre was directly coupled to the active area of the detector, which was of 50 µm diameter. The SPDE at a wavelength of 686 nm was 18%. The timing jitter at FWHM was 40 ps [2.9].

- **Superconducting Nanowire Single-Photon Detector** (SNSPD). The SNSPD consisted of a 100 nm wide nanowire, which was patterned by electron-beam lithography in a thin niobium nitride superconducting film. The detector was cooled down to 2.5 K. The SPDE of the SNSPD at λ = 686 nm was approximately 10% [2.40]. The jitter of the SNSPD was 60 ps [2.41]. Unlike the previous detectors the detector response function of the SNSPD had a Gaussian shape, while the detector response functions for the Si-SPADs were asymmetric.

Figure 2.24 shows histograms for three detectors. For clarity these histograms have been normalised and additionally the other thin junction SPADs (RC and IDQ) are not displayed in this figure. The trend for the RC and for the IDQ is very similar to the MPD. Details about the timing jitter for the detectors can be found in Table 2.10.

From Figure 2.24 it is easy to see that the Perkin Elmer detector in combination with the fibre combiner has a relatively high timing jitter of approximately 690 ps at FWHM, which leads to a significant overlap between two channels. In case of the MPD, RC and IDQ there is a relatively small overlap between the tail of the previous channel and the peak of the next channel. The overlap causes a broadening of the peak and adds counts to the adjacent channels. Only the SNSPD possesses such a low overall timing jitter (FW1/100M = 400 ps), which does not affect the neighbouring channels.

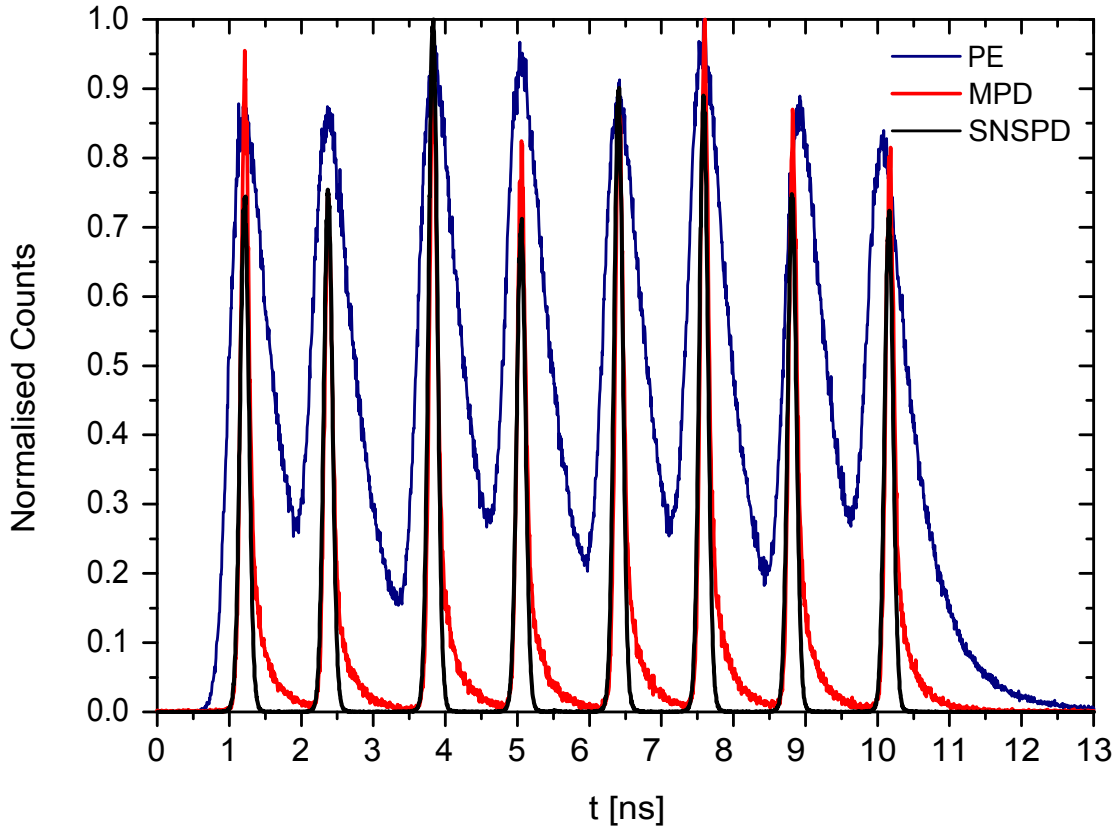

Figure 2.24: *Timing jitter for the full receiver system measured with different single-photon detectors. Only for the SNSPD the different channels do not overlap. For the thin junction SPADs there is an overlap at FW1/100M, while the thick junction SPAD overlaps at FW1/10M.*

Figure 2.25 shows timing histograms for the different detectors for a single channel from the fibre combiner. Here channel number eight was characterised. Table 2.10 summarises the timing jitter for the detectors and the fibre combiner in terms of FWHM, FW 1/10 Max jitter and FW 1/100 Max jitter for a single channel measurement from the fibre combiner and when all eight channels from the fibre combiner were connected to the V-Groove fibre array at once.

For all detectors, except the SNSPD, there is an overlap between neighbouring peaks as the temporal difference between two neighbouring peaks is designed to be 1.25 ns and the value for the FW 1/100 Max jitter exceeds this value. For the MPD and the RC the values for the single channel FW 1/100 Max jitter are just below 1.25 ns, but it is not possible to distinguish between the end of the first peak and the start of the second peak from the background noise. Therefore the FW 1/100 Max jitter in the all fibres combined cases were defined as “undefined”. In order to reduce the timing jitter by removing higher order modes, a 50 µm fibre had been inserted between the fibre combiner and the detector. The mismatch of the spot size between the large diameter fibre

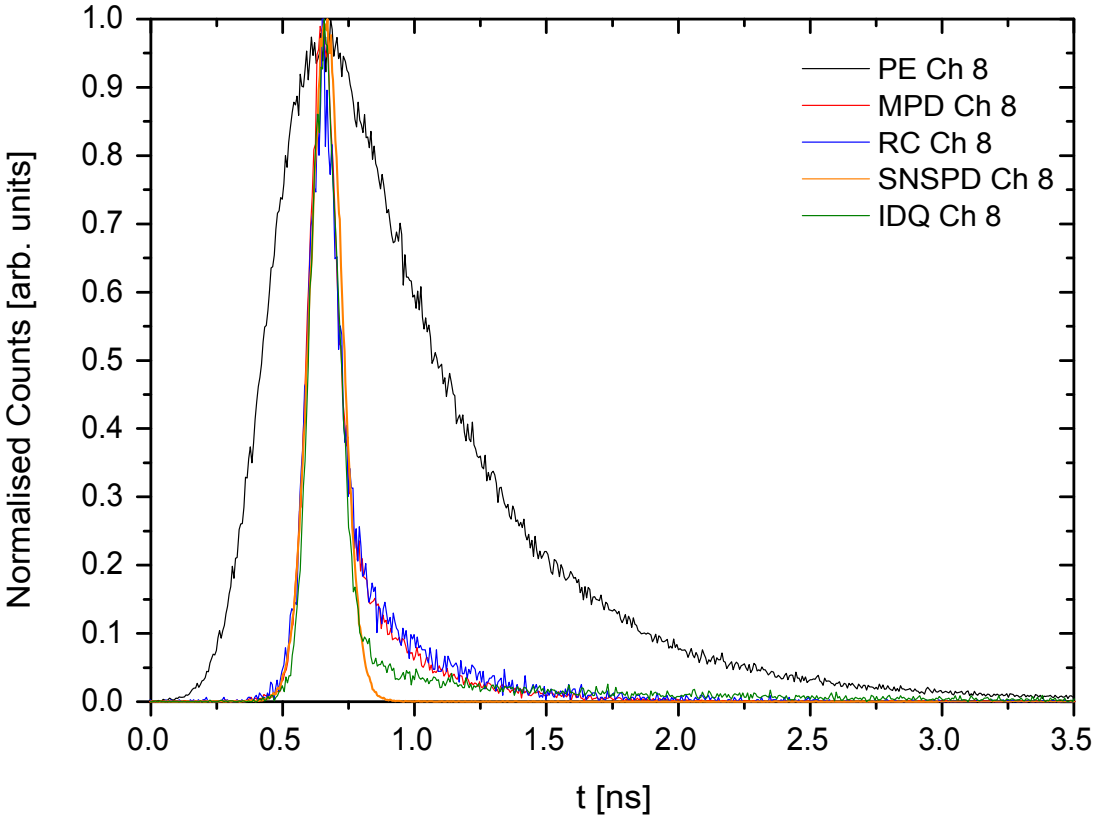

Figure 2.25: *Timing jitter in fibre combiner for a single channel. Due to the high overlap, when all channels are measured at once the measurement was repeated with a single channel from the fibre combiner to determine the timing jitter present in an individual channel.*

Detector	*Single Channel*			*All fibres combined*		
	FWHM [ps]	FW$\frac{1}{10}$M [ps]	FW$\frac{1}{100}$M [ps]	FWHM [ps]	FW$\frac{1}{10}$M [ps]	FW$\frac{1}{100}$M [ps]
PE	661±12	1593±45	3020±50	687±22	Overlap	undefined
PE + 50 µm	470±7	1040±17	1741±24	479±13	1055±40	undefined
MPD	134±3	385±8	1079±20	135±3	398±16	undefined
MPD + 50 µm	130±5	381±16	1075±29	128±7	391±14	undefined
RC	117±9	421±24	1159±51	133±6	436±15	undefined
IDQ	122± 2	256±5	1539±63	125±2	266±5	undefined
IDQ + 50 µm	123±5	260±11	1573±73	123±2	265±11	undefined
SNSPD	141±2	263±5	396±5	141±2	264±5	399±15

Table 2.10: *Comparison of timing jitter measured with different detectors. All timing jitter values are in [ps]. The jitter in each single channel of the fibre combiner had been measured and the average value for all eight single measurements were taken for the "Single Channel" values. In the "all fibres combined" case all eight channels of the fibre combiner had been used simultaneously and the average width of the peaks were taken. In order to reduce the timing jitter a* 50 µm *fibre had been integrated in the receiver system. These measurements are labelled as* '+50 µm'

and the smaller diameter led to inefficient coupling between the two fibres and some higher order modes were suppressed. In case of the PE, the FWHM was reduced by approximately 190 ps and the FW 1/10 Max jitter was reduced by 553 ps, but the overall efficiency decreased due to the inefficient coupling between the 105 µm fibre and the 50 µm fibre. For the MPD this effect is smaller, because the MPD is already coupled to a 62.5 µm fibre, which reduced the timing jitter beforehand. With the additional 50 µm fibre the FWHM and the FW 1/10 Max jitter are reduced by 7 ps. For the Perkin Elmer detector the peaks overlap due to the high jitter of the detector. In order to avoid the channel crosstalk, longer delays can be introduced by using a larger step change in fibre length. In the case of the SPAD detectors analysed in this thesis, the new delay should be in the order of at least 3.5 ns as this value exceeds the FW 1/100 Max jitter in all single channel timing jitter measurements with the PE.

Detector	FWHM with 50 µm fibre [ps]	FWHM with fibre combiner [ps]
PE	454±6	661±12
MPD	129±5	134±3
RC	121±7	117±9
IDQ	122±2	122±2
SNSPD	132±2	141±2

Table 2.11: *Jitter measurements for a* 50 µm *fibre directly connected to the detector compared to jitter measurements where the fibre combiner was connected to the detector.*

Table 2.11 shows a comparison in timing jitter between measurements where the single V-Groove channels and the detector were connected via a 50 µm fibre, and timing jitter measurements, where the V-Groove channels and the detector were connected via the fibre combiner. In case of the PE detector, it is easy to see, that the fibre combiner adds jitter to the timing jitter measurements. The additional jitter was caused from the variation in core diameter in the fibre combiner. For all other detectors this effect is not visible, due to the smaller core diameter fibres which were coupled to the detector. Due to the mismatch between the different fibre core diameters, the higher order (i.e. slower) modes were suppressed.

2.3.4 *Full-system detection efficiency measurements*

In order to calculate the detection efficiency of the individual detectors the throughput of a 50 µm fibre for the eight different V-Groove channels was measured with the Perkin Elmer SPAD. Histograms were recorded for each channel individually, where each

measurement lasted for 60 s. The number of photons in each peak was taken from a defined measurement window of 3 ns. The sum of all eight single channel measurements with the 50 µm fibre was defined as the overall throughput of the V-Groove fibre array. The Perkin Elmer SPAD had the highest photon detection efficiency and had an active area of 180 µm, which was the only detector with a larger diameter than the diameter from the fibre combiner's output fibre. In the next step the fibre combiner was integrated into the experimental setup. A histogram was recorded for all eight channels at once. Again, the acquisition time used was 60 s, and the number of photons were determined over a 15 ns measurement window. This measurement was then repeated with the MPD, RC, IDQ and the SNSPD.

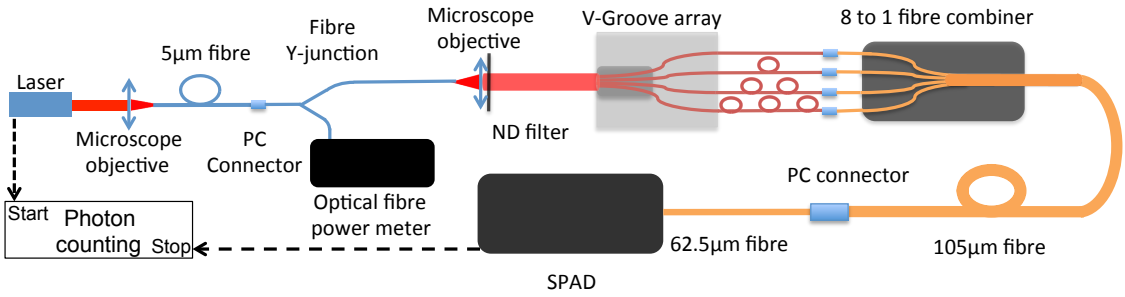

Figure 2.26: *Experimental setup for detection efficiency measurements.*

The timing jitter measurement setup was slightly modified, as shown in Figure 2.26. In order to monitor the laser power a fibre Y-junction and an optical fibre power meter were integrated into the existing setup. The laser power was monitored via a fibre Y-junction going to an optical fibre power meter (Newport Optical Power Meter Model 1830-C, Bullet 818-F-IR S/N 0453). The fibre Y-junction had a core diameter of 50 µm and was specified to operate at a wavelength of $\lambda = 850$ nm and at $\lambda = 686$ nm and only 25% of the total laser power was coupled to the power meter. After taking each histogram, the laser power was measured. The laser power transmitted through the 50 µm fibre represented the reference. For each subsequent power measurement, the laser power was compared with the value of the 50 µm fibre reference measurement and the deviations are given in Table 2.12. For the total count calculations, the dark counts and the change in laser power have been taken into consideration. The number of photons counted with the 50 µm fibre and Perkin Elmer detector combination and including dark count subtraction was 1333396.

For calculating the overall detection efficiency of the receiver system, the relative efficiency of the individual detectors was multiplied with the SPDE of the Perkin Elmer

Setup	Counts	Dark counts	ΔP_{LD}[%]	Total counts	Rel. Eff. [%]
PE	874987	5520	-3.4	928944	69.6
PE + 62.5 µm	286764	5520	-1.2	288014	21.6
MPD	128190	1445	+3.5	122313	9.2
RC	9858	36	+5.1	9321	0.7
IDQ	18280	22	+9.1	16597	1.24

Table 2.12: *Comparison of counts, dark counts, change in laser power compared to* 50 µm *measurement, and relative efficiency of the different detector and fibre setups.*

detector, as it had been used for the 50 µm fibre throughput measurement. The SPDE for the other detectors is just given as a reference.

Table 2.13 shows a comparison of relative efficiency and total efficiency through the fibre combiner for the different receiver systems, SPDE, DCR and NEP for the detectors used in the experiment.

Detector	Rel. eff. through combiner [%]	SPDE at 686 nm[%]	Total eff. through combiner [%]	DCR [cps]	NEP $\left[\mathrm{W}/\sqrt{\mathrm{Hz}}\right]$
PE	69.6	59.9	41.7	250	1.08×10^{-17}
PE + 62.5 µm	21.6	59.9	12.9	250	1.08×10^{-17}
MPD	9.2	30.8	5.5	179	1.78×10^{-17}
RC	0.7	32.2	0.4	23	6.10×10^{-18}
IDQ	1.24	18.0	0.7	20	1.02×10^{-17}

Table 2.13: *Comparison of relative efficiency and total efficiency through the fibre combiner for the different receiver systems and single-photon detection efficiency (SPDE), dark count rate (DCR), and noise equivalent power (NEP) at* $\lambda = 686$ nm *for the detectors used in the experiment.*

The smaller core diameter of the IDQ fibre, compared to the MPD, lead to an inefficient fibre to fibre coupling between the fibre combiner and the detector and thus reduced the efficiency further. The relative efficiency of the resonant cavity detector in these measurements is very low, since it was the detector with the smallest active area. At an emission wavelength of $\lambda = 686$ nm the relative efficiency should be similar to the MPD, if we did not overfill the active area. Hence, the resonant cavity detector used in this experiment was not of the ideal geometry for this setup. The major issue was that the resonant cavity includes a 1:1 imaging system which was specified for a fibre with a maximum core diameter of 20 µm (the detector was only 20 µm in diameter) and with the 105 µm core diameter fibre from the fibre combiner high losses were introduced. Also, the coupling efficiency of the RC could have been improved by changing the focus

of the system, which was set for an emission wavelength of 846 nm. A further problem was the mismatch of the numerical aperture between the 105 µm fibre and the optical system of the RC. The numerical aperture of the 105 µm fibre was 0.22, while the numerical aperture of the optical system was 0.12.

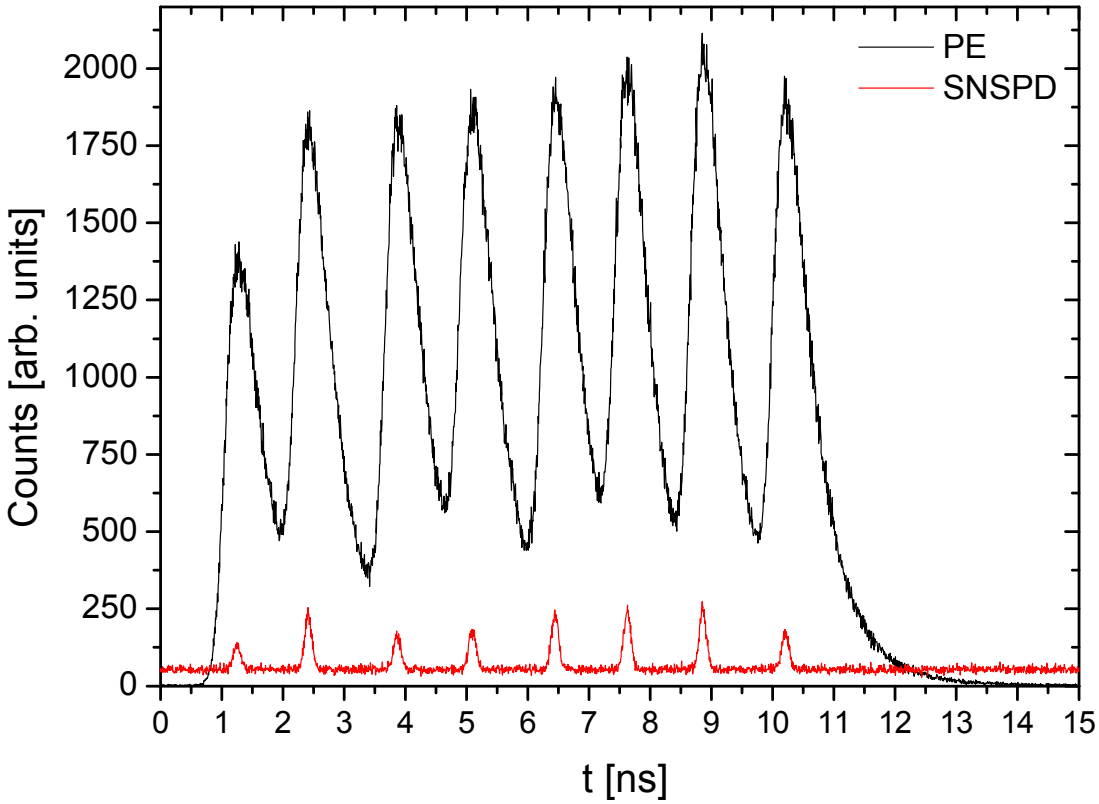

Figure 2.27: *Comparison of a* 60 s *measurement with PE reference detector with a* 3600 s *measurement of the SNSPD. Due to the long measurement duration the SNSPD possesses a very high background.*

Figure 2.27 shows the histogram for the SNSPD, which was recorded for 3600 s due to the low efficiency of the receiver setup. After the standard 60 s measurement only background noise was evident. After 180 s the peaks slowly started to become discernible and were clearly distinguishable from the background noise. Due to the long recording time the overall background noise level was very high compared to the SPAD measurements. After 3600 s the background noise level was roughly 50 counts per bin throughout the histogram. The number of counts for the 3600 s SNSPD measurement was 2626 counts. After subtracting the background (2274 counts), only 352 counts were above the noise level. Considering the Poissonian noise within the number of counts registered per time bin, the total number of counts varies. The Poissonian noise can be expressed as the standard deviation σ, which is defined as the square-root of the mean value $\overline{n}$ $\left(\sigma = \sqrt{\overline{n}}\right)$. In this case the number of counts including Poissonian fluc-

tuations was 352 ± 48 counts. In contrast 1,474,886 counts were recorded in a 60 s PE measurement. The low efficiency of approximately 0.024% ± 0.003% compared to the PE detector was caused by the lower single-photon detection efficiency of the SNSPD, which was roughly 10% at 686 nm. Additionally, the mismatch between the 105 µm output fibre from the fibre combiner and the 9 µm fibre in the SNSPD, led to a very inefficient fibre to fibre coupling.

$$\eta_{coupling} = \frac{\pi(9\mu m)^2 \times 4}{4 \times \pi(105\mu m)^2} \times 100\% = 0.73\% \tag{2.5}$$

By comparing the areas of the two fibres and neglecting any effects arising from Fresnel reflection and coupling losses caused by the butt-coupling, the 9 µm fibre can only receive 0.73% of the light emitted by the large area fibre.

The results of the timing jitter and the efficiency measurements of the V-Groove fibre array detection system are visualised in Figure 2.28.

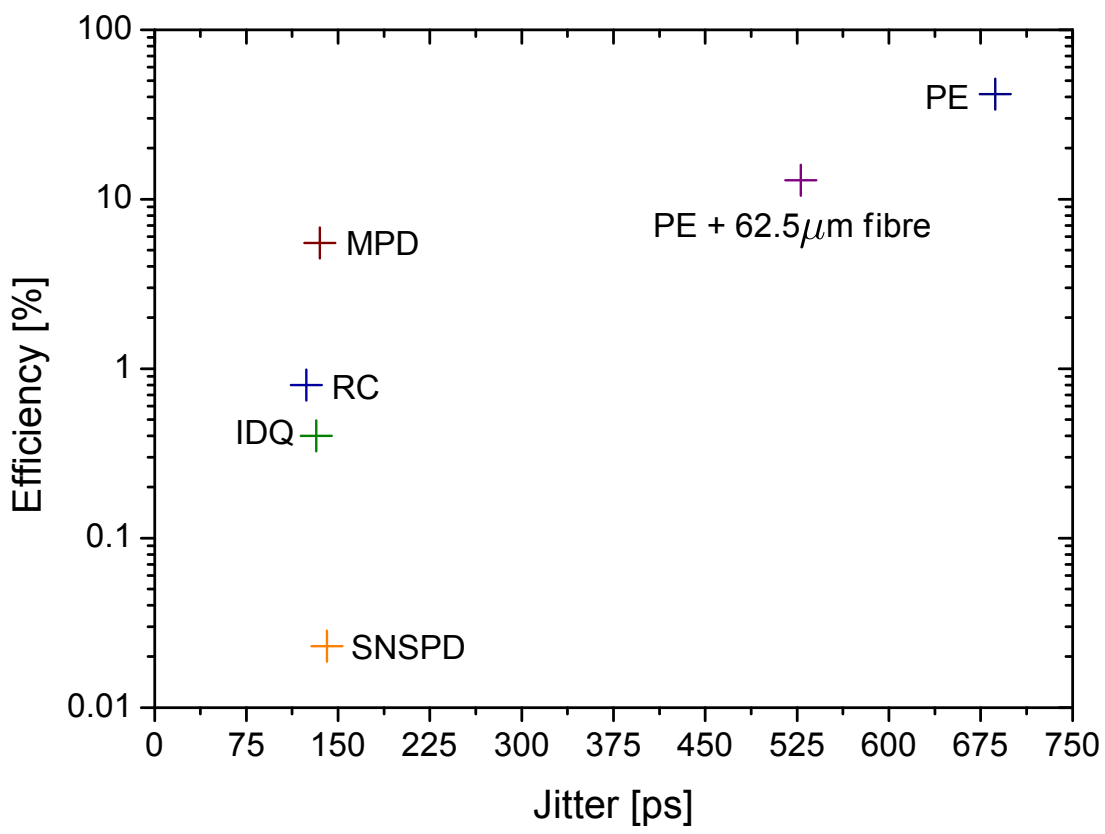

Figure 2.28: *Jitter and efficiency for different detector and fibre combiner setups.*

Figure 2.28 shows the characteristics for the different detectors in terms of efficiency and timing jitter. The PE detector had the highest overall efficiency but also a very high FWHM of 687 ps and a FW 1/10 Max jitter which was higher than the temporal spacing

between two adjacent peaks. Without adding additional delays in order to increase the spacing between neighbouring peaks, the current setup leads to channel crosstalk caused by the overall very high timing jitter. The MPD, RC, IDQ and SNSPD detectors possessed a lower timing jitter leading to less channel crosstalk, but they also exhibited a low efficiency. In applications where the overall efficiency is the most important factor the PE should be the detector of choice as the channel crosstalk could be reduced by using longer delays. The use of longer delays does mean that lower repetition frequencies must be used, leading to longer acquisition times.

2.3.5 *Channel capacity*

In order to show the capability of the V-Groove fibre array to convert position to time information, a transmission slit was placed in front of each V-Groove channel, as shown in Figure 2.29. The gap of the slit was 100 µm, which was less than the fibre separation (127 µm). The laser diode light was coupled into a 5 µm core diameter fibre to ensure single-mode operation. The light was then coupled out of the fibre and collimated. The V-Groove fibre array was uniformly illuminated. The timing signature for the eight position of the transmission slits was recorded with a thin junction SPAD from MPD and a thick junction SPAD from Perkin Elmer. The resulting traces for the MPD are plotted in Figure 2.30.

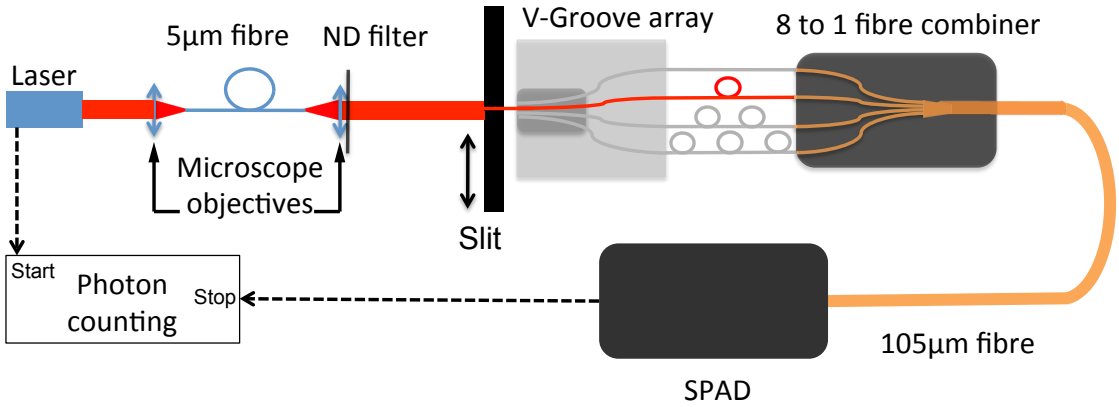

Figure 2.29: *Channel capacity setup. Light was selectively coupled into a single channel of the V-Groove fibre array by translating a transmission slit.*

The results from the channel capacity measurement can be analysed in terms of the number of effective channels that the combination of V-Groove fibre array, fibre combiner and different SPADs can measure. This is an important number to quantify, when such a receiver system is used for single-photon experiments. The input states

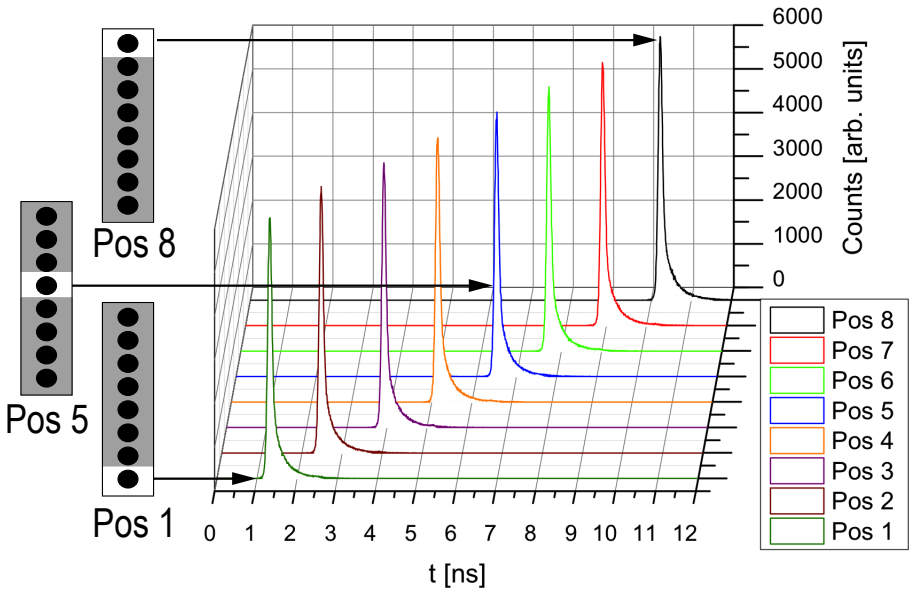

Figure 2.30: *Channel capacity measurement with a thin junction SPAD. Each peak position corresponds to a different transmission slit position.*

$\{a_1, a_2, \ldots, a_8\}$ are the eight different spatial positions of the transmission slit. The receiver states $\{b_1, b_2, \ldots, b_8\}$ are specific time windows in the recorded histogram. The different receiver states were separated by the optical delay introduced by the additional optical fibres of different pre-determined lengths. The probability of detecting a state $P(b_i)$ is calculated by summing the counts in the corresponding time window and by dividing it by the sum of all counts in all other windows. From information theory [2.42], the channel capacity C of the system is defined as:

$$C = H(a) - H(a|b) \tag{2.6}$$

where in our case:

$$H(a) = \sum_{a_i} P(a_i)\, log_2\, P(a_i) \tag{2.7}$$

is the entropy of the source and

$$H(a|b) = \sum_{a_i}\sum_{b_i} P(a_i, b_i)\, log_2\, P(a_i, b_i) \tag{2.8}$$

is the conditional entropy of the transmitted signal a given received signal b.

The maximum number of modes in the V-Groove fibre array is eight. If this receiver was to be used in a single-photon communication system, then the eight modes would in theory correspond to 3 bits photon^{-1}. Due to the finite temporal width of the detection signal and the background arising from the detector, this resulted in a reduced channel

capacity and a reduced number of modes. The channel capacity of the V-Groove fibre array and the thick junction SPAD was found to be 2.32 bits photon^{-1} corresponding to 4.99 effective modes, when the data was not binned. For the thin junction SPAD the channel capacity was 2.63 bits photon^{-1} with 6.17 effectives modes as shown in Table 2.14.

SPAD junction	Bits photon^{-1}	No. modes	Bits photon^{-1} (binned)	No. modes (binned)	Transmission rate (binned)
Thick	2.32	4.99	2.58	6.00	58%
Thin	2.63	6.17	2.93	7.60	53%

Table 2.14: *Experimental results for the channel capacity, effective number of modes and transmission rate for thick and thin junction SPADs used with the V-Groove fibre array receiver system.*

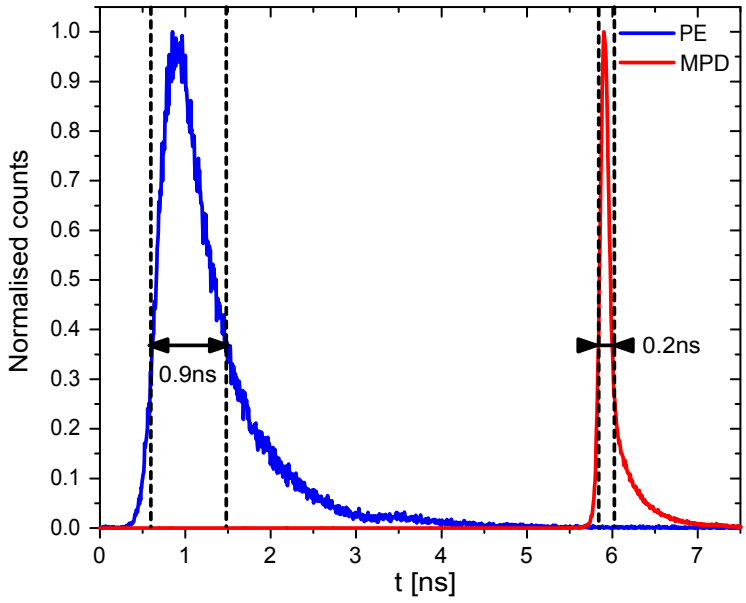

Figure 2.31: *Schematic illustration of binning for channel capacity measurement. For clarity only one example for the bin size for each detector is shown. The average FWHM for the PE detector is around* 0.9 ns*, while the average bin size for the MPD detector is* 0.2 ns.

At the expense of the overall data rate of the receiver system, the channel capacity and number of effective modes can be increased by binning the data. The amount of background noise caused by the detector and temporal overlap from the signal between adjacent channels can be reduced. For example, by setting the bin size of the receiver state to be the 1/e width (36.8%) of a Gaussian fitted to the data as shown in Figure 2.31, the channel capacity is increased to C = 2.58 bit/photons with 6.00 modes and C = 2.93 bits/photon with 7.60 effective modes for the thick and thin junction SPADs respectively. The transmission rate is decreased to 58% for the thick junction SPAD and 53% for the thin junction SPAD. Although the MPD detector has a higher channel capacity

and supports a higher number of modes, the PE detector was the detector of choice due to its higher SPDE. As seen in Table 2.13 the total efficiency of the full system is about 7.6 × higher when the PE detector instead of the MPD is used. The higher detection efficiency of the PE detector increases the chance to detect the entangled photon pairs in the Quantum Correlations experiment and potentially less information gets lost (see Chapter 3).

2.4 Conclusion

In this chapter, the theoretical background for different types of single-photon detectors and Time-Correlated Single-Photon Counting was outlined. Furthermore a V-Groove fibre array for single-photon position to time multiplexing was designed, built, and characterised in terms of single-photon detection efficiency, timing jitter and channel capacity for different types of single-photon detectors. The single-photon detectors were characterised in terms of SPDE and timing jitter. The thick junction Si-SPAD from Perkin Elmer possesses the highest SPDE of 59.9% at λ = 686 nm, but it also possesses the highest timing jitter of 323 ps at FWHM. The thin junction Si-SPAD from MPD has a SPDE of 33.1% and a FWHM of 70.8 ps.

The V-Groove fibre array was characterised in terms of its time of flight and the resulting time delay between two adjacent fibres. The time delay between neighbouring V-Groove fibres is δt= 1.26 ns ± 0.02 ns, which is about 0.01 ns more than originally specified. In the case, where the V-Groove was characterised with the additional delay fibres, the time delay is δt= 12.07 ns ± 0.09 ns, instead of 12 ns. These small delays were caused by inaccuracies during the manufacturing process of the fibres. The fibre combiner, was characterised in terms of transmission efficiency, time of flight and timing jitter. The transmission efficiency of the fibre combiner depends on the wavelength of laser. For a laser emitting at λ = 686 nm the averaged transmission efficiency is 71.7%. The overall system timing jitter depends on the fibre combiner. The averaged timing jitter in combiner #2 is 640 ps, while the timing jitter caused by combiner #1 is 610 ps. Compared to single fibre operation, the fibre combiner adds additional jitter, caused by the combining process. The jitter added by the fibre combiner is of the order of 200 ps. The change in time of flight between neighbouring fibres in the fibre combiner is less

than 0.1 ns for all fibres except fibre no. 5. These small extra time delays were caused by different fibre lengths due to inaccuracies during the manufacturing process.

The V-Groove fibre array receiver system was analysed with the different single-photon detectors in terms of detection efficiency and timing jitter. The receiver system with the highest detection efficiencies were the PE and the MPD detectors with SPDEs of 41.7% and 5.5% respectively. The Resonant Cavity SPAD, the thin junction SPAD from ID Quantique and the Superconducting Nanowire Single-Photon Detector possess, in combination with the fibre combiner, a SPDE of less than 1%. Therefore these detectors were not used for further channel capacity measurements.

The receiver system with the MPD detector possesses a high channel capacity of almost 2.63 bits photon^{-1} and 6.17 modes in the un-binned case. In contrast the V-Groove fibre array with the PE detector has a channel capacity of 2.32 bits photon^{-1} and a number of modes of 4.99. However the overall detection efficiency is higher for the PE detector, so potentially less information gets “lost” in quantum communication/ measurements.

2.5 References

[2.1] C. Kittel. *Introduction to Solid State Physics*. 5th edition. John Wiley & Sons, 1976 (cited on page: 9).

[2.2] R. E. Warburton. 'Infrared Time-Correlated Single-Photon Counting'. PhD thesis. Edinburgh, UK: Heriot-Watt University, 2008 (cited on page: 13).

[2.3] C. Webb and J. Jones. *Handbook of Laser Technology and Applications*. 1st edition. Institute of Physics Publishing, 2004 (cited on page: 13).

[2.4] S. Cova, M. Ghioni, A. Lacaita, C. Samori and F. Zappa. 'Avalanche photodiodes and quenching circuits for single-photon detection'. Appl. Opt., Vol. 35, (1996), pp. 1956–1976 (cited on page: 14).

[2.5] H. Dautet, P. Deschamps, B. Dion, A. D. MacGregor, D. MacSween, R. J. McIntyre, C. Trottier and P. P. Webb. 'Photon counting techniques with silicon avalanche photodiodes'. Appl. Opt., Vol. 32, (1993), pp. 3894–3900 (cited on page: 14).

[2.6] Perkin Elmer. *SPCM - AQRH Single Photon Counting Module - data sheet*. online, last accessed 2011-05-02. Perkin Elmer, (2007). URL: http://www.perkinelmer.co.uk/PDFS/downloads/dts_spcm%20aqrh.pdf (cited on pages: 14, 24, 27, 38).

[2.7] R. Krahl, A. Bülter and F. Koberling. *Performance of the Micro Photon Devices PDM 50CT SPAD detector with PicoQuant TCSPC systems*. Technical Note - online, last accessed 2011-05-02. (2005). URL: http://www.picoquant.com/technotes/technote_pdm.pdf (cited on page: 14).

[2.8] *MPD - PDF series data sheet*. online, last accessed 2011-05-02. Micro Photon Devices, (2008). URL: http://www.micro-photon-devices.com/media/pdf/PDF.pdf (cited on pages: 14, 15, 24, 27, 38).

[2.9] *IDQ - id100 series - data sheet*. online, last accessed 2011-05-02. ID Quantique, (2010). URL: http://www.idquantique.com/images/stories/PDF/id100-single-photon-detector/id100-specs.pdf (cited on pages: 15, 24, 27, 39).

[2.10] G. S. Buller and R. J. Collins. 'Single-photon generation and detection'. Meas. Sci. Technol., Vol. 21, (2010), p. 012002 (cited on pages: 15, 16).

[2.11] R. H. Hadfield. 'Single-photon detectors for optical quantum information applications'. Nat. Photonics, Vol. 3, (2009), pp. 696–705 (cited on pages: 15, 17).

[2.12] S. Cova, M. Ghioni, A. Lotito, I. Rech and F. Zappa. 'Evolution and prospects for single-photon avalanche diodes and quenching circuits'. J. Mod. Opt., Vol. 51, (2004), pp. 1267–1288 (cited on page: 15).

[2.13] M. Ghioni, A. Gulinatti, I. Rech, F. Zappa and S. Cova. 'Progress in silicon single-photon avalanche diodes'. IEEE J. Select. Topics Quantum Electron., Vol. 13, (2007), pp. 852–862 (cited on page: 15).

[2.14] Y. P. Varshni. 'Temperature dependence of energy gap in semiconductors'. Physica, Vol. 34, (1967), pp. 149–154 (cited on page: 16).

[2.15] S. Miki, M. Fujiwara, M. Sasaki, B. Baek, A. J. Miller, R. H. Hadfield, S. W. Nam and Z. Wang. 'Large sensitive-area NbN nanowire superconducting single-photon detectors fabricated on single-crystal MgO substrates'. Appl Phys Lett, Vol. 92, (2008), p. 061116 (cited on page: 17).

[2.16] E. A. Dauler, A. J. Kerman, B. S. Robinson, J. K. W. Yang, B. Voronov, G. Goltsman, S. A. Hamilton and K. K. Berggren. 'Photon-number-resolution with sub-30-ps timing using multi-element superconducting nanowire single photon detectors'. J. Mod. Opt., Vol. 56, (2009), pp. 364–373 (cited on page: 17).

[2.17] H. Takesue, S. W. Nam, Q. Zhang, R. H. Hadfield, T. Honjo, K. Tamaki and Y. Yamamoto. 'Quantum key distribution over a 40-dB channel loss using superconducting single-photon detectors'. Nat. Photonics, Vol. 1, (2007), pp. 343–348 (cited on page: 17).

[2.18] C. M. Natarajan, M. G. Tanner and R. H. Hadfield. 'Superconducting nanowire single-photon detectors: physics and applications'. Supercond. Sci. Technol., Vol. 25, (2012), p. 063001 (cited on page: 18).

[2.19] J. A. O'Connor, M. G. Tanner, C. M. Natarajan, G. S. Buller, R. J. Warburton, S. Miki, Z. Wang, S. W. Nam and R. H. Hadfield. 'Spatial dependence of output pulse delay in a niobium nitride nanowire superconducting single-photon detector'. Appl Phys Lett, Vol. 98, (2011), p. 201116 (cited on page: 17).

[2.20] P. B. Martins. *New Frontiers in Superconductivity Research*. 1st edition. Nova Science Pub Incorporated, 2006 (cited on page: 18).

[2.21] G. N. Gol'tsman, O. Okunev, G. Chulkova, A. Lipatov, A. Semenov, K. Smirnov, B. Voronov, A. Dzardanov, C. Williams and R. Sobolewski. 'Picosecond superconducting single-photon optical detector'. Appl. Phys. Lett., Vol. 79, (2001), pp. 705–707 (cited on page: 18).

[2.22] L. N. Cooper. 'Bound electron pairs in a degenerate Fermi gas'. Physical review, Vol. 104, (1956), pp. 1189–1190 (cited on page: 18).

[2.23] S. Pellegrini, R. E. Warburton, L. J. J. Tan, J. S. Ng, A. B. Krysa, K. Groom, J. P. R. David, S. Cova, M. J. Robertson and G. S. Buller. 'Design and Performance of an InGaAs-InP Single-Photon Avalanche Diode Detector'. IEEE J. Quantum Electron., Vol. 42, (206), pp. 397–403 (cited on page: 19).

[2.24] W. Becker. *The bh TCSPC handbook*. 2nd edition. Berlin: Becker & Hickl GmbH, 2005. URL: http://www.boselec.com/products/documents/BHTCSPCHandbook8-21-07LTR2.pdf (cited on pages: 20–22).

[2.25] M. Wahl. *Time-Correlated Single Photon Counting*. Technical Note - online, last accessed 2013-03-07. (2009). URL: http://www.picoquant.com/technotes/technote_tcspc.pdf (cited on page: 22).

[2.26] PicoQuant. *PicoHarp 300 - Data sheet*. online, last accessed 2013-03-07. (2012). URL: http://www.picoquant.com/datasheets/photon_counting/PicoHarp300.pdf (cited on page: 22).

[2.27] PicoQuant. *HydraHarp 400 - Data sheet*. online, last accessed 2013-03-07. (2012). URL: http://www.picoquant.com/datasheets/photon_counting/HydraHarp400.pdf (cited on page: 22).

[2.28] M. Ghioni, G. Armellini, P. Maccagnani, I. Rech, M. K. Emsley and M. Selim Ünlü. 'Resonant-cavity-enhanced single-photon avalanche diodes on reflecting silicon substrates'. IEEE Photonic Technol. Lett., Vol. 20, (2008), pp. 413–415 (cited on pages: 24, 27, 39).

[2.29] M. Ghioni, G. Armellini, P. Maccagnani, I. Rech, M. K. Elmsley and M. Selim Ünlü. 'Resonant-cavity-enhanced single photon avalanche diodes on double silicon-on-insulator substrates'. J. Mod. Opt., Vol. 56, (2009), pp. 309–316 (cited on page: 25).

[2.30] C. L. Niclass. 'Single-Photon Image Sensors in CMOS: Picosecond Resolution for Three- Dimensional Imaging'. PhD thesis. Lausanne, Switzerland: École Polytechnique Fédérale de Lausanne, 2008 (cited on page: 25).

[2.31] A. Lacaita, M. Ghioni and S. Cova. 'Double epitaxy improves single-photon avalanche diode performance'. Electron. Lett., Vol. 25, (1989), pp. 841–843 (cited on page: 25).

[2.32] A. Spinelli and A. L. Lacaita. 'Physics and numerical simulation of single photon avalanche diodes'. IEEE Trans. on Electron Devices, Vol. 44, (1997), pp. 1931–1943 (cited on page: 26).

[2.33] W. Becker. *Advanced Time-Correlated Single Photon Counting Techniques*. Vol. 81. Springer Series in Chemical Physics. Springer Berlin Heidelberg, 2005 (cited on page: 26).

[2.34] G. Ripamonti and S. Cova. 'Carrier diffusion effects in the time response of a fast photodiode'. Solid-State Electron., Vol. 28, (1985), pp. 925–931 (cited on page: 26).

[2.35] M. J. Declercq. 'New C-MOS technology using anisotropic etching of silicon'. IEEE J. Solid-State Circuits, Vol. SC-10, (1975), pp. 191–197 (cited on page: 28).

[2.36] C. L. Huang and T. van Duzer. 'Schottky diodes and other devices on thin silicon membranes'. IEEE Trans. Electron Devices, Vol. ED-23, (1976), pp. 579–583 (cited on page: 28).

[2.37] T. J. Rodgers and J. D. Meindl. 'Epitaxial V-groove bipolar integrated-circuit process'. IEEE Trans. Electron Devices, Vol. ED-20, (1973), pp. 226–232 (cited on page: 28).

[2.38] R. E. Warburton, F. Izdebski, C. Reimer, J. Leach, D. G. Ireland, M. Padgett and G. S. Buller. 'Single-photon position to time multiplexing using a fiber array'. Opt. Express, Vol. 19, (2011), pp. 2670–2675 (cited on page: 30).

[2.39] *Thorlabs Mating Sleeve*. online, last accessed 2013-02-19. URL: http://www.thorlabs.de/newgrouppage9.cfm?objectgroup_id=314 (cited on page: 33).

[2.40] R. H. Hadfield. private communication. (2010) (cited on page: 39).

[2.41] C. M. Natarajan, A. Peruzzo, S. Miki, M. Sasaki, Z. Wang, B. Baek, S. Nam, R. H. Hadfield and J. L. O'Brien. 'Operating quantum waveguide circuits with superconducting single-photon detectors'. Appl. Phys. Lett., Vol. 96, (2010), p. 211101 (cited on page: 39).

[2.42] C. E. Shannon. 'A mathematical theory of communication'. Bell Syst. Tech. J., Vol. 27, (1948), pp. 379–423 (cited on page: 48).

CHAPTER 3

QUANTUM CORRELATION MEASUREMENTS WITH MULTI-PIXEL FIBRE DETECTORS

In this chapter, quantum correlations were measured in the position and momentum bases and the superposition thereof with an 8×1 fibre array. We were able to measure 8 positions simultaneously without having to scan a single detector. The variance product of the momentum-sum and the position-difference is over 1 order of magnitude below the classical limit of separability, revealing EPR-like correlations of the entangled photon pairs generated through spontaneous parametric down-conversion. Spatial light modulators were used to switch between the image plane and the far-field of the nonlinear crystal, thus eliminating the need for manual changes of the experimental setup.

3.1 Theoretical Background

In this section, the production of entangled photons through spontaneous parametric down-conversion and the required properties for the nonlinear crystal will be detailed. A brief introduction to entanglement and the criteria for EPR-like correlations will be given.

3.1.1 *Spontaneous parametric down-conversion*

Entangled photons are most commonly produced by a technique called Spontaneous Parametric Down-Conversion (SPDC). SPDC can be understood as the time reversed sum frequency generation as the nonlinear crystal is driven at its sum frequency by the pump photon. The photon pair emitted possesses a strong temporal correlation, making them suitable for coincidence detection with a very narrow time window [3.1,

3.2]. The pump photon splits up into a photon pair. The down-converted photons are often called signal and idler photon. The energy of the pump photon is conserved as the frequency of the signal and idler photon add up to the frequency of the pump photon.

$$\omega_{pump} = \omega_{signal} + \omega_{idler} \tag{3.1}$$

For the degenerate case, down-converted light at $\omega_{signal} = \omega_{idler}$ is created. In this case a frequency tripled Nd:YAG laser (JDSU XCYTE) lasing at $\lambda = 355$ nm was used to produce signal and idler photons with a wavelength of $\lambda = 710$ nm. Besides the energy, the momentum of the pump photon is also conserved during SPDC.

$$k_{pump} = k_{signal} + k_{idler} \tag{3.2}$$

The down-converted photons possess equal, but opposite, transverse momenta to form a "cone" of light as shown in Figure 3.1.

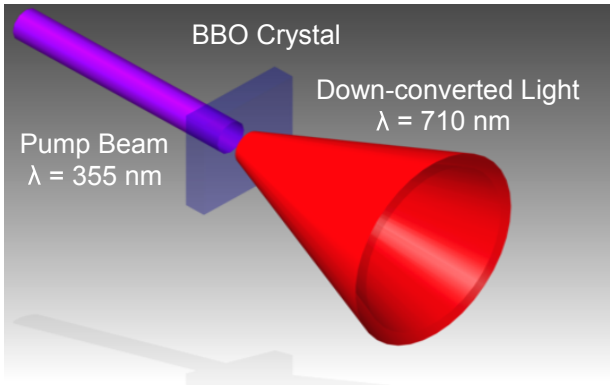

Figure 3.1: *Cone of down-converted photons for Type–I phase matching.*

The nonlinear crystal is a birefringent material, meaning that different polarisations of the incident light beam will experience different refractive indices. Figure 3.2 shows a birefringent crystal and how the crystal separates the different polarisations, which are orthogonal to each other, of the incident unpolarised light beam.

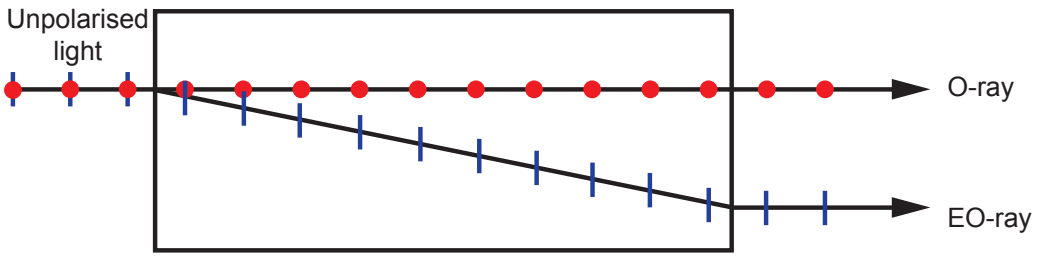

Figure 3.2: *Operating principle of a birefringent crystal. The different polarisations are separated as they experience different refractive indices.*

Depending on the type of phase matching, the emitted SPDC cones will be different. In type−I phase matching the polarisation of the down-converted photons is parallel to each other and orthogonal to the pump beam. For type−I phase matching only a single cone will be visible, because the signal and idler cones overlap. In type−II phase matching the polarisation of the down-converted photons are orthogonal to each other and the polarisation of the pump beam is parallel to one of the down-converted photons (and orthogonal to the other) [3.3]. For type−II phase matching two cones will be visible due to the separate optical paths for the different polarisations. Figure 3.3(a) depicts a summed frame measurement with an electron-multiplying CCD

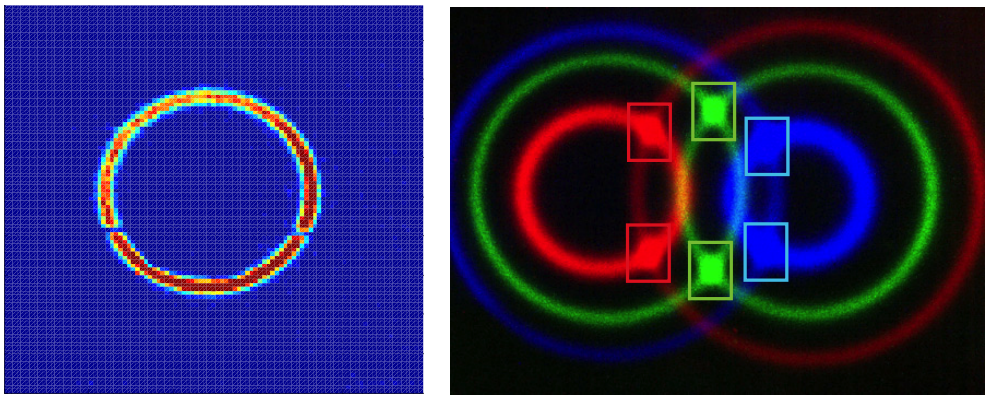

(a) Type−I phase matching (b) Type−II phase matching

Figure 3.3: *Emitted cones of down-converted photons for type−I (a) and type−II (b) phase matching [3.4, p. 278].*

camera (see Chapter 4) of a cone generated by type−I phase matching at degeneracy. In front of the camera, a bandpass filter centred at $\lambda = 710\,\text{nm}$ with a FWHM of 10 nm was placed. The ring is represented by the number of counts in the pixels after 2000 frames. Figure 3.3(b) shows three different images of type−II phase matched down-converted light. Each colour represents one long exposure with a different bandpass filter located in front of a high-speed infrared film and a 35 mm single-lens reflex camera with the lens removed [3.5]. In contrast to Figure 3.3(a) two cones are visible per colour ($\lambda_1 = 681\,\text{nm}$, $\lambda_2 = 702\,\text{nm}$, $\lambda_3 = 725\,\text{nm}$). At the intersection of the two cones, the photons are entangled in polarisation.

Only a small fraction of the pump photons decay spontaneously into pairs of photons by spontaneous parametric down-conversion. The conversion efficiency for a typical nonlinear material to convert pump photons into correlated photon pairs integrated over all emission directions for SPDC at $\lambda_{pump} = 500\,\text{nm}$ is approximately

$1.0 \times 10^{-8}\,\mathrm{mm^{-1}\,sr^{-1}}$ [3.6]. The overall pair production rate is independent of the pump beam's spot size [3.7] for the same output power.

3.1.2 *SPDC crystals*

For frequency conversion the nonlinear crystal must be transparent for both the the pump beam and the down-converted photons. Other important characteristics of nonlinear crystals include damage threshold, conversion efficiency, temperature tolerance and the thermo-optic coefficient, which is a measure of wavelength dispersion varying with temperature. Table 3.1 summarises theses characteristics for commonly used nonlinear crystals. In the following different nonlinear crystal will be compared in terms of their suitability for creating down-converted photons with type-I phase matching for $\lambda_{pump} = 355\,\mathrm{nm}$ and $\lambda_{SPDC} = 710\,\mathrm{nm}$.

	KTP	PPLN	LBO	BBO
d_{eff} [$\mathrm{pm\,V^{-1}}$]	3.64	17.2	1.16	1.94
Transparency [µm]	$0.35-4.0$	$0.50-5.0$	$0.16-2.6$	$0.19-2.5$
Damage threshold [$\mathrm{GW\,cm^{-2}}$]	0.5	0.2	2.5	5
Typical length [cm]	$1-2$	$2-6$	$0.5-1$	$0.5-1$
Thermal tolerance [$\mathrm{°C\,cm^{-1}}$]	25	0.6	3.6	55

Table 3.1: *Comparison of common nonlinear crystals [3.8, p. 612].*

The effective nonlinear coefficient, d_{eff}, depends on the nonlinear crystal material and is usually a combination of one or more coefficients of the second-order susceptibility $\chi^{(2)}$ and the wave propagation vector, which is defined by the angles θ and ϕ. θ is defined as the angle between the propagation vector and the crystalline $z-axis$ (the optic axis), while ϕ is defined as the azimuthal angle between the crystalline xz crystalline plane and the propagation vector [3.9, p. 40]. $\chi^{(2)}$ is responsible for the sum and difference frequency generation as the pump, signal, and idler optical field are coupled to each other through the second order susceptibility. Due to the coupling, the energy among the interacting fields can be exchanged. A high effective nonlinear coefficient d_{eff} is preferable, as it scales quadratically with the coupling coefficient [3.9, p. 80].

KTP (Potassium Titanyl Phosphate) is widely used for the generation of 2nd harmonics of Nd:YAG lasers. The wavelength of the pump beam used in the experiment lies at the edge of the transparency region, which might cause a high absorption

of the pump beam. KTP has a high conversion efficiency of up to 65% for the 1064 nm to 532 nm conversion. This high conversion efficiency can be achieved for type−II phase matching, but for type−I phase matching the nonlinear optical coefficient is very low, and therefore for this experiment not useful [3.10]. Another problem with KTP crystals is, that they suffer from gradual photochemical degeneration. Photochemical degeneration leads to an increased absorption in the crystal, which can cause crystal failure.

PPLN (Periodically Poled Lithium Niobate) offers the opportunity to quasi-phase match the pump and the generated beams. This leads to a highly efficient conversion process, which is not based on birefringence phase matching. Instead of depending on birefringence phase matching PPLN achieves quasi phase matching with a periodic structure engineered into the crystal. Unfortunately the transparency of PPLN does not cover the wavelength range needed for this experiment.

LBO (Lithium Triborate) shows a good transparency in the UV- region and has a very high damage threshold of 2.5 GW cm^{-2}. In contrast to BBO the nonlinear optical coefficient d_{eff} and therefore the conversion efficiency is low. It is important to have a high nonlinear coefficient as d_{eff} scales quadratically with the coupling efficiency.

BBO (β−Barium metaborate) The transparency range of the BBO crystal covers the pump beam as well as the down-converted beams. BBO possesses a high nonlinear optical coefficient for type−I phase matching, a high damage threshold and a large temperature tolerance. The main shortcoming with BBO is the low angular tolerance of 0.5 mrad cm^{-1}, which requires a diffraction limited beam for efficient frequency conversion.

Comparing these commonly used nonlinear crystals with the requirements of a high nonlinear coefficient, transparency at 355 nm and 710 nm and type−I phase matching, BBO is the material of choice. The BBO crystal used in the experiment was a negative uniaxial nonlinear crystal, meaning that the crystal possessed only one optic axis and that the refractive index for the extraordinary beam is smaller than the refractive index of the ordinary beam. In a negative uniaxial nonlinear crystal only one velocity of the travelling waves depends on the direction of propagation through the crystal. The po-

larised wave which experiences a lower refractive index is fast, while the polarisation experiencing a higher refractive index is slow. In BBO only the fast velocity depends on the propagation direction, which is the extraordinary wave.

The BBO crystal had to be specified for the experiment. The two most important specifications are the type of phase matching and the desired wavelengths. For this experiment type−I phase matching was needed as we were interested in the spatial correlations of the down-converted photons and not in polarisation entanglement. The crystal also had to be specified for the desired wavelengths of the pump beam and the down-converted photons in order to be able to cut the crystal at the right angle for phase matching. The refractive index of the crystal depends on the wavelength and the polarisation, and can be accurately estimated using the Sellmeier equations [3.11].

The Sellmeier equation for the ordinary beam is defined as:

$$n_o^2(\lambda) = A_o \frac{B_o}{\lambda^2 - C_o} - D_o \lambda^2, \tag{3.3}$$

while the Sellmeier equation for the extraordinary beam is defined as:

$$n_e^2(\lambda) = A_e \frac{B_e}{\lambda^2 - C_e} - D_e \lambda^2 \tag{3.4}$$

Axis	A_I	B_I	C_I	D_I
ordinary	2.7359	0.01878	0.01822	0.01354
extraordinary	2.3753	0.01224	0.01516	0.01516

Table 3.2: *Sellmeier coefficients for BBO crystals [3.12].*

From the Sellmeier equations and coefficients (Table 3.2) for the ordinary and extraordinary beam the refractive indices for the BBO crystal at λ = 355 nm and λ = 710 nm can be calculated.

n	λ = 355 nm	λ = 710 nm
ordinary	1.705	1.664
extraordinary	1.576	1.547

Table 3.3: *Calculated refractive indices for the BBO crystal at* λ = 355 nm *and* λ = 710 nm

Given the calculated refractive indices of the crystal at the pump and the down-converted wavelength, one can calculate the phase matching angle for a crystal

cut for collinear orientation. For a negative uniaxial crystal the pump beam is the extraordinary (fast) wave and the down-converted photons are the ordinary (slow) wave, in order to compensate for the dispersion with the birefringence of the crystal. The phase matching condition is: $k_{pump}(eo) = k_{signal}(o) + k_{idler}(o)$ or $\Delta k = k_{pump} - k_{signal} - k_{idler} = 0$.

It is theoretically possible that the pump beam is the slow wave, although in most cases this does not lead to phase matching [3.13].

From the following equation the phase matching angle for a negative uniaxial BBO crystal with type−I phase matching can be calculated [3.9, p. 99]:

$$\sin^2(\theta) = \frac{(n_o^{\omega})^{-2} - (n_o^{2\omega})^{-2}}{(n_e^{2\omega})^{-2} - (n_o^{2\omega})^{-2}} \tag{3.5}$$

Substituting the values for the calculated refractive indices from Table 3.3 into Equation (3.5) gives a phase matching angle of 32.76°. These calculations are valid for a crystal with collinear geometry, where the photons travel in the same direction, see Figure 3.4(a) for clarification.

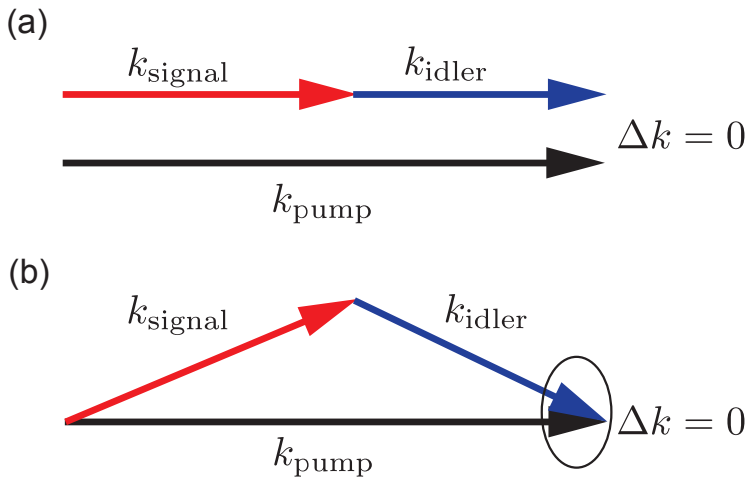

Figure 3.4: *Momentum of the photons for collinear crystal geometry (a) and non-collinear crystal geometry (b).*

However, the crystal used in the quantum correlations experiment had a non-collinear geometry and the photons travelled in different directions, see Figure 3.4(b). The phase matching angle for crystals cut for non-collinear output must be calculated numerically, as this problem can not be solved analytically. These calculations are not covered in this thesis, however a detailed description can be found in Ref. [3.13, 3.14]. The

non-collinear BBO crystal used in the experiment had a phase matching angle of 33.2° [3.15].

3.1.3 *Entanglement*

The term *Entanglement* was first used by Erwin Schrödinger [3.16] as a response to the famous *Gedankenexperiment* by Albert Einstein, Boris Podolsky and Nathan Rosen (EPR) [3.17]. Entangled particles can no longer be seen as separate systems as they are in the quantum mechanical state called superposition. The spatial position of the entangled particles has no effect on the entangled state and a measurement on one particle will instantaneously reveal information of the second particle. Einstein refers to this phenomenon as a "spooky action at a distance" [3.18, p. 158]. An alternative to the "spooky action" would be that each particle in an entangled pair possesses a set of well-defined local physical properties. These properties are quantified by *local hidden variables*. Performing Bell tests on the entangled particle pairs reveals, that local hidden variables do not exist [3.19] and this was experimentally proven by Aspect *et. al* in 1982 [3.20], to demonstrate the non-locality of the entangled particles.

Different types of entanglement exist, for example the nucleus can be entangled in spin, while photons can be entangled in polarisation, and/or position and momentum. In this thesis the entanglement of photons was measured in position and momentum for entangled photon pairs generated through spontaneous parametric down-conversion. The two photons from a photon pair are entangled, when their wave-function cannot be factorised into separate terms.

Mancini [3.21] developed criteria to calculate the separability for position and momentum measurements. Previous criteria for entanglement suffered from non-scalability as most of these criteria involved sums of dimensionless variances and therefore were not easy to apply to the dimensional measurements of position and momentum.

The criterion for separability is defined as

$$\Delta^2(\mathrm{mom}_1 + \mathrm{mom}_2) \cdot \Delta^2(\mathrm{pos}_1 - \mathrm{pos}_2) \geq [\mathrm{mom}_1, \mathrm{pos}_1]^2, \tag{3.6}$$

where $\Delta^2(\text{mom}_1 + \text{mom}_2)$ is the variance of the momentum-sum and $\Delta^2(\text{pos}_1 - \text{pos}_2)$ is the variance of the position-difference for the photon pair.

The criterion for EPR-like correlations or entanglement is defined as:

$$\Delta^2(\text{mom}_1 + \text{mom}_2) \cdot \Delta^2(\text{pos}_1 - \text{pos}_2) \leq 1/4\,[\text{mom}_1, \text{pos}_1]^2. \tag{3.7}$$

These equations were calculated for the scale-able joint probability distribution $P(\text{mom}_1, \text{mom}_2)$ and $P(\text{pos}_1, \text{pos}_2)$. Using these for $[\text{mom}, \text{pos}] = \text{mom} \cdot \text{pos} - \text{pos} \cdot \text{mom} = i\hbar$ Equations Equation (3.6) and Equation (3.7) can be rewritten as:

$$\Delta^2(\text{mom}_1 + \text{mom}_2) \cdot \Delta^2(\text{pos}_1 - \text{pos}_2) \geq \hbar^2 \tag{3.8}$$

and

$$\Delta^2(\text{mom}_1 + \text{mom}_2) \cdot \Delta^2(\text{pos}_1 - \text{pos}_2) \leq 0.25\,\hbar^2 \tag{3.9}$$

The condition for non-separability is weaker than the condition for entanglement. This means that not all non-separable system satisfy EPR, but non-separability is a condition for EPR.

In this thesis the measurements for down-converted photon pairs were measured either in momentum or in position basis. Only when the detectors were imaged onto each other high coincidence count rates were measured, see Section 3.3.3 for details. This means that it was not possible to measure the position of a photon in one measurement arm and the momentum of the other photon in the second measurement arm simultaneously. Instead two independent sets of measurements must be performed, one for each basis. Using these two independent measurement sets, it was possible to measure the position and momentum of the entangled photon pairs to a higher precision than given by the Heisenberg uncertainty principle:

$$\Delta_{\text{mom}} \cdot \Delta_{\text{pos}} \geq \hbar/2 \tag{3.10}$$

This shows that the two entangled photons are in a quantum mechanical state and not two individual separate systems.

Almost 70 years after Einstein, Podolsky and Rosen wrote their paper about the EPR-paradox, Howell *et. al* demonstrated the first experimental measurement of EPR-like

correlations in position and momentum in 2004 [3.22]. For this experiment a SPAD was translated in the image plane, and far-field, of the crystal to obtain coincidence counts. The lenses were changed manually to switch between the image plane and the far-field of the nonlinear crystal.

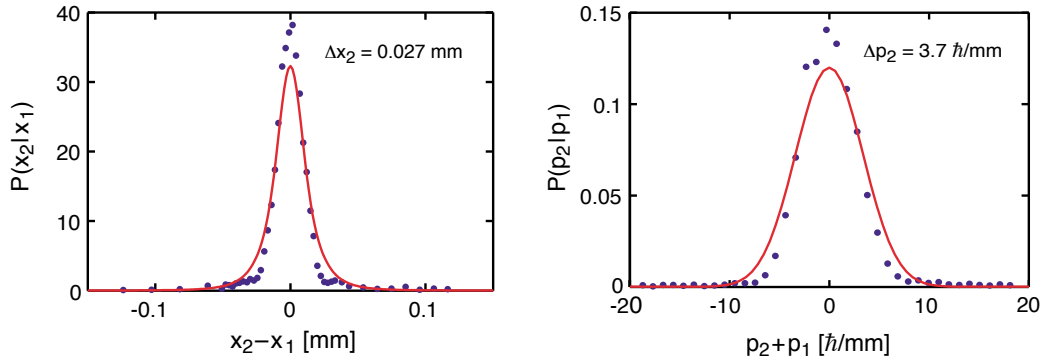

(a) Position (b) Momentum

Figure 3.5: *First experimental measurements of EPR-like correlations, showing the conditional distributions in position (a) and momentum (b). Figure taken from Ref. [3.22].*

Figure 3.5 shows the experimental results of the conditional probability distribution for the measurement of position correlations (a) and transverse momentum correlations (b) measured by Howell *et al.* [3.22]. The dots represent actual measured data, while the solid lines show theoretical predictions. The uncertainty for the position difference is 0.027 mm, while the uncertainty for the transverse momentum sum is $3.7\,\hbar\,\mathrm{mm}^{-1}$. The resulting variance product is $0.01\,\hbar^2 < \hbar^2/4$, giving a violation factor of 25. In the experiment, described in this chapter, 8 positions will be measured simultaneously with a SPAD in each arm and instead of manually changing the optical setup, spatial light modulators will be used to switch between the image plane and far-field of the crystal.

3.1.4 *Spatial Light Modulators*

Spatial Light Modulators (SLM) are devices which can alter the phase of the incoming beam without changing the intensity and without rotating the polarisation state of the incoming beam [3.23, p. 2]. SLMs which are designed for amplitude and phase modulation exist as well, however their performance to alter the phase is worse compared to the phase-only modulation SLMs. SLMs in general are a vital tool in photonics and used in many different applications including beam shaping [3.24, 3.25], wavefront correction [3.26, 3.27] and optical manipulation [3.28, 3.29].

Operating Principles of Spatial Light Modulators

Hamamatsu manufactures Liquid Crystal On Silicon (LCOS) Spatial Light Modulators, which reflect the incoming light beam. Inside the SLM head a mirror is incorporated. Hamamatsu offers several LCOS SLM heads which are designed to operate at different wavelengths. The customer can choose between LCOS SLMs with dielectric mirrors, which offer high efficiencies of up to 90% for a small wavelength range of several 10's of nm. In contrast "broadband" aluminium mirrors have a lower efficiency, but they can be used over a wavelength range of up to 500 nm (see Figure 3.8). Some wavelength regions for the aluminium mirror expose unwanted interference noise, which limits the performance of the SLM.

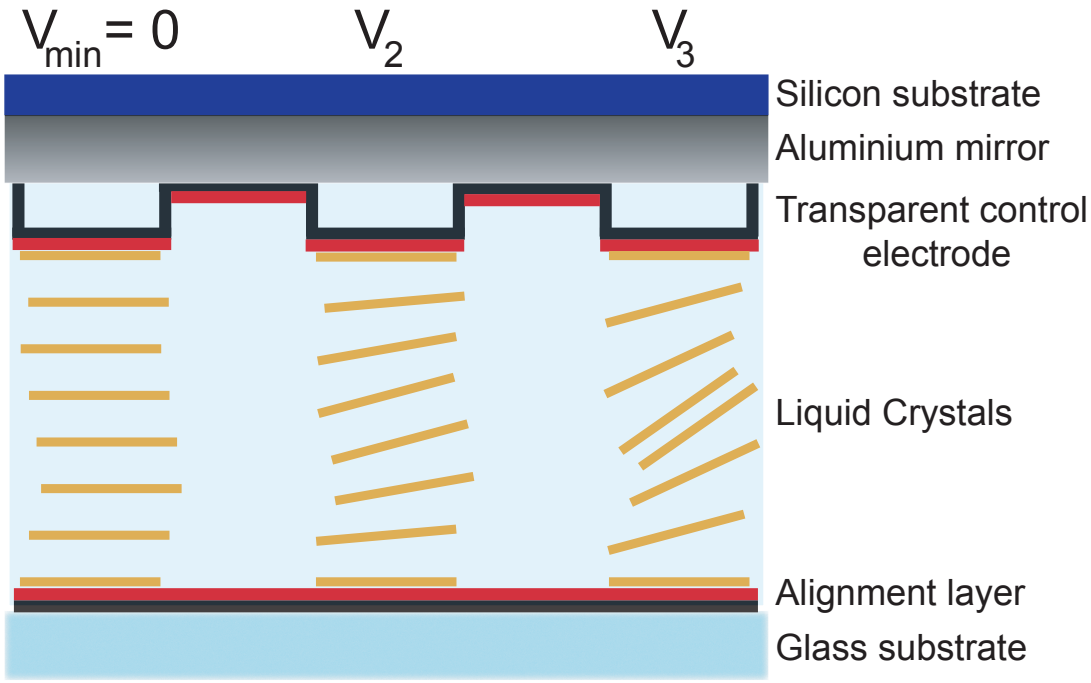

Figure 3.6: *Schematic for a reflective LCOS SLM with different applied voltages to the individual pixel with* $V_{min} = 0\,\mathrm{V} < V_2 < V_3$.

Figure 3.6 shows a schematic for a reflective LCOS SLM. The LCOS SLM head consists of a silicon substrate. On top of the silicon substrate either a dielectric or an aluminium mirror is grown. The alignment layers are brushed to provide the orientation of the liquid crystal layer. The liquid crystals consist of rod shaped molecules. These molecules can have different types of orientation to each other and to the crystal surface. The three basic types of orientation are nematic, cholesteric and smectic [3.30, p. 159]. The molecules in the Hamamatsu LCOS SLM are nematic [3.23, p. 2]. This means that they are aligned parallel to each other, but

are free to move around relative to each other, thus behaving like a liquid. Typical nematic crystal molecules consist of two benzene rings linked with a central group [3.30, p. 159]. The alignment layers could either be aligned orthogonal to each other, resulting in a twisted-nematic liquid crystal with a helical orientation of the liquid crystal to provide amplitude modulation in conjunction with crossed polarisers. Alternatively the alignment layers could be parallel aligned to each other, providing phase-only modulation. A glass plate is bonded to the top alignment layer. When the liquid crystal display is used as an optical modulator then polarisers are incorporated at the mirror-alignment layer and the glass plate alignment layer interface.

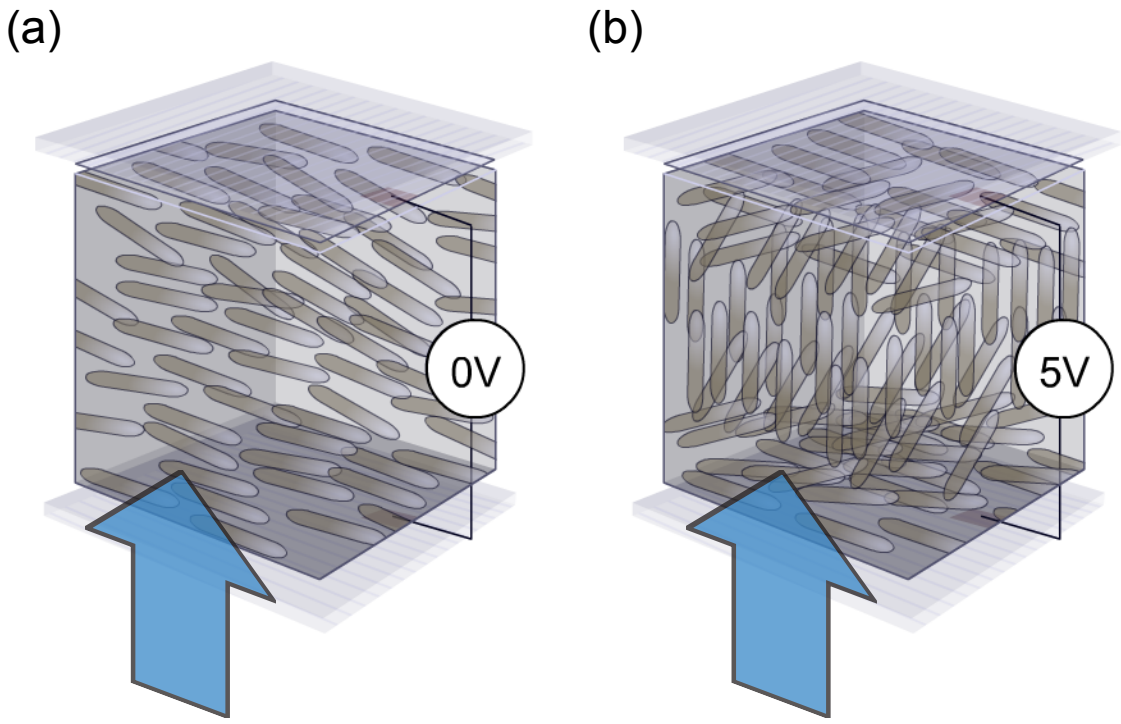

Figure 3.7: *Phase retardation of liquid crystals with and without applied voltage. The light travels from the bottom of the bottom of the SLM up to the top. The light is linear polarised and parallel to the orientation of the alignment layer (orientation of the liquid crystals in the off state). (a) shows a liquid crystal phase retarder when no voltage is applied. The phase of the incoming light is not retarded and passes through the polariser at the other side of the liquid crystal cell. In (b) a high voltage is applied to the cell, so that the majority of the liquid crystals are aligned vertically in the direction of the electric field. The incident light beam now experiences a medium with a higher refractive index for one polarisation direction. The phase of the incoming light is changed [3.31].*

Liquid crystals exhibit electrical anisotropy. When an electric field is applied to the liquid crystal then the molecules change their orientation. Molecules which were previously aligned parallel to each other now start to align perpendicular to the liquid crystal- solid interface along the field direction, as shown in Figure 3.7. The molecules furthest away from the interface begin to realign first. The liquid crystals also exhibit

optical anisotropy. Along the orthogonal optical axes, the refractive indices are different due to the birefringence of the nematic material, resulting in different phase retardations of the incoming light. For spatial light modulators to work, the incoming light beam must be linear polarised and parallel to the liquid crystal molecule direction in the off state. When no voltage is applied to pixels then the liquid crystal axis is parallel to the polarisation, resulting in a "switched off" pixel. By applying a voltage to the liquid crystal, the orientation of the molecules changes and the liquid crystal acts as a phase retarder, meaning that the pixel is "switched on". The vertically polarised light passes the liquid crystal layer and undergoes phase modulation. The amount of phase modulation depends on the difference in the refractive index of the ordinary and extraordinary beam, the wavelength and the thickness of the liquid crystal cell. The phase modulation is defined as:

$$\delta = \frac{2\pi\, d}{\lambda} \cdot (n_{eo} - n_o) \tag{3.11}$$

During the phase modulation the polarisation of the incoming light is maintained because the liquid crystal molecules are parallel to each other. SLMs which modulate the intensity amplitude of the incoming beam use twisted nematic liquid crystal cells, which rotate the polarisation of the incoming beam and depending on the polarisation a well defined amount of the incoming light will pass the crossed polarisers in the SLM. The pixels for both types of SLMs are addressed via an active matrix circuit, which is formed on the silicon substrate. Each pixel can be switched on or off by applying a voltage on the pixel electrode.

Safe operating conditions

SLMs can be easily damaged. In order to maintain a working SLM the following precautions must be followed. Thermal damage occurs when the average power of the incident laser beam is too high. Over time the liquid crystal will heat up and while the liquid crystal heats up, the birefringence of the liquid crystal will decrease until no birefringence remains. Once the liquid crystal passes the isotropic phase temperature the liquid crystal is irreversibly damaged. The damage threshold of the LC depends on different factors including the average power, illumination area, wavelength of the incident beam, and the exposure time. Since these factors depend on the chosen experimental setup, Hamamatsu Photonics should be consulted for specific information

about the damage threshold of their SLM series. A guide for the damage threshold capabilities of Hamamatsu's LCOS SLM X10468 series can be found in the technical information brochure [3.32]. Abrasion damage of the dielectric or aluminium mirrors can occur when the peak power of the incident light beam is too high. The SLM will be damaged when the peak power density is above the abrasion threshold of the mirror. Photochemical damage can be caused by UV-light. The absorption coefficient of liquid crystals increases at wavelengths below λ = 350 nm. The absorbed UV-light can break down the LC molecules and irreversible damage the SLM. In order to avoid damaging the SLM the average and the peak power should be kept below the damage threshold of the SLM and UV-light should not be incident upon the SLM's readout surfaces.

3.2 Experimental Setup

3.2.1 *Pump laser*

The pump laser used in this experiment was the XCYTE model CY-PS2 from JDSU. The laser was a frequency-tripled Nd:YAG laser emitting light at $\lambda \approx 355$ nm. The laser was mode-locked and had a typical pulse duration of 10−20 ps with a repetition rate of 100 MHz. The average output power at λ = 355 nm was 150 mW. However a lower average output power was required for the experiment, therefore the pump beam was attenuated to approximately 2 mW. The diameter of the pump beam was 1 mm.

3.2.2 *BBO crystal*

The nonlinear crystal used to generate the down-converted photons was a type−I BBO crystal from CLaser Photonics Incorporation. The BBO crystal specifications are summarised in Table 3.4.

The incident photons from the pump laser (λ = 355 nm) were down-converted to entangled photon pairs at λ = 710 nm. Due to the type−I phase matching the down-converted photons were entangled in position and momentum, but not in polarisation. The crystal was orientated to provide a near-collinear output, meaning that the

Manufacturer:	CLaser Photonics Inc.
Width:	5 mm±0.1 mm × 5 mm±0.1 mm
Length:	3 mm
Orientation:	Type−I
Geometry:	Non-collinear
Wavefront distortion:	$\lambda/6$
Surface quality:	10/5
Clear aperture:	>90%
Chip:	0.1 mm
Parallelism:	<20″
Coating:	S_1 and S_2 anti-reflection for 710 nm and 355 nm
Remarks:	Ø 25.4 mm

Table 3.4: *Specifications for BBO crystal used for Quantum Imaging experiment. [3.15].*

down-conversion ring was collapsed in the far-field of the crystal and only a spot was visible.

3.2.3 *Spatial Light Modulator*

The SLMs were used as variable focal length lenses in this experiment. The SLM was programmed to provide a pre-determined level of optical power in the first diffracted order. When no optical power was applied to the incident beam, then the SLM acted as a "mirror". By applying additional optical power to the SLM, it acted as a "lens", thus removing the need to manually change the optical system, to switch between the image plane and far-field of the nonlinear crystal for the position- and momentum correlation measurements.

The major for requirement for the SLM was that it works at $\lambda = 710$ nm. Hamamatsu offers different SLMs which are designed to operate at this wavelength see Figure 3.8.

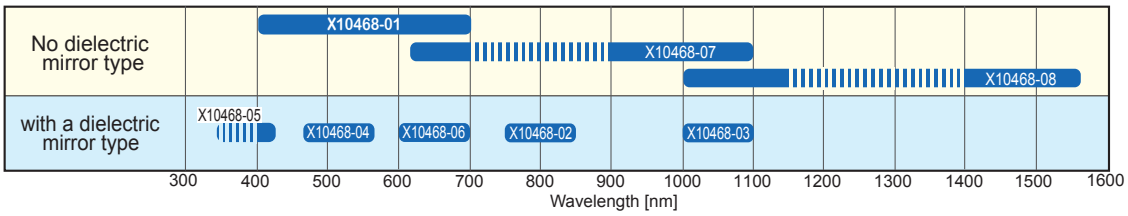

Figure 3.8: *Available Spatial Light Modulators for different wavelengths [3.23, p. 2]*

At the required wavelength of 710 nm two aluminium mirror SLMs are available. Although the X10468-07 series can be used at a wavelength range from 620 nm to 1100 nm. However, this SLM is not suitable for this experiment as the SLM exposes

unwanted interference noise at a wavelength range from 700 nm − 900 nm. Therefore the X10468-01 series was chosen. (The X10468-06 series SLM with a dielectric mirror was not commercially available at the time when the SLMs were purchased for the project.) The specifications of the LCOS SLM X10468-01 series are given in Table 3.5.

Number of pixel:	792×600
Pixel pitch:	20 µm
Maximum spatial frequency:	25 lp/mm
Effective area:	16 mm × 12 mm
Aperture ratio:	95%
Liquid crystal orientation:	parallel alignment
Phase modulation levels:	2π (radians) or higher
Input signal level:	256 for 8−bit
DVI signal settings:	SVGA (800×600), 60 Hz
Effective number of pixel:	475200
Typical response time - rise:	10 ms
- fall:	10 ms
Input voltage (AC):	100 V to 230 V (50 Hz − 60 Hz)
Power consumption:	50 V A
Weight:	420 g

Table 3.5: *Specifications for Hamamatsu spatial light modulator LCOS SLM X10468-0 [3.23, p. 4].*

The SLMs were pre-calibrated at the factory for a specified wavelength range to have 2π (or more) radians of phase modulation and a linear increase of the phase modulation (see Figure 3.9). Within the phase modulation curve, 95% of the pixel lie within $\pm 2\sigma$.

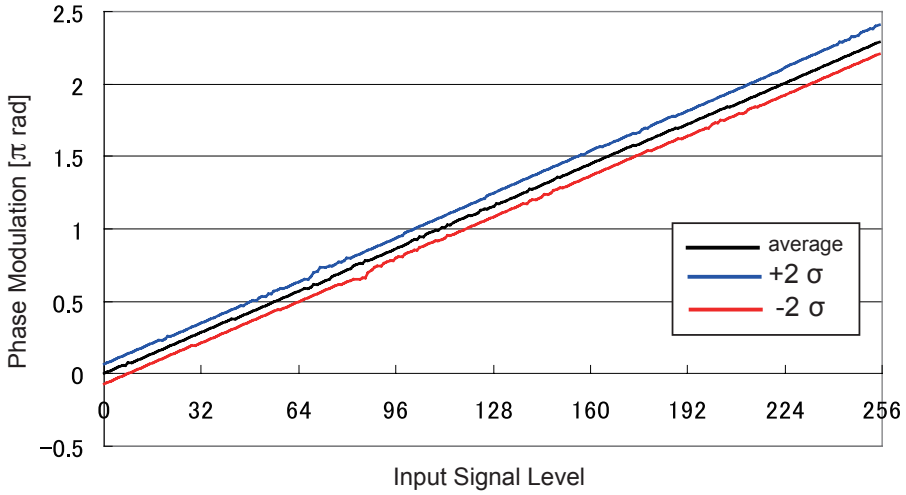

Figure 3.9: *Typical phase modulation for Hamamatsu LCOS SLM [3.23, p. 2]*

The diffraction efficiency of the SLM is defined as I_1/I_0 where I_1 is the intensity of the first diffraction order spot, while I_0 is the intensity of the zeroth order beam, when no

diffraction is applied to the beam. The diffraction efficiency for the LCOS SLM X10468-01 is given in Table 3.6.

Spatial frequency [lp/mm]:	5	12.5	25
Diffraction efficiency [%]	86	69	37

Table 3.6: *Diffraction efficiency of Hamamatsu LCOS SLM X10486-01 series [3.23, p. 2].*

It was assumed, that the diffraction efficiency for the first diffraction order was approximately 60% after measuring the power from the incoming beam and the diffracted beam in the first diffraction order [3.33, p. 61].

3.2.4 *Multi-pixel fibre detector*

The quantum correlations were measured with the multi-pixel fibre detector characterised in Chapter 2. The receiver system consisted of the 8×1 fibre combiner and a thick junction SPAD from Perkin Elmer (model: SPCM-AQRH). In the following, the importance of the fibre length in order to avoid or reduce signal overlap and the importance of a low- noise SPAD with carefully designed read-out electronics is detailed.

Importance of SPAD detector

The Optics group within the University of Glasgow had acquired two SPADs from Laser Components (model: COUNT®- Single-Photon Counting Module). These detectors have been characterised at different wavelengths in terms of their electronic output pulse, relative single-photon detection efficiency (SPDE) (compared to Perkin Elmer SPCM), timing jitter, dark count rate, and afterpulsing for different count rates.

Electrical Output pulse

The properties of the electrical output pulse from the laser driver and the SPADs are important to know. For example the photon counting card used in the timing jitter and single-photon detection efficiency experiments could suffer damage if the output voltage coming from the laser driver or the SPAD is too high and/or has the wrong

polarity. The following setup, shown in Figure 3.10, was used to characterise the amplitude, duration and the polarity of the output pulse from the laser driver and the two Perkin Elmer and two Laser components detectors. The picosecond pulsed diode laser

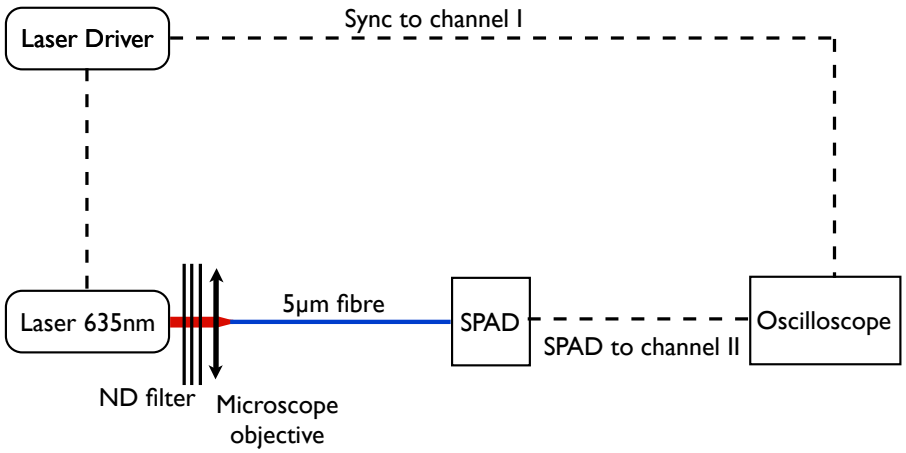

Figure 3.10: *Experimental setup for the characterisation of the output pulses coming from the laser driver and the detectors to be tested.*

driver PDL 800 from PicoQuant drove a λ = 635 nm laser diode. Due to the high output power, and in order to ensure statistically correct measurements and to avoid afterpulsing, the laser output was heavily attenuated with ND-filters in free space. The laser output was then coupled into a 5 µm core diameter fibre, ensuring single-mode operation. The sync output from the laser driver was connected to channel I of a fast oscilloscope (Agilent Infinium) and the SPAD output was connected to channel II. For each detector, two measurements (one for the laser driver and one for the detector) were performed successively. These two measurements provided information about the time delay between the laser pulse and the detector firing.

Figure 3.11 shows the electrical output pulse characteristics for the Perkin Elmer (a) and (b), and the Laser Components detectors (c) and (d). Knowing the time delay, polarity and amplitude of the electrical output pulse are important parameters to know. The time delay is important for certain applications like heralded single-photon ghost imaging [3.34], where for example a camera is triggered after a photon is registered by a SPAD. If the camera is triggered at the wrong time, the correlated photon is lost, as it can not be detected by the camera. For the Perkin Elmer detectors the output pulse is a square wave with a FWHM of 32 ns. The output pulse amplitude is in both cases 4.5 V. The time delay between the laser driver pulse and the detector pulse is 74 ns for PE 13848 and 76 ns for PE 13849 respectively.

The Laser Components detectors have different output pulse characteristics. Unlike

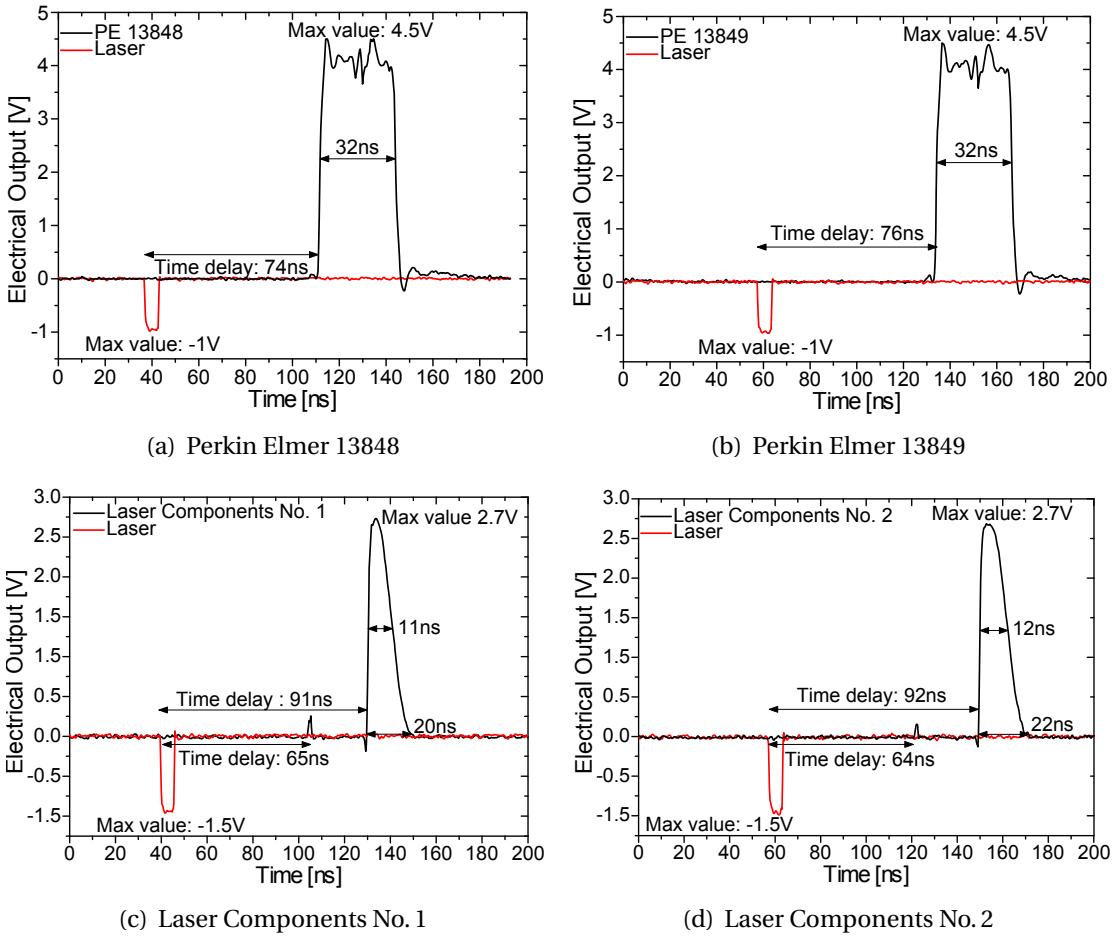

(a) Perkin Elmer 13848

(b) Perkin Elmer 13849

(c) Laser Components No. 1

(d) Laser Components No. 2

Figure 3.11: *The top figures show the electrical output pulse characteristics for Perkin Elmer 13848 and Perkin Elmer 13849 respectively. The bottom figures show the electrical output pulse characteristics for the Laser Components detectors No. 1 and No. 2.*

the Perkin Elmer detectors the output pulse shape is not rectangular. The output pulse has a fast rising edge and a long decaying tail. The output pulse length is of the order of 20 ns for both detectors. The output pulse amplitude is 2.7 V. The time delay between the laser driver pulse and the detector pulse is 91 ns for Laser Components No 1 and 92 ns for Laser Components No 2 respectively. Both Laser Components detectors possess an additional small output pulse, which appears roughly 65 ns after the laser driver output pulse as shown in Figures 3.11(c) and 3.11(d).

The additional peak is sufficiently large to be detected by the National Instruments card used in quantum correlations experiments. Correspondingly, the count rates were apparently twice as high, compared to the Perkin Elmer detectors, when the Laser Components detectors were used. However, using the Laser Components detectors did not improve the number of detected correlated photons pairs accordingly.

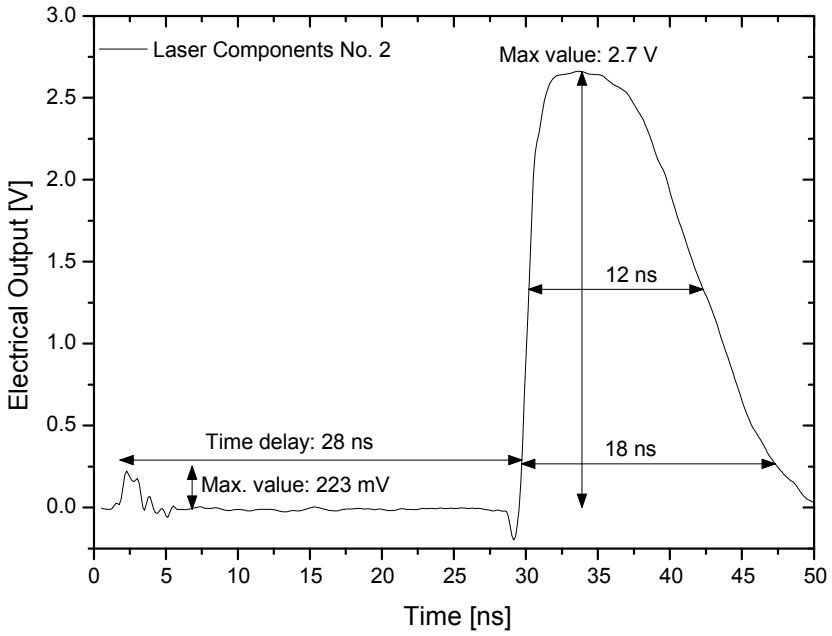

Figure 3.12: *Rescaled electrical output pulses for Laser Components No. 2 showing the small additional peak.*

Experiments with Becker & Hickl Photon Counting Card

Figure 3.13 shows the experimental setup for the detector characterisation. The electrical synchronisation pulse from the laser driver was electrically attenuated to ensure safe operation for the Becker and Hickl photon counting card (SPC-600). The laser driver was used to drive two different diode lasers ($\lambda = 635$ nm and $\lambda = 780$ nm) for two different sets of measurements. The optical output from the laser diodes was attenuated by ND filters in free space and then coupled into a 5 µm fibre for single-mode operation. The fibre was connected to the SPAD under test. The attenuated SPAD outputs were connected to the CFD input of the photon counting card. The photon counting card was connected to a PC, which was running the photon counting card operation software. The data was analysed either by using the Becker and Hickl software (timing jitter) or Origin (relative SPDE and dark count rate).

Figure 3.14 shows an example histogram obtained with a Perkin Elmer SPAD. For each measurement the same duration for the time windows was chosen to determine the number of counts in the signal peak. As there is a noise floor present in the measurements, a flat portion of each histogram was chosen to determine the background for each measurement. A 10 ns window was chosen for the background measurement in order to obtain accurate statistics and the average number of background counts per time bin was calculated.

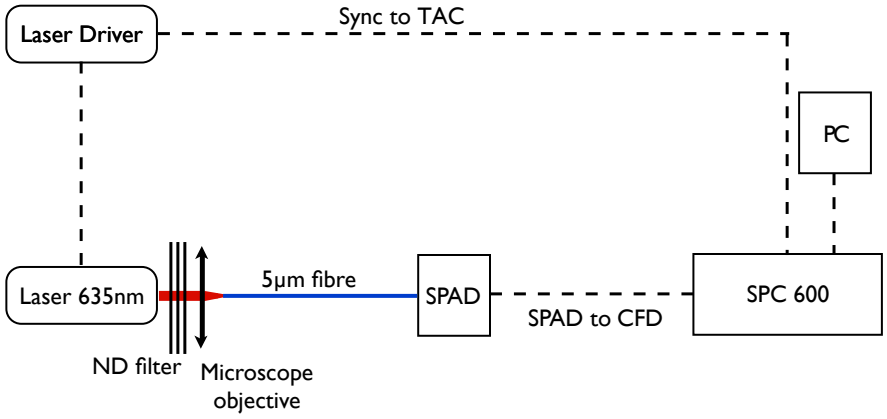

Figure 3.13: *Experimental setup for timing jitter, relative SPDE and dark count rate measurements. Two different laser diodes were used in different sets of measurements. The detectors were characterised at* $\lambda = 635$ nm *and at* $\lambda = 780$ nm.

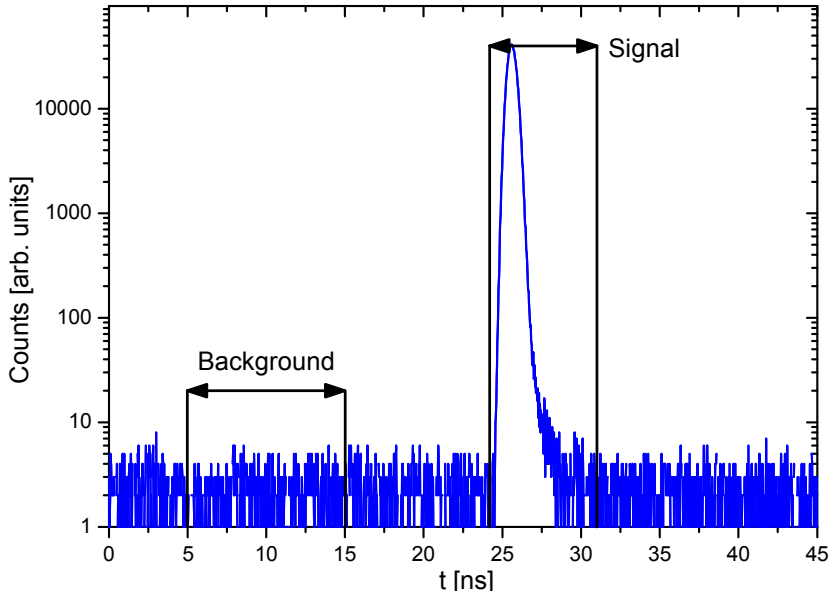

Figure 3.14: *Example histogram obtained during detector characterisation with Becker & Hickl photon counting card showing the signal peak and an arbitrarily chosen flat part for background measurement.*

Relative Single-Photon Detection Efficiency

The relative single-photon detection efficiencies of the Perkin Elmer and Laser Components detectors were characterised by using the experimental setup shown in Figure 3.13. The clock rate of the laser driver was set to 5 MHz, the count rate at the detector was of the order of 5.000 cps and each measurement lasted for 180 s. Each detector was characterised at $\lambda = 635$ nm and at $\lambda = 780$ nm. The number of counts for each signal peak was background corrected, where the value for the background correction was derived from a 10 ns window in each histogram. For both wavelengths PE 13848 is the most efficient detector, closely followed by PE 13849 which possess a relat-

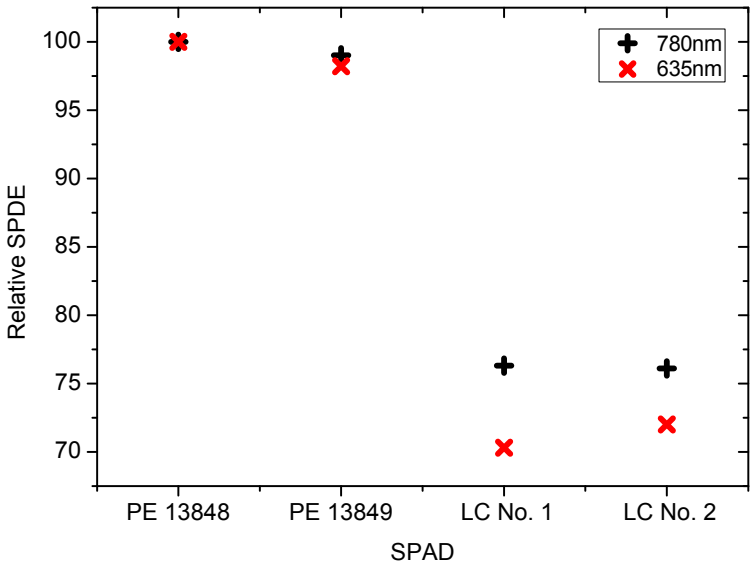

Figure 3.15: *Background-corrected relative single-photon detection efficiencies of the detectors characterised at* $\lambda = 635$ nm *and* $\lambda = 780$ nm.

ive SPDE of 98.2% at 635 nm and 99.4 % at 780 nm respectively. The Laser Components detectors possessed a lower SPDE than the Perkin Elmer detectors. The overall SPDE decreases by almost 30% for the 635 nm laser measurement and approximately 24% for the 780 nm laser measurement compared to PE 13848.

Timing jitter

The timing jitter measurements were performed with the 780 nm laser diode. The 635 nm laser diode was unsuitable for this type of measurement due to the broad output pulse (FWHM $\geq$ 2 ns for both types of detectors) from the laser diode. The clock rate from the laser driver was set to 5 MHz. The TAC window was 100 ns. Each detector was characterised at 4 different photon induced count rates and 4 different acquisition times because the maximum number of counts in one time bin was limited to 64,000 counts. The photon induced count rates were varied by changing the laser to fibre coupling efficiency.

Count rate [kcps]	Acquisition time [s]
1	300
10	180
50	30
100	10

Table 3.7: *Count rates and their respective acquisition times for timing jitter and dark count rate measurements.*

For the values given in Table 3.7, the FWHM of each detector was evaluated with the Becker and Hickl software.

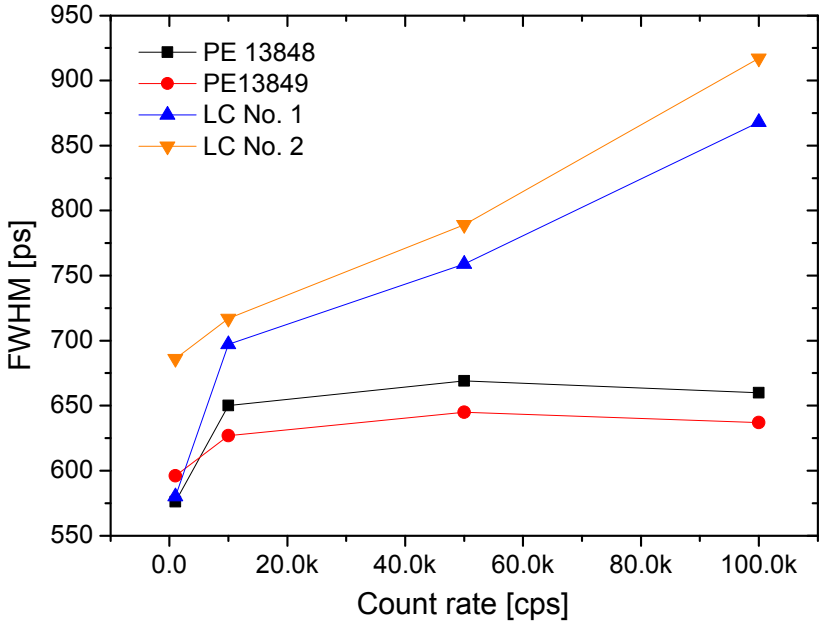

Figure 3.16: *Comparison of timing jitter at different count rates for Perkin Elmer and Laser Components detectors. The FWHM was evaluated with the Becker and Hickl software.*

Both Perkin Elmer detectors possess a smaller FWHM than the Laser Components detectors, as shown in Figure 3.16. While for low count rates up to 10,000 cps the difference in FWHM between Perkin Elmer and Laser Components is of the order of roughly 75 ps, this figure increases with higher count rates. At 100,000 cps the FWHM of the Laser Components detectors is 231 ps higher than Perkin Elmer 13848. For count rates higher than 10,000 cps, the FWHM of the Perkin Elmer detectors varies only slightly by ± 10 ps. The FWHM for the Laser Components detectors however increases linearly with higher count rates. The FWHM of the detector must be low for the fibre correlation experiment to order to minimise the overlap between neighbouring channels (see Section 2.3.3). In case the neighbouring channels overlap, coincidence counts might get added to the wrong channel, which increases the error. Also a small FWHM would be advantageous, as this leads to a narrower correlation peak with a higher peak to background ratio, compared to a lower and broader correlation peak.

Dark count rate and effects of afterpulsing

Using the data obtained at different photon induced count rates, the apparent dark count rates were calculated. The dark count rate varied for the different photon in-

duced count rates, as a result of afterpulsing. Afterpulsing is caused when carriers are trapped during avalanche events and released later, causing further avalanches. The dark count rate was calculated from the integrated background counts in the measurement window [s], the acquisition time [s] and the clock rate of the laser driver [Hz].

$$\text{Dark count rate} = \frac{\text{Integrated background counts}}{\text{Measurement window} \times \text{Acquisition time} \times \text{Clock rate}} \tag{3.12}$$

The measurement window was set to 10 ns for the Perkin Elmer detectors and 20 ns for the Laser Components detectors. The clock rate from the laser driver was set to 10 MHz. The different acquisition times can be found in Table 3.7. Figures 3.17(a)

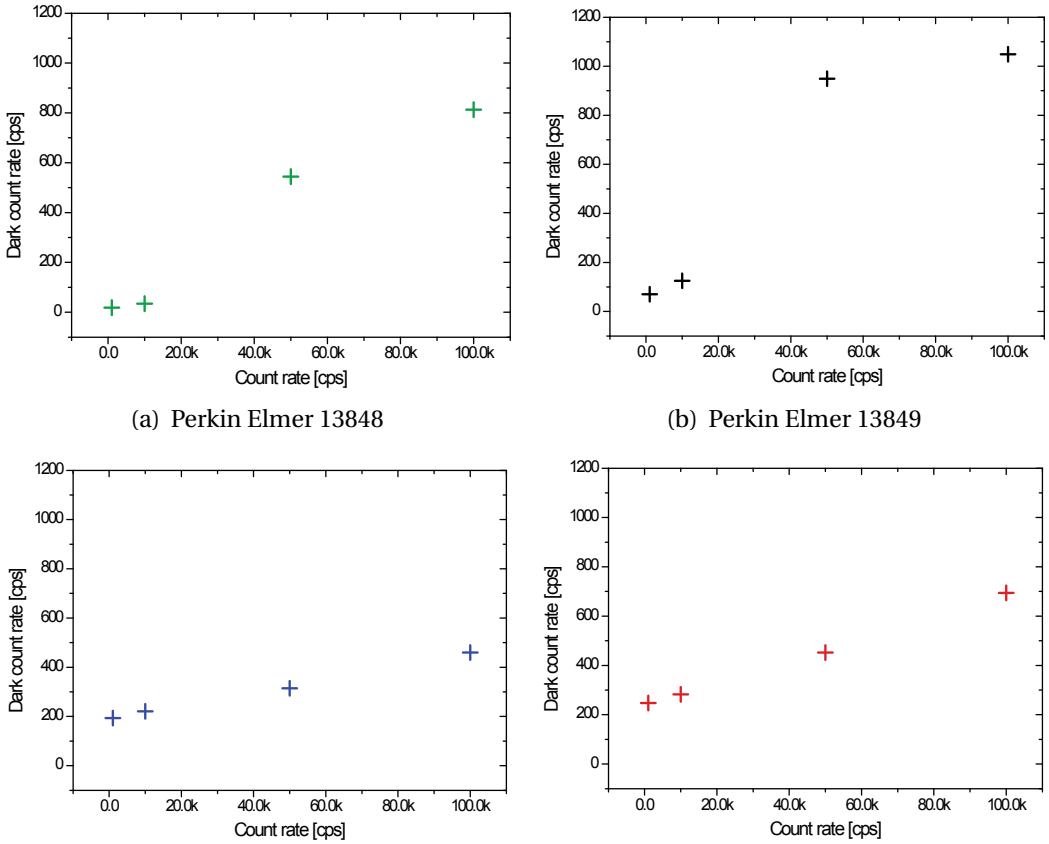

(a) Perkin Elmer 13848

(b) Perkin Elmer 13849

(c) Laser Components No. 1

(d) Laser Components No. 2

Figure 3.17: *Comparison of increasing dark count rate for the four detectors at different count rates.*

and 3.17(b) show the increasing dark count rates for the Perkin Elmer detectors. Although both detectors possess a low dark count rate for low count rates, the dark count rate increases rapidly with rising count rate. For a count rate of 100,000 cps the dark count rate is roughly 11× as much as for the measurement with a photon count rate of 1,000 cps. In contrast the Laser Components detectors (Figures 3.17(c) and 3.17(d)) possess a slightly higher dark count rate of roughly 200 cps for Laser Components No 1

and 250 cps for Laser Components No 2 for a photon induced count rate of 1,000 cps. However, the dark count rates only increases by a factor 2.4 for Laser Components No 1 and 2.8 for Laser Components No 2 respectively.

In terms of relative SPDE, timing jitter, and dark count rates at low count rates, the Perkin Elmer detectors are superior compared to the Laser Components detectors. The Laser Components detectors possess a lower dark count rate at higher count rates and the increase in dark count rate is much lower compared to Perkin Elmer detectors. However in the final quantum correlations experiment the photon induced count rates were reduced to less than 10 kcps, where the Perkin Elmer detectors possess a better performance as well.

Importance of fibre length

In this experiment, the intensity correlation of entangled photon pairs should be measured in position, momentum and intermediate bases with two 8×1 fibre combiners. The full detection system should be able to resolve 64 coincidence peaks. The fibre lengths for the timing signature must be carefully chosen. Ideally there should be no overlap between neighbouring channels and no combination of "start" and "stop" channel should result in the same delay time. The fibre detection system characterised in Chapter 2 was designed to match the laser repetition rate of 100 MHz. The full-system timing jitter characterisation (see Section 2.3.3) showed that there is a significant overlap between neighbouring channels, when the thick junction SPAD was used.

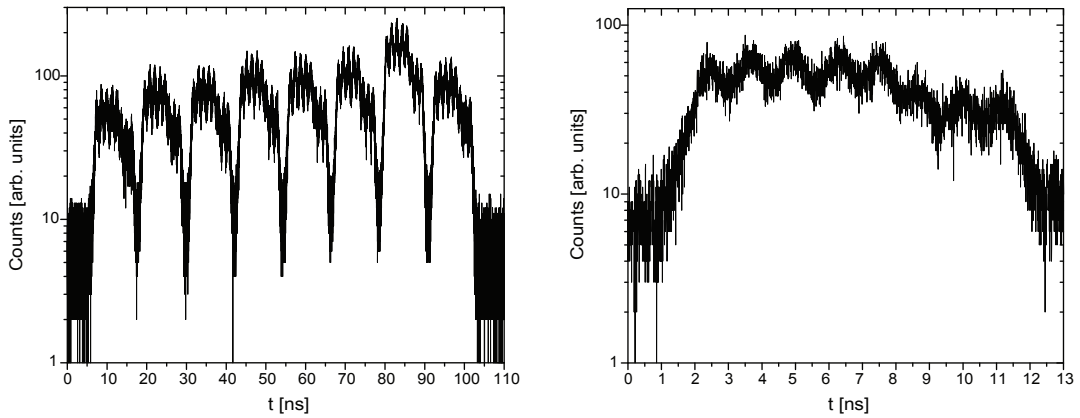

(a) 64 peak positions measured with "start" and "stop" detector

(b) Rescaled first "stop" peak showing eight "start" peaks

Figure 3.18: *64 Peak positions showing overlap due to too short delay fibre lengths.*

The histograms depicted in Figure 3.18 were recorded with a photon counting card from PicoQuant. The start and stop detector were illuminated with a laser diode emitting at λ = 780 nm. Figure 3.18(a) shows the 64 possible peak positions for the "start" and "stop" detector. All combinations of fibre lengths occur only once. Figure 3.18(b) shows the rescaled first "stop" peak with its eight "start" peaks. There is a significant overlap between neighbouring channels and therefore longer fibre delays need to be used for the quantum correlations experiment.

A computer program was written in LabView to simulate different delay fibre lengths and the resulting time delay. The individual peaks were simulated with actual data recorded from a single fibre going through the fibre combiner connected to a thick junction SPAD. The time delays between channels in the "start"- arm were chosen to have no overlap at the FW1/10M value. The time delay for the "start" arm was chosen to be 4.9 ns and the time delay for the "stop" arm was 44.1 ns. Each fibre in the V-Groove had a length of 1 m and only the delay fibres differ in length. The Time of Flight (TOF) in a V-Groove fibre was 4.9 ns. For the delay fibre lengths and time of flights see Table 3.8.

	Start Arm			*Stop Arm*		
Channel	Length of Delay Fibre [m]	TOF-Delay Fibre [ns]	TOF [ns]	Length of Delay Fibre [m]	TOF-Delay Fibre [ns]	TOF [ns]
1	1	4.9	9.8	10	48.9	53.8
2	2	9.8	14.7	19	92.9	97.8
3	3	14.7	19.6	28	136.9	141.8
4	4	19.6	24.5	37	180.9	185.8
5	5	24.5	29.4	46	224.9	229.8
6	6	29.3	34.2	55	268.9	273.8
7	7	34.2	39.1	64	313.0	317.9
8	8	39.1	44.0	73	357.0	361.9

Table 3.8: *Calculation of time of flight (TOF) for new V-Groove Fibre Array and Delay Fibres in the start- and stop arm*

In order to calculate the delay time, the following equation can be used:

$$t_{Delay} = \frac{l_{stop} \times n}{c} - \frac{l_{start} \times n}{c}, \tag{3.13}$$

where l denotes the length to the chosen fibre, n is the effective refractive index of the optical fibre and c is the speed of light in vacuum.

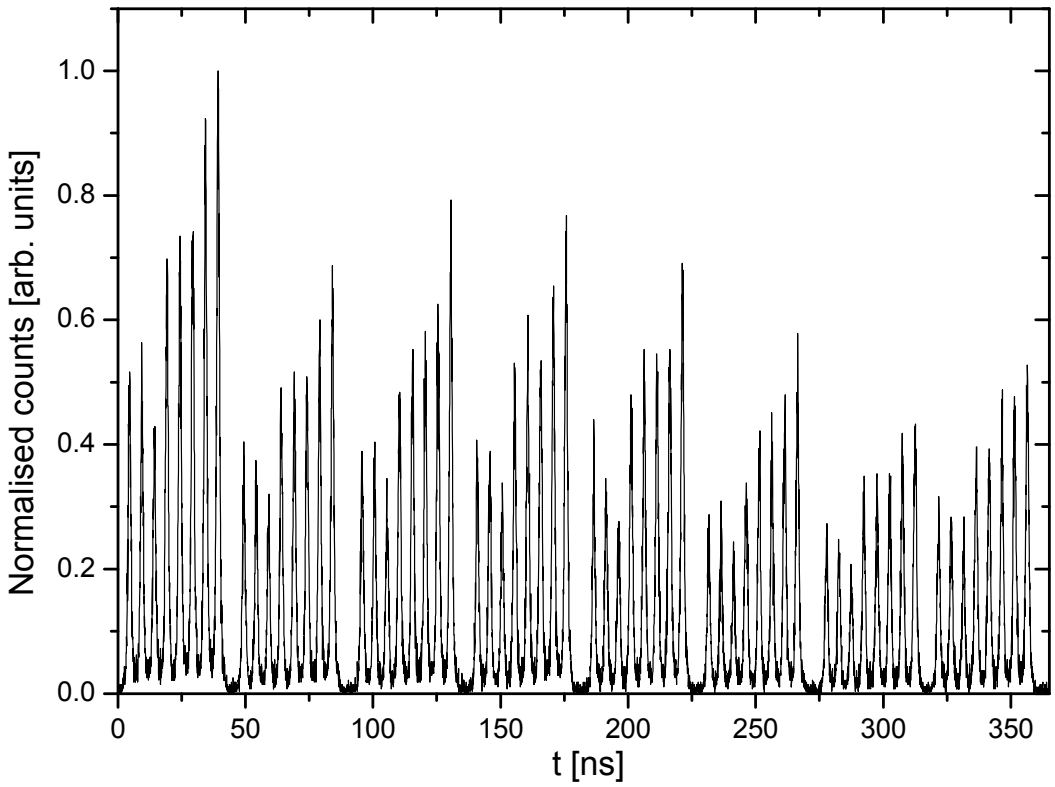

Figure 3.19: *64 peak positions with increased delay fibre lengths.*

Figure 3.19 shows a histogram with 64 peak positions but with an increased delay between neighbouring channels in the "start" and "stop" arm. There is only a small overlap at the FW1/10M for the channels in the "start" arm. The histogram was recorded with a PicoQuant photon counting card and the detectors were illuminated with an attenuated pulsed laser diode emitting at λ = 780 nm. The measurement lasted for 6 minutes.

3.2.5 *Full experimental setup*

The pulsed frequency tripled Nd:YAG laser (λ = 355 nm) used in this experiment possessed a repetition rate of 100 MHz. The average output power of the beam was attenuated down to 2 mW and the beam diameter was 1 mm. The beam was incident on a 3 mm long type−I BBO-crystal cut for non-collinear, degenerate phase matching. Entangled photons were created through spontaneous parametric down-conversion and the down-converted photons had a wavelength of λ = 710 nm. Using an afocal telescope, the exit face of the crystal was re-imaged with a magnification of 5 in order to increase the correlation length of the photon pairs. A 50:50 beam splitter was used

to separate the down-converted photons into two separate optical arms. Each arm contained a spatial light modulator, which was placed midway between the re-imaged crystal plane and the fibre array detector. In combination with a fixed 400 mm focal length lens, the SLM was used to switch between the image plane and the far-field of the re-imaged crystal. The SLM was programmed to provide pre-determined optical powers in the first diffraction order. When no additional power was applied to the SLM, the fibre array was in the far-field of the crystal. The combined focal length of the SLM and the fixed lens was 400 mm. Alternatively, when measuring correlations in the image plane of the crystal, the combined focal length of the SLM and the fixed lens was 200 mm. A bandpass filter centred at λ = 710 nm and a FWHM of 10 nm was located in front of each fibre detector. The transmission of the bandpass filter was 45%.

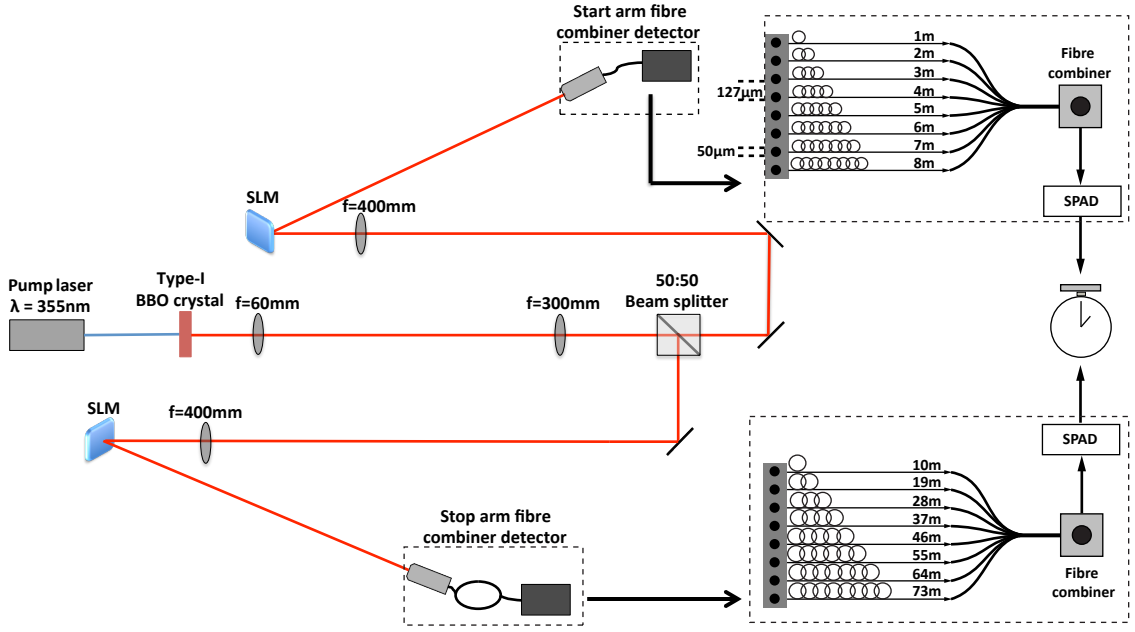

Figure 3.20: *The underlying principle behind our detector arrays was that multiple fibres were all connected to the same SPAD. The fibres differed in length from each other so that the fibre into which the photon was coupled dictated the time of detection. Using two such arrays of different length meant that 64 different time intervals were possible, each of which corresponded to a particular combination of two fibres at which the photon pair was detected. In order to switch between the image plane and the far-field of the crystal, the phase hologram on the SLM was altered; giving different combined focal lens lengths of the SLM and coupling lens [3.35].*

The fibre arrays contained eight multimode fibres with a 50 µm core diameter and a 125 µm cladding. The fibres were spaced with a 127 µm pitch. Each consecutive fibre was of a greater length (see Table 3.8 for details), giving a unique time signature (see Figure 3.22). The eight input fibres from the fibre combiner had a 50 µm core diameter. These fibres were tapered and fusion-spliced onto a single multimode output fibre with a core diameter of 105 µm. The output fibre was coupled into a thick junction SPAD.

The transmission efficiency of the 8 × 1 fibre combiner was approximately 70% [3.36]. Compared to scanning a single detector, the fibre detector provided an 8−fold increase of the number of measurement states. The thick junction SPAD was the detector of choice, due to the good compromise of detection efficiency and detector- induced timing jitter. As shown in Section 2.3.1 typical values for the detector timing jitter were 350 ps and the detection efficiency at λ = 710 nm was 59.9%. In additional to the detector timing jitter, the fibre V-Groove, the fibre combiner and the delay fibres increase the total timing jitter of the full detection system. As shown in Sections 2.3.3 and 2.3.4, the overall detection efficiency decreases to 41.7 % and the timing jitter increases to ≈ 690 ps. The efficiency decreases due to coupling and transmission losses, while the FWHM increases due to dispersion effects within the fibres and the fibre combiner.

3.2.6 *Alignment of experimental setup*

Two different modules (National Instruments and Ortec) were used to align the setup and for the actual measurements. For the alignment of the optical system no delay fibres were used. The National Instruments counting card was set to measure coincidences, when both detectors detect an event within a 25 ns window. The National Instruments card registered coincidences, when either two entangled photons, two classical photons, two noise events or any combination of events were detected by both detectors within the 25 ns window. When the detectors were covered up and no light was incident on the detectors, each detector registered up to 1000 cps. Since this experiment was not located in a light tight environment, there was still a chance that stray light entered the detectors and therefore contributed to the dark count rate. For the alignment of the experiment count rates of approximately 35 kcps (far-field measurement) and 20 kcps (image plane measurement) were measured. The count rate in each arm was defined as:

$$\text{Count rate}\left[\text{s}^{-1}\right] = \frac{\text{Counts}}{\text{Update time [s]}}, \tag{3.14}$$

where the update time was set to 1 s to increase the chance of detecting entangled photon events. Beside correlated photon events, also the classical coincidence rate (CCR), which is caused by uncorrelated photon events and dark counts, was calculated:

$$\text{CCR} = \text{Count rate}_{\text{start}} \cdot \text{Count rate}_{\text{stop}} \cdot \text{estimated time response}, \tag{3.15}$$

where the estimated time response was set to 25 ns to account for the timing jitter, which led to coincidence peak broadening.

The count rate for the correlated photon pairs is the total coincidence count rate minus the classical coincidence rate. The quantum contrast is the ratio of the total coincidence rate and the classical coincidence rate. For a well aligned setup a quantum contrast of 5 for the far-field measurement and a quantum contrast of 4 for the image plane measurement were usually obtained.

The fine alignment of the experimental setup was performed with the SLMs. For this alignment procedure no delay fibres were used. Each SLM was mounted on a rotational stage and a goniometer. The coarse alignment to maximise the count rate was done with the controls on the goniometer for tilt and the rotation stage for aligning the first diffraction order of the SLM with the detector. The fine adjustment for count rate and coincidence rate were done by changing the hologram on the SLM with a LabView program. The first fine alignment was done for the far-field measurement. The SLM was programmed to give a combined focal length of 400 mm with the f = 400 mm fixed focal length lens. No additional optical power was applied to the SLMs and the phase hologram used was that of a diffraction grating. The first diffraction order coming from the SLM was directed onto the detector array. By scanning the x-angle and the y-angle of the phase hologram the count rate was maximised in both arms. To ensure that we aligned the detector to the first diffraction order of the phase hologram, the SLMs were switched off and the count rate should have dropped significantly in case the detector was aligned to the first diffraction order. For the case in which the count rate stayed at a high level, the count rate was maximised for the zeroth diffraction order and switching the SLM off would have resulted in no change, as the SLM acted as a “mirror”.

After maximising both arms for the highest count rate, only one arm was changed to maximise the coincidence rate. For statistically correct measurements, the update time was increased to 5 s. Again, the x-angle and the y-angle were scanned for the highest coincidence count rate, a quantum contrast of 5 was easily obtained when using this technique.

After aligning the the far-field measurements, the hologram on the SLM was changed to give a combined focal length of 200 mm with the f = 400 mm fixed focal length lens in each arm. Figure 3.21 shows two examples for the phase holograms applied to the

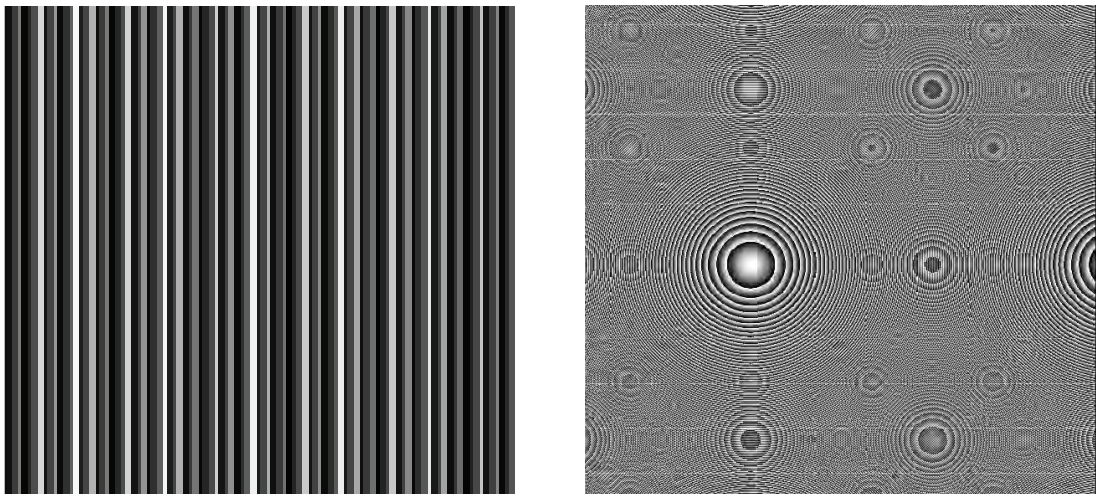

(a) Far-field hologram (b) Image plane hologram

Figure 3.21: *In order to be able to switch between the image plane and the far- field of the crystal, the phase hologram on the SLM was altered; giving different combined focal lens lengths of the SLM and coupling lens. (a) shows a typical phase hologram for the far-field measurement, when no additional optical power is applied. (b) shows a phase hologram for an aligned "lens" used in the image plane measurement.*

SLMs. The same scanning procedure was repeated for the image plane measurements, but instead of changing the angle of the grating orientation, the position of the x- and y- lens centre point was scanned for maximum count rate and later maximum coincidence rate. Quantum contrasts of 4 were achieved this way.

3.2.7 *Peak positions*

After the fine alignment of the SLM was finished, the delay fibres were added to the experimental setup and a Time-to-Amplitude-Converter (TAC) from Ortec was used. The Ortec card was capable of resolving the required time window for all 64 coincidence peaks. Each time bin was approximately 0.06 ns wide. The experimental setup contained two separate optical paths. Each path contained an eight pixel fibre detector, giving a total of 64 different delay times, which identified the entrance fibres of the two photons. A detected photon in the start arm, with the short delay fibres, started the TAC and a detected photon in the stop arm stopped the TAC. Depending on the chosen measurement basis, the down-converted photons entered different combinations of start and stop fibres. The different combinations of start and stop fibres are shown in Figure 3.22. For the far-field (momentum) measurement the down-converted photons had equal and opposite transverse momenta; the detection fibres of the down-converted photons were anti-correlated. This means that when a down-

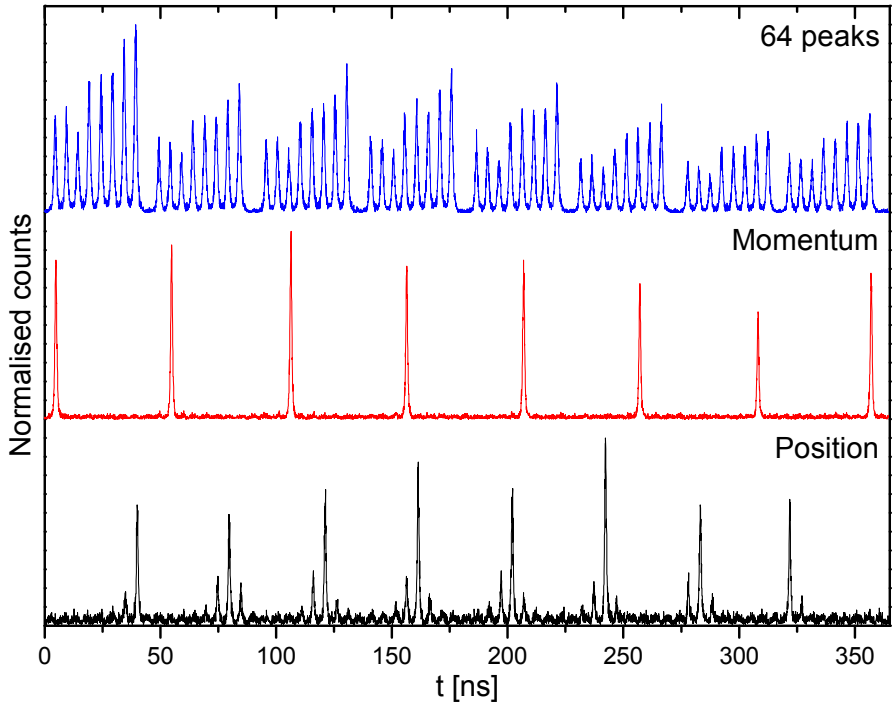

Figure 3.22: *The top graph shows coincidence counts of all 64 possible positions for the start and stop arrays. This data was obtained with an attenuated pulsed laser diode (λ = 686 nm) using an external trigger. The middle and bottom graphs represent actual data obtained with the down-converted photon source. As expected the experimental data lines up with the 64 possible peak positions and each main peak has a unique position. The side peaks in the bottom graph were caused by photons entering adjacent fibre, due to the measured correlation length being slightly larger than the fibre spacing.*

converted photon entered fibre no. 1 in the start arm, the entangled photon would enter fibre no. 8 in the stop arm. The resulting coincidence peak appeared at a delay of 352 ns. Deviations from the calculated values could have been caused by small deviations of the fibre lengths due to the manufacturing process. The bottom graph shows an example position measurement. Here the photons entered the same channel (1-1, 2-2, etc) in their respective fibre detector. Ideally only the centre peak would be present, but side-peaks are visible as well. These side-peaks were caused by photons entering adjacent fibres, because the measured correlation length was slightly bigger than the fibre core spacing. From Equation (3.19) the theoretical correlation length was calculated to be 65 µm, the spacing between two adjacent fibre cores was roughly 75 µm. Even for a correlation length of 65 µm there is a small probability that the entangled partner enters the 'wrong' channel.

3.3 Results

In this section, the temporal development of the coincidence peaks for the image plane and far-field measurements will be detailed. The coincidence peaks were evaluated in terms of their variance products and tested if they meet the criterion for EPR-entanglement. The spatial light modulators were used as variable focal length lenses and coincidence measurements were performed in the image plane, far-field and intermediate bases of the nonlinear crystal.

3.3.1 *Temporal development of correlation peaks*

The temporal development of the correlation peaks in the image plane and far-field of the crystal were characterised. Each measurement lasted for 30 minutes and intermediate results were saved in 1 minute intervals. Figure 3.23 shows the temporal development of the correlation peaks for time intervals of 10 minutes. For the image plane (position) measurements side peaks developed next to the main peak. These peaks were caused by correlated photons entering adjacent fibres. It is assumed, that the correlation length of the entangled photon pairs is slightly larger than the spacing between two fibre cores.

For the position measurement, the Gaussian shape of the pump beam is observable, as shown in Figure 3.23 (a). If a bigger magnification of the SPDC beam would have been used, then the fibre detector would have been illuminated more evenly (see Figure 3.22 bottom for comparison). Fewer counts than expected were registered in the third main peak, this could have been caused by a faulty fibre to fibre connector, which decreased the coupling efficiency between the V-Groove and the delay fibres. The Signal-to-Noise-Ratio (SNR) is defined as [3.37]:

$$SNR = \frac{n_P}{\sqrt{n_P + n_B}}, \tag{3.16}$$

where n_P is the average signal height in the 8 main peaks, and n_B is the mean background. The average background level for the position measurement was calculated from the $100th - 1000th$ time bin. For the momentum measurement shown in Figure 3.23 (b), the mean background was calculated from the $100th - 700th$ time bin.

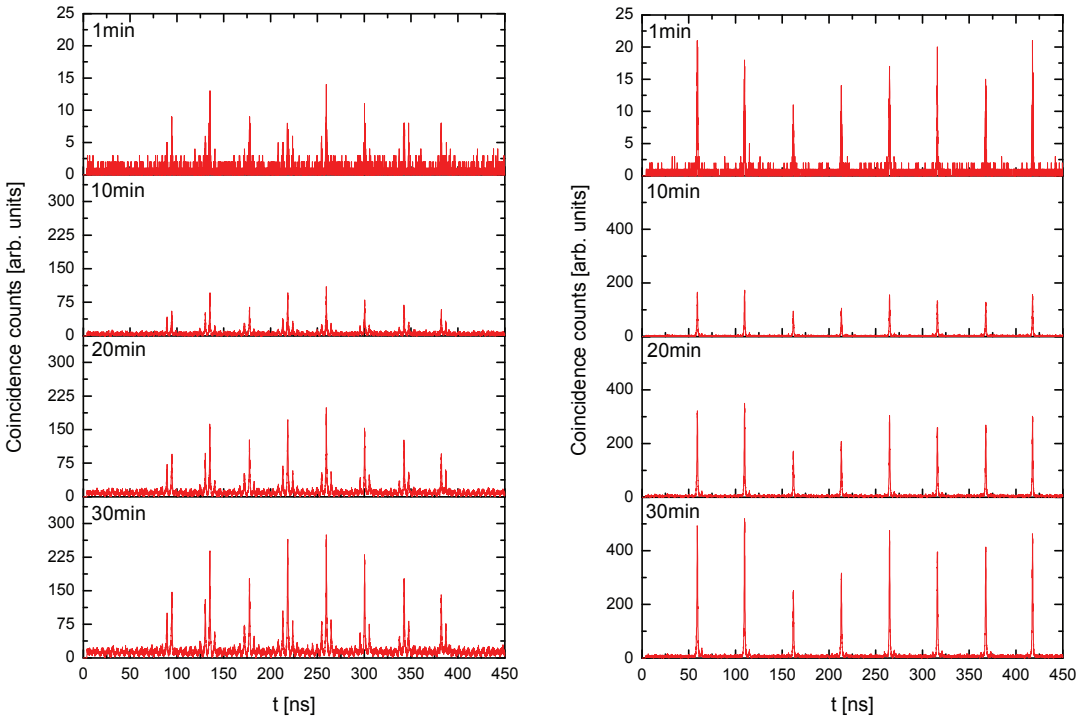

(a) Image plane measurement

(b) Far- field measurement

Figure 3.23: *(a) shows the temporal development of the coincidence peaks for an image plane measurement. The side peaks have been caused by photons entering adjacent fibres. (b) shows the temporal development of the coincidence peaks for a far-field measurement. In contrast to the image plane measurements, there are no side peaks present.*

This shorter time window was chosen due the the earlier position of the first momentum peak.

	Position				Momentum			
t [min]	n_P	n_B	σn_B	SNR	n_P	n_B	σn_B	SNR
1	9.8	0.4	0.6	3.1	17.1	0.2	0.5	4.1
10	78.6	4.1	2.3	8.6	138.3	1.9	1.4	11.7
20	141.3	8.0	3.4	11.5	272.6	3.9	2.2	16.4
30	184.0	12	4.6	13.1	416.3	5.9	2.8	20.3

Table 3.9: *SNR calculations for temporal peak development in position and momentum.*

Table 3.9 summarises the signal height, background and SNR for position and momentum measurements. For the position and momentum measurements. the SNR is increasing over time. The momentum measurements possess a higher SNR compared to the position measurements due to its higher signal height and lower background.

3.3.2 *Correlation measurements in the image plane and far-field of the BBO crystal*

The aim of this experiment was to measure quantum correlations of the entangled photon pair. Beside the loss of coincidence counts due to non-detected partner photons, one challenge which occurs in all experiment of this type are coincidence counts arising from accidental correlations. These accidental correlations were caused by dark counts present in the detector and/or stray photons, which were not of quantum origin. Another issue was the fixed spacing for a finite number of optical fibres. This resulted in measurements, which were sampled at discrete positions over a limited number of available fibres.

Not all measured coincidences were of a quantum nature. By considering the count rates from the two SPAD detectors and the estimated response time δt, one can calculate the classical coincidence rate (CCR) from Equation (3.15). In this experiment, we decreased the power of the pump beam with an ND-filter. Instead of having a count rate in excess of 35,000 cps for each detector, the count rates were reduced to 6000 cps for the momentum measurement and 9000 cps for the position measurement respectively. The estimated response time was 2.5 ns to account for the jitter present in the detection system. The accidental coincidence rates per time bin for these measurements were $B_p = 0.1\,s^{-1}$ and $B_x = 0.2\,s^{-1}$ respectively.

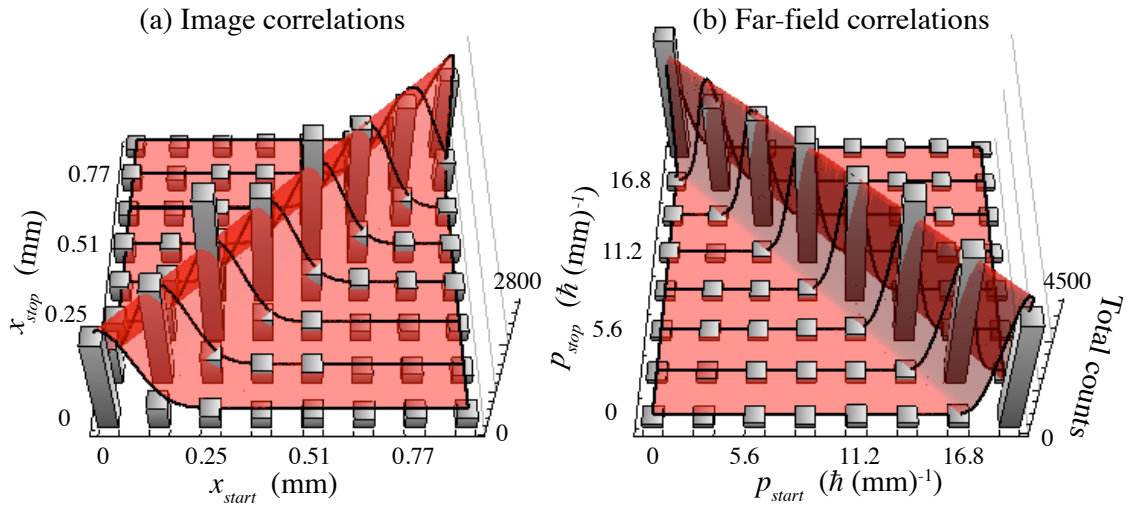

Figure 3.24: *Summed coincidence counts for position and momentum measurement [3.38].*

Figure 3.24 shows the coincidence counts in the image plane (position) and far-field (momentum) of the nonlinear crystal as measured by the eight fibres in the two arms

over 30 minutes. The sampling interval for the position measurement was the fibre spacing, i.e. δ_x = 127 µm. The sampling interval for the transverse momentum is δp_x = $(\delta x/f)\hbar k_0$, where f = 400 mm is the combined focal length of the fixed focal length lens and the SLM. k_0 is the wave number of the down-converted light. The sampling interval for the transverse momentum for the experiment was $\delta p_x = 2.8\ \hbar$ mm^{-1}.

From the Gaussian intensity profile of the pump beam, it was expected that the form of the observed correlations were approximately Gaussian and that the overall count rate would have a Gaussian profile across the fibre arrays as well. Based on the calculations of the two-photon wave function, the anticipated coincidence count rate in the image plane C_x and far-field C_p of the crystal can be written as [3.39, 3.40]:

$$C_x\left(x_{start}, x_{stop}\right) = A_x\left[\exp\left(\frac{-(x_{start}-x_{stop})^2}{2\sigma_x^2}\right)\exp\left(\frac{-\sigma_p^2(x_{start}+x_{stop})^2}{2\hbar^2}\right)\right] + B_x, \tag{3.17}$$

and

$$C_p\left(p_{start}, p_{stop}\right) = A_p\left[\exp\left(\frac{-(p_{start}+p_{stop})^2}{2\sigma_p^2}\right)\exp\left(\frac{-\sigma_x^2(p_{start}-p_{stop})^2}{2\hbar^2}\right)\right] + B_p, \tag{3.18}$$

where x_{start} and x_{stop} denote the position of the start and stop fibres, σ_x is the standard deviation of the position correlations, p_{start} and p_{stop} denote the position of the fibres for the momentum measurement, σ_p denotes the standard deviation of momentum correlations, B_x and B_p are the offset backgrounds and A_x & $A_p = \frac{1}{\pi\sigma_-\sigma_+}$ are normalisation constants. $\sigma_\pm$ are the standard deviations of the two Gaussians, giving the strength of the position and momentum correlations, σ_- and σ_+^{-1}.

The width of the position and momentum correlations are functions of the magnified crystal length L, the size of the pump beam ω_{pump} and the magnification between the crystal and the fibre array M. The standard deviations of these correlations are given by

$$\sigma_x = M \cdot \sqrt{\frac{L\lambda_{pump}}{2\pi}} \tag{3.19}$$

and

$$\sigma_p = \frac{\hbar}{\omega_{pump} M} \tag{3.20}$$

The theoretical values for the standard deviation of the correlations for the image plane

would be $\sigma_x = 0.065$ mm, respectively the standard deviation for the correlations in the far- field would be $\sigma_p = 0.4\hbar\,\mathrm{mm}^{-1}$.

The coincidence counts in each 2.5 ns time window were summed to give the total number of coincidence counts per "stop" fibre for all eight "start" fibres as shown in Figure 3.24. The background was calculated from the flat part of the diagram. Fitting our background-corrected data to these equations gives standard deviation of $\sigma_x = (0.101 \pm 0.007)$ mm for the position measurement and $\sigma_p = (1.24 \pm 0.11)\hbar\,(\mathrm{mm})^{-1}$ for the momentum measurement respectively. In both cases these measured values are somewhat broader than those predicted by theory. This additional width can be attributed to a slight under sampling of the down-converted light by the discrete nature of the fibre arrays.

In order to demonstrate the EPR paradox [3.41–3.43], it is sufficient to show that the product of the two variances, $\Delta^2(x_{start} - x_{stop})$ and $\Delta^2(p_{start} + p_{stop})$, is less than $\hbar^2/4$. From the fitted data we find the position-difference variance to be

$$\Delta^2(x_{start} - x_{stop}) = (1.02\mathrm{x}10^{-2} \pm 0.10\mathrm{x}10^{-2})\ \mathrm{mm}^2, \tag{3.21}$$

and the corresponding variance for momentum-sum to be

$$\Delta^2(p_{start} + p_{stop}) = (1.53 \pm 0.20)\,\hbar^2\ (\mathrm{mm})^{-2}. \tag{3.22}$$

The variance product obtained is $(0.016 \pm 0.003)\hbar^2$, which is over one order of magnitude below the classical limit and indicates quantum behaviour of the down-converted photons.

3.3.3 *Spatial Light Modulator as variable focal length lens*

By applying different pre-determined optical powers on the SLMs, they act as variable focal length lenses. The advantages of the SLMs is that they remove the need to manually change the lenses and can be used for continuous different wavelengths. At lower focal lengths (f $<$ 200 mm) the SLM can no longer produce sufficiently high quality holograms due to the finite size and spacing of the pixels and the limit in achievable focal lengths is reached. In this experiment, we were driving the SLM at its limit.

The previous measurement in the image plane and far-field of the nonlinear crystal are special cases of detector-to-detector imaging. Satisfying the two-photon geometrical optics conditions developed by Klyshko [3.44] it is possible to accomplish high coincidence count rates. Here the crystal acts as a "mirror" when the light "emerging" from the start detector is traced to the stop detector. For certain combinations of focal lengths the detectors are imaged onto each other. The Klyshko picture predicts that the correlation signal is high, whenever the detector planes are imaged onto each other. Besides accessing the image plane and the far-field of the crystal, also intermediate planes can be measured. The condition for this detector-to-detector imaging can be described as the following:

$$f_{start} = \left(\frac{1}{d} + \frac{1}{2d - (1/f_{stop} - 1/d)^{-1}} \right)^{-1}, \tag{3.23}$$

which gives a magnification of:

$$M\left(f_{start}\right) = \frac{(1/f_{start} - 1/d)^{-1}}{2d - (1/f_{start} - 1/d)^{-1}}. \tag{3.24}$$

The image plane ($f_{start} = f_{stop} = d/2$) and far-field ($f_{start} = f_{stop} = d$) are just special, symmetrical, examples of this condition, where the magnification between detector planes is +1 and -1 respectively. Symmetry between the two arms is not essential, and strong correlations can be predicted for other magnifications too.

Figure 3.25 shows the coincidence count rate summed over all eight fibres as a function of the focal length in the start and stop optical paths. Changing the additional optical power provided by the SLM can alter the combined focal length in the optical path. Whenever the detector planes are imaged onto each other and therefore the Klyshko picture for the two-photon geometrical optic condition is satisfied, high count rates can be observed (coloured traces). The red dot denotes the special case when both detectors are in the image plane of the crystal ($f_{start} = f_{stop} = d/2$) . The blue dot represents the far-field plane of the crystal ($f_{start} = f_{stop} = d$) and the green dot is an example for an intermediate plane ($f_{start} = 0.8d$ and $f_{stop} = 2d$), while the yellow dot is an intermediate plane at $f_{start} = 2d$ and $f_{stop} = 0.8d$. The position of the intermediate planes is not representative. The actual positions for these intermediate planes are outside the scanned region shown in Figure 3.25.

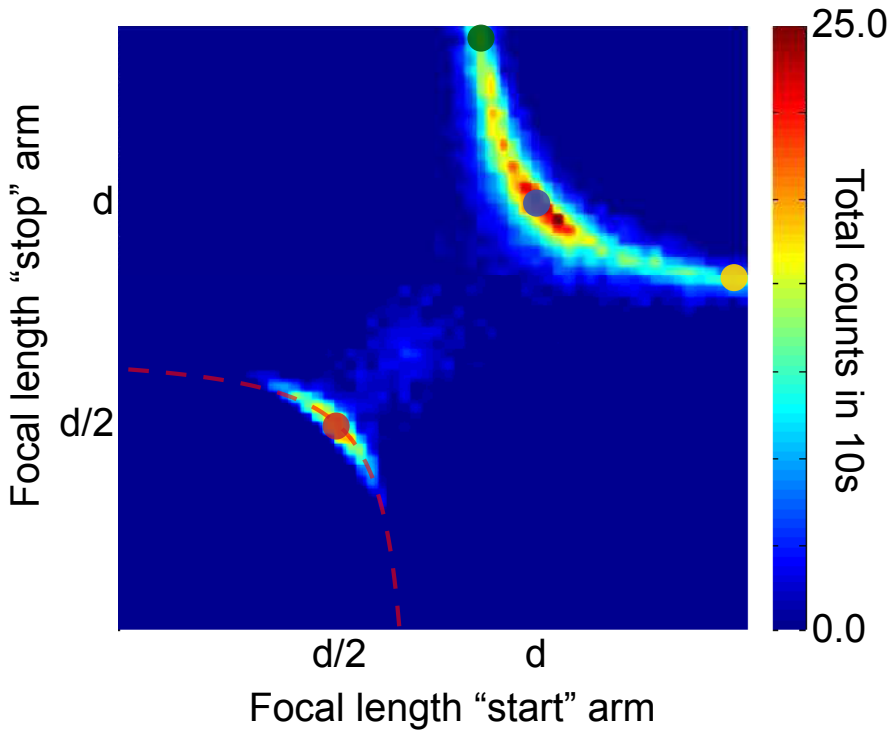

Figure 3.25: *A plot showing the coincidence count rate summed over all eight fibres as a function of the focal length in start and stop optical paths [3.38]. The red dot denotes* $f_{start} = f_{stop} = d/2$*, which is the image plane of the crystal. The blue dot represents* $f_{start} = f_{stop} = d$*. The yellow and green dot show intermediate bases. The position of the yellow and green dots are not representative and lie outside the scanned region. See Figure 3.26 for the corresponding observed (anti-) correlations. For focal lengths smaller than d/2 only very few or no counts were recorded as the SLM was not able to produce sufficiently high quality holograms of the lens due to pixel restrictions.*

Figure 3.26 shows the observed (anti-) correlations for various focal length settings of the SLM. By satisfying the requirements for two-photon geometrical optics, we observed high coincidence counts for certain combinations of the two SLMs. When the crystal was imaged onto the detectors we observed position correlations, and in the far-field of the crystal we observed momentum anti-correlations. The ability to easily switch between the image plane, far- field and intermediate bases might be useful for applications in quantum communications, where the use of spatial states could significantly increase the information capacity of the photon.

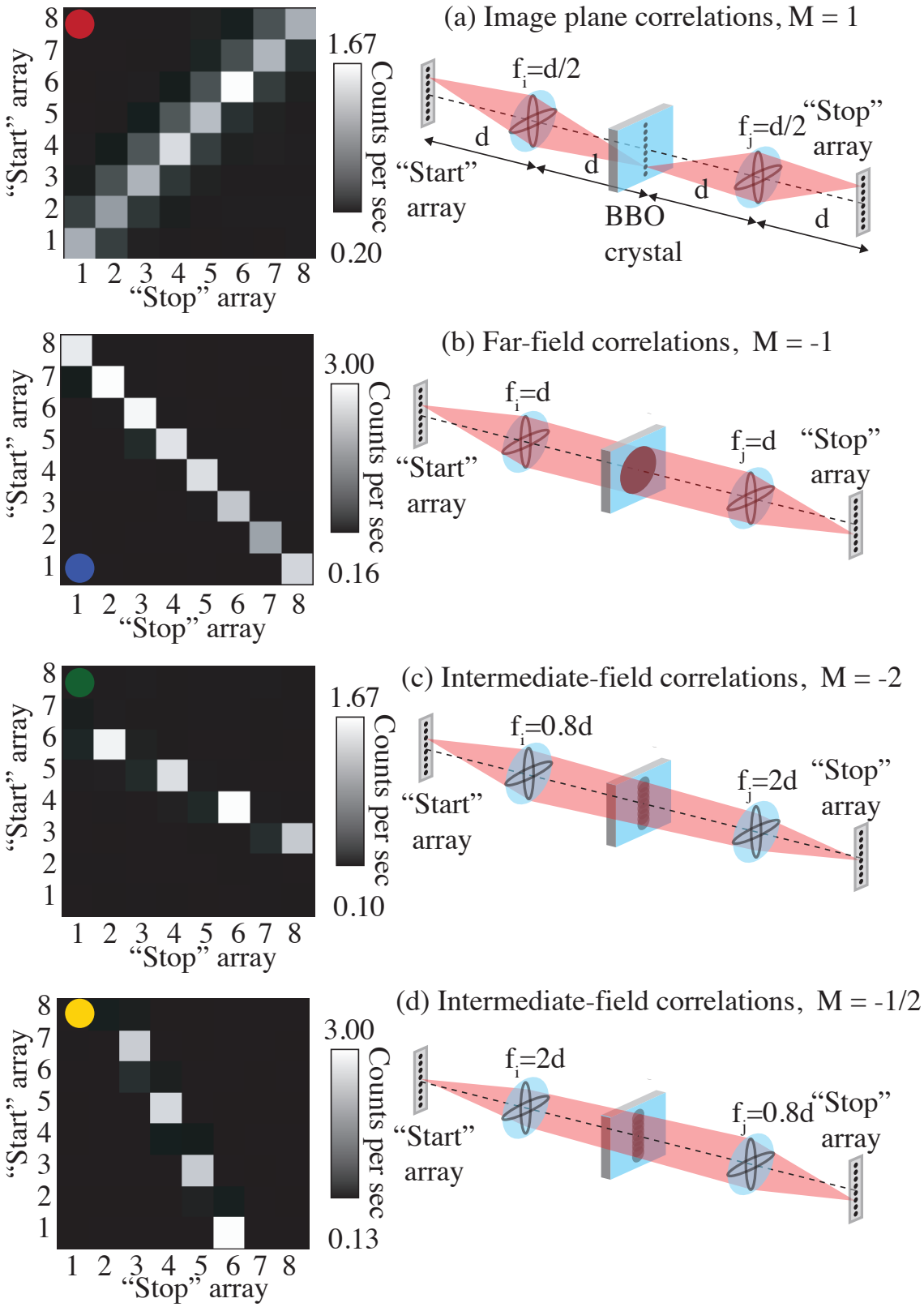

Figure 3.26: *The details of the (anti-) correlations observed for various focal lengths. A magnification of +1 corresponds to both detector arrays being in the image plane of the crystal, and a magnification of -1 corresponds to when both detectors are in the far-field of the crystal. Magnifications of -2 and -1/2 are shown also. [3.38].*

3.4 Alternative detection systems

The fibre detector used in this experiment has many advantages like single-photon sensitivity, timing resolution and a single-photon detection efficiency of ≈ 50%. However, the amount of light seen by the detector is very small. The down-converted light beam has a diameter of approximately 2 mm, while the diameter of one fibre core is 50 µm. This means that the 8 × 1 fibre detector can only detect 0.5% of the down-converted light's area as shown in Figure 3.27. In order to capture more light the number of fibres must be increased. A larger number of fibres is not feasible due to the lengths and number of delay fibres needed to cover the full down-converted beam.

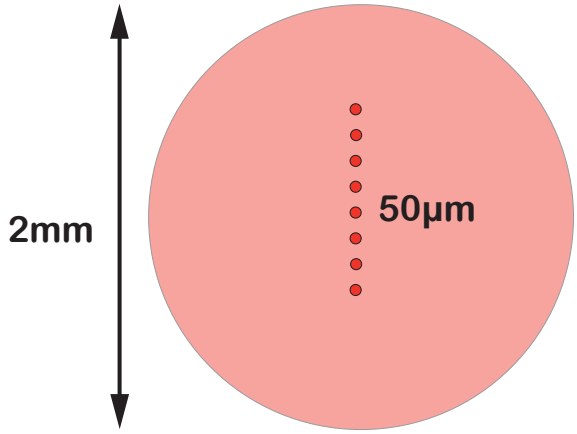

Figure 3.27: *Area covered by detector. The fibre array is able to see 0.5% in area of the down converted light.*

Alternative multi-pixel detectors for low light levels exist. The ideal multi-pixel detector would be able to capture the whole down-converted beam, would possess small pixels for a high resolution, have a high SPDE at the desired wavelength, while being sensitive enough to detect single-photons. For correlation experiments timing resolution might be desirable as well.

An alternative detector array, which offers timing resolution are Si-SPAD arrays. These arrays have been developed at the Politechnico di Milano in Italy. Here the need for fibres is omitted, since the coincidence counting can be done electronically. Monolithic 1D SPAD arrays with 32 × 1 detectors [3.45] are available. More recently prototypes of 2D SPAD arrays with 32 × 32 detectors [3.46] have been developed. For the 1 × 32 SPAD array each pixel contains a 20 µm diameter detector on a 100 µm × 100 µm chip, which leads to a very low fill factor of 3.14% per pixel. The fill factor can be in-

creased with customised micro-lenses with a square geometry. The micro-lenses have to be specified for the wavelength used in the experiment and great care has to be taken for the alignment of the micro-lens array. Any misalignment in position or angle will greatly reduce the number of photons which can be detected by the photo-sensitive area of the pixel. Additionally, micro-lenses reduce the angular field of view. In the worst case, the detection efficiency of the Si-SPAD array with misaligned micro-lenses can be smaller than the detection efficiency of the same Si-SPAD array without the micro-lenses [3.47, p. 134]. Without additional lenses detection efficiencies of 10% up to 17% can be obtained, depending on the excess bias used [3.46].

The theoretical count rates for the fibre detector and the 32 × 1 Si-SPAD array with and without the micro-lenses are shown in Table 3.10. The SPDE was set to 15%. The fill factor for the micro-lenses was assumed to be 90%, the transmission was set to 99% and the diffraction efficiency was set to 85%. For customised diffractive optics diffraction efficiencies of 75% up to 90% are commercially available [3.48]. Additionally, the measured jitter for the different detectors is listed in Table 3.10.

Detector	Count rate per pixel [cps]	Count rate detector [kcps]	Jitter [ps]
8 × 1 Fibre Detector	4375	35.0	690
32 × 1 SPAD array	250	8.0	100
32 × 1 SPAD array μ-lenses	4743	151.7	100

Table 3.10: *Theoretical count rates and measured jitter at FWHM for different detection systems. The jitter for the* 32 × 1 *SPAD array was measured with additional termination electronics. Otherwise the jitter would be* >300 ps *[3.49].*

Potentially Si-SPAD arrays with diffractive micro-lenses will only bring a small improvement in terms of count rate and number of pixels. However, the SPAD array possesses a smaller timing jitter than the fibre detector. Recently, the Fraunhofer Institute in Duisburg (Germany) in cooperation with the MiSPiA project consortium have developed an ultra-sensitive image sensor based on SPADs with on-chip CMOS (Complementary Metal Oxide Semiconductor) electronics. The pixels on the camera can count individual photons with very fast read-out speeds and possess single-photon sensitivity, making them suitable for extremely weak light sources [3.50, 3.51].

Other multi-pixels detectors, however, without timing resolution are available as well. Scientific CMOS arrays are commercially available. These detectors offer arrays of up to 5 million pixels, and pixel sizes of 6.5 µm × 6.5 µm, providing a very high resolution.

The SPDE of scientific CMOS cameras [3.52, 3.53] is comparable to the SPDE of the fibre detector at $\lambda = 710\,\text{nm}$. However, these cameras are not sensitive enough to operate at the single-photon level, as scientific CMOS cameras are comparatively noisy in this regime [3.54, 3.55]. Instead different camera technologies with the ability to amplify the input signal above the read-out noise, like electron-multiplying CCD (EMCCD) cameras, should be used for extreme low light level imaging applications [3.52].

EMCCD cameras with 512×512 pixels and pixel sizes as small as $8\,\mu\text{m} \times 8\,\mu\text{m}$ are commercially available. However, most EMCCD camera models from different manufacturers (Andor, Hamamatsu, Nüvü camēras and Princeton Instruments) have a standard pixel size of $16\,\mu\text{m} \times 16\,\mu\text{m}$. Due to the small pixel size, these cameras have a high resolution and can capture the whole down-converted light. EMCCD cameras offer single-photon sensitivity, have low dark counts and high quantum efficiencies in excess of 90%, albeit compared to SPAD cameras and the fibre detector, EMCCD cameras are slow, as a typical frame rate, for a chip measuring 512×512 pixels, is 35 Hz. Also EMCCD cameras are not capable of time resolved measurements in contrast to the SPAD camera or the fibre detector. However, in Chapter 4 quantum correlations of photon pairs were measured with an EMCCD camera and EMCCD cameras are explained in detail.

3.5 Conclusion

In this chapter, the theoretical background for generating entangled photons through spontaneous parametric down-conversion was outlined. This includes an explanation of the selection process for the nonlinear crystal, phase-matching for the down-conversion of the pump photon and a brief explanation of entanglement and the EPR paradox. Additionally, the working principle of spatial light modulators, which were used to change the phase of the incident light, was outlined.

For the experimental setup the length of the delay fibres in the detectors is very important. If the fibres are too short and therefore provide only a small pre-determined time difference, the coincidence peaks will overlap due to timing jitter caused by the SPAD, fibre combiner, and the delay fibres, see Section 2.3.3 for a detailed characterisation of the full system timing jitter. For this experiment the fibre length was increased to

provide a time delay between adjacent fibres of 4.5 ns in the "start" arm and 44.1 ns in the "stop" arm. There is no longer an overlap at the FWHM.

Additionally, thick junction SPADs from different manufacturers were characterised in terms of their electronic output, jitter and dark count rate and relative detection efficiency. The thick junction SPADs manufactured by Perkin Elmer provided superior characteristics compared to the equivalent SPADs from Laser Components. All the following measurements were performed with the PE detectors.

The fine alignment with the spatial light modulators to maximise the coincidence count rate and the hands- off switching between the image plane and the far-field of the nonlinear crystal was described. By changing between position and momentum measurements, the peak positions changed, as the entangled photons entered different combinations of channels in both detectors. Strong correlation peaks were observed for the momentum measurements. The position measurements were compromised by side peaks arising from photons entering the "wrong" channel due to a slight under-sampling of the fibre detector.

Correlations were measured in the image plane and far-field of the crystal. To test for EPR-like correlations, the variance product of the position difference and the momentum sum must be smaller than $\hbar^2/4$. Our experimental results indicate that our variance product is $\Delta^2 = (0.016 \pm 0.003)\hbar^2$, which is one order of magnitude below the classical limit for separability.

Additionally, coincidence measurements were performed in intermediate bases, by changing the focal lengths provided by the SLMs. Whenever the two detectors were imaged onto each other and therefore fulfilling the conditions for two-photon geometric optics, we observed high coincidence count rates.

A theoretical analysis of the suitability of a thin junction 32×1 SPAD array in correlation experiments was performed. The advantage of using a SPAD array would be the increased number of available channels in each arm and the coincidence counts can be evaluated electronically, removing the need for using optical fibres. Diffractive microlenses need to be mounted in front of the detector array in order to increase the count rate of the individual detectors and make use of the total chip size. The active area has a diameter of 20 µm, while the pixel size measures 100 µm × 100 µm. Other multi-pixel

detectors without timing resolution have been discussed in terms of their suitability for quantum correlation experiments of entangled photons.

The novelty of this work was the ability to access an eight-dimensional state space for each of the down-converted photons simultaneously without recurse to scanning. The SLMs can be used as variable focal length lenses and therefore it is possible to switch between position, momentum, and intermediate bases without manually changing the experimental setup. Potentially applications in quantum information processing and quantum communications can benefit from the increased information capacity provided by the state space of the entangled photons. The information capacity might be increased further by combining other degrees of freedom with the transverse degrees of freedom.

3.6 References

[3.1] D. C. Burnham and D. L. Weinberg. 'Observation of simultaneity in parametric production of optical photon pairs'. Phys. Rev. Lett., Vol. 25, (1970), pp. 84–87 (cited on page: 57).

[3.2] C. K. Hong, Z. Y. Ou and L. Mandel. 'Measurement of subpicosecond time intervals between two photons by interference'. Phys. Rev. Lett., Vol. 59, (1987), pp. 2044–2046 (cited on page: 57).

[3.3] J. E. Midwinter and J. Warner. 'The effects of phase matching method and of uniaxial crystal symmetry on the polar distribution of second-order non-linear optical polarization'. Br. J. Appl. Phys., Vol. 16, (1965), pp. 1135–1142 (cited on page: 59).

[3.4] S. M. Blinder. *Introduction to Quantum Mechanics: in Chemistry, Materials Science, and Biology*. 1st edition. Elsevier Science, 2004 (cited on page: 59).

[3.5] P. G. Kwiat, K. Mattle, H. Weinfurter, A. Zeilinger, A. V. Sergienko and Y. Shih. 'New high-intensity source of polarization-entangled photon pairs'. Phys. Rev. Lett., Vol. 75, (1995), pp. 4337–4341 (cited on page: 59).

[3.6] D. N. Klyshko. *Photons and Non-Linear Optics*. Rev. Enl. edition. Taylor & Francis, 1988 (cited on page: 60).

[3.7] D. A. Kleinman. 'Theory of optical parametric noise'. Physical review, Vol. 174, (1968), pp. 1027–1041 (cited on page: 60).

[3.8] W. Koechner. *Solid-State Laser Engineering*. 6 edition. New York, Heidelberg, Berlin: Springer, 2006 (cited on page: 60).

[3.9] R. W. Boyd. *Nonlinear Optics*. 2nd edition. Elsevier Science, 2003 (cited on pages: 60, 63).

[3.10] V. N. Belyi, N. S. Kazak, V. A. Orlovich and B. B. Sevruk. 'Performance of the optical parametric generation in nonlinear KTP crystal at Nd: YAG laser pumping'. Nonlinear Phenomena in Complex Systems - Minsk, Vol. 3, (2000), pp. 41–48 (cited on page: 61).

[3.11] Sellmeier. 'Zur Erklärung der abnormen Farbenfolge im Spectrum einiger Substanzen'. Ann. Phys., Vol. 219, (1871), pp. 272–282 (cited on page: 62).

[3.12] K. Kato. 'Second-harmonic generation to 2048 Å in β-Ba_2O_4'. IEEE J. Quantum Electron., Vol. 22, (1986), pp. 1013–1014 (cited on page: 62).

[3.13] N. Boeuf, D. Branning, I. Chaperot, E. Dauler, S. Guérin, G. Jaeger, A. Muller and A. Migdall. 'Calculating characteristics of noncollinear phase matching in uniaxial and biaxial crystals'. Opt. Eng., Vol. 39, (2000), pp. 1016–1024 (cited on page: 63).

[3.14] H. J. Liu, G. F. Chen, W. Zhao, Y. S. Wang, T. Wang and S. H. Zhao. 'Phase matching analysis of noncollinear optical parametric process in nonlinear anisotropic crystals'. Opt. Commun., Vol. 197, (2001), pp. 507–514 (cited on page: 63).

[3.15] *BBO crystal specifications*. attached documentation. CLaser Photonics Inc (cited on pages: 64, 71).

[3.16] E. Schrödinger. 'Die gegenwärtige Situation in der Quantenmechanik'. Die Naturwissenschaften, Vol. 50, (1935), pp. 844–849 (cited on page: 64).

[3.17] A. Einstein, B. Podolsky and N. Rosen. 'Can quantum-mechanical description of physical reality be considered complete?' Physical review, Vol. 47, (1935), pp. 777–780 (cited on page: 64).

[3.18] A. Einstein, M. Born and H. Born. *The Born-Einstein letters: correspondence between Albert Einstein and Max and Hedwig Born from 1916-1955, with commentaries by Max Born*. Macmillan, 1971 (cited on page: 64).

[3.19] J. S. Bell. 'On the Einstein-Podolsky-Rosen paradox'. Physics, Vol. 1, (1964), pp. 195–200 (cited on page: 64).

[3.20] A. Aspect, P. Grangier and G. Roger. 'Experimental realization of Einstein-Podolsky-Rosen-Bohm Gedankenexperiment: A new violation of Bell's inequalities'. Phys. Rev. Lett., Vol. 49, (1982), pp. 91–94 (cited on page: 64).

[3.21] S. Mancini, V. Giovannetti, D. Vitali and P. Tombesi. 'Entangling macroscopic oscillators exploiting radiation pressure'. Phys. Rev. Lett., Vol. 88, (2002), p. 120401 (cited on page: 64).

[3.22] J. C. Howell, R. S. Bennink, S. J. Bentley and R. W. Boyd. 'Realization of the Einstein-Podolsky-Rosen paradox using momentum- and position-entangled photons from spontaneous parametric down conversion'. Phys. Rev. Lett., Vol. 92, (2004), p. 210403 (cited on page: 66).

[3.23] *LCOS-SLM X10468 series - Optical phase modulator for system integration and OEM applications*. online, last accessed 2012-11-06. Hamamatsu, (2010). URL: http://sales.hamamatsu.com/assets/pdf/parts_X/x10468_series_kacc1172e10.pdf (cited on pages: 66, 67, 71–73).

[3.24] N. Matsumoto, T. Inoue, T. Ando, Y. Takiguchi, Y. Ohtake and H. Toyoda. 'High-quality generation of a multispot pattern using a spatial light modulator with adaptive feedback.' Opt Lett, Vol. 37, (2012), pp. 3135–3137 (cited on page: 66).

[3.25] P. S. Salter, A. Jesacher, J. B. Spring, B. J. Metcalf, N. Thomas-Peter, R. D. Simmonds, N. K. Langford, I. A. Walmsley and M. J. Booth. 'Adaptive slit beam shaping for direct laser written waveguides.' Opt Lett, Vol. 37, (2012), pp. 470–472 (cited on page: 66).

[3.26] H. Itoh, N. Matsumoto and T. Inoue. 'Spherical aberration correction suitable for a wavefront controller.' Opt. Express, Vol. 17, (2009), pp. 14367–14373 (cited on page: 66).

[3.27] E. J. Fernandez, P. M. Prieto and P. Artal. 'Wave-aberration control with a liquid crystal on silicon (LCOS) spatial phase modulator'. Opt. Express, Vol. 17, (2009), pp. 11013–11025 (cited on page: 66).

[3.28] M. Esseling, B. Kemper, M. Antkowiak, D. J. Stevenson, L. Chaudet, M. A. A. Neil, P. W. French, G. von Bally, K. Dholakia and C. Denz. 'Multimodal biophotonic workstation for live cell analysis'. J. Biophoton., Vol. 5, (2011), pp. 9–13 (cited on page: 66).

[3.29] M. L. Torres-Mapa, M. Antkowiak, H. Cizmarova, D. E. K. Ferrier, K. Dholakia and F. J. Gunn-Moore. 'Integrated holographic system for all-optical manipulation of developing embryos.' Biomed. Opt. Express, Vol. 2, (2011), pp. 1564–1575 (cited on page: 66).

[3.30] J. Wilson and J. F. B. Hawkes. *Optoelectronics: an introduction*. 3rd edition. Prentice Hall Europe, 1998 (cited on pages: 67, 68).

[3.31] S. Ifor. *PH5209 Polymer and Liquid Crystal Displays - Lecture notes*. University of St. Andrews, (2006) (cited on page: 68).

[3.32] *LCOS-SLM X10468 series - Technical Information*. online, last accessed 2012-11-06. Hamamatsu, (2008). URL: http://sales.hamamatsu.com/assets/pdf/parts_X/x10468_series_kacc9002e02.pdf (cited on page: 70).

[3.33] M. J. Romero. 'Orbital Angular Momentum Entanglement'. PhD thesis. University of Glasgow, 2012 (cited on page: 73).

[3.34] R. S. Aspden, D. S. Tasca, R. W. Boyd and M. J. Padgett. 'EPR-based ghost imaging using a single-photon-sensitive camera'. New J. Phys., Vol. 15, (2013), p. 073032 (cited on page: 74).

[3.35] F. Izdebski, J. Leach, R. E. Warburton, D. G. Ireland, S. M. Barnett, A. M. Yao, G. S. Buller and M. J. Padgett. 'Quantum correlations in position, momentum and intermediate bases, measured using fiber arrays'. Proc. SPIE 8274, Complex Light and Optical Forces VI, (2012), 82740E (cited on page: 84).

[3.36] R. E. Warburton, F. Izdebski, C. Reimer, J. Leach, D. G. Ireland, M. Padgett and G. S. Buller. 'Single-photon position to time multiplexing using a fiber array'. Opt. Express, Vol. 19, (2011), pp. 2670–2675 (cited on page: 85).

[3.37] S. F. Seward, P. R. Tapster, J. G. Walker and J. G. Rarity. 'Daylight demonstration of low-light-level communication system using correlated photon pairs'. Quantum Opt., Vol. 3, (1991), pp. 201–207 (cited on page: 89).

[3.38] J. Leach, R. E. Warburton, D. G. Ireland, F. Izdebski, S. M. Barnett, A. M. Yao, G. S. Buller and M. J. Padgett. 'Quantum correlations in position, momentum, and intermediate bases for a full optical field of view'. Phys. Rev. A, Vol. 85, (2012), p. 013827 (cited on pages: 91, 95, 96).

[3.39] K. W. Chan, J. P. Torres and J. H. Eberly. 'Transverse entanglement migration in Hilbert space'. Phys. Rev. A, Vol. 75, (2007), 050101(R) (cited on page: 92).

[3.40] D. S. Tasca, S. P. Walborn, P. H. Souto Ribeiro, F. Toscano and P. Pellat-Finet. 'Propagation of transverse intensity correlations of a two-photon state'. Phys. Rev. A, Vol. 79, (2009), p. 033801 (cited on page: 92).

[3.41] M. D. Reid, P. D. Drummond, W. P. Bowen, E. G. Cavalcanti, P. K. Lam, H. A. Bachor, U. L. Andersen and G. Leuchs. 'Colloquium: The Einstein-Podolsky-Rosen paradox: From concepts to applications'. Rev Mod Phys, Vol. 81, (2009), pp. 1727–1751 (cited on page: 93).

[3.42] M. D. Reid. 'Demonstration of the Einstein-Podolsky-Rosen paradox using nondegenerate parametric amplification'. Phys. Rev. A, Vol. 40, (1989), pp. 913–923 (cited on page: 93).

[3.43] Z. Y. Ou, S. F. Pereira, H. J. Kimble and K. C. Peng. 'Realization of the Einstein-Podolsky-Rosen paradox for continuous variables'. Phys. Rev. Lett., Vol. 68, (1992), pp. 3663–3666 (cited on page: 93).

[3.44] T. B. Pittman, D. V. Strekalov, D. N. Klyshko, M. H. Rubin, A. V. Sergienko and Y. H. Shih. 'Two-photon geometric optics'. Phys. Rev. A, Vol. 53, (1996), pp. 2804–2815 (cited on page: 94).

[3.45] S. Tisa, F. Guerrieri and F. Zappa. 'Monolithic array of 32 SPAD pixels for single-photon imaging at high frame rates'. Nucl. Instrum. Methods Phys. Res., Sect. A, Vol. 610, (2009), pp. 24–27 (cited on page: 97).

[3.46] F. Guerrieri, S. Tisa, A. Tosi and F. Zappa. 'Two-dimensional SPAD imaging camera for photon counting'. IEEE Photonics J., Vol. 2, (2010), pp. 759–774 (cited on pages: 97, 98).

[3.47] F. Guerrieri. 'High-speed single-photon camera'. PhD thesis. Milano, Italy: Dipartimento di Elettronica e Informazione, Politecnico di Milano, 2010 (cited on page: 98).

[3.48] B. Herdt and M. Bril. 'Ein Strahl — Eine Matrix'. Optik & Photonik, Vol. 3, (2008), pp. 45–49 (cited on page: 98).

[3.49] S. Bellisai. *32x1 SPAD Array Analysis*. Unpublished progress report. (2011) (cited on page: 98).

[3.50] D. Durini. *Ultrasensitive photon hunter*. Press release, online, last accessed 2013-03-22. (2013). URL: http://www.mikroelektronik.fraunhofer.de/en/press-media/microelectronics-news/article/ultrasensitive-photon-hunter.html (cited on page: 98).

[3.51] D. Durini and F. Zappa. *Advances in time-of-flight and time-correlated single-photon-counting devices*. online, last accessed 2013-04-23. (2013). URL: http://spie.org/x93517.xml (cited on page: 98).

[3.52] Andor Technology. *Scientific CMOS - Neo and Zyla sCMOS Cameras - data sheet*. online, last accessed 2013-03-21. (2013). URL: http://www.andor.com/pdfs/literature/Andor_sCMOS_Brochure.pdf (cited on page: 99).

[3.53] PCO AG. *pco.edge scientific CMOS camera - Data sheet*. online, last accessed 2013-03-21. URL: http://www.pco.de/fileadmin/user_upload/db/download/BR_pco_edge_105.pdf (cited on page: 99).

[3.54] I. Rech, A. Gulinatti, F. Zappa, M. Ghioni and S. Cova. 'High-performance silicon single-photon avalanche diode array'. *Proc. SPIE 7320, Advanced Photon Counting Techniques III.* (2009), 73200H (cited on page: 99).

[3.55] J. R. Joubert and D. K. Sharma. *EMCCD vs. sCMOS for Microscopic Imaging.* online, last accessed 2013-03-22. URL: http://www.photonics.com/ArticlePrint.aspx?AID=46174 (cited on page: 99).

CHAPTER 4

SPATIAL ENTANGLEMENT OF PHOTON PAIRS MEASURED WITH AN ELECTRON-MULTIPLYING CCD CAMERA

In this chapter, spatial correlations of photon pairs were measured with an electron-multiplying CCD camera. Within one frame, it was possible to measure 201×201 positions simultaneously, and the whole Spontaneous Parametric Down-Conversion (SPDC) beam was captured with the camera. The variance product for the momentum-sum and the position-difference is almost 3 orders of magnitude below the classical limit of separability, revealing EPR-like correlations of the entangled photon pairs generated through SPDC. In order to verify that the results were of a quantum nature and not an artefact of the camera operation, the measurements were repeated with a pseudo-classical light source. When no photon pairs were present in the measurement, no correlations of quantum nature were measured. The correlation peak in the $y-$axis for the position measurement was caused by accidental correlations due to charge smearing originating from the read-out process of the camera. The capability to measure quantum correlations allowed the observation of around 2500 entangled spatial states, which, to-date, represents the largest dimensionality for any experiment using entangled spatial states of photons.

4.1 Theoretical Background

The theoretical background concerning the nonlinear crystal, spontaneous parametric down-conversion and entanglement can be found in Sections 3.1.1 to 3.1.3. In this section the focus will be on electron-multiplying CCD cameras.

4.1.1 *Charge-Coupled-Device sensors*

Charge- Coupled Devices (CCD) were developed in 1969 by W. S. Boyle and G. E. Smith at Bell Laboratories. A CCD is "a monolithic semiconductor shift register in which the shifted information is in the form of a charge packet stored on a capacitor" [4.1]. The main use of CCDs was the storage of information, but it was soon discovered, that the CCDs are sensitive to light and that it is possible to record 2D images with an array of pixels. In 1970 the first CCD-sensor was fabricated [4.2] and in 2009 Boyle and Smith were jointly awarded the Nobel prize for "the invention of an imaging semiconductor circuit - the CCD sensor" [4.3].

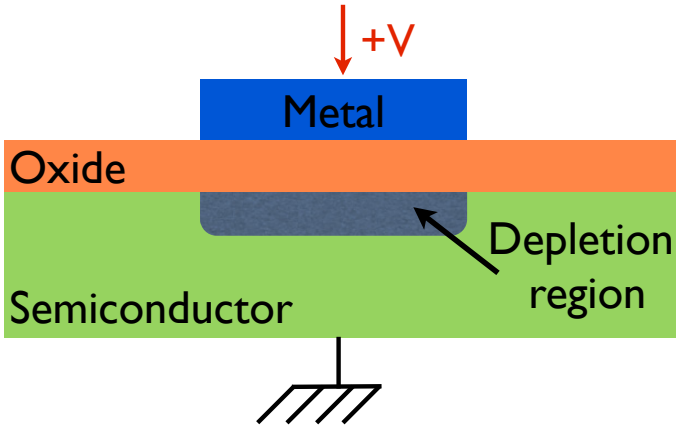

Figure 4.1: *MOS capacitor structure. In case of a p-type semiconductor material and a positively biased metal (gate), photo-generated electron-hole pairs become separated and the electrons become trapped at the oxide - semiconductor boundary beneath the metal electrode.*

A CCD consists of an array of Metal Oxide Semiconductor (MOS) capacitors, which are used for storing charge. Figure 4.1 shows a positively biased MOS capacitor structure. The semiconductor is p-type Si, and an insulator, in this case silicon dioxide (SiO_2), is grown on top of the semiconductor material. A metal electrode is evaporated on the top of the oxide layer. The metal electrode is the gate and is positively biased with respect to the p-type silicon. Until the 1970's the gate was made of metals such as aluminium. However in later years, heavily doped polycrystalline silicon became the standard gate material, due to its ability to resist high temperatures without reacting with the SiO_2 layer [4.4, p. 157]. The heavily doped poly-crystalline Si layer is highly conductive and thus behaves like a "metal". Electron-hole pairs are generated when light is incident on the MOS structure. The electrons and holes are separated by the electric field and the electrons become trapped at the oxide-semiconductor boundary beneath the electrode (the depletion region), whilst a positive voltage is applied to it.

In order to shift the charge through the device, the individual MOS capacitors must be located close together and to pass the charge from one capacitor to the following, a high voltage must be applied to it as well, which causes the depletion regions to overlap and the charge flows along the surface to the silicon-silicon dioxide interface of the second capacitor [4.5] as shown in Figure 4.3.

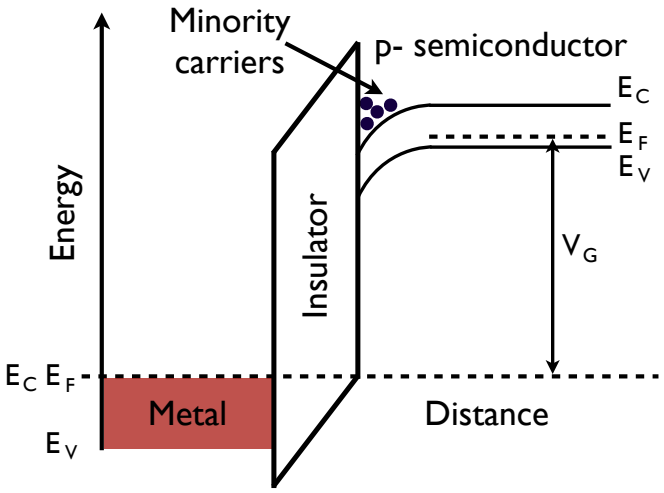

Figure 4.2: *MOS band-structure for a p-type semiconductor and surface channel configuration.*

Figure 4.2 shows the band structure for a single MOS capacitor with a p-type semiconductor and a surface channel configuration. The diagram shows the electron energy versus distance into the structure. In surface channel MOS the potential wells are formed at the semiconductor-oxide interface. A challenge which had to be overcome was that this structure provides inefficient charge transfer as charge might become trapped at the silicon & silicon-dioxide interface. The so-called *fast surface states* fill up quickly, when the potential wells are filling up with charge. However, when the potential wells are emptied, these states do not easily release this charge. These trapped charges would be released later and cause smearing of the image. One solution to this problem would be to use a “fat-zero” signal in surface channel MOS, which guarantees that the interface traps are always filled and the signal charges are transferred unhindered, by applying a high enough bias for the “zero”-potential to fill all the interface and bulk traps [4.6, p. 496]. However, this causes a reduction of the dynamic range of the signal charge as the read noise of the detector is increased.

Instead of using the surface channel configuration, a buried channel configuration can be used. Here an additional thin silicon layer with n-type doping (for a p-type semiconductor) is grown between the p-type semiconductor and the silicon-dioxide interface, causing a potential well below the surface. In buried channel devices, the charge trans-

fer efficiency is higher compared to surface channel devices and the noise is lower, as there is no trapping by fast interface states. However the maximum charge capacity is considerably lower than for the surface channel device as the depth of the potential well is decreased [4.7]. Most modern CCD sensors have a buried channel configuration [4.8, p. 921].

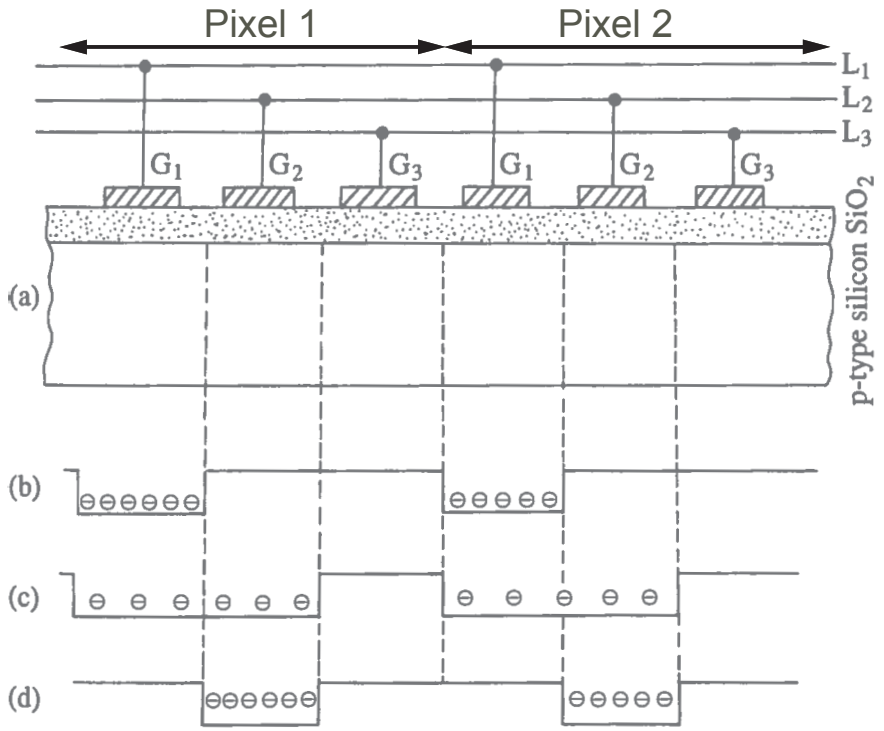

Figure 4.3: *"Basic CCD array composed of a line of MOS capacitors (a). The initial charge distribution within the potential wells when* G_1 *has a positive voltage applied (=* V_g*) and* $G_2 = G_3 = 0$ *is shown in (b). In (c)* $G_1 = G_2 = V_g$, $G_3 = 0$ *and the charge is now spread out under both* G_1 *and* G_2*. In (d),* $G_1 = 0$, V_g *and* $G_3 = 0$*. The charge that initially was under* G_1 *has now moved to the right to be under* G_2*. Note that no charge should be generated under the gates* G_2 *and* G_3*; these elements are therefore screened from incident light". Figure and caption taken from [4.9, p. 345].*

The charge transport for read-out, as shown in Figure 4.3, is known as a *three-phase scheme* and is used in the camera described in Section 4.2. Here each pixel contains three electrodes and the gate potentials are supplied from three different voltage lines (L_1, L_2 and L_3), each one is connected to every third electrode (G_1, G_2 and G_3). The initial electrode G_1 has a positive voltage, V_g, applied to it, while G_2 and G_3 are at zero potential. Any photo-generated electrons will be trapped underneath G_1. The number of photo-generated electrons depends proportionally on the intensity of the incident light beam. After a certain exposure time, the charge will be moved along the MOS capacitor chain, by applying a repeated sequence of potentials to the gate supply lines. The electrodes G_1 and G_2 will have the same voltage, V_g, applied to them. As a result

the charge is spread between the two electrodes. By setting the potential of G_1 to 0, all charge, which was previously contained under G_1, will be now be trapped underneath G_2. By repeating this sequence, the charge will progressively move to the detector output. This three-phase scheme will give information about the G_1 electrode outputs, but no information about electrodes G_2 and G_3, unless charge diffuses into G_1. Alternative schemes exist, like four-phase scheme, pseudo/true two-phase schemes, and virtual phase scheme. An introduction to these schemes can be found in Ref. [4.10] and [4.6, Section 9.4].

Faster read-outs are possible, when for example, a transport register is used. This transport register lies parallel to the sensor and is shielded from any incident light. After the exposure time of the detector array, the charge is shifted to the transport register, and is read out sequentially. The read-out can take place alongside a new image acquisition.

For 2D full frame sensors, the charge of each row is shifted into the read-out register, which then reads out the charge for each individual pixel in that row. Figure 4.4 shows the operating principle of a 2D full frame CCD sensor.

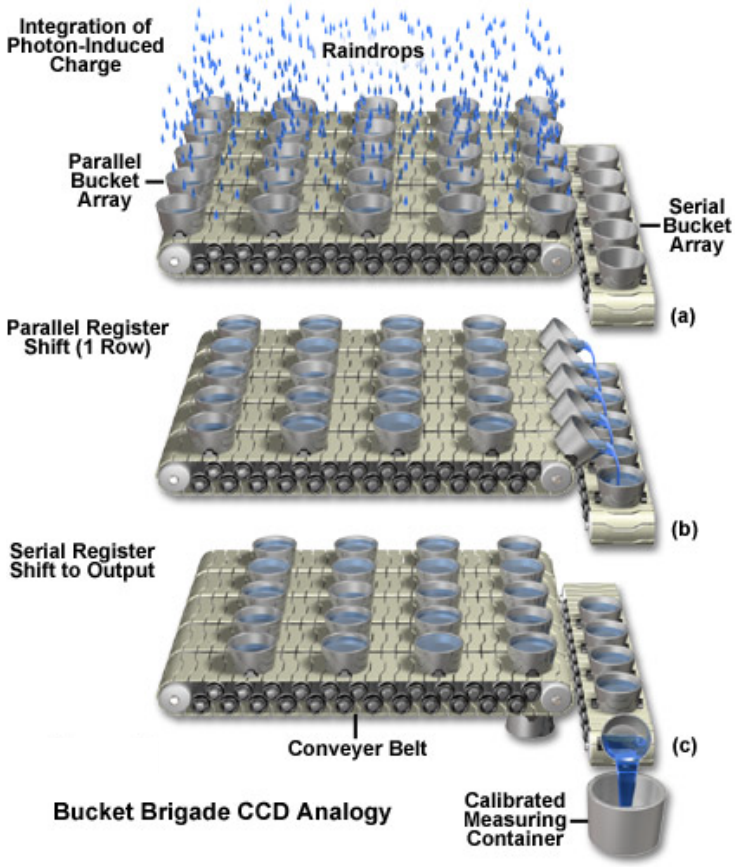

Figure 4.4: *Read-out mechanism of full frame CCD camera [4.11].*

In Figure 4.4(a) the CCD camera during exposure is shown. The buckets represent the potential wells, in which the charge is collected during the exposure time of the sensor. After exposure the chip is protected from any further light exposure by closing the mechanical shutter and a single row of pixels is vertically shifted into the read-out register (Figure 4.4(b)). In Figure 4.4(c) the charge in the read-out register is horizontally shifted and the charge in each individual pixel is read-out by the read-out electronics. After all pixels in the read-out register have been read out, the next row pixels is parallel shifted into the read-out register and the sequence is repeated until all pixels in the sensor are read-out. After the read-out process is complete, the shutter of the sensor is opened again and a new image can be taken.

One important parameter of the CCD sensor is the *charge transfer efficiency* (CTE) η_{CT}. It is essential that only a very small amount of charge is lost while being transferred. After m transfers, the charge will be reduced by a factor of $(\eta_{CT})^m$. The maximum number of charge transfers depends on the number of pixels and the type of shift. Daigle *et al.* [4.12] have characterised the CTE in the horizontal shift register in detail and mean CTEs in the order of 0.99999245 have been measured. For a horizontal shift register consisting of 512 pixels this would lead to the following amount of transferred charge: $(\eta_{CT})^m = 0.99999245^{512} = 0.996$, meaning that out of 1000 electrons 4 will be lost during transfer.

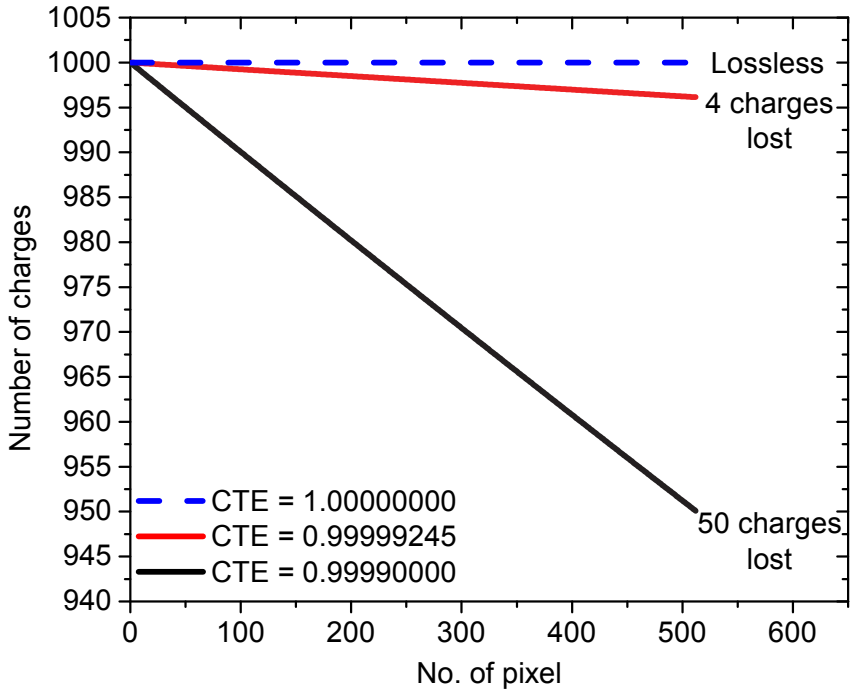

Figure 4.5: *Effect of CTE on charge transfer. Ideally the CTE should be 1, but due to material imperfections, the CTE is <1.*

Figure 4.5 shows the amount of lost charge for three different CTEs and the resulting transfer loss. The amount of lost charge can be calculated with the following equation:

$$\text{Transfer loss} = m \cdot (1 - \text{CTE}) \tag{4.1}$$

For the ideal CTE of 1, no charge would be lost, but due to traps in the semiconductor material only smaller CTEs can be achieved. The CTE of 0.99999245 is taken from Ref. [4.12] and is a typical value for commercially available EMCCD cameras from Nüvü camēras. Although the difference between the CTE from Nüvü camēras and a CTE with a value of 0.99990000 is <0.01%, the amount of transfer loss is ≈ 12× larger.

4.1.2 *Electron-Multiplying CCD cameras*

The camera used in the experiment was an electron-multiplying CCD (EMCCD) camera. In contrast to CCD cameras, EMCCD cameras have a multiplication register incorporated after the read-out register and before the output.

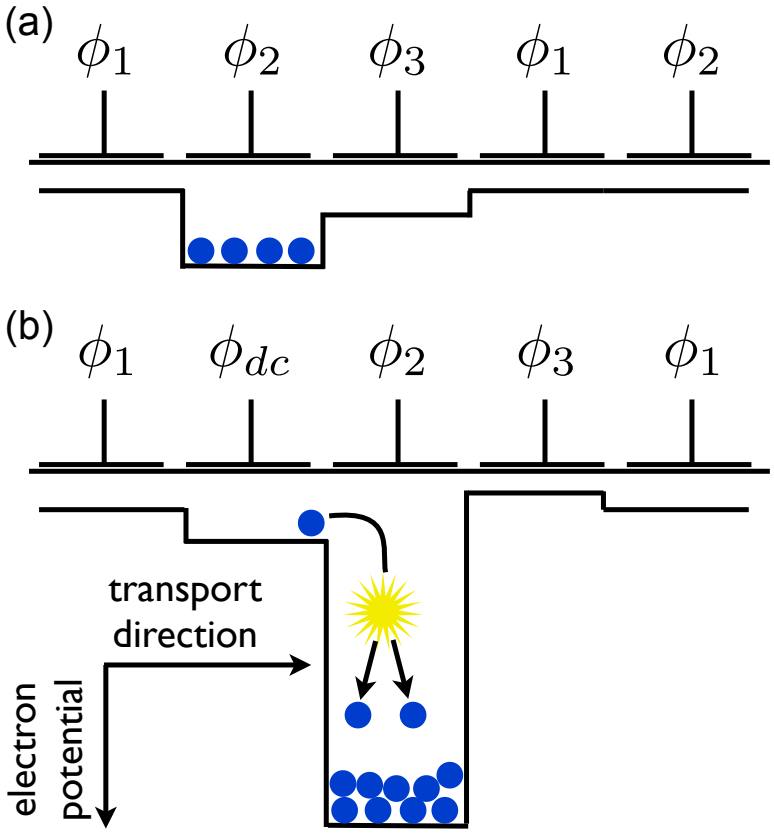

Figure 4.6: *Comparison of a CCD shift register (a) and the EMCCD multiplication register (b).*

Figure 4.6(a) shows the horizontal shift register for a CCD sensor. Here the charge is only transported from one potential well to another. The depth of the potential well

is rather small. In contrast the multiplication register in the EMCCD camera has a deeper potential well (Figure 4.6(b)). For charge transport typical Voltages are of the order of 15 V, but in the multiplication register Voltages in excess of 35 V − 40 V are used [4.8, p. 925]. There is a small chance that within the deep potential well impact ionisation takes place. The probability of multiplication in any one pixel is around ×1.01 to ×1.015. However over the entire length of the multiplication register the probability is very high and substantial gains of up to thousands can be achieved [4.13, p. 24]. The probability of an electron creating a secondary electron through impact ionisation is increased by giving the initial electron more energy. This is usually done by replacing one of the electrodes of the multiplication register with two electrodes. The electrode ϕ_{dc} is kept at a fixed potential, while ϕ_2 is operated as normal, except, that higher positive voltages are applied to this electrode compared to charge transfer on its own. The large electric field generated between ϕ_{dc} and ϕ_2 is high enough for the electrons to cause impact ionisation events as they transfer.

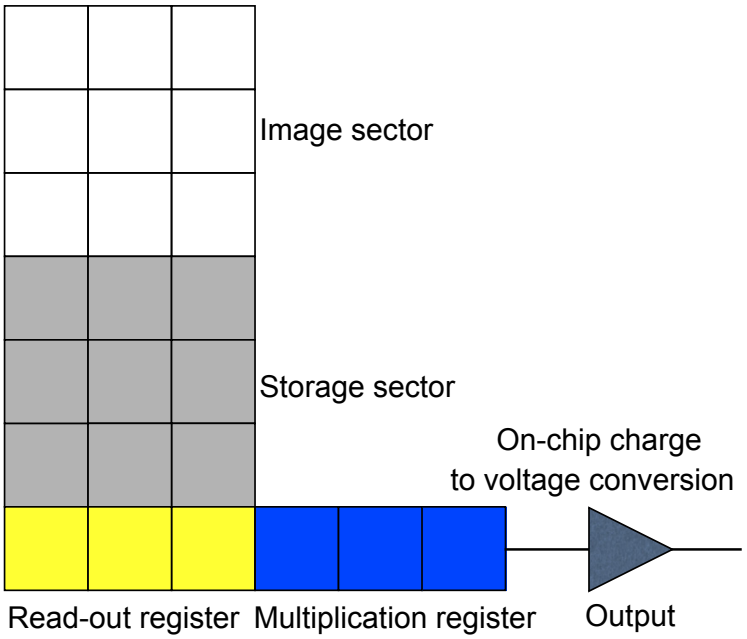

Figure 4.7: *Frame- Transfer EMCCD camera read-out mechanism.*

The read-out mechanism of the camera used in the experiment is slightly different from than the one shown in Figure 4.4. The camera does not possess a simple full frame read-out technology, instead it is a Frame-Transfer (FT) EMCCD camera as shown in Figure 4.7. In FT- EMCCD cameras the charge from the image section is rapidly moved to the storage section of the chip, which is protected from incident light by an opaque mask. Due to the storage section, the number of potential wells is twice as high as the number of potential wells needed for full frame cameras, which makes this type of

camera more expensive. The stored image is read out via the read-out register and then amplified in the multiplication register, while another image is acquired. Therefore the shift time must be much smaller than the exposure time, otherwise the effect known as charge smearing will be prominent.

Traditionally CCD sensors were illuminated from the front, where the photon had to be transmitted through the polycrystalline Si electrode, the gate oxide film, and a surface protective film [4.14, p. 8], which can absorb or reflect the incident photons and thus limits the detection efficiency to <40 % in the visible wavelength range. Modern EMCCD cameras use a back illumination approach as shown in Figure 4.8.

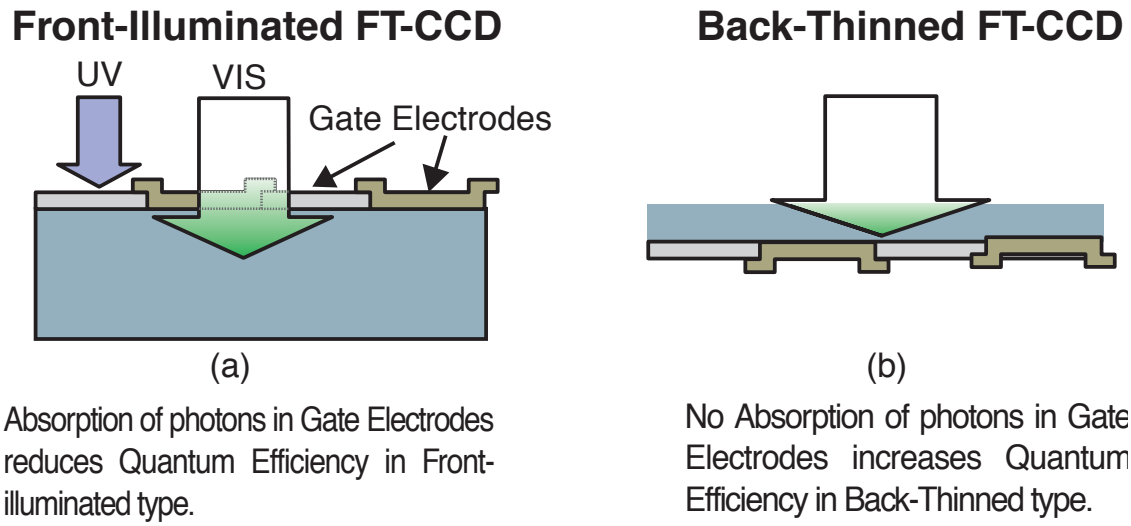

Figure 4.8: *Differences of front- and back- illuminated EMCCD camera [4.15, p. 3]*

In back- illuminated EMCCD cameras, the sensor is turned upside down, and the back side is thinned to 10 to 15 µm thickness with acid etching techniques [4.16, p. 23]. The photons can be imaged directly onto the photosensitive depletion region, leading to quantum efficiencies in excess of 90 % in the visible wavelength range as shown in Figure 4.9. As the incident photons no longer have to be transmitted through the polycrystalline Si layer and the oxide layer, back-illuminated EMCCD cameras are also suitable for imaging applications in the UV wavelength range as these photons no longer get absorbed by these layers.

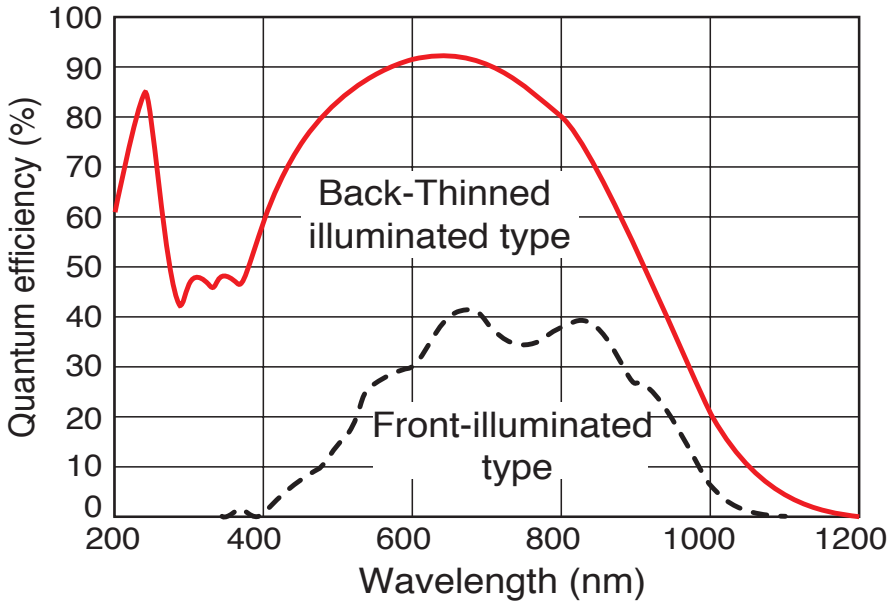

Figure 4.9: *Comparison of quantum efficiency for front- and back- illuminated EMCCD cameras [4.15, p. 3].*

4.1.3 *Noise in EMCCD cameras*

In an ideal world, there would be no noise present in the measurements. Figures 4.10(a) and 4.10(b) show the camera output for ideal measurements of photon pairs in position and momentum respectively. For the position measurement, the correlated photons arrive in neighbouring pixels and are randomly distributed over the whole SPDC beam. For the momentum measurement, the correlated photons have equal and opposite momenta and a common centre.

However, in all measurement there is noise present as shown in Figures 4.10(c) and 4.10(d). The noise sources for this experiment are uncorrelated photons, which could be stray light, or photons which have "lost" their partner, and there is also additional detector noise present in the camera. Three main types of detector noise in the EMCCD camera are: *read-out noise*, *thermal noise* and *Clock-Induced-Charges*. The read-out noise is caused by the minimum electronic noise floor and is mainly caused by the output amplifier and the digitisation electronics. The read-out noise sets the minimum signal level that can be detected by the camera, as any signal below the read noise level will be indistinguishable from the read-out noise [4.13, p. 25]. The amount of read-out noise can be minimised by thresholding as shown in Section 4.2.4.

The second source of noise is thermal noise and is also known as dark current. The dark current is temperature dependent. It also depends on the duration of each im-

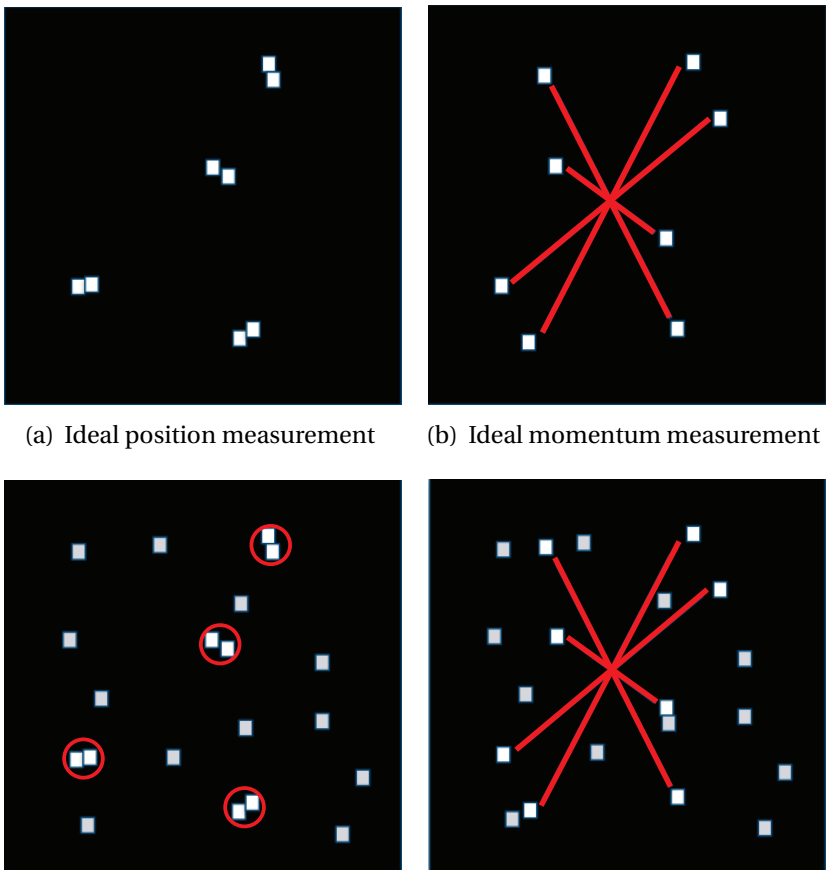

(a) Ideal position measurement

(b) Ideal momentum measurement

(c) Realistic position measurement

(d) Realistic momentum measurement

Figure 4.10: *(a) shows the ideal camera output for a position measurement of photon pairs. The photons of the photon pairs arrive in neighbouring pixels. In (b) an ideal measurement for the momentum is shown. The photons of the same pair have equal, but opposite transverse momenta and have a common centre. In (c) and (d) realistic measurements are shown. Not only correlated photon pairs, but also uncorrelated photons and noise events are present.*

age acquisition as an increased exposure time would lead to an increased amount of dark current. In EMCCD cameras the dark current is expressed in $e^-\,\text{pixel}^{-1}/\text{s}$. Due to thermal generation of electrons at or near the surface, the potential well fills up [4.6, p 467], giving the false impression that the CCD is being exposed to a faint light source although the camera shutter is closed [4.17]. Cooling the camera to temperatures below −85 °C virtually eliminates any dark current [4.17, 4.18].

The third main source of detector noise are the Clock-Induced-Charges (CIC). The origin of this noise is electrical and possesses only a very weak temperature dependence. Unlike the read-out noise the CIC do not depend on the exposure time and they are usually expressed as $e^-\,\text{pixel}^{-1}/\text{frame}$. The CIC are generated during the read-out of the pixels. While the pixels are shifted vertically in the register, there is a chance that random electrons are created during charge transfer, which are then multiplied as any

photon-generated electron. The number of CIC varies for different camera manufactures. Cameras with CIC from $0.01e^{-}\,pixel^{-1}$/frame down to $0.001e^{-}\,pixel^{-1}$/frame [4.19] are commercially available. The camera used in the experiment possesses $\approx 0.005e^{-}\,pixel^{-1}$/frame as measured by Ref. [4.20] and measured in the Quantum Optics lab within the University of Glasgow. Unlike read-out noise it is not possible to apply a threshold to reject the CIC as these have the same read-out values as the real photon events.

According to Reference [4.17] the CIC can contaminate the image 200× worse than the dark current. Different possibilities to decrease the number of CIC present in each frame are being investigated. The shaping of the clock transitions to remove sharp edges and keeping the parallel clock voltage low, while retaining the CTE and the full potential wells are being improved [4.16, p. 36]. Another strategy is to increase the vertical shift speed, however this reduces the charge transfer efficiency and the potential well depth is decreased [4.13, p. 38]. Nüvü camēras have developed special patented read-out electronics, which "allows an EMCCD to operate faster and more reliably for low light applications" [4.17] and offer cameras with the lowest CIC of $0.001e^{-}\,pixel^{-1}$/frame [4.19] .

Without binary thresholding (Section 4.2.4) another noise source, called the *Excess Noise Factor* (ENF) would be present. The ENF's origin is the stochastic process of the electron multiplication in the multiplication register. Only the mean value of the multiplication can be determined, but it is impossible to know the gain for each individual pixel. This causes an uncertainty of $\sqrt{2}$, which has the same effect on the Signal to Noise Ratio as halving the single-photon detection efficiency [4.17]. By using a photon counting mode, this noise source can be eliminated. By setting a threshold for the minimum amount of charge, a "photon" will only be counted when the amount of charge in the potential well is above a set threshold. All other pixels are then regarded as empty. This binary thresholding technique was used in the experiment in order to obtain a high camera sensitivity without losing the image quality. As mentioned before CIC have the same read-out values as real photon events and therefore they will be counted as "photon events" as well. By setting the threshold high enough and sufficiently cooling the camera, most noise sources can be minimised and only CIC will be present in the measurement.

Another noise source for the position correlation measurements is charge smearing.

During charge transfer, some charge can be "left behind", which is then added to the following pixel in the same column. This can cause correlations in the $y-$axis, which are not of quantum nature and therefore falsifies the resulting correlation peaks for the marginal (Section 4.3.2) and conditional (Section 4.3.3) correlations.

4.1.4 *Advantages of EMCCD cameras in correlation measurements*

The useage of EMCCD cameras in correlation measurements has many advantages. EMCCD cameras are commercially available from different manufactures like for example Andor [4.21], Nüvü camēras [4.19, 4.22], Hamamatsu [4.23, 4.24] and Princeton Instruments [4.25]. If the camera is operated in an ultra-low light level environment it has single-photon sensitivity, providing the opportunity to perform experiments at the single-photon level with off-the-shelf technology. The single-photon detection efficiency is very high for back-illuminated EMCCD cameras. For $\lambda = 710\,\text{nm}$ the detection efficiencies in excess of 90 % can be reached. In comparison the Perkin Elmer SPADs have a single-photon efficiency of <70 % [4.26, p. 5]. When the Perkin Elmer detector is used in combination with for example the fibre combiner, the single-photon detection efficiency decreases further as shown in Section 2.3.4.

In previous experiments, the spatial correlations of photon pairs created through SPDC were measured either by scanning a single detector [4.27, 4.28] or by detectors with a very limited number of available pixels [4.29]. EMCCD cameras with arrays consisting of 512×512 or more pixels are commercially available. With these 2D arrays it is possible to capture the whole SPDC beam in one measurement, increasing the total information capacity of a single measurement.

Another advantage is the relative small pixel size in the order of a few $10\,\mu\text{m}$. The photons in a photon pair have the same place of birth and without changing the correlation length (see Equation (4.3)) the photons would be incident on the same pixel. However, one disadvantage of EMCCD cameras is that they do not possess photon number resolving capabilities. If two photons are incident on the same pixel during the same exposure time, the EMCCD camera cannot distinguish them. Ideally the camera should be able to resolve the photon number as this would be the highest probability to detect photon pairs. Instead the photons in a photon pairs must be separated by changing the magnification of the optical system. This increases the probability that

the two photons are registered by two different pixels. Figure 4.11 shows an example for different photon density distributions simulated with LabView's *Gaussian White Noise Waveform vi*. VI is an acronym for Virtual Instrument and represents a basic building block in LabView, comparable to functions and subroutines in other programming languages. This vi creates random photons with a Gaussian distribution centred at $\mu = 0$ and a standard deviation σ set by the user. For small correlation lengths <2 pixels there are distinctive peaks visible with a high probability that the photons land in neighbouring pixels. If the correlation length is higher, the probability that the photons land in neighbouring pixels decreases and the probability function spreads out to higher numbers of pixels. In this case, the correlation peak for the marginal correlations (see Sections 4.3.1 and 4.3.2) would decrease in height and spread out instead. This would increase the standard deviation of the correlation peak for the position measurement and subsequently increase the variance product of the position-difference and the momentum sum, leading to a smaller violation of the classical limit of separability.

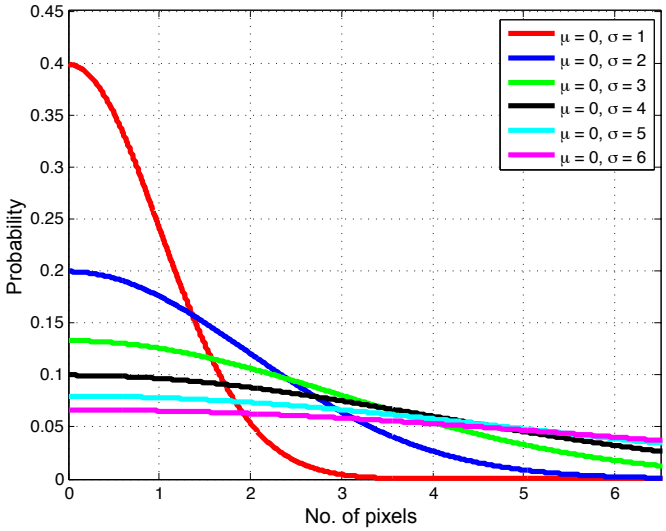

Figure 4.11: *Example for photon pair distribution for correlated photon source as simulated with LabView.*

The ability to use a smaller correlation length increases the probability to detect photons in neighbouring pixels and therefore increases the height of the correlation peak and decreases its standard deviation, leading to a greater violation of the classical limit of separability indicating high transverse correlations of the photon pairs.

4.2 Experimental Setup

The experimental setups used to measure the spatial correlations of the entangled photon pairs in position (Figure 4.12) and momentum (Figure 4.14) are explained in the following. The pump laser was a frequency-tripled passively mode-locked Nd:YAG laser emitting at $\lambda_{pump} \approx 355\,\text{nm}$ with a pulse repetition rate of 100 MHz. The average output power of 150 mW was attenuated to 2 mW. The diameter d_p of the Gaussian pump beam was expanded to $d_p = 0.56 \pm 0.05\,\text{mm}$. The entangled photon pairs were created through SPDC. The nonlinear crystal used was a 5 mm long type-I β-barium borate (BBO) crystal cut for the generation of degenerate down-converted photons at $\lambda_{SPDC} \approx 710\,\text{nm}$. The crystal was angled to provide a near-collinear output. The subsequent choice of lens configurations was chosen to maintain a constant separation of 700 mm between the nonlinear crystal and the EMCCD camera for easy manual switching between the image plane and the far-field of the crystal. In order to spectrally filter the degenerate light, a 10 nm bandpass filter, centred at 710 nm with a transmission efficiency of 90%, was located in front of the EMCCD camera (Andor iXon3). The EMCCD camera was optimised for visible wavelengths with a back-illuminated array of 512×512 pixels each with a size of $16 \times 16\,\mu\text{m}$, however for these experiments a smaller region of interest, measuring 201×201 pixels, was used to improve the read-out time and to increase the frame rate to approximately 7 Hz. Note that the LabView program used for saving and analysing the data in real time was the bottleneck, which reduced the frame rate of the camera. By using the Andor Solice software to capture the images and by doing the correlation analysis after finishing the measurement, the camera would have been able to run at a frame rate of 35 Hz for the full chip measuring 512×512 pixels or approximately 90 Hz for the chosen region of interest of 201×201 pixels [4.20]. The advantage of using our LabView program was the ability to monitor the number of measured correlations and the properties of the correlation peak in real-time.

4.2.1 *Image plane setup*

The experimental setup used for measuring position correlations in the image plane of the BBO crystal is depicted in Figure 4.12. The nonlinear crystal was imaged onto the detection plane of the EMCCD camera with a simple telescope consisting of two lenses.

The first lens possessed a focal length of f = 100 mm and was placed 100 mm after the BBO crystal. The second lens had a focal length of f = 250 mm and was placed 350 mm after the first lens and 250 mm before the pixel array of the camera. The magnification of the imaging system was −2.5.

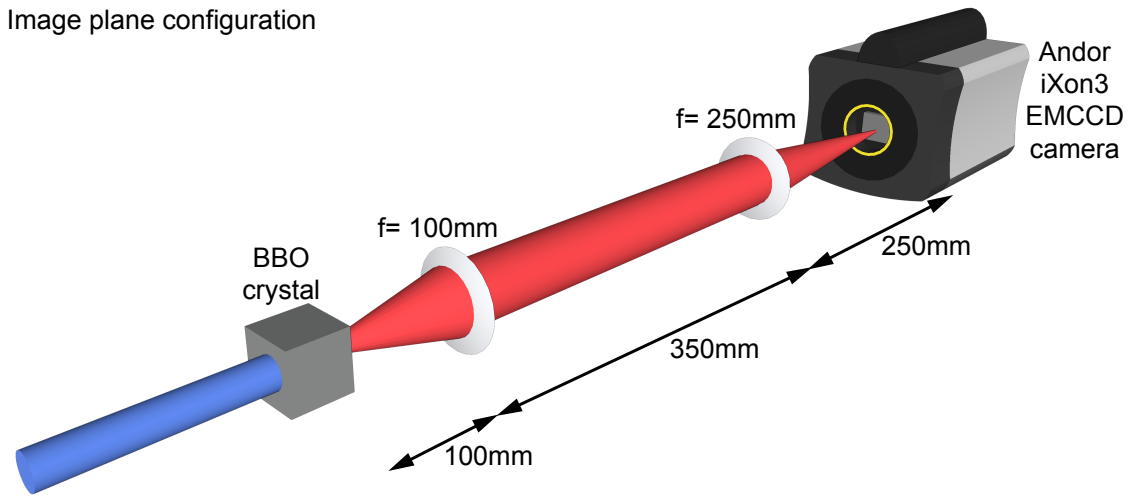

Figure 4.12: *Schematic for the experimental setup used to measure correlations in the image plane of the BBO crystal. The nonlinear crystal is imaged onto the EMCCD camera with a -2.5× magnification using a simple telescope.*

In this configuration the place of birth for the entangled photon pair was measured. Summing a sufficient number of images, the near-Gaussian intensity profile of the degenerate light beam can be reconstructed, as shown in Figure 4.13. Different pixel and camera defects can be seen in Figures 4.13(b) and 4.15(b). There are individual *hot pixels* present with very high counts. These pixels are in a constant on-state and were removed from the data analysis. Beside the hot pixels, *dead pixels* are present as well. These pixels are in a constant off-state and no counts were registered with them. The grey shaded areas are most likely caused by dust particles on the EMCCD. For both measurements (as shown in Figures 4.13(b) and 4.15(b)) the grey shaded areas are in the same plane, not sharply focussed. How the dust particles block the incident light on the EMCCD camera depends on the distance from the EMCCD camera's focal plane. The closer the dust particle is located to the chip, the sharper it will be in focus. If the dust particle is located on the cover glass it will be partially in focus, while dust on the optics near the camera will cast a circular shadow [4.30].

100,000 thresholded images were summed, and as expected, from the Gaussian intensity profile from the pump beam, the Gaussian intensity profile for the degenerate light was recovered.

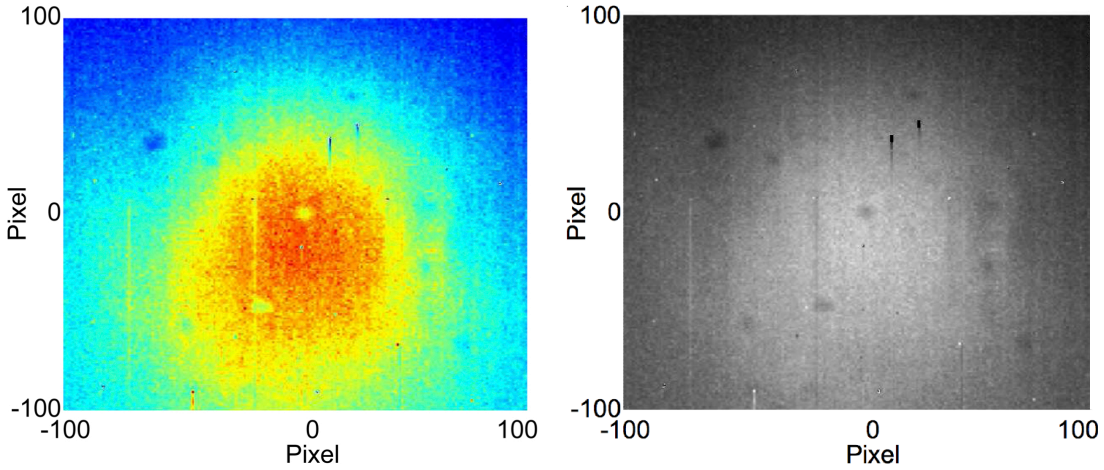

(a) Image plane intensity (b) Image plane showing defects

Figure 4.13: *(a) the intensity of the SPDC beam after 100,000 images were acquired. In (b) a grey scale representation is shown in order to show pixel defects and dust particles on the EMCCD.*

The spatial structure of the bi-photon field produced by SPDC at the nonlinear crystal can be described using a Gaussian model [4.31, 4.32], where the transverse wave function of the post-selected two-photon field [4.33] is expressed as.

$$\Psi(\rho_1,\rho_2) = N\exp\left[-\frac{|\rho_1+\rho_2|^2}{4\sigma_+^2}\right]\exp\left[-\frac{|\rho_1-\rho_2|^2}{4\sigma_-^2}\right], \tag{4.2}$$

where $N = 1/(\pi\sigma_-\sigma_+)$ is a normalisation constant, $\rho_i = (x_i, y_i)$ is the transverse position of the photon i ($i = 1,2$) and $\sigma_\pm$ are the standard deviations of the two Gaussians, giving the strength of the position and momentum correlations σ_- and σ_+^{-1} respectively. σ_+ is defined as the standard deviation of the Gaussian field profile of the pump beam σ_p, while σ_- depends on the length of the SPDC crystal L and the wavelength of the pump beam λ_p, given by

$$\sigma_- = \sqrt{\frac{\alpha L\lambda_p}{2\pi}}, \tag{4.3}$$

where $\alpha = 0.455$ is an adjustment constant [4.34] to match the $1/e^2$ intensity of the approximated Gaussian function, which was derived from the initial *sinc*- function for the entangled two photon field [4.32].

Inserting the experimental parameters into Equation (4.3) resulted in a correlation length of 11.3 µm. This means that the correlation length of the photon pair was smaller than the pixel size of 16 µm. The camera was not capable of resolving the number of individual photons simultaneously incident on a single pixel, thus in order to detect an entangled photon pair, the photons had to be detected by two different pixels. One

approach to accomplish this was to increase the correlation length of the bi-photon at the plane of the camera $\sigma_{pos} = M\sigma_{-}$, by changing the magnification M of the imaging system, and measuring correlations that occur at separations greater than or equal to 1 pixel [4.35]. For a magnification of 2.5 the resulting increased correlation length was 28 µm.

4.2.2 *Far-field setup*

For measuring the transverse momenta of the entangled photon pairs, we used the experimental setup shown in Figure 4.14. The far-field image is obtained by using a composite Fourier system with an effective focal length of f_e = 100 mm

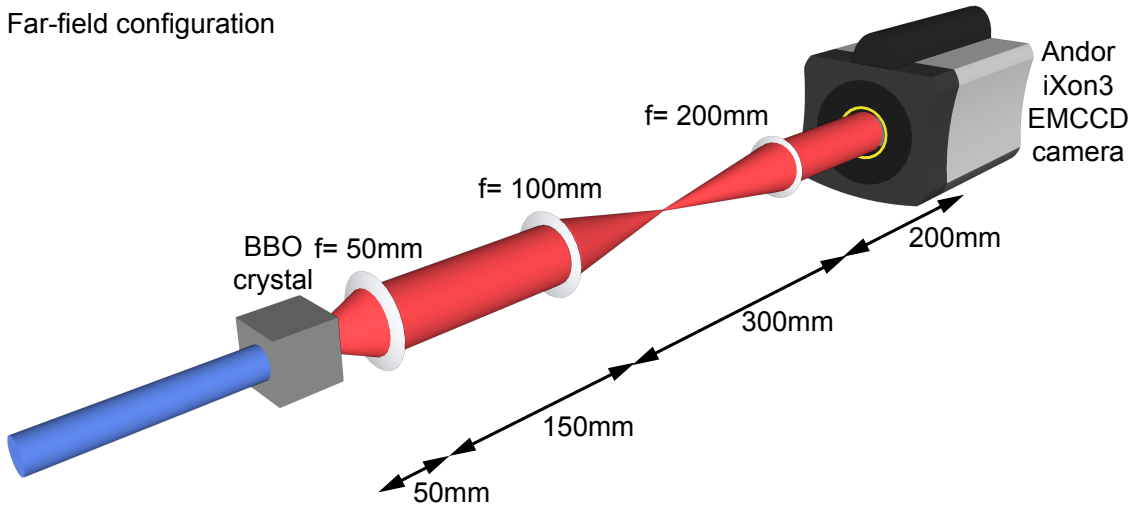

Figure 4.14: *Schematic for the experimental setup used to measure correlations in the far-field of the BBO crystal. The EMCCD camera is in the Fourier plane of the nonlinear crystal.*

When measuring the transverse momenta of the entangled photon pair, the orientation of the nonlinear crystal is very important. When the nonlinear crystal is orientated to have a collinear output then the down-conversion ring can be observed with the EMCDD camera as shown in Figure 4.15(c). However, the crystal was orientated in a near-collinear setup, so that the down-conversion ring collapsed and only a spot was visible, as shown in Figure 4.15(a).

The correlation length of the entangled photons for the momentum measurement can be calculated from:

$$\sigma_{mom} = \frac{f_e}{k_{SPDC}\sigma_{+}}, \tag{4.4}$$

where k_{SPDC} is the wavenumber of the down-converted photons, σ_{+} is the standard

deviation of the pump beam and f_e is the effective focal length of the composite Fourier system. For the experimental parameters σ_{mom} was approximately 17 µm.

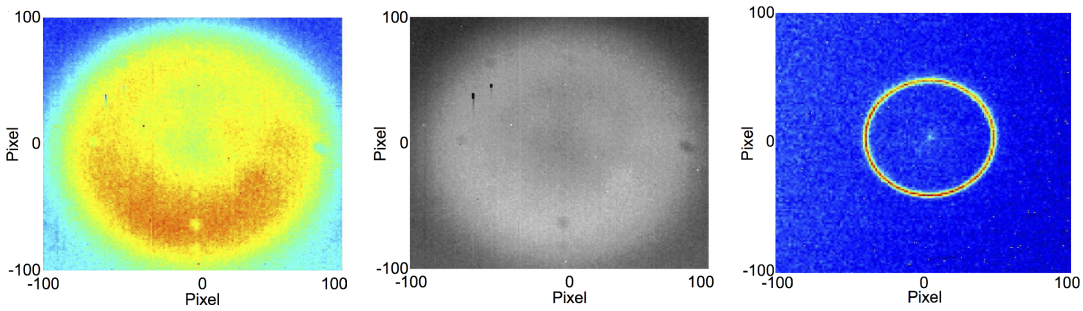

(a) Near-collinear intensity (b) Near-collinear output (c) Non-collinear intensity

Figure 4.15: *(a) shows the intensity of a near-collinear crystal orientation after 100,000 images were acquired. The ring is almost collapsed. (b) shows a grey scale image to enhance the pixel defects and dust particles on the camera. In (c) the crystal is orientated for a non-collinear output. The down-conversion ring is clearly visible in the far-field of the crystal.*

4.2.3 *EMCCD camera settings*

The following camera settings were used for the correlation measurements:

Temperature setting: The camera was air-cooled via a built-in fan over the heat sink, which was mounted on the back of the pixel array. The cooling element was a four stage Peltier cooling assembly, which utilised the thermoelectric effect to rapidly cool the sensor down to the stable operating temperature [4.13, p. 77]. The minimum temperature obtained with air cooling was −85 °C. A low operating temperature was desired as a low temperature reduces the amount of dark noise. The dark noise was produced by the flow of dark current during the exposure time and had typical values of tenths of mA per pixel. According to Andor [4.13, p. 82] a temperature drop of 7 °C halves the dark signal.

Figure 4.16 shows example measurements performed by Andor [4.18, p. 6]. By reducing the operating temperature of the camera, the number of thermally generated and amplified electrons (spikes in the figure) and dark current were reduced.

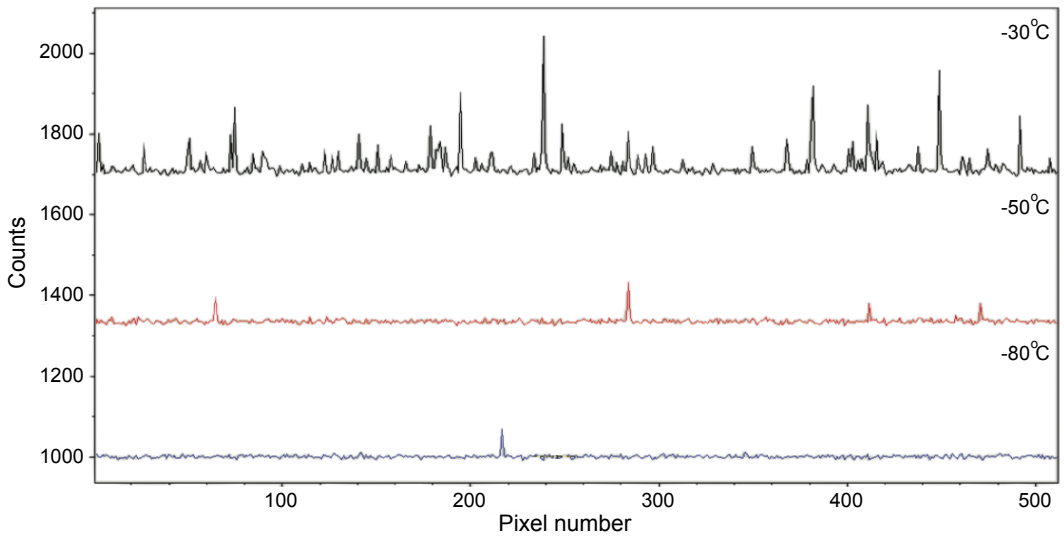

Figure 4.16: *Change of dark signal for different operating temperatures. The lower the temperature of the camera, the lower is the background level and cleaner is the noise floor. Figure taken from iXon+ Back-illuminated EMCCD - Technical Article from Andor Technology [4.18, p. 6]*

Horizontal pixel read-out rate: The horizontal pixel read-out rate defines the rate at which the pixels are read from the shift register. For high frame rates, a fast horizontal read-out rate should be used. However a slower read-out rate reduces the amount of the generated read noise and provides a higher dynamic range. Since a low amount of noise was desired for our experiment, the slowest horizontal read-out rate available was used. For the iXon3 - 897, the slowest horizontal read out rate was 1 MHz.

Vertical shift speed: The vertical shift speed defines the time it takes to shift all pixels one row down, with the bottom row entering the shift register. A slow vertical shift speed results in a higher pixel well depth, which ensures a better charge transfer efficiency. A fast shift speed reduces the charge transfer efficiency but it also reduces the number of CIC. For this experiment the fastest vertical shift speed available for our camera model of 0.3 µs was used.

Vertical Clock Amplitude Voltage: The Vertical Clock Voltage Amplitude can be used to increase the amplitude of the clock pulses used to perform row shifts on the CCD. The vertical clock voltage amplitude was optimised at the factory and beside the “normal” setting, 4 more settings with an increased voltage amplitude were available. A high vertical clock voltage amplitude increases the

charge transfer efficiency at the expense of a slightly higher CIC [4.36, p. 41]. The highest vertical clock voltage amplitude of +4 was used.

Exposure time: The photon flux was chosen to maximise the strength of the position/momentum correlation signal relative to noise sources, giving approximately 0.02 photons pixel^{-1} / frame, which was equivalent to the level of noise present in the camera. The exposure time for the position correlation measurements was set to 0.4 ms, while the momentum measurements were obtained using an exposure time of 1 ms.

4.2.4 *Thresholding*

In order to identify a photon, the output of the camera was characterised. The output contained both noise and signal. The EMCCD camera was affected by different noise phenomena; including thermally excited electrons, read-out noise, and Clock-Induced-Charge (CIC). To characterise the noise, the camera was operated at maximum gain and 10,000 images with the shutter open, while the pump laser was blocked, were recorded. The EMCCD camera was located in a light-tight environment to minimise the amount of ambient light.

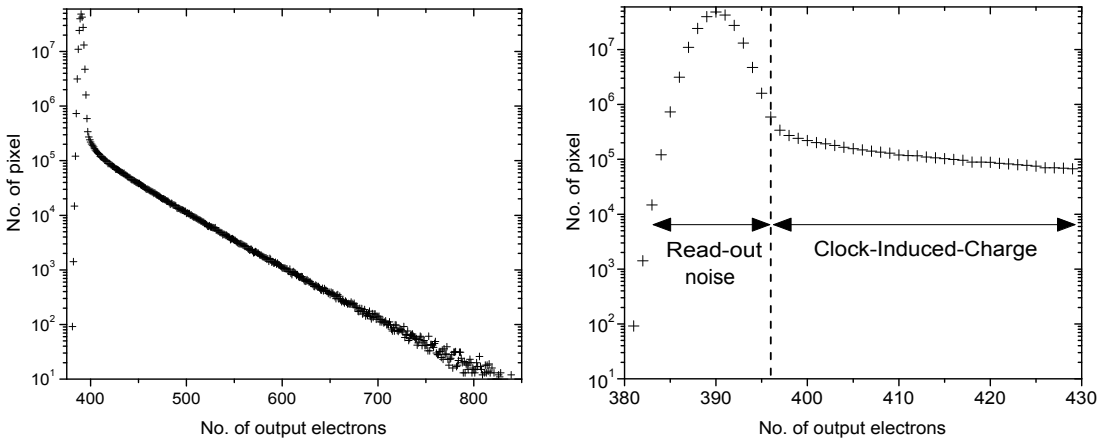

(a) EMCCD noise (b) Rescaled EMCCD noise

Figure 4.17: *(a) EMCCD camera noise characteristics after 10,000 recorded images. (b) Rescaled EMCCD camera read-out characteristics after 10,000 recorded images showing read-out noise, Clock-Induced-Charge and the threshold setting.*

By comparing the output level per pixel against the number of pixels, an analysis similar to Ref. [4.37] was performed. As shown in Figure 4.17(a), the read-out noise caused a Gaussian distribution of output electrons centred at 390 counts and with a standard

deviation of σ_{noise} = 6 counts [4.35]. The threshold was set to the value of σ_{noise}. For higher read-out values a exponentially decaying tail is visible. This tail was caused by CIC and was not distinguishable from single-photon events, as these possessed similar read-out values.

Additional to the noise characteristics analysis, a second analysis to determine the optimal threshold setting was performed. 10,000 raw images were record, without any data processing, for a momentum correlation experiment. The average background level in each individual pixel in our ROI was determined and the raw data, including the background measurements were loaded into an analysis program. The analysis software compared the difference of the raw image and the background measurement with the set software threshold. If the the difference was higher than the variable threshold, an "event" was added to the thresholded image and then the image analysis was performed (see Section 4.2.5). Figure 4.18 shows the change in SNR with increasing threshold.

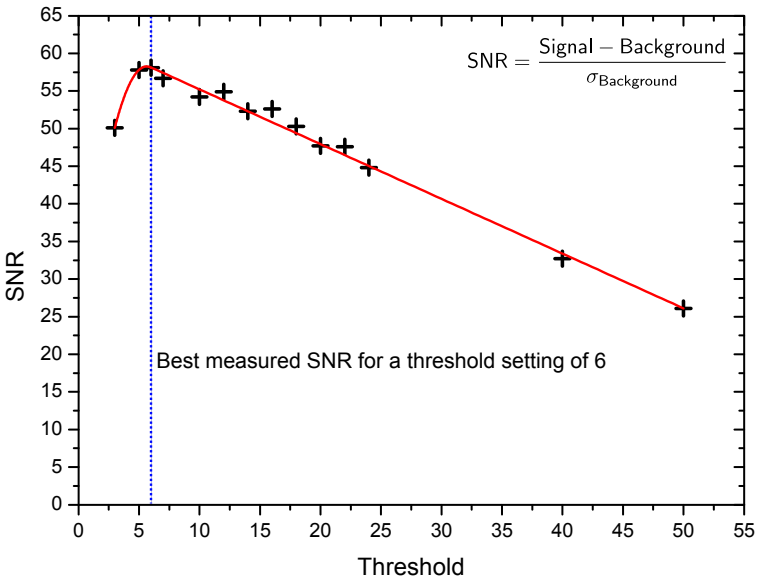

Figure 4.18: *Analysis of the SNR for various threshold settings. For low threshold settings the read-out noise dominates in the measurements and decreases the SNR. For high thresholds real photon events are ignored and fewer correlations were measured. Best results were obtained for a threshold of 6 counts above the averaged background level per individual pixel.*

For a low threshold setting of 0 – 4 counts, the SNR was low, due to the high number of read-out noise. Due to the large number of registered events in each image, the overall background level was very high. On the other hand, if the threshold was set to values above 6 electrons, the SNR decreased because real photon events were rejected and so fewer real correlations were measured. In the analysis, the optimum threshold

setting was found to be 6 counts above the average background for each individual pixel, which coincided with the results obtained in the camera noise characteristics analysis.

4.2.5 *Image processing*

Before each correlation measurement, a background measurement with the pump laser blocked was taken in order to determine the mean read-out value for every individual pixel in our region of interest. For the measurements, a binary thresholding was used by assigning a "1" to each pixel which had a greater read-out value than σ_{noise} plus the mean background level for the pixel and we assigned a "0" to all pixels with a smaller value to remove read-out noise.

The thresholded images were processed in two different ways to determine if the photons possessed EPR-like correlations, and if these correlations were real or a camera feature. Each frame was cross-correlated with itself as shown in Figure 4.19. This is also known as autocorrelation. The zero-coordinates in the analysis program were set to be in the centre of the region of interest measuring 201×201. An odd number of pixels was used to ensure symmetry. For every registered photon in the same image, the distance to every other photon in the same image was calculated with respect to the centre position. It is important to distinguish between position correlations, where the correlated photons were detected in nearby pixels, and momentum correlations, where the partner photons were located the the opposite side of the centre position. For the position correlations the position difference in the x- and y coordinates $pos_1 - pos_2$ was calculated. For example if one photon was detected in pixel $x_1 = -45$ and $y_1 = 78$ and its partner was located in pixel $x_2 = -44$ and $y_2 = 76$ the resulting position difference was $\Delta x = -1$ and $\Delta y = 2$.

For the momentum correlations the momentum sum was calculated. For example photon 1 was located in pixel $x_1 = -100$ and $y_1 = 50$ and its partner was in pixel $x_2 = 100$ and $y_1 = -49$, the resulting momentum sum would have been at $x = -100 + 100 = 0$ and $y = 50 + (-49) = 1$. A "1" was added to each coordinate set for the position/momentum correlation measurement in the coincidence graphs (see Figure 4.22(a) and Figure 4.22(b)). The spatial information of the photon locations in each individual frame was summed and also the registered coincidence counts over

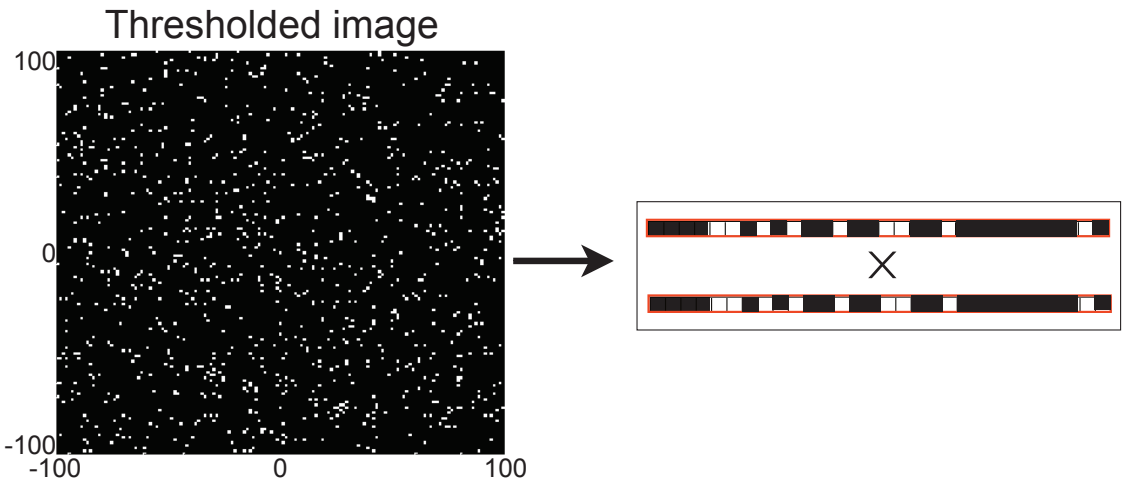

Figure 4.19: *Each individual images is correlated with itself to analyse the spatial positions of the detected photons relative to each other.*

all 100,000 images were summed. It was expected that a small coincidence peak on top of a huge background would be detected, as there was a slightly higher probability to find photons with a position-difference or momentum-sum in a range of ±3 pixels of the centre coordinates.

In order to distinguish between *quantum* and *accidental* correlations, each frame was correlated with the previous one, as shown in Figure 4.20. In this case the registered coincidences arose from random accidental correlations and the probability to detect photons was proportional to the intensity profile of the down-converted light. These uncorrelated correlations were used as a reference for background subtraction for the EPR calculations.

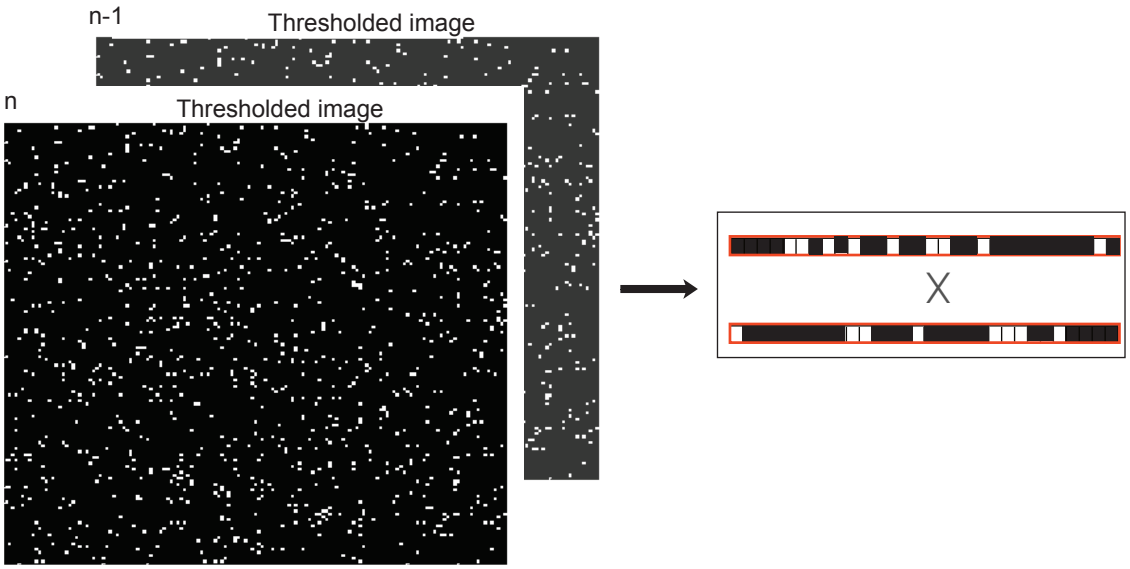

Figure 4.20: *Each individual images is correlated with the previous image to analyse the number of accidental coincidences.*

As shown in Figure 4.21, the level of accidental coincidences measured in consecutive images is of the same order of magnitude as the uncorrelated coincidences measured with the same-image analysis.

It is very important to note that all recorded images were used to determine the strength of the correlations. In previous experiments [4.38–4.40] measuring the spatial correlations of photon pairs using intensified CCD (ICCD) cameras, the threshold was set to a very high level, resulting in most recorded frames being empty or they contained a single detected event [4.40]. Only a very small number of the recorded images contained two events. Only those images with two events were used for data analysis and the other frames were disregarded. In this experiment, no images were rejected.

4.3 Results

In this section, the temporal development of the correlation peak for the image plane and far-field measurements is discussed. The data was analysed in terms of marginal correlations as a test for spatial entanglement in the transverse directions and conditional correlations as a test for EPR-like correlations. From the conditional correlations the dimensionality was calculated.

4.3.1 *Temporal development of correlation peaks*

A series of 100,000 images was recorded for the image plane and far-field configurations respectively. The probability distributions $P_{\rho-}$ and $P_{\rho+}$ were calculated by counting the number of coincidences as a function of the difference (image plane) or sum (far-field) of the pixel coordinates in the x and y directions. Here ρ_- and ρ_+ were defined as $\rho_- = \rho_1 - \rho_2$ and $\rho_+ = \rho_1 + \rho_2$, where $\rho_i(\rho x_i, \rho y_i)$ was the transverse momentum of the photon i. The transformation of the crystal plane to the detection plane was made by using the scaling factors $\gamma_{pos} = 1/M$ and $\gamma_{mom} = \hbar k_{SPDC}/f_e$. The results were obtained by summing the spatial-correlation function over all recorded images. The correlation peak for the photon pairs is clearly visible on top of a broader background which was caused by uncorrelated events, as shown in Figure 4.21.

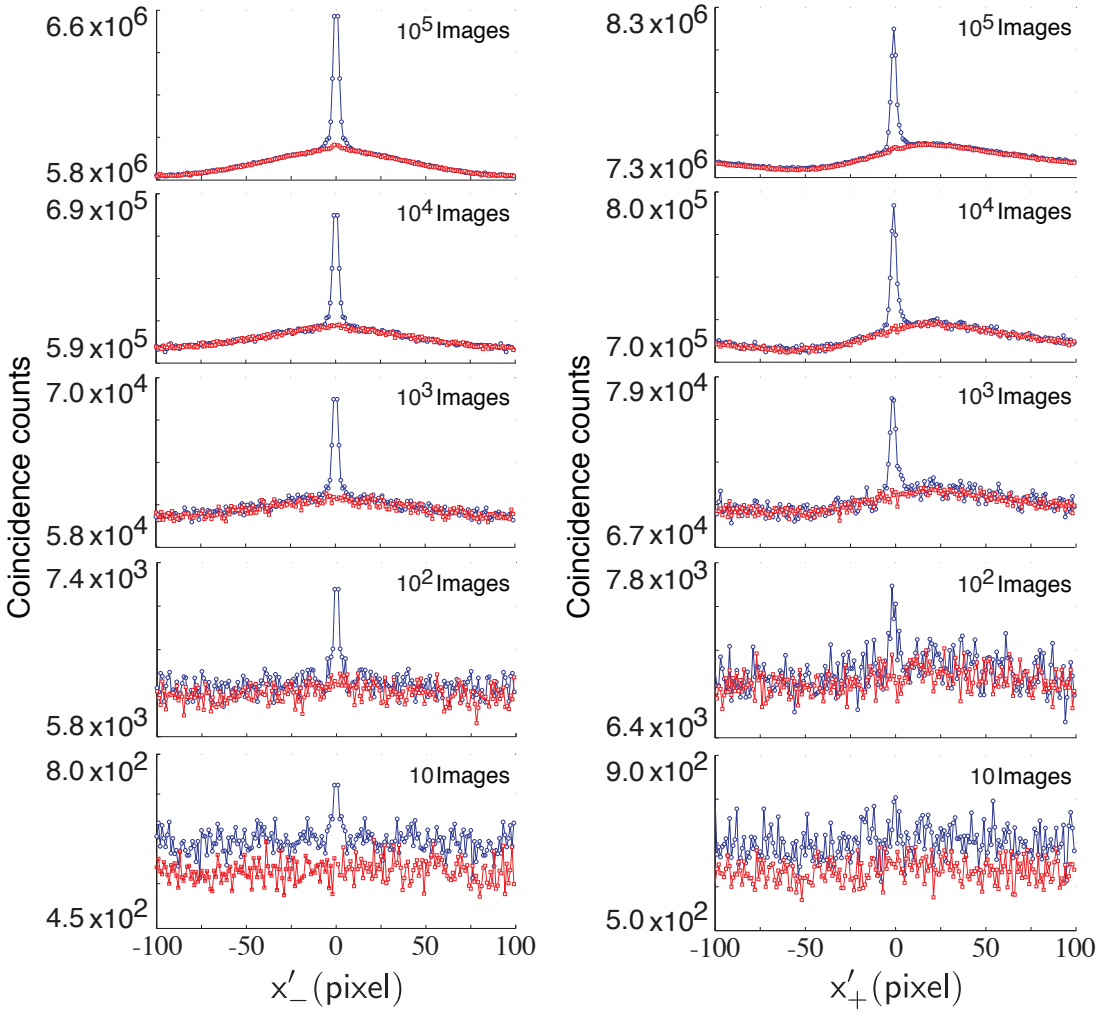

(a) Position measurement (b) Momentum measurement

Figure 4.21: *Cross sections of the correlation functions in the x' dimension in image plane (a) and far-field (b), for an increasing number of images. Blue circles represent the spatial-correlation and red squares represent the reference-correlation. The asymmetry of the far-field correlation function is the result of a non-uniform near-collinear degenerate light cone, as shown in Figure 4.15(a).*

Figure 4.21 (a) shows the measured coincidence counts in the image plane as a function of x'_- coordinates, while coincidence counts measured in the far-field as a function of px'_+ are shown in Figure 4.21 (b). A correlation peak in both position and momentum could already be seen after a few images and became significant above noise as more images were processed. The difference in background for 10 summed images is due to the fact that for the reference correlations only $n-1$ images were processed. For the other summed images this difference becomes negligible.

4.3.2 *Marginal correlations*

Subtracting the reference correlations from the spatial correlation function produces a strong correlation for the position measurement and a strong anti-correlation for the momentum measurements as indicated in Figure 4.22 (a) and Figure 4.22 (b) respectively. Since the EMCCD camera was not capable of distinguishing two photons simultaneously incident on the same pixel, it was impossible to measure the correlation function for $\rho_1 = \rho_2$, for which a value equal to 0 was assigned. To confirm that these correlations arose from correlations between photon pairs, one ND-filter used to attenuate the pump beam was placed after the BBO crystal in the down-converted beam to reduce the heralding efficiency to approximately 2.0%. The exposure time was slightly increased to ensure the same photon flux compared to the previous experiments. However, the increase in exposure time had no measurable influence in the number of noise events. As shown in Figure 4.22 (c) and Figure 4.22 (d), strong correlations were not observed in these measurements; however along the y'_- axis an increased number of coincidence counts were observed. These counts were caused by charge smearing during the read-out of the EMCCD camera and did not represent true photon correlations. For clarity the correlation functions for $y'_- = \pm 1$ in Figure 4.22 (a) and Figure 4.22(c) were set to 0, as the high coincidence counts masked the real photon coincidence counts.

Entanglement in continuous variables (CV) can be detected through the violation of inequalities involving variances of the distributions [4.41, 4.42] shown in Figure 4.22. One inequality is the variance product from the position difference and the momentum sum $\Delta^2(r_i - r_j)\Delta^2(pr_i + pr_j) \geq \hbar^2$, where the CV obey $[\hat{r}, \hat{pr}] = i\hbar$. The variance product could be calculated from the x' and y' axis in position (Figure 4.22 (a)) and px'_+ and py'_+ in momentum (Figure 4.22(b)) from the background corrected autocorrelations. However, since the y' axis is affected by charge smearing, a different orthogonal basis set as indicated in Figure 4.23 was chosen. These different orthogonal bases are $x_- = (x_- + y_-)\sqrt{2}$ and $y_- = (x_- - y_-)\sqrt{2}$ and $px_+ = (px_+ + py_+)\sqrt{2}$ and $py_+ = (px_+ - py_+)\sqrt{2}$. Fitting Gaussian functions to the data, the variances shown in Table 4.1 were found, thus giving variance products of:

$$\Delta^2 x_- \Delta^2 px_+ = (8.9 \pm 0.1) \times 10^{-4}\hbar^2, \tag{4.5}$$

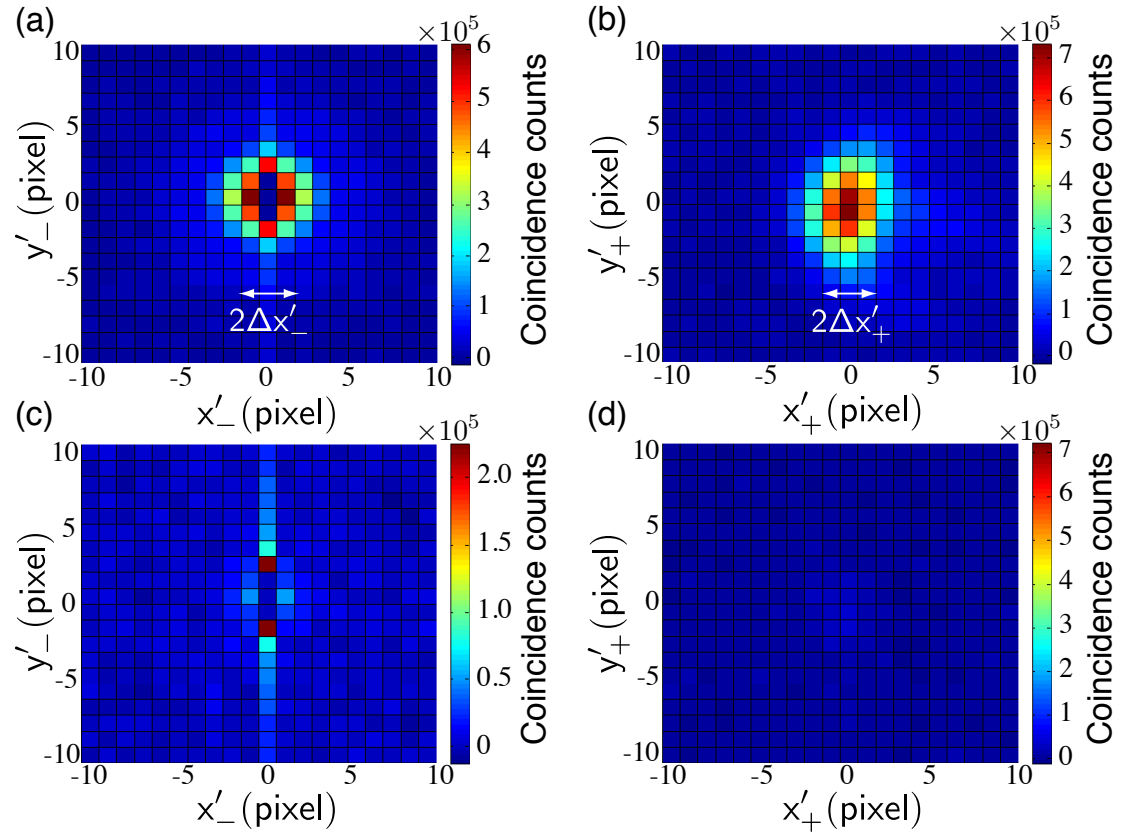

Figure 4.22: *Background-corrected auto-correlation functions for high and low heralding efficiency configurations for (a) the image plane and (b) the far-field of the crystal, summed over 100,000 images and with the measured background correlations removed. In (c) and (d), the same measurements performed with a lower heralding efficiency are presented. Variances along the x'_- direction of the high heralding efficiency configuration are indicated. Because of increased coincidence counts attributed to smearing, the correlation function for $y'_- = \pm 1$ were set to 0 in (a) and (c) for clarity.*

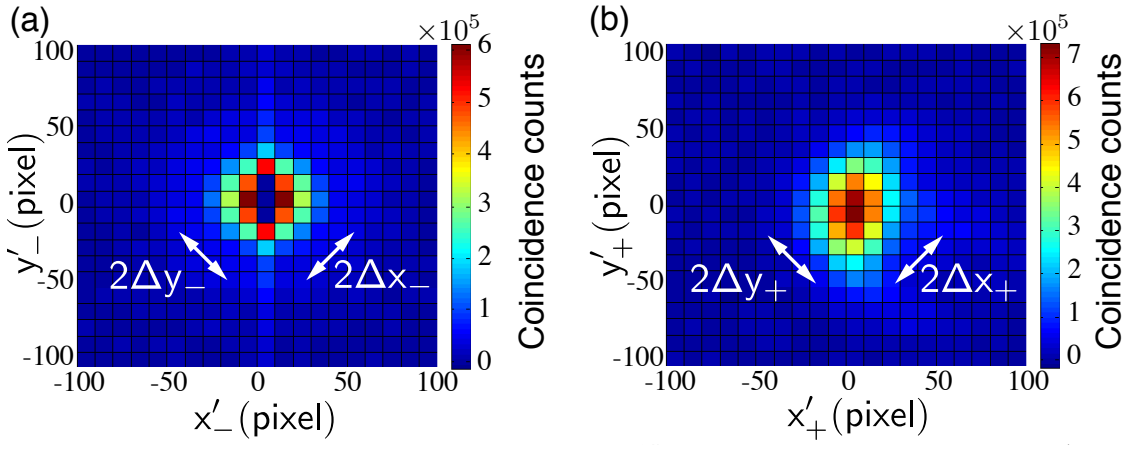

Figure 4.23: *Background-corrected auto-correlation functions for high heralding efficiency configurations for (a) the image plane and (b) the far-field of the crystal, summed over 100,000 images and with the measured background correlation removed, showing a different orthogonal basis set.*

and

$$\Delta^2 y_- \Delta^2 p y_+ = (6.5 \pm 0.1) \times 10^{-4} \hbar^2, \tag{4.6}$$

which are both almost 3 orders of magnitude below the classical limit, indicating that the two-photon field is entangled in both transverse directions.

Variances	Experimental value
$\Delta^2(x_i - x_j)$	$(145 \pm 1)\mu m^2$
$\Delta^2(y_i - y_j)$	$(143 \pm 1)\mu m^2$
$\Delta^2(px_i + px_j)$	$(5.53 \pm 0.06) \times 10^{-6} \hbar^2 \mu m^{-2}$
$\Delta^2(py_i + py_j)$	$(4.06 \pm 0.05) \times 10^{-6} \hbar^2 \mu m^{-2}$

Table 4.1: *Experimental values for the marginal correlation variances as shown in Figure 4.23*

4.3.3 *Conditional correlations*

From the same set of thresholded images, the joint probability distributions for the x' and y' coordinates in the image plane and far-field of the nonlinear crystal can be calculated. Figures 4.24(a) and Figure 4.24(b) show the coincidence counts in the planes (x'_1, x'_2) and (y'_1, y'_2), while Figure 4.24(c) and Figure 4.24(d) show the coincidence counts in the planes (px'_1, px'_2) and (py'_1, py'_2). In the y' direction, a strong correlation resulting from charge smearing can be observed, as shown in Figure 4.24 (b). This strong correlations prevents any meaningful analysis from the image plane measurements. However, the expected anti-correlation in the far-field (Figure 4.24 (d)) is still evident. Therefore the following analysis will only be performed in the x' axis. It has been shown that EPR-like correlations can be identified by violating the inequality [4.43, 4.44]

$$\Delta^2_{min}(x'_1|x'_2)\Delta^2_{min}(px'_1|px'_2) \geq \frac{\hbar^2}{4}, \tag{4.7}$$

where $\Delta^2_{min}(r_1|r_2)$ is the minimum inferred variance, describing the minimum uncertainty in measuring variable r_1 conditional on the measurement of variable r_2. The minimum inferred variance for the x'- coordinates in the far-field is defined as:

$$\Delta^2_{min}(px'_1|px'_2) = \int P(px'_2)\Delta^2(px'_1|px'_2)dpx'_2 \tag{4.8}$$

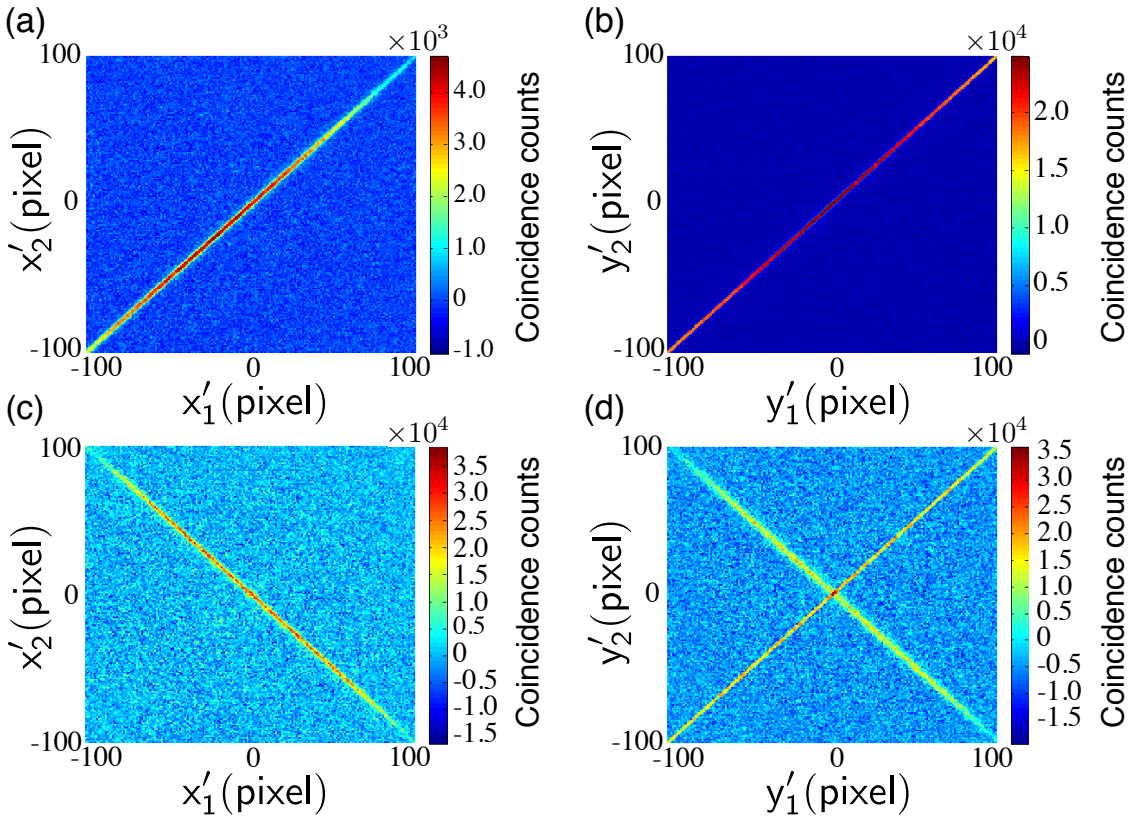

Figure 4.24: *Joint probability distributions for x' and y' coordinates. The probability distributions for joint detections in both x' and y' coordinates in the image plane (a)+(b) and far-field (c)+(d) are shown respectively. Charge smearing gives rise to an artificial correlation in the y' direction (b)+(d).*

The minimum inferred variance for the x'- coordinates in the image plane of the nonlinear crystal is defined with a similar approach:

$$\Delta^2_{min}(x_1'|x_2') = \int P(x_2')\Delta^2(x_1'|x_2')dx_2' \tag{4.9}$$

By fitting Gaussians to the joint probabilities on the x' direction, as shown in Figure 4.24(a) and Figure 4.24(c), the variances shown in Table 4.2 were obtained. Substituting these variances into Equation (4.7) gives:

$$\Delta^2_{min}(x_1'|x_2')\Delta^2_{min}(px_1'|px_2') = (6.6 \pm 1.0) \times 10^{-4}\hbar^2, \tag{4.10}$$

and

$$\Delta^2_{min}(x_2'|x_1')\Delta^2_{min}(px_2'|px_1') = (6.2 \pm 0.9) \times 10^{-4}\hbar^2, \tag{4.11}$$

indicating that the transverse Degrees of Freedom (DOF) of the two photon field exhibits its EPR non-locality. This result is in good agreement with the theoretical prediction (from Equation (4.2) and Equation (4.9)) of $\approx 3 \times 10^{-4}\,\hbar^2$ and, although performed with

background subtraction, is an order of magnitude smaller than those in References [4.27, 4.31].

Variances	Experimental value
$\Delta^2_{min}(x'_1\|x'_2)$	$(119 \pm 15)\mu m^2$
$\Delta^2_{min}(x'_2\|x'_1)$	$(119 \pm 15)\mu m^2$
$\Delta^2_{min}(px'_1\|px'_2)$	$(5.5 \pm 0.04) \times 10^{-6}\hbar^2\mu m^{-2}$
$\Delta^2_{min}(px'_1\|px'_2)$	$(5.2 \pm 0.04) \times 10^{-6}\hbar^2\mu m^{-2}$

Table 4.2: *Experimental values for the conditional correlation variances as shown in Figure 4.24*

If the background was included in the data, it would lead to an overestimation of the standard deviations of the correlations. Furthermore, to satisfy non-locality, the measurement of each photon must be performed outside the light-cone of its entangled partner. This issue could be solved in a modified set-up in which the photon pairs are split and sent to two spatially separated cameras. However, our results are in close agreement with the theoretical predictions, providing evidence that EMCCD technology can already be used in the characterisation of spatial correlations of photons. Moreau *et al.* [4.45, 4.46] performed a similar experiment with a type−II BBO crystal, where the differently polarised down-converted photons were separated and the correlations were measured in two separate parts of the same EMCCD camera. They also measured EPR-like correlations. However their variance product for the position-difference and momentum-sum was $(0.06 \pm 0.01)\hbar^2$, which is two orders of magnitude larger than the variance product obtained in this experiment.

4.3.4 *Dimensionality*

From the joint distributions in Figure 4.24 the ratio (σ_+/σ_-) for the x and y transverse DOF can be estimated for the image plane (IP) and far-field (FF). The maximum number of joint detections for the position and momentum measurements are defined as:

$$D^{max}_{pos} = \left[\left(\frac{\sigma x'_+}{\sigma x'_-}\right)\left(\frac{\sigma y'_+}{\sigma y'_-}\right)\right]_{IP} \tag{4.12}$$

and

$$D^{max}_{mom} = \left[\left(\frac{\sigma x'_-}{\sigma x'_+}\right)\left(\frac{\sigma y'_-}{\sigma y'_+}\right)\right]_{FF} \tag{4.13}$$

Figure 4.25 shows an example for the determination of $\sigma x'_+$ and $\sigma x'_-$ for the position

measurement *along* the $x'-$ coordinates. The data shown was extracted from Figure 4.24(a). $\sigma x'_+$ is the standard deviation from the Gaussian fit along the diagonal starting at the $x'-$ coordinates (-100, -100) and ending at (100, 100). Because the camera does not possess photon number resolving capabilities, and therefore the values for Δx were previously set to 0, the values used here are the mean value calculated from the neighbouring pixels. $\sigma x'_-$ is the standard deviation of the Gaussian fit *across* the diagonal as shown in Figure 4.25(b).

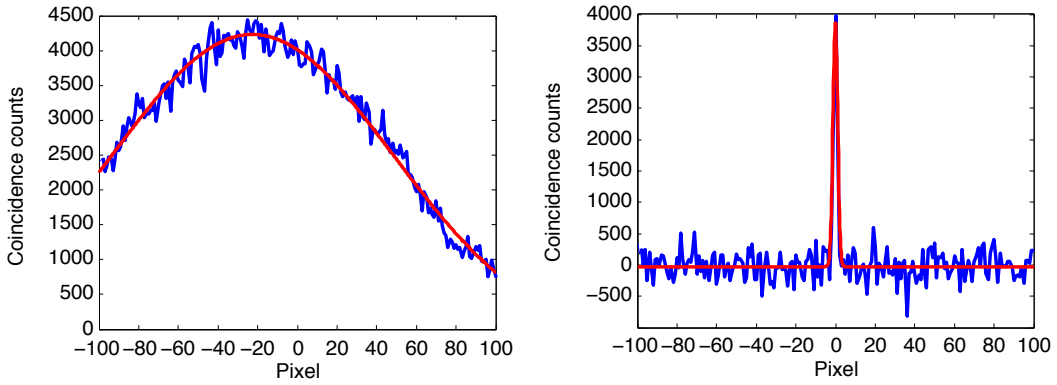

(a) Position - $x'-$ coordinates - State length (b) Position - $x'-$ coordinates - State width

Figure 4.25: *State length (a) and state width (b) for a position measurement showing the $x'-$ coordinates. The blue line represents the measured data, while the red line shows the Gaussian fit. The measured data was taken from Figure 4.24(a). The state length can be determined by fitting a Gaussian along the diagonal, while the state width can be determined by fitting a Gaussian across the diagonal.*

Substituting the experimental values from Table 4.3 into Equation (4.12) gives a maximum number of joint detections in the image plane of $D_{\text{pos}}^{\max} = 3491$ and inserting the values from the far-field measurement into Equation (4.13) gives $D_{\text{mom}}^{\max} = 3065$. Because of charge smearing in the image plane measurement, the max number of joint detections in y' was estimated based on that of the x' dimension, which was supported by the circular symmetry of Figure 4.22(a).

Position measurement			Momentum measurement		
Plane	Type	Experimental value	Plane	Type	Experimental value
IP	$\sigma x'_+$	70.9 pixels	FF	$\sigma x'_-$	73.7 pixels
IP	$\sigma x'_-$	1.2 pixels	FF	$\sigma x'_+$	1.4 pixels
IP	$\sigma y'_+$	70.9 pixels	FF	$\sigma y'_-$	99.0 pixels
IP	$\sigma y'_-$	1.2 pixels	FF	$\sigma y'_+$	1.7 pixels

Table 4.3: *Experimental values for $D^{\max}$ for the image plane (IP) and far-field (FF). Due to charge smearing in the y' direction in the image plane measurement, the state length and width were estimated based on the x' direction.*

Due to the finite size of the EMCCD camera, not all states were accessible by the detector. The proportion of the beam measured by the finite detector array was calculated by integrating the fitted Gaussian functions of the state length over the array size and comparing these results to integrating the Gaussian functions over an infinite array. In all cases, more than 85% of the available states were accessible. The measured dimensionality in position and momentum were found to be $D_{pos} = D_{pos}^{max} \times 0.95^2 \approx 3150$ and $D_{mom} = D_{mom}^{max} \times 0.95 \times 0.85 \approx 2500$, respectively. To the best of our knowledge this represents the largest dimensionality for any experiment using entangled spatial states of photons.

4.4 Conclusion

In this chapter, the theoretical background for charge coupled devices was described. The CCD cameras were introduced by explaining MOS capacitors and the charge transport for a basic full-frame camera and more sophisticated frame-transfer cameras, as used in the experiment. EMCCD cameras are essentially CDD cameras with an additional multiplication register, providing single-photon sensitivity. The different sources of camera noise and techniques for minimising the noise were outlined. The advantages of using an EMCCD camera compared to fibre detectors or SPAD arrays were described as well.

The experimental setup was described for the position and momentum correlation measurements. The camera settings were optimised for the smallest amount of camera generated noise, by increasing the vertical shift rate and by minimising the horizontal pixel read-out speed. The camera was operated at a temperature of $\approx -85\,^{\circ}\mathrm{C}$ in order to be able to minimise the amount of dark current. In order to eliminate ENF, a binary thresholding technique was used. By setting a sufficiently high threshold the read-out noise was minimised. The optimised threshold setting was characterised in terms of camera read-out characteristics and the SNR of the of the correlation peak. For both characterisations, the optimal threshold setting was found to be 6 counts above background. Mainly CIC were present during the measurements, as they possess the same read-out values as the real photon events. The exposure times for the position and momentum measurements were different, in order to match the photon flux. The ideal

photon flux was found to be 0.02 photons pixel^{-1}/frame, which was the same amount as noise events in each frame.

The images were processed and analysed with specifically designed LabView programs. For the position measurement, the position difference for the photons locations was calculated. Due to the lack of photon number resolving capabilities of the camera, the position for $\Delta x' = \Delta y' = 0$ was neglected in the data analysis. Because of the charge smearing in the $y'-$axis, the positions $y' = \pm 1$ were disregarded as well, as a high number of correlations which were not of quantum nature masked the correlations of quantum nature. For the momentum measurement the momentum-sum was calculated and no pixels were rejected. For background correction, each frame was correlated with the previous one to determine the reference correlations. In order to test if the measured correlations were of quantum nature or an artefact of the camera, a second set of position and momentum measurements was recorded, this time with a pseudo-classical light source. By inserting an ND-filter into the SPDC path, the number of correlated photon pairs was greatly reduced and consequently only very few correlations of quantum nature were recorded in these measurements.

After background correction the variance product for the position- difference and the momentum- sum was calculated for two different sets of orthogonal bases. As the $y'-$axis was compromised by charge smearing the variance products for the x and y orthogonal basis set are given: $\Delta^2 x_- \Delta^2 p x_+ = (8.9 \pm 0.1) \times 10^{-4} \hbar^2$ and $\Delta^2 y_- \Delta^2 p y_+ = (6.5 \pm 0.1) \times 10^{-4} \hbar^2$, which are both three orders of magnitude below the classical limit of separability indicating quantum behaviour of the photon pairs.

The conditional correlations for the $x'-$ and $y'-$ axes were calculated from background corrected data. For subsequent data analysis only the $x'-$axis can be used due to charge smearing issues in the $y'-$axis. Fitting Gaussians to the joint-probabilities gives

$$\Delta^2_{min}(x'_1|x'_2)\Delta^2_{min}(px'_1|px'_2) = (6.6 \pm 1.0) \times 10^{-4}\hbar^2$$

and

$$\Delta^2_{min}(x'_2|x'_1)\Delta^2_{min}(px'_2|px'_1) = (6.2 \pm 0.9) \times 10^{-4}\hbar^2,$$

indicating that the transverse degrees of freedom of the two photon field exhibits EPR non-locality. It has to be acknowledged that the performed experiment does not meet the strong requirements for non-locality test, as the data was background-corrected

and the measurements of the entangled photons were not performed outside the light cone of their entangled partners.

The dimensionality was calculated from the joint distributions for the x and y transverse degrees of freedom. The measured dimensionality in position and momentum were found to be $D_{pos} \approx 3200$ and $D_{mom} \approx 2500$, respectively. To the best of our knowledge this represents the largest dimensionality for any experiment using entangled spatial states of photons.

4.5 References

[4.1] G. E. Smith and W. S. Boyle. 'Citation Classic - Charge coupled semiconductor-devices'. CC/ Eng. Tech. Appl. Sci., Vol. 29, (1982), p. 190 (cited on page: 109).

[4.2] G. F. Amelio, M. F. Tompsett and G. E. Smith. 'Experimental verification of the charge coupled device concept'. Bell Syst. Tech. J., Vol. 49, (1970), pp. 593–600 (cited on page: 109).

[4.3] *The Nobel Prize in Physics 2009*. online, last accessed 2013-02-13. URL: http://www.nobelprize.org/nobel%5C_prizes/physics/laureates/2009/index.html (visited on 13/02/2013) (cited on page: 109).

[4.4] C. C. Hu. *Modern Semiconductor Devices for Integrated Circuits*. 1st edition. Prentice Hall, 2009 (cited on page: 109).

[4.5] G. E. Smith. 'The invention and early history of the CCD'. J. Appl. Phys., Vol. 109, (2011), p. 102421 (cited on page: 110).

[4.6] B. G. Streetman and S. Banerjee. *Solid State Electronic Devices*. 6th edition edition. Prentice Hall Series in Solid State Physical Electronics. Pearson Prentice Hall, 2006 (cited on pages: 110, 112, 118).

[4.7] R. H. Walden, R. H. Krambeck, R. J. Strain, J. McKenna, N. L. Schryer and G. E. Smith. 'The buried channel charge coupled device'. Bell System Technical Journal, (1972), pp. 1635–1640 (cited on page: 111).

[4.8] J. B. Pawley. *Handbook of Biological Confocal Microscopy*. 3rd edition. Springer, 2006 (cited on pages: 111, 115).

[4.9] J. Wilson and J. F. B. Hawkes. *Optoelectronics: an introduction*. 3rd edition. Prentice Hall Europe, 1998 (cited on page: 111).

[4.10] *Kodak Image Sensors - Users Manual*. online, last accessed 2013-02-07. Kodak, (2008). URL: http://www.kodak.com/ek/uploadedFiles/chargeCoupledDevices.pdf (cited on page: 112).

[4.11] *Introduction to Charge-Coupled Devices (CCDs)*. online, last accessed 2013-02-13. URL: http://www.microscopyu.com/articles/digitalimaging/ccdintro.html (cited on page: 112).

[4.12] O. Daigle, O. Djazovski, D. Laurin, R. Doyon and É. Artigau. 'Characterization results of EMCCDs for extreme low-light imaging'. *Proc. SPIE 8453, High En-*

ergy, Optical, and Infrared Detectors for Astronomy V. (2012), p. 845303 (cited on pages: 113, 114).

[4.13] Andor Technology. *Hardware Guide - Andor iXon3*. DVD - supporting documentation for purchased EMCCD camera. Andor Technology, (2011) (cited on pages: 115, 117, 119, 126).

[4.14] Hamamatsu. *Characteristics and use of FFT-CCD area image sensor*. online, last accessed 2013-03-07. URL: http://people.na.infn.it/~garufi/didattica/CorsoAcq/Trasp/Lezione3/Characteristics_and_use_of__FFT-CCD.pdf (cited on page: 116).

[4.15] Hamamatsu. *EM-CCD Technical Note*. online, last accessed 2013-03-08. URL: http://www.hamamatsu.com/resources/pdf/sys/e_imagemtec.pdf (cited on pages: 116, 117).

[4.16] *ProEM+ Performance | Precision | Peace of Mind*. online, last accessed 2013-02-11. Princeton Instruments, (2012). URL: http://www.princetoninstruments.com (cited on pages: 116, 119).

[4.17] Nüvü Cameras. *EMCCD Tutorial - Understanding underlying principles | Nüvü Cameras*. online, last accessed 2013-02-13. URL: http://www.nuvucameras.com/emccd-tutorial/ (cited on pages: 118, 119).

[4.18] Andor Technology. *iXon+ Back-illuminated EMCCD - Technical Article from Andor Technology*. online, last accessed 2011-05-02. Andor Technology, (2006). URL: http://www.microimage.com.cn/uploadfile/xwjs/uploadfile/201009/20100915021449671.pdf (cited on pages: 118, 126, 127).

[4.19] *HNü 512 - data sheet*. online, last accessed 2013-02-04. Nüvü Cameras, (2013). URL: http://www.nuvucameras.com/wp-content/uploads/2013/01/Nuvu-Cameras-HNu-512-Specsheet.pdf (cited on pages: 119, 120).

[4.20] Andor Technology. *Andor iXon3 897 Specifications*. online, last accessed 2011-09-26. (2011). URL: http://www.andor.com/pdfs/specifications/Andor_iXon_897_Specifications.pdf (cited on pages: 119, 122).

[4.21] Andor Technology. *Andor iXon3 EMCCD Brochure*. online, last accessed 2013-02-11. Andor Technology, (2012). URL: http://www.andor.com/pdfs/literature/Andor%5C_iXon3%5C_EMCCD%5C_Brochure.pdf (cited on page: 120).

[4.22] *EMN2 512 - data sheet*. online, last accessed 2012-05-07. Nüvü Cameras, (2011). URL: http://www.nuvucameras.com/wp-content/uploads/2013/01/Nuvu-Cameras-EM-N2-512-Specsheet.pdf (cited on page: 120).

[4.23] Hamamatsu. *Electron Multiplying CCD camera C9100-13, -14*. online, last accessed 2013-02-13. (2012). URL: http://jp.hamamatsu.com/resources/products/sys/pdf/eng/e%5C_c910013.pdf (cited on page: 120).

[4.24] *ImagEM X2*. online, last accessed 2013-02-11. Hamamatsu, (2013). URL: http://hamamatsucameras.com/assets/pdfs/e%5C_c910023b.pdf (cited on page: 120).

[4.25] *ProEM+_ 512B_and_512BK_eXcelon3*. online, last accessed 2013-02-11. Princeton Instruments, (2012). URL: http://www.princetoninstruments.com (cited on page: 120).

[4.26] Perkin Elmer. *SPCM - AQRH Single Photon Counting Module - data sheet*. online, last accessed 2011-05-02. Perkin Elmer, (2007). URL: http://www.perkinelmer.co.uk/PDFS/downloads/dts_spcm%20aqrh.pdf (cited on page: 120).

[4.27] J. C. Howell, R. S. Bennink, S. J. Bentley and R. W. Boyd. 'Realization of the Einstein-Podolsky-Rosen paradox using momentum- and position-entangled photons from spontaneous parametric down conversion'. Phys. Rev. Lett., Vol. 92, (2004), p. 210403 (cited on pages: 120, 138).

[4.28] M. D'Angelo, Y.-H. Kim, S. P. Kulik and Y. Shih. 'Identifying entanglement using quantum ghost interference and imaging'. Phys. Rev. Lett., Vol. 92, (2004), p. 233601 (cited on page: 120).

[4.29] J. Leach, R. E. Warburton, D. G. Ireland, F. Izdebski, S. M. Barnett, A. M. Yao, G. S. Buller and M. J. Padgett. 'Quantum correlations in position, momentum, and intermediate bases for a full optical field of view'. Phys. Rev. A, Vol. 85, (2012), p. 013827 (cited on page: 120).

[4.30] *A darker view - Debris*. online, last accessed 2013-03-11. URL: http://darkerview.com/CCDProblems/debris.php (cited on page: 123).

[4.31] D. S. Tasca, S. P. Walborn, P. H. Souto Ribeiro, F. Toscano and P. Pellat-Finet. 'Propagation of transverse intensity correlations of a two-photon state'. Phys. Rev. A, Vol. 79, (2009), p. 033801 (cited on pages: 124, 138).

[4.32] C. K. Law and J. H. Eberly. 'Analysis and interpretation of high transverse entanglement in optical parametric down conversion'. Phys. Rev. Lett., Vol. 92, (2004), p. 127903 (cited on page: 124).

[4.33] C. H. Monken, P. H. Souto Ribeiro and S. Pádua. 'Transfer of angular spectrum and image formation in spontaneous parametric down-conversion'. Phys. Rev. A, Vol. 57, (1998), pp. 3123–3126 (cited on page: 124).

[4.34] K. W. Chan, J. P. Torres and J. H. Eberly. 'Transverse entanglement migration in Hilbert space'. Phys. Rev. A, Vol. 75, (2007), 050101(R) (cited on page: 124).

[4.35] M. P. Edgar, D. S. Tasca, F. Izdebski, R. E. Warburton, J. Leach, M. Agnew, G. S. Buller, R. W. Boyd and M. J. Padgett. 'Imaging high-dimensional spatial entanglement with a camera'. Nat. Commun., Vol. 3, (2012), p. 984 (cited on pages: 125, 129).

[4.36] Andor Technology. *iXonEM+ Software Guide*. DVD - supporting documentation for purchased EMCCD camera. Andor Technology, (2011) (cited on page: 128).

[4.37] E. Lantz, J.-L. Blanchet, L. Furfaro and F. Devaux. 'Multi-imaging and Bayesian estimation for photon counting with EMCCDs'. Mon. Not. R. Astron. Soc., Vol. 386, (2008), pp. 2262–2270 (cited on page: 128).

[4.38] S. S. R. Oemrawsingh, W. J. van Drunen, E. R. Eliel and J. P. Woerdman. 'Two-dimensional wave-vector correlations in spontaneous parametric downconversion explored with an intensified CCD camera'. J. Opt. Soc. Am. B: Opt. Phys., Vol. 19, (2002), pp. 2391–2395 (cited on page: 132).

[4.39] B. M. Jost, A. V. Sergienko, A. F. Abouraddy, B. E. A. Saleh and M. C. Teich. 'Spatial correlations of spontaneously down-converted photon pairs detected with a single-photon-sensitive CCD camera'. Opt. Express, Vol. 3, (1998), pp. 81–88 (cited on page: 132).

[4.40] A. F. Abouraddy, M. B. Nasr, B. E. A. Saleh, A. V. Sergienko and M. C. Teich. 'Demonstration of the complementarity of one- and two-photon interference'. Phys. Rev. A, Vol. 63, (2001), p. 063803 (cited on page: 132).

[4.41] S. Mancini, V. Giovannetti, D. Vitali and P. Tombesi. 'Entangling macroscopic oscillators exploiting radiation pressure'. Phys. Rev. Lett., Vol. 88, (2002), p. 120401 (cited on page: 134).

[4.42] L. M. Duan, G. Giedke, J. I. Cirac and P. Zoller. 'Inseparability criterion for continuous variable systems'. Phys. Rev. Lett., Vol. 84, (2000), pp. 2722–2725 (cited on page: 134).

[4.43] M. D. Reid, P. D. Drummond, W. P. Bowen, E. G. Cavalcanti, P. K. Lam, H. A. Bachor, U. L. Andersen and G. Leuchs. 'Colloquium: The Einstein-Podolsky-Rosen paradox: From concepts to applications'. Rev Mod Phys, Vol. 81, (2009), pp. 1727–1751 (cited on page: 136).

[4.44] M. D. Reid. 'Demonstration of the Einstein-Podolsky-Rosen paradox using nondegenerate parametric amplification'. Phys. Rev. A, Vol. 40, (1989), pp. 913–923 (cited on page: 136).

[4.45] F. Devaux, J. Mougin-Sisini, P. A. Moreau and E. Lantz. 'Towards the evidence of a purely spatial Einstein-Podolsky-Rosen paradox in images: measurement scheme and first experimental results'. Eur. Phys. J. D, Vol. 66, (2012), p. 192 (cited on page: 138).

[4.46] P.-A. Moreau, J. Mougin-Sisini, F. Devaux and E. Lantz. 'Realization of the purely spatial Einstein-Podolsky-Rosen paradox in full-field images of spontaneous parametric down-conversion'. Phys. Rev. A, Vol. 86, (2012), 010101(R) (cited on page: 138).

CHAPTER 5

LOW-LIGHT LEVEL CONTRAST ENHANCEMENT WITH CORRELATED PHOTONS

In this chapter, the contrast enhancement when utilising a light source emitting photon pairs in extreme low-light level imaging was measured, and simulated, for different probabilities of the emitted photon pairs to arrive in adjacent pixels. In order to avoid counting false correlations arising from charge smearing during the camera read-out, and to minimise the amount of recorded background, a pair detection algorithm was developed. Using the pair detection algorithm on its own enhances the contrast of the recorded image by a factor of $\times 1.54$, and the Signal-to-Noise-Ratio (SNR) and the Signal-to-Background-Ratio (SBR) are improved by a factor of $\times 1.66$ and $\times 1.81$, respectively. Using the pair detection algorithm in combination with a simulated correlated photon source, for which the correlated photon pairs have a probability of 25% to arrive in adjacent pixels, the contrast is enhanced by a factor of $C_C = 1.95$, while the SNR and SBR are improved by a factor of $SNR_C = 3.1$ and $SBR_C = 3.33$ respectively compared to the raw data for a camera with 0.02 dark counts pixel^{-1} /frame. For a camera with a low noise level and a high probability of 25% for the photons of a pair to arrive in adjacent pixels and the pair detection algorithm, the contrast is enhanced by a factor of $C_C = 2.71$, while the SNR and SBR are improved by a factor of $SNR_C = 4.74$ and $SBR_C = 9.55$ respectively, compared to the raw data.

5.1 Theoretical Background

The theoretical background concerning the generation of correlated photon pairs through Spontaneous Parametric Down-Conversion (SPDC) and the nonlinear crystal used in this process can be found in Sections 3.1.1 and 3.1.2. EMCCDs have been

explained in detail in Section 4.1. In this section, a short revision of the different types of camera noise will be given and the pair detection algorithm will be introduced.

5.1.1 *Noise in EMCCD cameras*

In order to obtain images with a high contrast, the overall noise level must be minimised. In EMCCD cameras three different types of noise are usually present. *Thermal noise* (also know as dark current) is caused by the thermal excitation of electrons. The thermal noise is temperature dependent and scales with the exposure time. The thermally excited electrons will slowly fill up the potential wells of the pixels, giving the false impression that the camera is exposed to a faint light source. Sufficiently cooling the camera will virtually eliminate any dark current [5.1, p. 8]. The second type of noise is the *read-out noise*. The read-out noise is mainly caused by the output amplifier and digitisation electronics. The read-out noise sets the minimum signal level that can be detected by the camera, as any signal below this electronic noise floor will be indistinguishable from the read-out noise. The read-out noise can be minimised by applying a threshold to each pixel of the camera as shown in Sections 4.2.4 and 5.1.2. The main source of noise present in the EMCCD camera are *Clock-Induced-Charges* (CIC), which is electrical noise caused by the vertical pixel shift during read-out [5.2, p. 36]. As shown in Section 5.1.2 this type of noise possesses the same number of output electrons as a photon event, and therefore CIC are indistinguishable from real photon events.

5.1.2 *Identifying photons and photon pairs*

In order to distinguish photons from noise, the output of the camera was characterised. The EMCCD camera was affected by different noise phenomena as mentioned in the previous section. in order to characterise the noise, the camera was operated at maximum gain and 10,000 images were recorded with the shutter open while the pump laser was blocked. The EMCCD camera was located in a light-tight environment to minimise the amount of ambient light.

By comparing the output level per pixel against the number of pixels, an analysis similar to Ref. [5.3] was performed. A Gaussian distribution of read-out noise, centred at a value of 390 counts with a standard deviation σ_{noise} = 6 counts [5.4] and in ad-

dition a long tail that decreased exponentially for higher read-out values, as seen in Figure 5.1, were found. This exponentially decaying tail was caused by CIC and could not be distinguished from single-photon events, as these possessed similar read-out values. Before each measurement, a background measurement with the pump laser blocked in order to determine the mean read-out value for every individual pixel in the region of interest was taken. For the measurements, a binary thresholding by assigning a "1" to each pixel which had a greater read-out value than σ_{noise} plus the mean background level for the pixel was used. A "0" was assigned to all pixels with a smaller value to minimise the read-out noise was used.

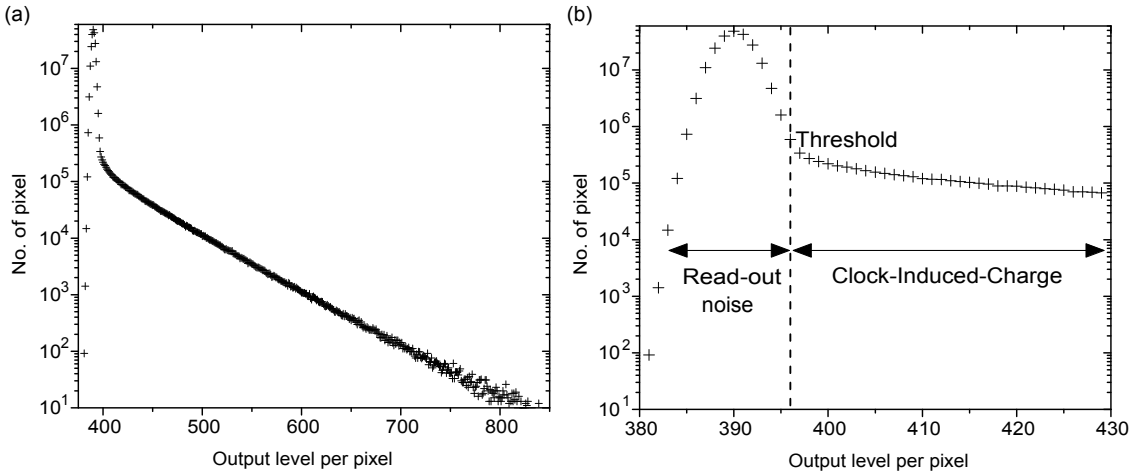

Figure 5.1: *(a) EMCCD camera noise characteristics after 10,000 recorded images. (b) Rescaled EMCCD camera read-out characteristics after 10,000 recorded images showing read-out noise, Clock-Induced-Charge and the threshold setting.*

Furthermore, a suitable mechanism was required for identifying photon pairs. The camera is not capable of unambiguously distinguishing one photon from two photons incident on a single pixel, thus in order to detect a correlated photon pair, the photons had to be detected by two different pixels. One approach to accomplish this was to increase the correlation length of the photon pair at the plane of the camera, $\sigma_{pos} = M\sqrt{\frac{\alpha L\lambda_p}{2\pi}}$, where $\alpha = 0.455$ is an adjustment constant [5.5], L is the length of the non-linear crystal and λ_p is the wavelength of the pump photons. The correlated photons can be detected by changing the magnification M of the imaging system and therefore increasing the correlation length of the photon pairs, and by measuring correlations that occur at separations ≥ 1 pixel [5.4]. Alternatively, it would have been possible to use a type−II BBO crystal and to separate the differently polarised signal and idler photons with a Wollaston prism, while identifying correlations in two separate regions of interest on the camera [5.6]. However, no type−II BBO crystal was available.

One limitation of EMCCD technology is the presence of charge smearing between pixels, a consequence of the readout mechanism. When the charge of a pixel was not fully removed after a pixel shift, the charge that was left behind was added to the following pixel, and resulted in additional correlations in the y-axis. Any method to identify photon pairs in the images acquired should thus account for charge smearing in the y-axis, yet should enable the measurement of correlated photons in adjacent pixels, for which the strength of the correlation is expected to be greatest. With these considerations, a pair detection algorithm (see Figure 5.2) was applied to each pixel with a registered event in every image to be able to identify photon pairs. In order to avoid false correlations caused by charge smearing, any events recorded in the same column as the initial event were excluded. It is worth noting that there was a probability for photons to be measured at greater separations than 1 pixel, however the level of camera noise of approximately 0.02 dark counts pixel^{-1} /frame prevented this in the analysis. Measuring correlated photons in greater separations resulted in many more false event correlations being counted: those between photons from different pairs, a photon and a noise event, and between two noise events.

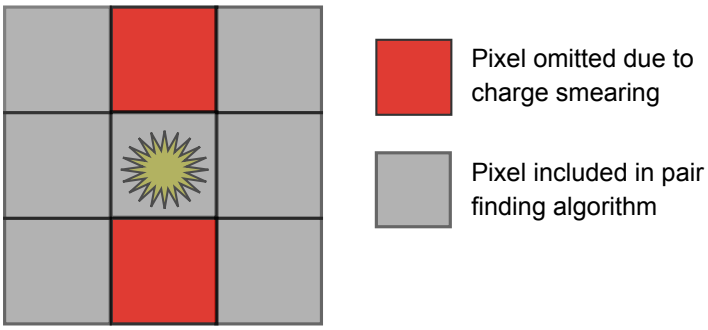

Figure 5.2: *Schematic representation of the pair detection algorithm used to identify photon pairs arriving in adjacent pixels. Grey pixels denote locations where the detection of another event will result in a pair being counted. Red pixels are omitted by the pair detection algorithm to remove the effects of charge smearing, as described in the text.*

5.2 Experiment

In this section, the experimental setup used to measure the contrast enhancement will be detailed. The correlated photons were created through SPDC. In order to investigate the benefit of using a correlated light source, an uncorrelated light source was built by inserting a neutral density filter into the SPDC beam path. The neutral density filter reduced the probability of detecting photon pairs due its low transmission efficiency.

5.2.1 *Experimental setup*

The experimental setup used to measure the low-light contrast enhancement with correlated light is shown in Figure 5.3. The pump laser was a frequency-tripled passively mode-locked Nd:YAG laser emitting at $\lambda \approx 355$ nm with a pulse repetition rate of 100 MHz. The average output power of 150 mW was attenuated to 2 mW with neutral density (ND) filters. The diameter d_p of the Gaussian pump beam was expanded to $d_p = 1.32 \pm 0.05$ mm. The correlated photon pairs were created by SPDC. The nonlinear crystal used was a 5 mm long type-I β-barium borate (BBO) crystal cut for the generation of degenerate down-converted photons at $\lambda = 710$ nm. The crystal was angled to provide a near-collinear output. The crystal was imaged onto the sample with an imaging system comprising two lenses with focal lengths of 50 mm and 150 mm, providing a magnification of $M = -3$. A standard test target (USAF-1951) with cut-out slits, thus providing a clear optical path, was mounted in the image plane of the crystal where it was then imaged onto the EMCCD camera with a 1 : 1 imaging system consisting of two lenses, each with a focal length of 100 mm. In order to filter the degenerate light spectrally, a bandpass filter with a FWHM of 10 nm and centred at $\lambda = 710$ nm, with a transmission efficiency of 90%, was located in front of the EMCCD camera (Andor iXon3). The EMCCD camera was optimised for visible wavelengths with a back-illuminated array of 512×512 pixels each with a size of 16×16 µm. However, for these experiments a smaller region of interest, measuring 100×100 pixels, was used to improve the read-out time and to increase the frame rate to approximately 10 Hz.

The overall quantum efficiency of detection, without the test target, is the product of detection efficiency of the EMCCD and the transmission efficiencies of the individual optical components. Given our experimental parameters, the predicted single-photon detection efficiency, without the target, was $\eta \approx 75\%$.

In order to investigate the contrast enhancement with the correlated light source, element 1 in group 2 of the standard test target, as indicated by the arrow in Figure 5.3, was uniformly illuminated. This element consisted of three alternating opaque and transparent slits each with a width of 125 µm and a height of 750 µm.

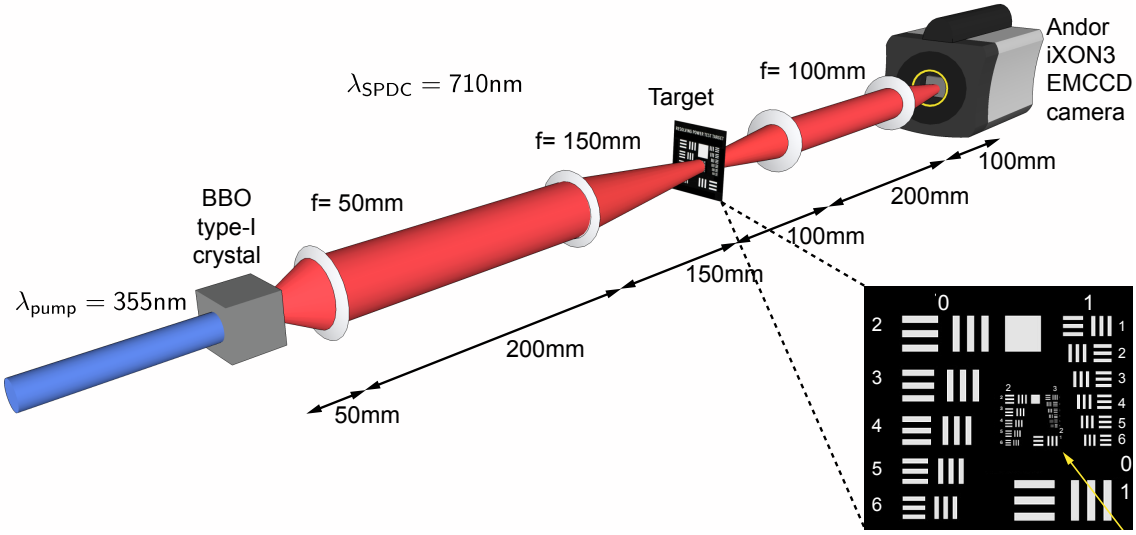

Figure 5.3: *Schematic of the experimental setup used for measuring contrast enhancement. We illuminated element 1 in group 2 of the available test patterns on the clear optical path test target as indicated by the yellow arrow.*

5.2.2 *Acquiring images with correlated and uncorrelated light sources*

The camera was operated at −85 °C with a vertical clock amplitude voltage of +4 above the default factory setting, a horizontal pixel read-out rate of 1 MHz, and a vertical pixel shift every 0.3 µs. The photon flux was chosen to maximise the strength of the position correlation signal relative to noise sources without the target inserted, giving approximately 0.02 photons pixel^{-1} /frame, which was equivalent to the level of noise present in the camera [5.7]. For each recorded image using the correlated photon source, an exposure time of 20 ms was used.

Two different images were acquired in real-time during operation of the experiment; one image was generated from all events and the other image was generated from event pairs determined by the pair detection algorithm. These images were recorded for the same number of frames, which were used for subsequent image analysis. The extent to which any image enhancement was the result of the correlated light source was characterised by comparing these images with those obtained using an uncorrelated light source. In this experiment this was achieved by moving an ND filter from the pump beam into the path of the down-converted photons. In this configuration only 17% of the correlated photons were transmitted by the ND filter. The probability to detect a single-photon, taking the detection efficiency of the camera, the transmission of the 710 nm bandpass filter, the lenses, and the ND filter into account was 12.75%. The probability to detect a correlated photon pair was the square of the probability to de-

tect a single-photon. It is worth noting that the exposure time used to acquire images for the uncorrelated light source was increased to 30 ms to account for the change in transmission efficiency of the ND filter at the different wavelengths (λ = 355 nm and λ = 710 nm).

5.3 Results

In this section, the experimentally obtained results for the contrast measurement for both light sources are compared with the results obtained by numerical simulations.

5.3.1 *Experimental results*

Figure 5.4 shows a normalised and averaged cross-section for the summed images after 12,384 frames were recorded. By comparing the normalised counts, the uncorrelated light without further data processing possessed the highest background. By applying the pair detection algorithm to the uncorrelated light images, the overall background level was reduced, as noise was rejected. By only using the pair detection algorithm, as described in Figure 5.2, the quality of the image can be improved. However, the correlated light source with the pair detection algorithm applied to the images had the lowest background. Figure 5.5 shows a comparison of all experimentally obtained final images without normalisation. It is clear to see that the pair detection algorithm improved the SBR and therefore the contrast of the optical system compared to the raw data.

The final images for the correlated and uncorrelated light sources shown in Figure 5.5(a) and Figure 5.5(c) should ideally possess the same signal height of $\approx$ 540 counts per pixel for the slits. However there is a difference of roughly 90 counts per pixel between these images. This discrepancy can be explained by the different photon fluxes present in the measurements. Assuming the number of dark counts was constant for both measurements, as the camera was operated at similar temperatures, only the number of registered photon events varied. On average, 26 photons per frame were registered in the slit region for the correlated light source, but only 13 photons per frame were registered inside the slits for the uncorrelated light source. Over 12,384

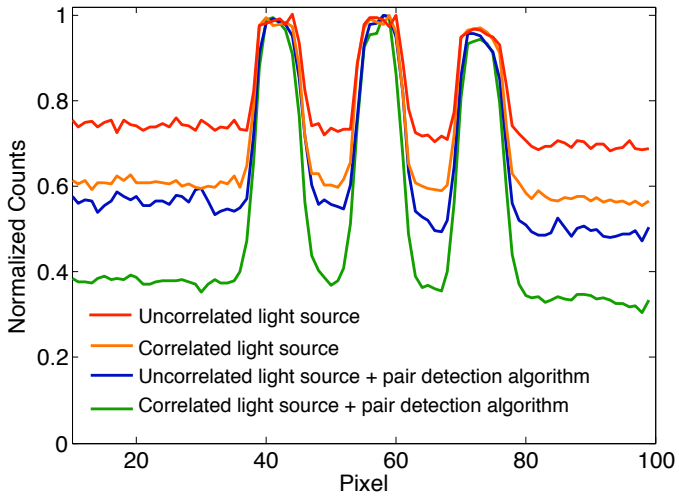

Figure 5.4: *Comparison of the different normalised to peak height image cross-sections after 12,384 frames were taken. The correlated light source with the applied pair detection algorithm has the highest relative peak above background, while the uncorrelated light possesses the smallest peak above background.*

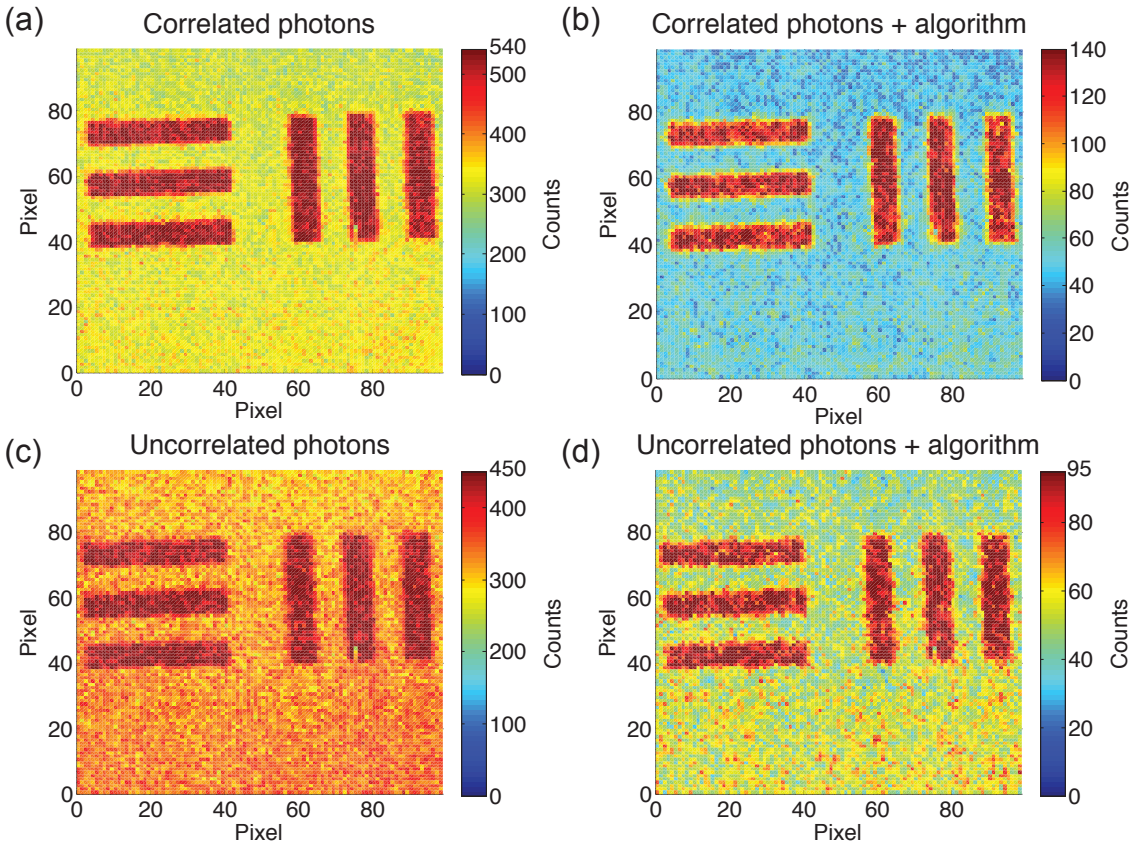

Figure 5.5: *Comparison of final images after 12,384 frames were acquired: correlated light source (top) and uncorrelated light source (bottom) without (left) and with (right) applied pair detection algorithm.*

frames this sums up to 160,092 "missing" photons for the uncorrelated light source, or on average 92 events per pixel. (The slits covered 1749 pixels on the EMCCD camera, excluding hot and dark pixels, which were excluded from the data evaluation.) The mean background for the region outside the slits is ≈ 350 counts per pixel, which needs

to be taken into account, when calculating the total number of events inside the slits. For example, for the correlated light source the signal peak of 540 counts per pixel consists of 350 noise events and 190 real photons.

The average number of events per frame was monitored with the LabView program, but it did not distinguish between events (photons and noise) inside the slits and dark counts outside the slits. The average number of events per frame was 5 counts lower for the uncorrelated light source, compared to the correlated light source. Additionally an increased number of dark counts could have masked the number of real photon events, as well. This could explain the discrepancy of detecting on average 5 events less per frame, while the data evaluation shows that on average 13 photons per frame were "missing".

The number of dark counts depends weakly (≈1 out of 200 noise events for operation temperatures of −85 °C) on the exposure time. Due to the ND filter having different transmission efficiencies at λ_{pump} = 355 nm and λ_{SPDC} = 710 nm, the exposure time was increased from 20 ms for the correlated light source to 30 ms for the uncorrelated light source, in order to maintain roughly the same photon flux for both measurements. Due to the increased exposure time, it was possible to register additional dark counts caused by the dark current, which unlike the CIC depends on the exposure time and is additionally temperature dependent.

Another source of error could have been the operation conditions of the camera *before* the actual measurement. Before the measurement with the correlated light source, the camera was constantly switched on, causing it to stabilise at a slightly higher operational temperature of −85 °C. The background measurement for the thresholding was therefore done at this temperature. Before the start of the measurement with the uncorrelated light source, the camera was in a "stand-by mode" and cooled down to a lower temperature of −87 °C. The background measurement for thresholding was then performed at the slightly lower temperature. During the experiment, the camera temperature increased to its operational temperature of −85 °C and therefore there has been an increase in dark current and there was an increased probability that more pixels possessed read-out values above the threshold, causing slightly more dark counts to be counted towards the number of events per frame. Hence the point at which measurements could have a bearing on the averaged dark count rate.

Ideally, the LabView program should have distinguished between the number of events inside the slits (photons and noise) and outside the slits (only noise), so that the number of events could have been monitored separately. This could have been accomplished by creating a mask after a single long-time exposure of the target and by defining all pixels with a higher than average number of counts as inside the slit or those pixels with a lower number as outside the slits. This mask could then been applied to the running measurement and to monitor the different types of averaged number of events in a frame.

By the time the true significance of an identical photon flux was discovered, the camera was no longer available for this experiment. Therefore the measurements could not been repeated with the same photon flux and with a modified LabView program which was capable of monitoring the number of events inside and outside the slits, within the time-frame of this PhD. However, the simulations resulting from these preliminary measurements did reveal a number of interesting and potentially useful aspects for correlated photons used in imaging applications.

5.3.2 *Numerical simulations*

A computer simulation was written in LabView for a comparison with our experimental results. The simulation was designed to match the measured number of dark counts and photon fluxes used in the experiment for a region of interest measuring 100×100 pixels. In LabView the photon pairs were created with the "Gaussian White Noise Waveform.vi", which is a subroutine provided by the LabView software. This vi creates a Gaussian distributed pseudorandom pattern with a statistical profile of (μ, σ), where μ is the position of the initial pixel and σ is the standard deviation of the Gaussian [5.8]. The probability that the photons of a photon pair arrive in adjacent pixels can be changed by changing the value for the standard deviation of the vi. Figure 5.6 shows the different probability functions to detect photons at different pixels for standard deviations varying from 1 to 6 if one photon is detected at pixel 0.

For a standard deviation of 3 pixels, there is a probability of 13% to detect photons in adjacent pixels. However, the probability to detect two photons in adjacent pixels decreases for higher standard deviations. The "best" fitting simulation for the experimental data was found to be for a setting of 6.4 standard deviations, which corresponds

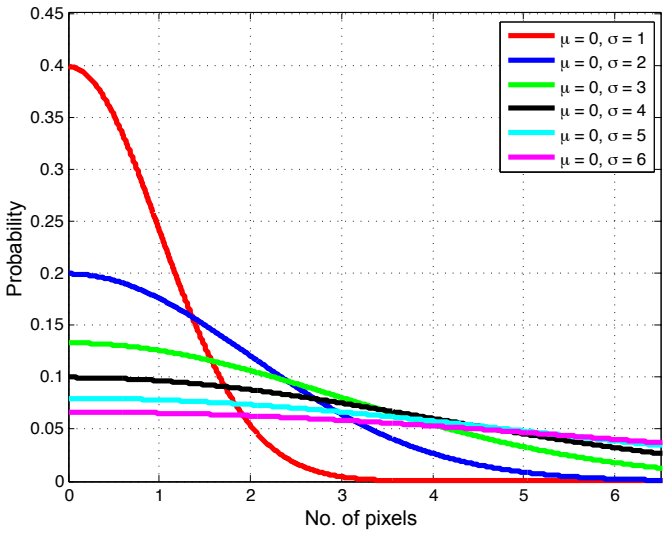

Figure 5.6: *Photon pair distribution for different standard deviations, if one photon is detected at pixel 0.*

to a probability of 6% to detect the partner photons in adjacent pixels and therefore they could be detected by the pair detection algorithm. For a standard deviation of 6.4 pixels it was possible to overlap the simulation with the experimental results for the raw and the processed data for the contrast, SNR, and SBR evaluations. The SBR here is defined as the signal *above* the background level, meaning that a background-subtraction was performed for the signal. The true signal level was then compared to the averaged background level, as shown in Equation (5.3). In the experiment, the probability to detect photon pairs in adjacent pixels depends on the correlation length of the photon pair and any experimental imperfections. For example the position of the first imaging lens after the nonlinear crystal is crucial. In an earlier experiment, similar to Section 4.3.1 and without any target, this lens was placed on an x-stage and the height of the correlation peak after 5000 frames was evaluated for different positions of the lens. Within 0.5 mm displacement from the optimum position, the correlation peak vanished. So even a slight misalignment can cause large losses for the number of recorded correlations.

The simulated intensity profile for the down-converted photons without the target was flat over the entire region of interest, similar to our experiment. The region of interest was smaller than the total area in which the down-converted photons were generated. In 100×100 pixels there were on average 200 photons because our photon flux was approximately 0.02 photons pixel^{-1} /frame. Considering a detection efficiency of 75%, 142 ± 14 photons were detected in an simulated image, when no target was used. However the transmissive slits comprised only 20% of the image. This means 26 ± 6 photons

were detected in an simulated image with the target. The number of dark counts for the simulated correlated light was 254 ± 2 counts per frame. Combining the number of detected photons and the dark counts, 280 ± 6 events were detected in the simulated images, matching the number of events measured in the experiment. For the uncorrelated light source we detected 13 ± 4 photons, when taking the target, the ND-filter in the down-conversion path and therefore the reduced detection efficiency of 12.45% into consideration. The number of dark counts was set to an average number of 254 ± 2 dark counts in an image. On average 267 ± 4 events were registered in each image, matching the measured average number of events for the uncorrelated light source.

The standard deviation for the correlated light source was set to a value of 6.4 pixels, which corresponds to a probability of 6%, that the photons of a pair arrive in adjacent pixels. An in-depth analysis for the dependency of the probability in contrast, SNR, and SBR can be found in Section 5.4.3.

5.3.3 *Comparison of experimental and simulated results*

Due to the different photon fluxes, the contrast, SNR, and SBR of the correlated and uncorrelated light sources with and without additional data processing cannot be compared with each other, as the results for the correlated light source without further data processing should overlap with the results for the unprocessed data of the uncorrelated light source. However, Figure 5.7 clearly shows that this is not the case.

Figure 5.7(a) shows the simulated and measured results for the contrast. The contrast is defined as:

$$C = \frac{n_S - n_B}{n_S + n_B}, \tag{5.1}$$

where n_S is the mean signal and n_B is the mean background. The background was predominantly caused by CIC originating from the read-out process of the EMCCD camera, as photons were not transmitted through the opaque sections of the mask.

Figure 5.7(b) represent the results for the SNR for the experimental data and the numerical simulations for the two different light sources. The SNR is defined as:

$$SNR = \frac{n_S - n_B}{\sigma n_B}, \tag{5.2}$$

where n_S is the mean value of the signal, n_B is the mean background value, and σn_B is the standard deviation of the camera noise.

Figure 5.7(c) shows the Signal to Background ratio. The SBR is defined here as the signal *above* the background:

$$SBR = \frac{n_S - n_B}{n_B} \tag{5.3}$$

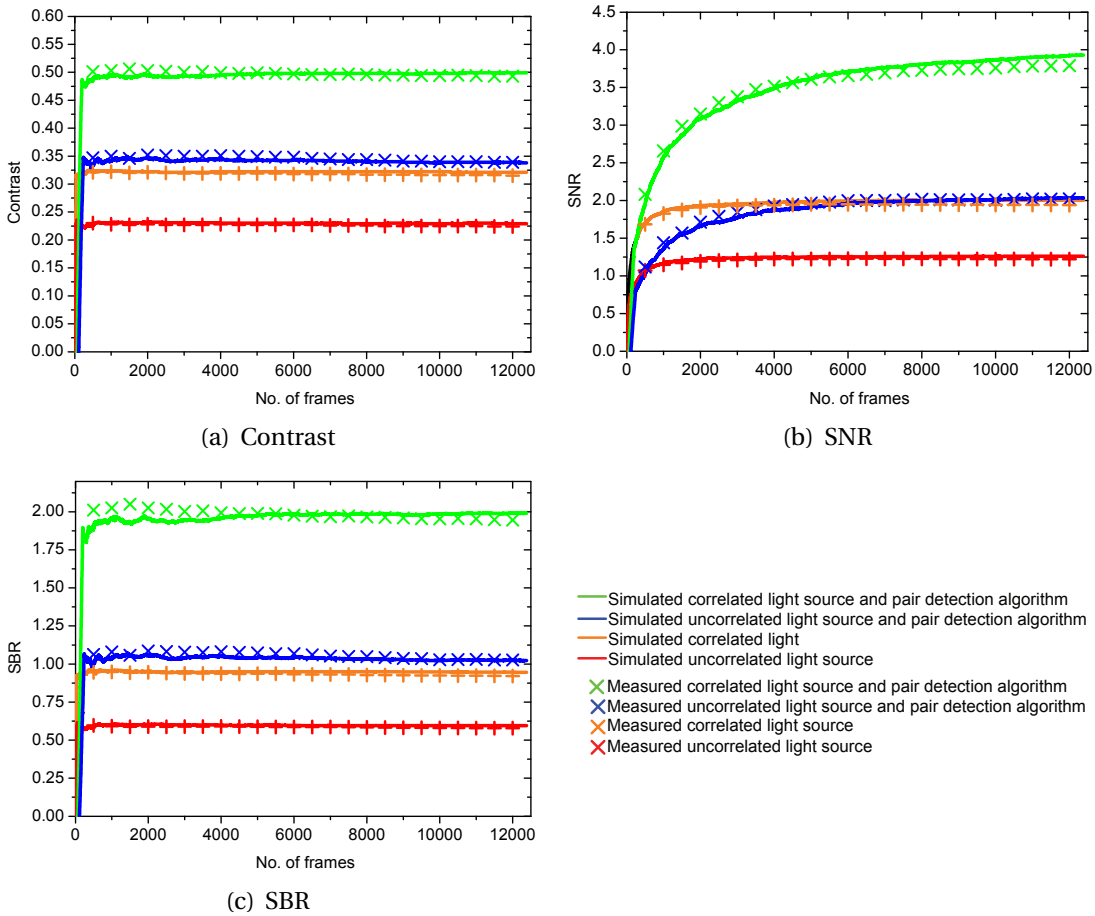

(a) Contrast (b) SNR

(c) SBR

Figure 5.7: *(a) shows the simulated (solid line) and measured contrast for the correlated and uncorrelated light source with and without the pair detection algorithm for different photon fluxes. (b) shows the SNR and (c) represents the SBR for the simulated and measured light sources.*

Type	Contrast	SNR	SBR
Correlated light + algorithm	0.498 ± 0.004	3.794 ± 0.001	1.983 ± 0.030
Correlated light	0.318 ± 0.002	1.942 ± 0.001	0.933 ± 0.008
Uncorrelated light + algorithm	0.346 ± 0.004	2.024 ± 0.001	1.056 ± 0.021
Uncorrelated light	0.226 ± 0.001	1.219 ± 0.001	0.585 ± 0.004

Table 5.1: *Comparison of average contrast and SBR for all, except the first 500, recorded frames and the SNR for the final summed image.*

By comparing the enhancement caused by noise rejection, there is only a small differ-

ence in contrast between the correlated light source and the uncorrelated light source. The contrast ratio between the data processed with the pair detection algorithm and the raw data is $C_C = 1.57$ for the correlated light source, while the contrast ratio for the uncorrelated light source is $C_U = 1.53$. The SNR ratio between the processed and the raw data is $SNR_C = 1.95$ for the correlated light source and the SNR ratio for the uncorrelated light source is $SNR_U = 1.66$. Also the SBR ratio for the correlated light source is higher compared to the uncorrelated light source. For the correlated light source the ratio for the processed and raw data is $SNR_C = 2.13$, while the ratio for the uncorrelated light source is $SNR_U = 1.81$. The difference in ratio for the processed contrast data is almost negligible, as the probability for the photon pair to arrive in adjacent pixels is approximately 6 %. Therefore the correlated light source with the applied pair detection algorithm shows only a slight increase compared to the uncorrelated light source with the pair detection algorithm applied to it.

5.4 Simulations for identical photon fluxes

In the following section the theoretical contrast enhancement was investigated for the correlated and the uncorrelated light source, with both sources having identical photon fluxes and background levels. Additional simulations were run for varying probabilities of the photon pairs to arrive in adjacent pixels and the amount of detector noise was changed, as well.

5.4.1 *Identical photon flux*

As mentioned before, the unprocessed data for the correlated and uncorrelated light sources should overlap. This can be accomplished, when the photon fluxes for both measurements are the same. Here the light sources were simulated with LabView. The number of dark counts were set to 260 and on average 26 photons per frame were registered in both simulations. It was expected that the unprocessed data overlaps in terms of contrast, SNR and SBR. However, the data processed with the pair detection algorithm should be distinctively different with a bigger improvement for the correlated light source. Figure 5.8 shows the simulated counts for a probability of correlated photons arriving in adjacent pixels of 6%, matching the experimental results. For this

rather low probability, the difference for the data processed with the pair detection algorithm is marginal.

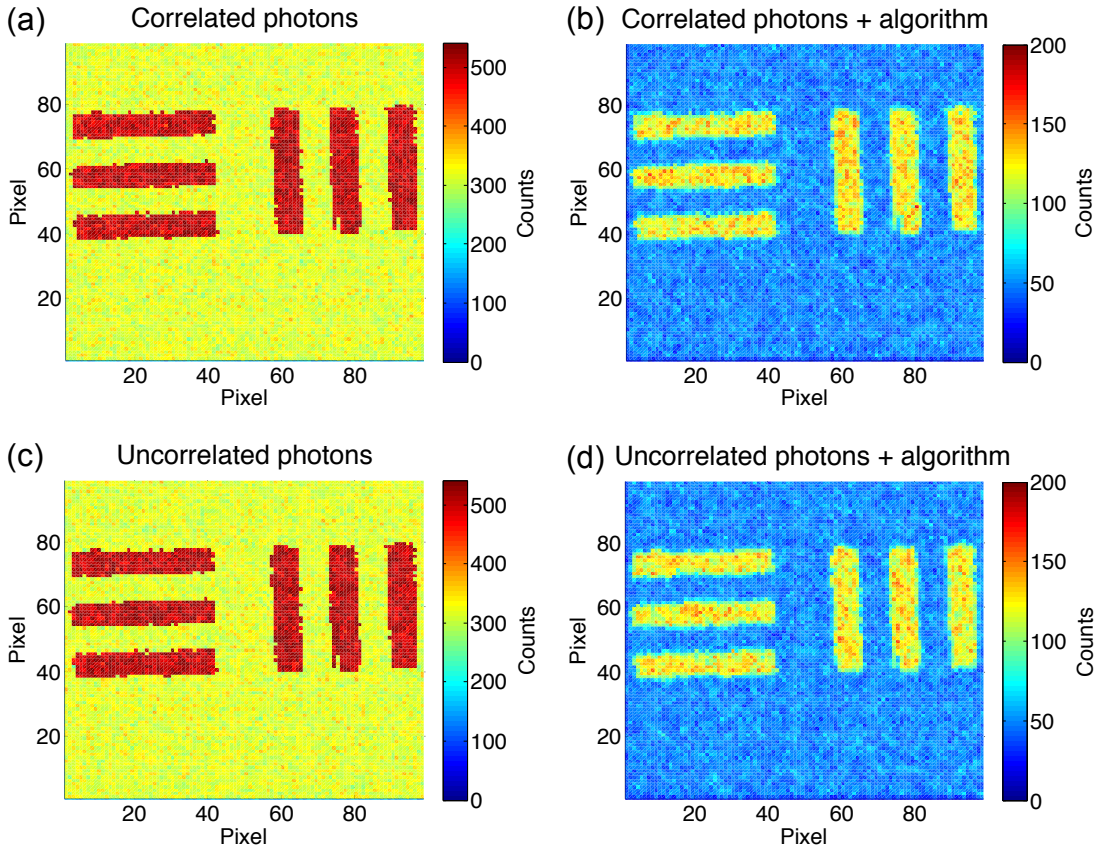

Figure 5.8: *Comparison of simulated counts pixel^{-1} for identical photon flux for the different simulated light sources (top - correlated, bottom - uncorrelated) without or with the pair detection algorithm (left - raw data, right - processed data) and a probability of 6% for photon pairs arriving in adjacent pixels.*

For a second set of simulations, the probability to detect photons in adjacent pixels was increased to 25%. These simulated counts are shown in Figure 5.9. As expected, the correlated light source with the pair detection algorithm possesses an increased amount of signal compared to the uncorrelated photon source with the applied pair detection algorithm.

The results shown in Figures 5.10(a), 5.10(c) and 5.10(e) and Table 5.2 indicate that the use of a correlated light source can enhance the quality of an image obtained with low-light levels, when the emitted photons in a pair possess a high probability to be detected by adjacent pixels. The image benefits from the pair detection algorithm, which rejects single noise events, and due to the correlated light source, the probability to detect pairs of photons is increased, compared to using an uncorrelated photon source.

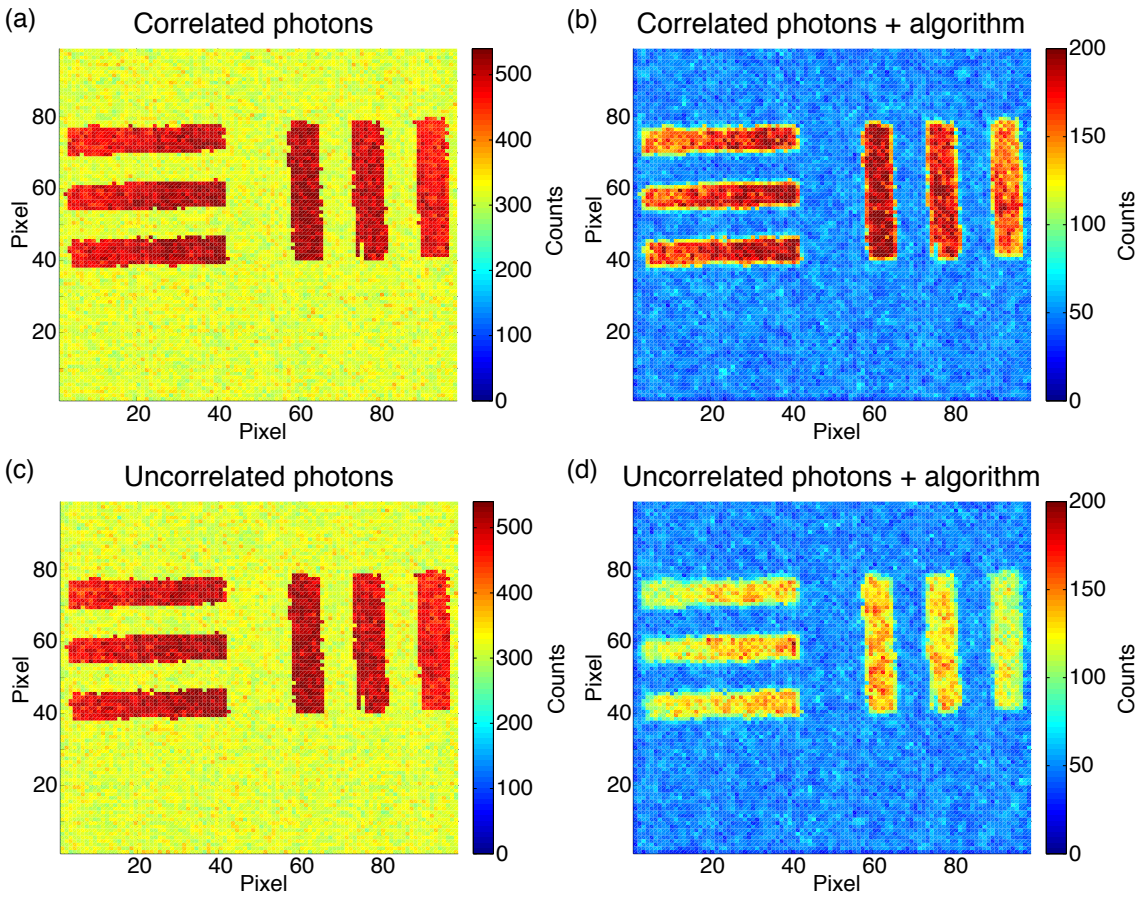

Figure 5.9: *Comparison of simulated counts pixel^{-1} for identical photon flux and a probability of 25% for photon pairs arriving in adjacent pixels, for the different simulated light sources (top - correlated, bottom - uncorrelated) and without or with the pair detection algorithm (left - raw data, right - processed data).*

In order to double-check these results, the correlations were “switched off”, in the LabView programme, for the correlated light source and the simulations were repeated with the same parameters which were used for the correlations “switched on” simulations. In this case, the correlated light source acted as an uncorrelated light source and the emitted photons no longer traveled in pairs. Figures 5.10(b), 5.10(d) and 5.10(f) show the results for the uncorrelated light source and the correlated light source with the correlations “switched off”. In both cases, the photon flux was approximately the same and the photons arrived randomly at the camera, resulting in identical outcomes for both simulations.

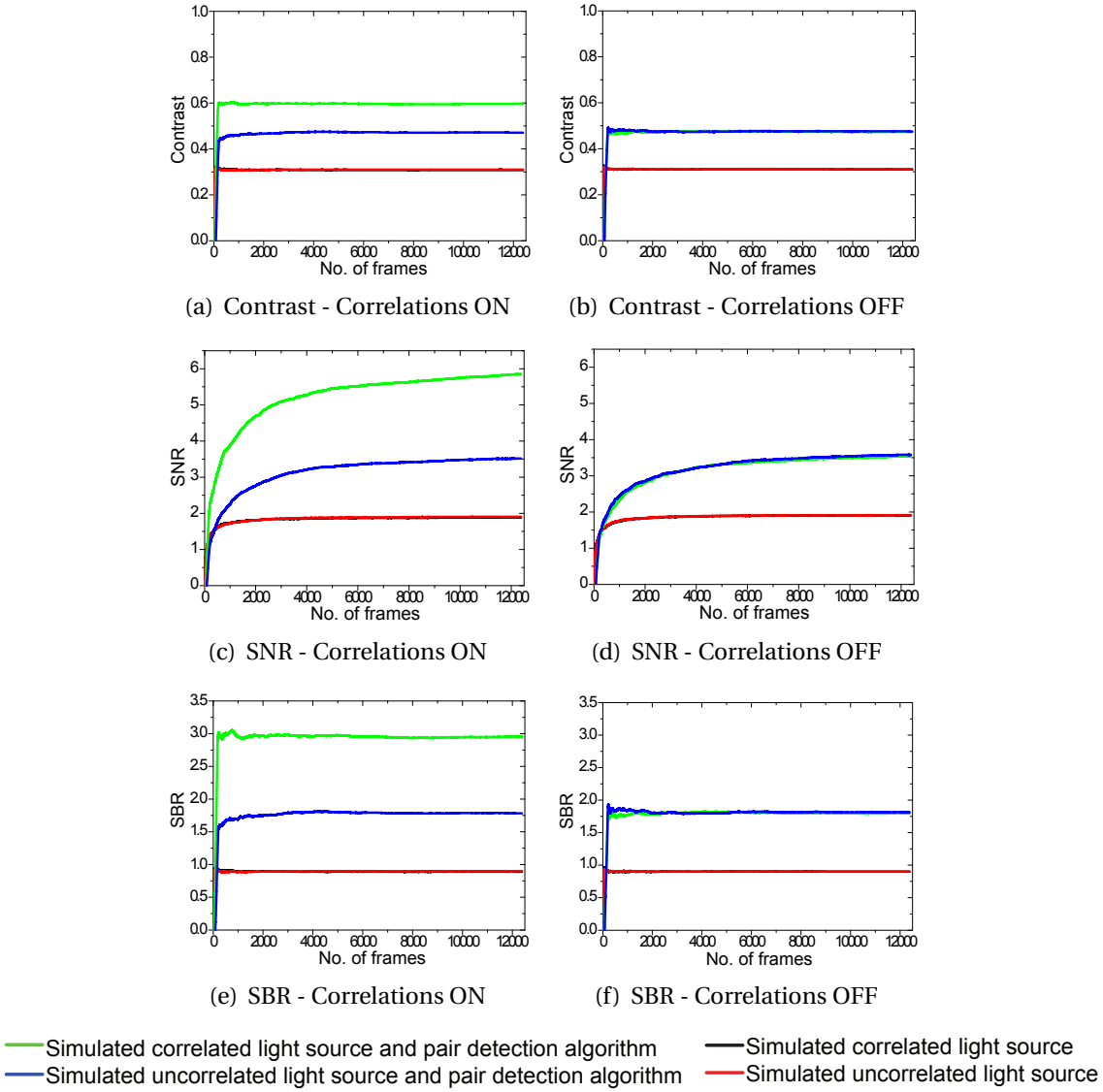

(a) Contrast - Correlations ON (b) Contrast - Correlations OFF

(c) SNR - Correlations ON (d) SNR - Correlations OFF

(e) SBR - Correlations ON (f) SBR - Correlations OFF

Figure 5.10: *(a), (c) and (e) show the simulated contrast, SNR, and SBR for the correlated and uncorrelated light sources with and without the pair detection algorithm for identical photon fluxes and for correlations "switched on" for the correlated light source. (b), (d) and (f) show the simulated contrast, SNR, and SBR for the correlated and uncorrelated light sources with and without the pair detection algorithm for identical photon fluxes and correlations "switched off" for the correlated light source. Here the correlated light source acts as an uncorrelated light source. For the unprocessed data, the correlated (red) and uncorrelated (black) light sources overlap, hence only one trace is visible.*

Type	C_{Pairs}	$C_{Singles}$	SNR_{Pairs}	$SNR_{Singles}$	SBR_{Pairs}	$SBR_{Singles}$
Correlations on	0.597	0.308	5.85	1.89	2.96	0.89
Uncorrelated	0.471	0.310	3.52	1.90	1.78	0.90
Correlations off	0.473	0.310	3.54	1.91	1.80	0.90
Uncorrelated	0.475	0.311	3.58	1.91	1.81	0.90

Table 5.2: *Simulated contrast, SNR, and SBR for identical photon fluxes for both light sources with a probability of 25% for photon pairs arriving in adjacent pixels.*

Table 5.2 shows the simulated results for a a probability of 25% for photon pairs arriving in adjacent pixels in terms of contrast, SNR, and SBR for both light sources. $Pairs$ denominates the usage of the pair detection algorithm, while $Singles$ represents the raw data. The values for the contrast, the SNR, and the SBR now overlap for the unprocessed data for both light sources. This proves that the difference of the contrast, SNR and SBR in the simulations was due to the high probability of the correlated photons landing in adjacent pixels as shown in Figure 5.10.

5.4.2 *Changing the photon flux*

In the following, the photon flux for a given probability of the photons arriving in adjacent pixels was varied in order to find the optimum photon flux for the best relative improvement of the contrast, SNR, and SBR. These simulations were recorded for 5000 frames for each photon flux. The number of dark counts was set to 240 and the single-photon detection efficiency for the correlated light was set to 75%, while the single-photon detection efficiency of the uncorrelated was set to 12.45% to take the ND filter in the SPDC path into account.

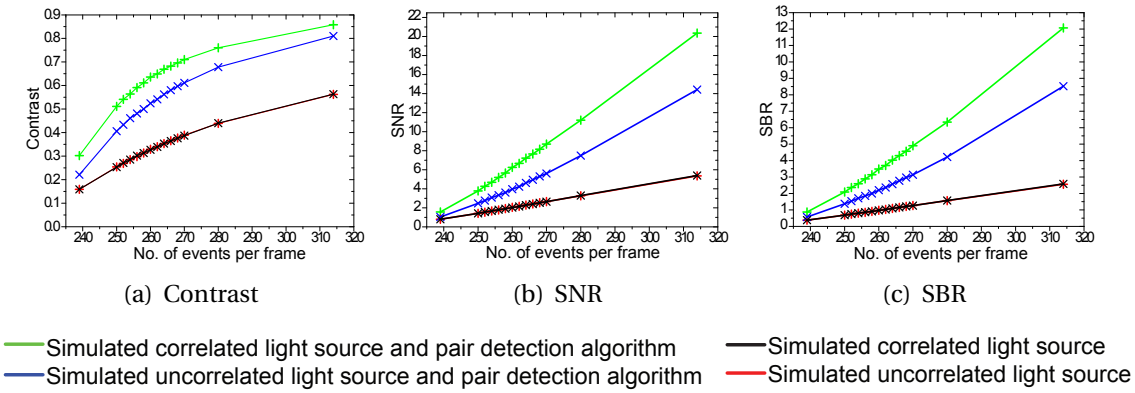

(a) Contrast (b) SNR (c) SBR

Figure 5.11: *Varied low photon fluxes with a probability of 25% of photons getting detected in adjacent pixels. For the unprocessed data, the correlated (red) and uncorrelated (black) light sources overlap, hence only one trace is visible.*

Figure 5.11 shows a comparison of the improvement in contrast, SNR, and SBR for a probability of 25% for the photons arriving in adjacent pixels, when the overall photon flux is varied. In all cases, the raw data obtained with the correlated and uncorrelated light sources overlaps, and only for the processed data two distinct data sets are present. Beside having an improvement in the image quality when using the pair detection algorithm, having a high probability for the photons arriving in adjacent pixels, improves the quality even further. For the contrast an additional improvement in excess of 17% can be achieved compared to the uncorrelated light source with the pair detection algorithm. The contrast ratio of the processed and the raw data for the uncorrelated light source is $\times 1.6$ for 250 up to 275 events per simulated frame. The SNR ratio for the processed and the raw data is approximately $\times 2$.

The contrast ratio between the correlated light source with the pair detection algorithm and the raw data is $C_C = 1.9$ for the same number of events. The ratios between the processed and the raw data for the correlated light source for the SNR and SBR are of the order of $SNR_C \approx SBR_C \approx 3$ for the simulated photon fluxes. For high photon fluxes, the ratios for the processed correlated and uncorrelated light sources begins to decrease, as there are too many events present in the slits and the pair detection algorithm detects many more false pairs caused by correlations between photons from different pairs and correlation from a photon and a dark count, therefore both light sources become indistinguishable.

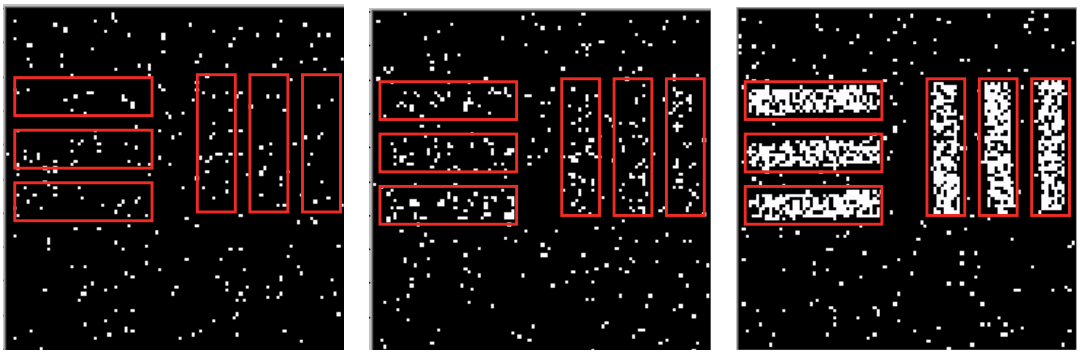

(a) 272 events (b) 419 events (c) 1336 events

Figure 5.12: *Single simulated frame with varied photon fluxes with a probability of 25% of photons getting detected in adjacent pixels.*

In Figure 5.12 single simulated frames for different numbers of events are shown. For 272 events no slits are recognisable and mainly single events are present. This number of events represents the extreme low light level used in the experiment. For higher photon fluxes, the slits slowly become visible. In Figure 5.12(b) there are more clusters of illuminated pixels present, which were caused by the tightly correlated photon pairs. Outside the slit region, mainly single pixel events are present. Figure 5.12(c) shows a simulated light source with a very high photon flux, as almost all pixels within the slits in the single frame are illuminated.

Figure 5.13 shows the ratios between the correlated light source with the pair detection algorithm and the uncorrelated light source with the pair detection algorithm at different photon fluxes. For lower photon fluxes, higher values for the contrast ratio were calculated (Figure 5.13(b)), as the pair detection algorithm works better for lower photon numbers. Figure 5.13(a) shows the calculated contrast for both light sources and with/-out the pair detection algorithm applied to it. For the unprocessed data, both light sources overlap. For the processed data, the difference for the correlated and the uncorrelated light source, is bigger for low photon fluxes and becomes zero at 550 events /frame. The highest ratios for the SNR and SBR were measured for 275 events per frame, which means that ≈ 40 photons /frame were detected inside the slits. For higher photon fluxes, the two different light sources become more and more indistinguishable as many more correlations are registered. Due to the higher photon flux, more false correlations (those between photons from different pairs and those between noise and photons) are getting detected. For very high photon fluxes, as shown in Fig-

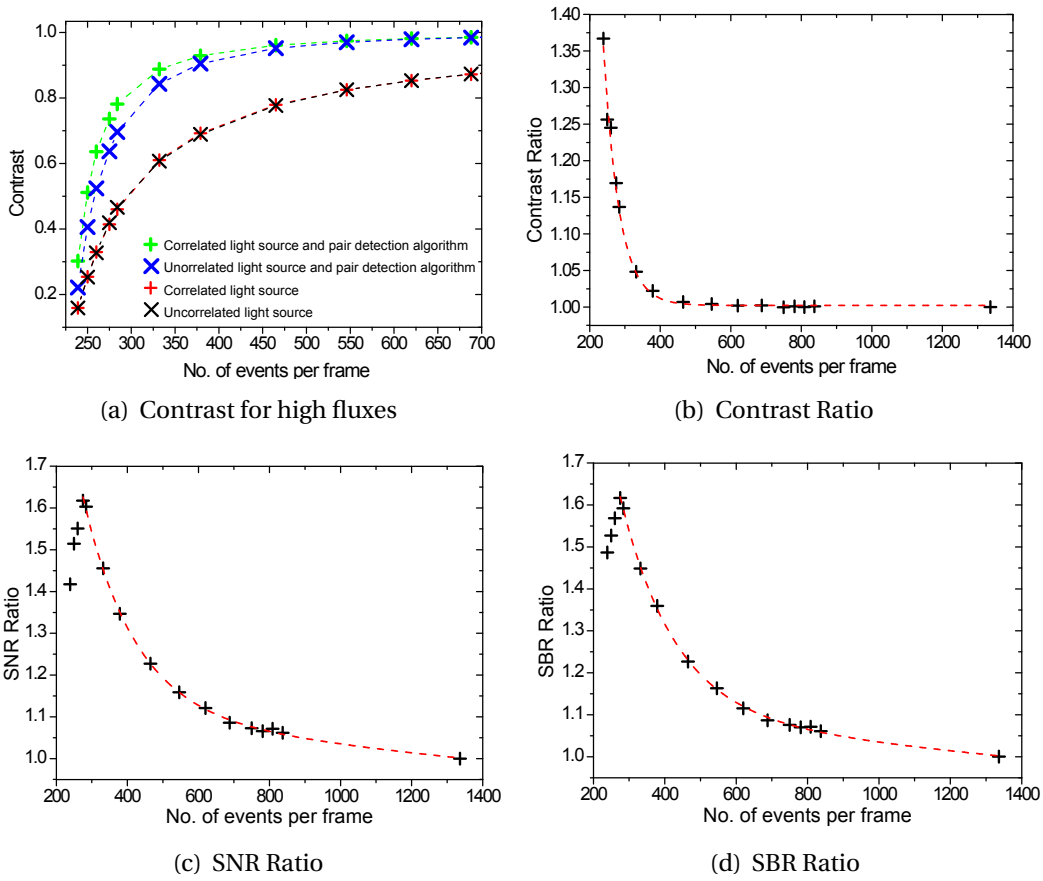

(a) Contrast for high fluxes

(b) Contrast Ratio

(c) SNR Ratio

(d) SBR Ratio

Figure 5.13: *Ratios between the correlated light source with pair detection algorithm and the uncorrelated light source with pair detection algorithm for contrast SNR, and SBR. High photon fluxes with a probability of 25% of photons arriving in adjacent pixels were simulated. The simulated camera had 0.024 dark counts pixel^{-1} /frame. The dashed lines indicate fits for the simulated data (+) in Figures 5.13(b) to 5.13(d). Figure 5.13(a) shows a comparison for the contrast calculations for both light sources with/-out the pair detection algorithm.*

ure 5.12(c), using a correlated light source does not give any improvement compared to using an uncorrelated light source.

5.4.3 *Varying dark counts and probability of photons arriving in adjacent pixels*

In this section, the number of dark counts was varied. As mentioned in Section 5.1.1 three different types of noise are usually present in EMCCD cameras. By sufficiently cooling the camera and by applying a threshold, the influence of read-out noise and dark current can be minimised and CIC is the main source of noise present in the measurements. Here the number of dark counts was varied for three different cameras. The setting for the dark count was 240 dark counts for the 100 × 100 pixels ROI, which was approximately the same number of dark counts present in the EMCCD camera used

in the experiment. The second set of simulations was run for 120 dark counts. Simulations were run for 48 dark counts as well. For example, Nüvü camēras offer EMCCD cameras which claim to have ×5 less CIC than Andor cameras [5.9, 5.10].

Additionally the probability of photons arriving in adjacent pixels was varied in order to investigate its effect on the contrast of the summed image. From the simulations one can conclude that the probability of the partner photons arriving in adjacent pixels in the experiment was rather low. In the following the contrast, SNR, and SBR were simulated for standard deviations of the Gaussian function of 1, 3, and 6.4 pixels to see if there is any improvement of the correlated light in combination with the pair detection algorithm. As seen in Figure 5.6 the standard deviation of 1 pixel possesses a probability of 25% that the photons from a pair arrive in adjacent pixels, while the probability to detect photons in adjacent pixels for a standard deviation of 3 pixels is 13% and 6% for a standard deviation of 6.4 pixels respectively.

Contrast

Figure 5.14 and Table 5.3 show the simulated results for the contrast enhancement for both light sources compared to the raw data and between the both sets of processed data, for different standard deviations of the photon pair and different total dark counts. The contrast was calculated with Equation (5.1).

Probability [%]	Dark counts	C_C	C_U	C_R
25	48	1.46	1.30	1.12
25	120	1.82	1.50	1.21
25	240	1.95	1.54	1.27
13	48	1.40	1.35	1.04
13	120	1.61	1.51	1.07
13	240	1.64	1.31	1.25
6	48	1.36	1.35	1.01
6	120	1.52	1.49	1.02
6	240	1.56	1.53	1.02

Table 5.3: *Contrast simulations for different probabilities of photon pairs getting detected in adjacent pixels, and dark counts.* C_C *denotes the ratio between the contrast of the correlated light source with and without applying the pair detection algorithm to the data.* C_U *is the contrast ratio for the uncorrelated light source.* C_R *denotes the ratio between* C_C *and* C_U.

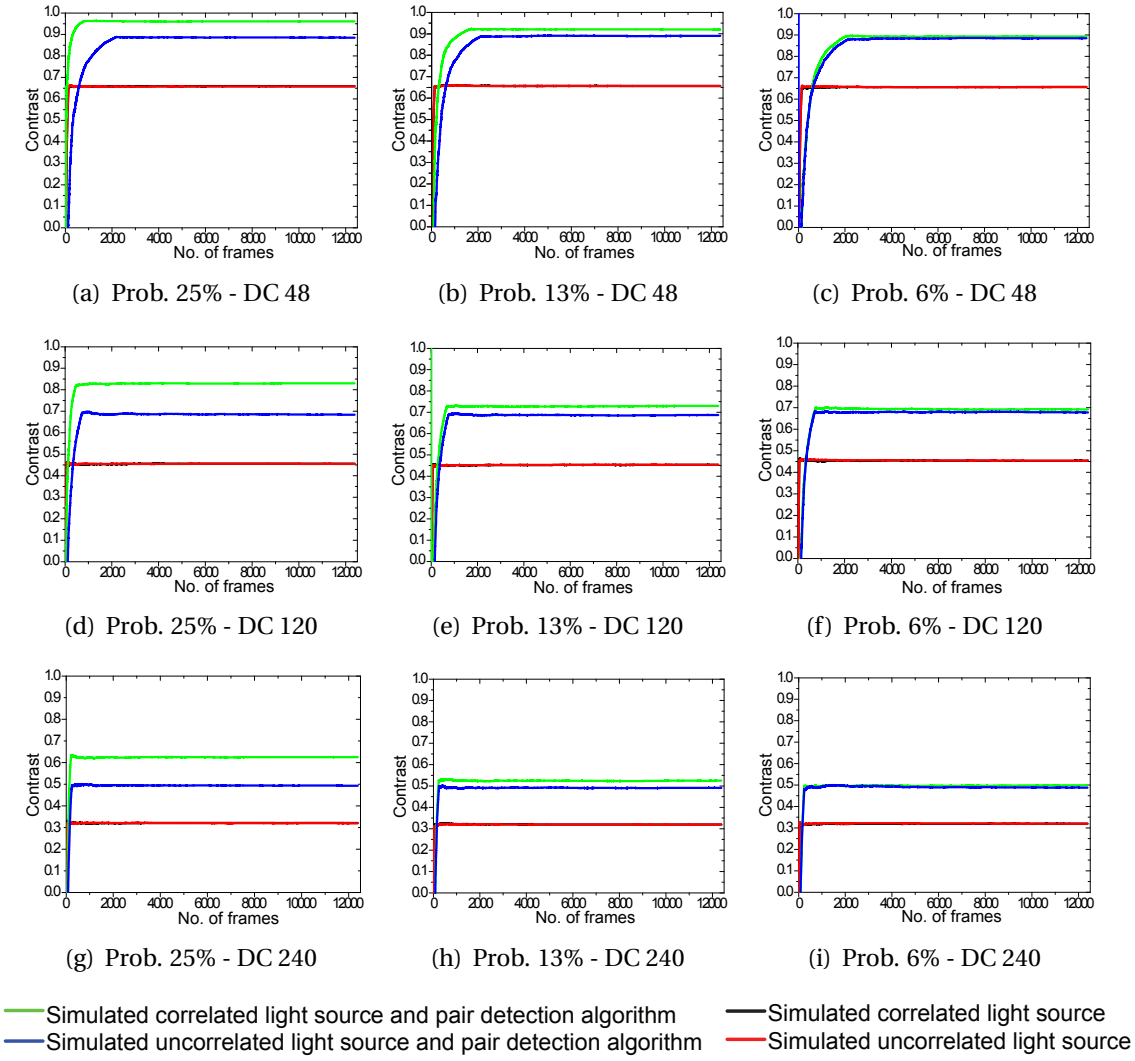

(a) Prob. 25% - DC 48 (b) Prob. 13% - DC 48 (c) Prob. 6% - DC 48

(d) Prob. 25% - DC 120 (e) Prob. 13% - DC 120 (f) Prob. 6% - DC 120

(g) Prob. 25% - DC 240 (h) Prob. 13% - DC 240 (i) Prob. 6% - DC 240

Figure 5.14: *Comparison of the contrast for different numbers of dark count (from top to bottom: 48, 120, 240) and different probabilities of the photons to arrive in adjacent pixels (from left to right 25%, 13%, 6%). Green represents the correlated light with the applied pair detection algorithm, blue is the uncorrelated light with the pair detection algorithm. The red (& black) curves represent the raw data. The black curves for the uncorrelated light are not visible as they are overlapped by the red curve representing the correlated light source.*

Depending on the number of dark counts, the contrast for the unprocessed data varies. As shown in Figure 5.14 (solid red and black lines), the simulations with a high number of dark counts possess a lower contrast. The contrast varies from $C = 0.32$ for 240 dark counts and increases up to $C = 0.66$ for 48 dark counts. The improvement for the data processed with the pair detection algorithm depends on the number of dark counts and additionally depends also on the probability of photons arriving in adjacent pixels. The solid blue line in Figure 5.14 represents the uncorrelated light source with the pair detection algorithm applied to it. As for the uncorrelated light source, the photons arrive randomly at the EMCCD camera and therefore the contrast is constant for the uncorrelated light source with the pair detection algorithm applied to it. Here the contrast solely depends on the number of dark counts for a fixed photon flux.

The probability to detect photon pairs in adjacent pixels is important, when the correlated light source is used. Photon pairs with a high probability for both photons to arrive in adjacent pixels, have a higher chance for the both photons getting registered by the pair detection algorithm. The solid green light represents the correlated light source with the pair detection algorithm applied to the data. For a rather low probability of 6% and 240 dark counts present in the camera, the ratio between the contrast of the correlated light source with the pair detection algorithm and between the processed and the raw data for the correlated light source is of the order of $C_R = 1.02$. However, when using a high probability of 25% , the ratio between the contrasts is $C_R = 1.27$ for a noisy camera. The improvement gained by the correlated light source is comparatively smaller, when a low noise camera is used, as very few dark counts were registered in the first place. For example when using a camera with 48 dark counts and a probability of photons arriving in adjacent pixels of 25%, the enhancement of the correlated light source in combination with the pair detection algorithm will be increased by a factor of $C_R = 1.12$ compared to an uncorrelated light source with the pair detection algorithm applied to the raw data.

SNR

Figure 5.15 and Table 5.4 show the simulated results for the SNR, for different probabilities of the photon pairs arriving in adjacent pixels, and different numbers of dark counts. The SNR was calculated with Equation (5.2).

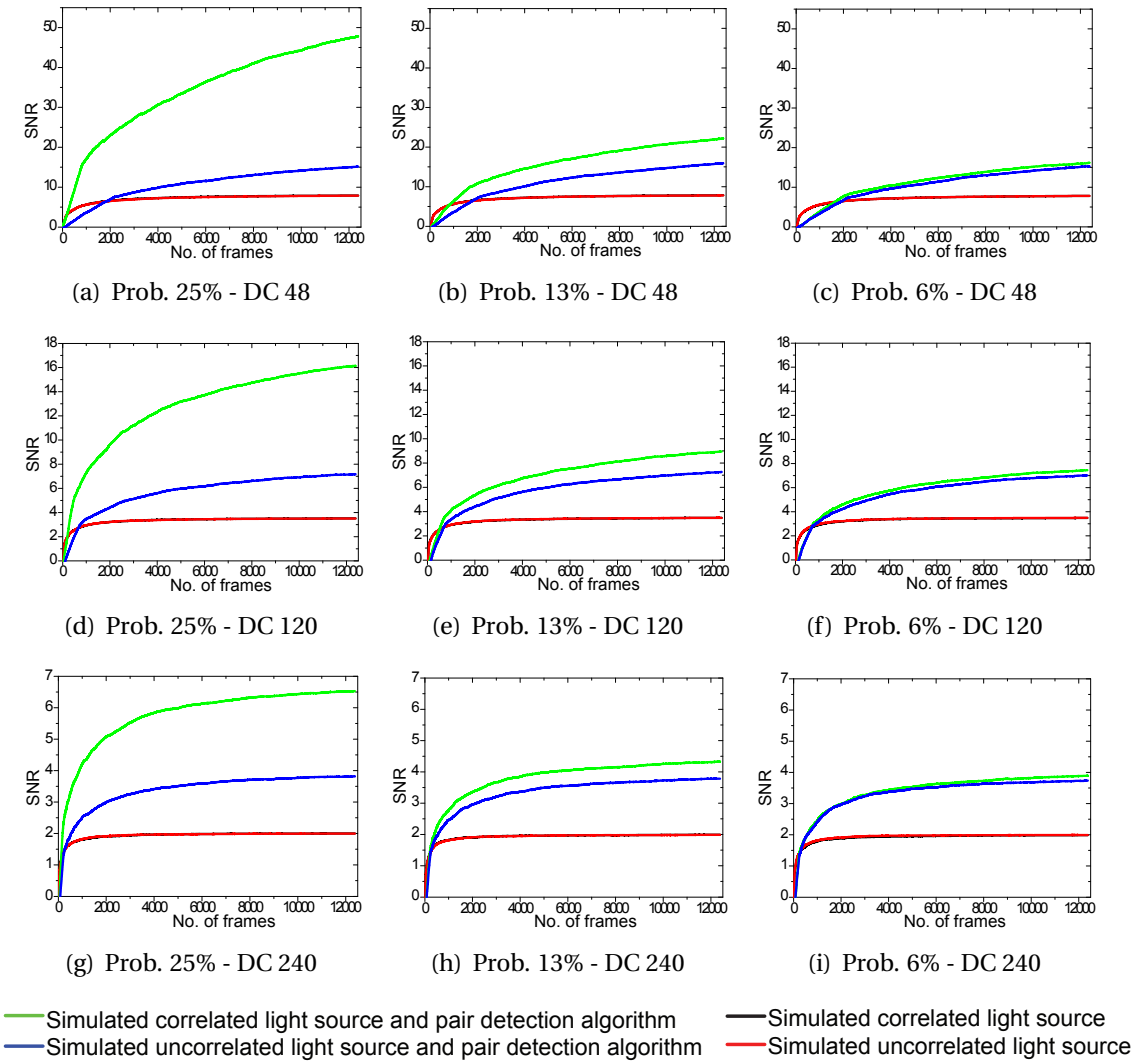

(a) Prob. 25% - DC 48 (b) Prob. 13% - DC 48 (c) Prob. 6% - DC 48

(d) Prob. 25% - DC 120 (e) Prob. 13% - DC 120 (f) Prob. 6% - DC 120

(g) Prob. 25% - DC 240 (h) Prob. 13% - DC 240 (i) Prob. 6% - DC 240

Figure 5.15: *Comparison of the SNR for different numbers of dark count (from top to bottom: 48, 120, 240) and probabilities of the photons to arrive in adjacent pixels (from left to right 25%, 13%, 6%). Green represents the correlated light with the applied pair detection algorithm, blue is the uncorrelated light with the pair detection algorithm. The red (& black) curves represent the raw data. The black curves for the uncorrelated light are not visible as they are overlapped by the red curve representing the correlated light source.*

Probability [%]	Dark counts	SNR_C	SNR_U	SNR_R
25	48	6.05	1.92	3.15
25	120	4.60	2.05	2.24
25	240	3.27	1.91	1.71
13	48	2.91	2.07	1.41
13	120	2.57	2.08	1.24
13	240	2.18	1.90	1.15
6	48	2.07	1.96	1.06
6	120	2.14	2.01	1.06
6	240	1.95	1.88	1.04

Table 5.4: *SNR of the final summed image for different probabilities of photon pairs arriving in adjacent pixels and dark counts. SNR_C denotes the ratio between the SNR of the correlated light source with and without applying the pair detection algorithm to the data. SNR_U is the SNR ratio for the uncorrelated light source, respectively.* SNR_R *denotes the ratio between SNR_C and SNR_U.*

Similar to the contrast simulations, the SNR for the correlated light source depends on the number of dark counts present in the camera and the probability of the photon pairs arriving in adjacent pixels, when the pair detection algorithm is used. For the uncorrelated light source and the raw data from the correlated light source, the SNR depends solely on the number of dark counts for a fixed photon flux. Using the pair detection algorithm enhances the SNR by a factor of $SNR_R = 1.88$ for the uncorrelated light source compared to the unprocessed data for a camera with 240 dark counts. In comparison, using a correlated light source, and a probability of 6% for the correlated photons to arrive in adjacent pixels for the same setup with the pair detection algorithm, improves the SNR by a factor of $SNR_R = 1.95$ compared to the unprocessed data of the same light source. The difference for the un-/correlated light sources with the pair detection algorithm is merely a factor of $SNR_R = 1.04$ for a probability of 6% that the photons of a pair arrive in adjacent pixels. However, using a correlated light source with a probability of 25% and the pair detection algorithm improves the SNR by a factor of $SNR_R = 1.71$, compared to the uncorrelated light source with the pair detection algorithm.

SBR

Figure 5.16 and Table 5.5 show the simulated results for the SBR, for different probabilities of the photon pairs to land in adjacent pixels, and different numbers of dark

noise. The SBR was calculated with Equation (5.3) and is defined as the signal *above* the background.

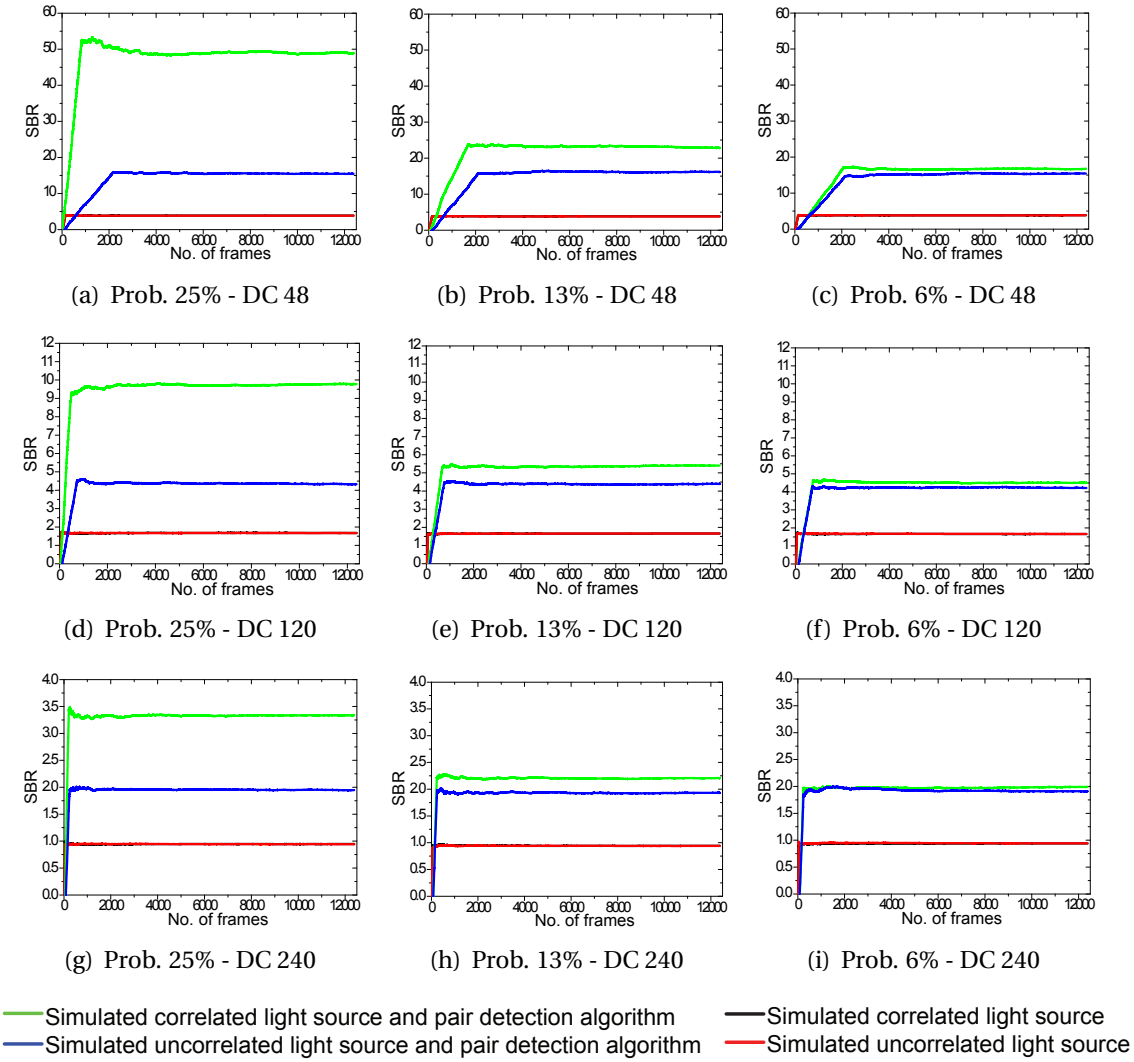

Figure 5.16: *Comparison of the SBR for different numbers of dark count (from top to bottom: 48, 120, 240) and different probabilities of the photons to arrive in adjacent pixels (from left to right 25%, 13%, 6%). Green represents the correlated light with the applied pair detection algorithm, blue is the uncorrelated light with the pair detection algorithm. The red (& black) curves represent the raw data. The black curves for the uncorrelated light are not visible as they are overlapped by the red curve representing the correlated light source.*

As for the contrast and the SNR only the correlated light source with the applied pair detection algorithm depends on the amount of dark noise present in the camera and the probability of the photon pairs to arrive in adjacent pixels. In all other cases the calculated SBR depends on the amount of dark noise.

The highest SBR was calculated for a camera with 48 dark counts and a probability of 25% for the photons of a pair to arrive in adjacent pixels. In this case the SBR was almost ×3.2 higher than the corresponding SBR for the uncorrelated photon source with

Probability [%]	Dark counts	SBR_C	SBR_U	SBR_R
25	48	12.64	4.01	3.15
25	120	5.82	2.59	2.25
25	240	3.52	2.07	1.70
13	48	5.99	4.22	1.42
13	120	3.25	2.65	1.23
13	240	2.35	2.05	1.15
6	48	4.37	4.03	1.08
6	120	2.71	2.54	1.07
6	240	2.12	2.03	1.04

Table 5.5: *SBR simulations for different probabilities of the photon pairs landing in adjacent pixels, and dark counts. SBR_C denotes the ratio between the SBR of the correlated light source with and without applying the pair detection algorithm to the data. SBR_U is the SBR ratio for the uncorrelated light source, respectively.* SBR_R *denotes the ratio between SBR_C and SBR_U*

the pair detection algorithm applied to the data and ×12.6 higher than the correlated light source without any further data processing.

5.4.4 *Optimised photon flux for 48 dark counts*

In Section 5.4.3 the photon flux was set to a high level in order to simulate the results for a high noise level camera, and to match the number of detected events in the experiment. The improvement for the contrast, SNR, and SBR were calculated for a fixed photon flux for the different levels of dark counts. However, for a low-noise camera, the photon flux must be reduced in order to optimise the improvement of the images obtained with the raw data and the images, which where processed with the pair detection algorithm. Figure 5.17 shows the final summed image after 12,386 frames for a correlated light source, where the correlated photons possess a probability of 25% of arriving in adjacent pixels, and a low noise camera with 48 dark counts per frame. The number of recorded events per frame for the correlated and the uncorrelated light sources were set to 51 events, matching the number of recorded events for the highest improvement of the SNR and SBR, as shown in Figures 5.18(b) and 5.18(c). The total number of events per frame consists of 47 ± 1 dark counts and 4 ± 2 photons per frame.

In contrast to Figure 5.8, the slits in Figure 5.17 for the uncorrelated light source with the pair detection algorithm are only barely visible, as the read-out values for these

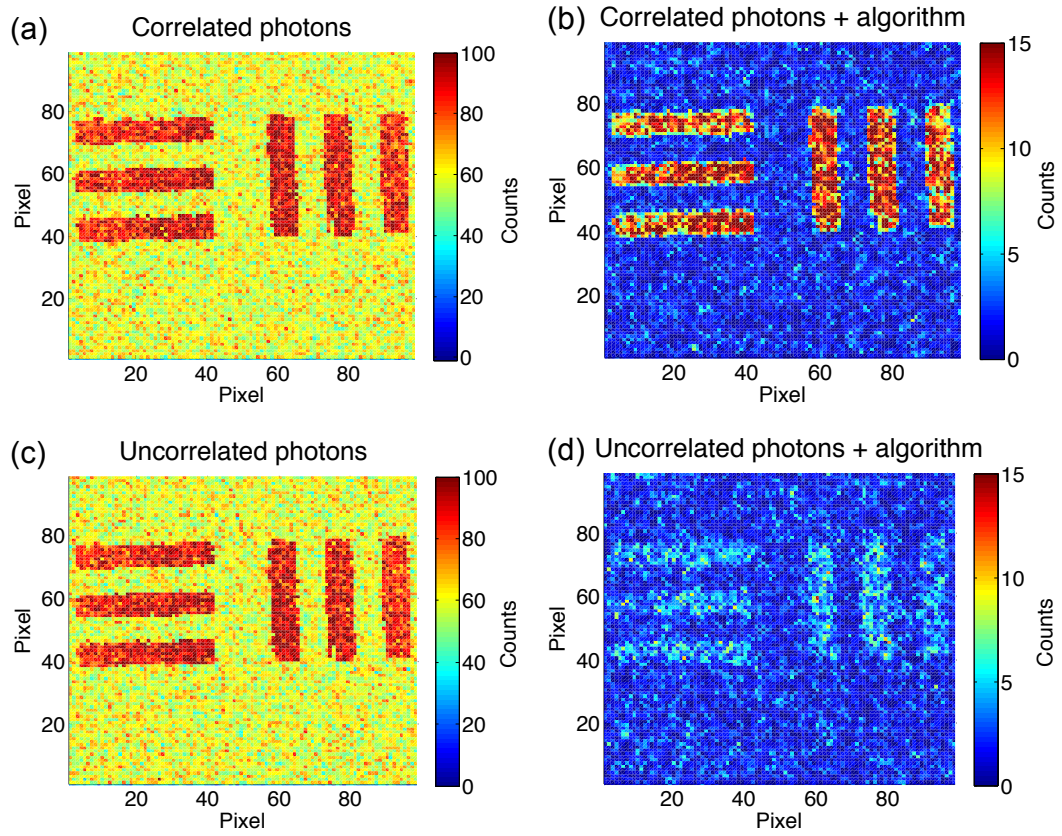

Figure 5.17: *Simulated summed image after 12,384 frames for a low noise camera with a photon flux of 4 photons /frame.*

pixels is just twice as high as the background. However, the read-out value for the correlated light source with the pair detection algorithm is almost ×10 higher than the background, giving an improvement of ×5 by processing the data from the correlated light source compared to the processed data from the uncorrelated light source.

Figure 5.18 shows the ratios for the contrast, SNR, and SBR at different simulated photon fluxes. The highest ratios for the SNR and SBR were reached, when on average 51 events were present in a single frame. This corresponds to 47 dark counts and 4 photons per frame. For higher photon fluxes, these ratios decrease due to the increase of false correlations (between other photon pairs and correlations with noise events), making the two different photon sources indistinguishable for very high photon fluxes.

Table 5.6 shows a comparison of the ratios for the data processed with the pair detection algorithm in conjunction with a correlated light source for a high photon flux (59 photons /frame) and for a correlated light source with a low photon flux (4 photons /frame). For both simulations a camera with a low noise of ≈ 48 dark counts /frame

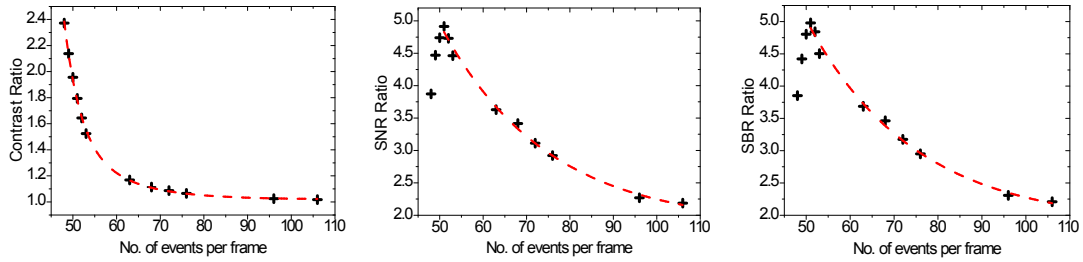

(a) Contrast Ratio (b) SNR Ratio (c) SBR Ratio

Figure 5.18: *Simulated ratios between the correlated light source with the pair detection algorithm and the processed data of the uncorrelated light source for a low noise camera.*

Photon flux	Contrast			SNR			SBR		
[photons /frame]	C_C	C_U	C_R	SNR_C	SNR_U	SNR_R	SBR_C	SBR_U	SBR_R
59	1.21	1.19	1.02	6.14	2.81	2.19	14.69	6.65	2.21
4	2.71	1.51	1.79	4.74	0.97	4.91	9.55	1.92	4.98

Table 5.6: *Ratios for low noise camera (48 dark counts) with different photon fluxes and applied pair detection algorithm. The high photon flux corresponds to ≈ 59 photons /frame, while the low photon flux was simulated with ≈ 4 photons /frame. The subscripts C and U denote the ratios between the data processed with the pair detection algorithm and the raw data for the correlated and the uncorrelated light source respectively. The subscript R represent the ratio between the correlated light source with the pair detection algorithm and the uncorrelated light source with the pair detection algorithm.*

is used. As shown in Figures 5.18(b) and 5.18(c) the ratio decays exponentially for an increasing number of photons in a frame and for values near the optimum, even small changes in photon flux can cause a large reduction for the ratios. For 59 photons /frame the contrast ratio is reduced by a factor of ×1.75, while the SNR and SBR ratios are reduced by a factor of ≈ ×2.25.

5.5 Conclusion

In this chapter, the different types of noise present in EMCCD cameras were reviewed. Furthermore, the thresholding technique to distinguish photons from dark noise noise and the pair detection algorithm to avoid counting false correlations caused by the camera read-out mechanism were explained.

The experimental setup and the clear optical path target were detailed. The illuminated slits of the test target consisted of three alternating opaque and transparent slits

each with a width of 125 µm and a height of 750 µm. For the experiment, two different light sources were used. The correlated light was produced through SPDC and the emitted photon pair was set to have a theoretical correlation length of 34 µm. The uncorrelated light was produced by moving a neutral density filter from the pump beam into the SPDC path of the correlated photon source. Due the neutral density filter, the probability to detect photon pairs was greatly reduced.

The experimental results for the contrast enhancement were compromised by the non-identical photon fluxes for both light sources. However, it was still possible to evaluate the contrast, SNR, and SNB for the data with and without the pair detection algorithm applied to the raw data for each light source individually. The contrast improved by a factor of ×1.5 for both light sources by applying the pair detection algorithm to the raw data. The SNR was improved by a factor of $SNR_C = 1.95$ and the SBR was enhanced by a factor of $SBR_C = 2.13$ for the correlated light sources compared to the raw data.

From numerical simulations fitted to the experimental data, the probability to for correlated photons to arrive in neighbouring pixels was calculated to be of the order of 6%. Due to the low probability to detect a photon pair in adjacent pixels, the contrast enhancement of the correlated light source was comparable to the enhancement of the uncorrelated light source.

Furthermore, numerical simulations were run for both light sources having the same photon flux. Additionally, the probability of the photon pair arriving in adjacent pixels, and the number of dark counts were varied in order to investigate their influence on the image quality. A high probability for the photons of a pair arriving in adjacent pixels would be beneficial for this type of experiment. This probability can be altered in the experiment by modifying the correlation length of the photon pairs, which can be done by changing the magnification of the optical system.

The camera used in the experiment possesses roughly 0.02 dark counts pixel^{-1} /frame. Lower noise cameras are commercially available and the lowest noise camera possesses ≈ ×5 less noise than the camera used in this experiment. The theoretical contrast, SNR, and SBR for this camera were modelled. Additionally a camera with half the number of dark events present in the camera was simulated and evaluated, as well.

The greatest theoretical enhancements were achieved with a low noise camera, pos-

sessing ≈ 46 dark counts in a region of interest measuring (100 × 100) pixels and a probability of 25% that the photons of a pair arrive in adjacent pixels. The highest contrast enhancement was calculated to be a factor of $C_C = 3.23$ for the correlated light source compared to the raw data ($C_U = 1.36$ for the uncorrelated light source), giving an enhancement of $C_R = 2.37$. The highest SNR was calculated to be $SNR_C = 4.74$ higher for the correlated light source with the pair detection algorithm compared to the raw data ($SNR_U = 0.96$ for the uncorrelated light source) and enhancement of $SNR_R = 4.91$ was obtained. The highest enhancement for the SBR was calculated to be $SBR_C = 9.51$ for the correlated light source with the pair detection applied to the raw data, while for the uncorrelated light source with the pair detection algorithm the enhancement was calculated to be $SBR_U = 1.92$, leading to a total enhancement of $SBR_R = 4.98$ for the correlated light source with the pair detection algorithm.

For an optimised imaging performance, a camera with a low number of dark counts would be preferential, but also probability of photons arriving in adjacent pixels and the photon flux are important and need to be carefully selected. The ideal photon flux, without the target, should match the number of dark counts present in the camera. For the pair detection algorithm to work sufficiently, the correlation length of the photon pairs should be set to a value, where the highest probability to detect the two photons in adjacent pixels is accomplished.

5.6 References

[5.1] Andor Technology. *iXon+ Back-illuminated EMCCD - Technical Article from Andor Technology*. online, last accessed 2011-05-02. Andor Technology, (2006). URL: http://www.microimage.com.cn/uploadfile/xwjs/uploadfile/201009/20100915021449671.pdf (cited on page: 149).

[5.2] *ProEM+ Performance | Precision | Peace of Mind*. online, last accessed 2013-02-11. Princeton Instruments, (2012). URL: http://www.princetoninstruments.com (cited on page: 149).

[5.3] E. Lantz, J.-L. Blanchet, L. Furfaro and F. Devaux. 'Multi-imaging and Bayesian estimation for photon counting with EMCCDs'. Mon. Not. R. Astron. Soc., Vol. 386, (2008), pp. 2262–2270 (cited on page: 149).

[5.4] M. P. Edgar, D. S. Tasca, F. Izdebski, R. E. Warburton, J. Leach, M. Agnew, G. S. Buller, R. W. Boyd and M. J. Padgett. 'Imaging high-dimensional spatial entanglement with a camera'. Nat. Commun., Vol. 3, (2012), p. 984 (cited on pages: 149, 150).

[5.5] K. W. Chan, J. P. Torres and J. H. Eberly. 'Transverse entanglement migration in Hilbert space'. Phys. Rev. A, Vol. 75, (2007), 050101(R) (cited on page: 150).

[5.6] P.-A. Moreau, J. Mougin-Sisini, F. Devaux and E. Lantz. 'Realization of the purely spatial Einstein-Podolsky-Rosen paradox in full-field images of spontaneous parametric down-conversion'. Phys. Rev. A, Vol. 86, (2012), 010101(R) (cited on page: 150).

[5.7] D. S. Tasca, M. P. Edgar, F. Izdebski, G. S. Buller and M. J. Padgett. 'Optimizing the use of detector arrays for measuring intensity correlations of photon pairs'. Phys. Rev. A, Vol. 88, (2013), p. 013816 (cited on page: 153).

[5.8] National Instruments. *Gaussian White Noise VI*. online, last accessed 2013-05-02. URL: http://zone.ni.com/reference/en-XX/help/371361J-01/lvanls/gaussian_white_noise/ (cited on page: 157).

[5.9] O. Daigle, P.-O. Quirion and S. Lessard. 'The darkest EMCCD ever'. *Proc. SPIE 7742, High Energy, Optical, and Infrared Detectors for Astronomy IV*. (2010), p. 774203 (cited on page: 169).

[5.10] *HNü 512 - data sheet.* online, last accessed 2013-02-04. Nüvü Cameras, (2013). URL: http://www.nuvucameras.com/wp-content/uploads/2013/01/Nuvu-Cameras-HNu-512-Specsheet.pdf (cited on page: 169).

CHAPTER 6

CONCLUSIONS & FUTURE WORK

Spatial correlations between photon pairs generated by spontaneous parametric down-conversion have been investigated over the past two decades. The high dimensionality of the transverse spatial degrees of freedom of the photon pairs can be explored either by a projection onto a discrete basis [6.1] or by using a continuous basis defined by the transverse position and momentum of the photons [6.2]. It has been shown that their transverse position and momentum possess Einstein-Podolsky-Rosen type correlations [6.3, 6.4]. Historically, these measurements were performed by scanning a single-photon avalanche photodiode (SPAD) across the detection planes, negating any information capacity advantage in the use of spatial states. In all protocols using the spatial states of entangled photons for high dimensional quantum key distribution [6.5, 6.6], quantum computation [6.2] and quantum teleportation [6.7], it is essential to perform full-field measurements of the transverse photon positions.

In this thesis, multi-pixel detectors were used to measure the full-field of the transverse photon positions. In Chapter 2 an 8×1 pixel detector using position to time multiplexing was designed, built, and characterised. This detector measured eight positions simultaneously with a single SPAD, which was more cost effective than using eight individual single photon detectors. The final detector consisted of an 8-channel fibre array with pre-determined different fibre lengths, which was connected to an 8 to 1 fibre combiner. The fibre combiner was coupled into a thick-junction SPAD from Perkin Elmer. The full-system single-photon detection efficiency was measured to be 41.7% with a FWHM of 640 ps. The channel capacity was calculated to be 2.32 bits photon^{-1}. For future experiments, this detector could be used for example in time-bin encoded Quantum Key Distribution (QKD), where entangled photons are used to communicate information [6.8, 6.9]. The information capacity could be improved by a factor of eight. Instead of using eight SPADs in each measurement arm, using the fibre array detector would be an cost effective alternative.

In Chapter 3, the bespoke detector was used to measure quantum correlations in momentum, position and intermediate bases sets for eight positions simultaneously. The calculated variance product of the position-difference and the momentum-sum was one order of magnitude below the classical limit, indicating that the photon pairs possessed EPR-type correlations. The novelty of this work was the ability to access an eight-dimensional state space for each of the down-converted photons without the need of scanning. Potential applications in quantum information processing and quantum communications can benefit from the increased information capacity provided by the state space of the entangled photons. By combining additional degrees of freedom, like Orbital Angular Momentum [6.10], with the transverse degrees of freedom, the information capacity might be increased further. This could be implemented by changing the phase hologram of the SLMs to a forked diffraction grating for the far-field measurements [6.11] and by using single-mode instead of multi-mode fibres in the fibre array.

However, with the fibre detector used in Chapter 3 only a very limited portion of the down-converted light was detected due to the limited number of available pixels. Another approach to measure the full-field of the down-converted photons was to use a camera with single-photon sensitivity. Commercially available single-photon sensitive cameras include intensified CCD (ICCD) cameras and electron-multiplying CCD (EMCCD) cameras. In Chapter 4 correlations in position and momentum bases were measured with an EMCCD camera capturing the whole down-converted beam. Following subsequent data analysis, it was found that the variance product of the position-difference and the momentum-sum was almost three orders of magnitude below the classical limit. It was also possible to access more than 2500 states, which is, to date, the highest dimensionality achieved in an experiment using the entangled spatial states of photons.

Although it is possible to observe quantum behaviour of single-photons with off-the-shelf technology, EMCCD cameras suffer from charge smearing caused by the read-out process and noise, which results in the measurement of many false correlations between photons and noise events. For future experiments, the amount of detector noise must reduced, or different single-photon sensitive detector arrays must be developed. Currently, EMCCD manufacturers are trying to minimise the amount of noise generated by the camera, by developing better read-out electronics [6.12, 6.13]. Altern-

ative single-photon sensitive cameras include intensified CCDs, although they suffer from a lower single-photon detection efficiency and SPAD arrays with on-chip CMOS technology [6.14]. The SPAD array would allow time resolved measurements, which cannot be done with EMCCD cameras. Currently back-thinned SPAD arrays with on-chip CMOS technology and a fill-factor of potentially 70% are being developed [6.15]. With a low noise detector array it might be possible to perform EPR-measurements without the need of background-correction and therefore fulfilling the strong requirements for non-locality tests. Low noise level cameras with single-photon sensitivity might be used in quantum communications or quantum key distribution with protocols relying on entanglement, for example E91 [6.16], which can potentially revolutionise the data capacity of quantum secured communications: A picture might be worth a thousand words, but a quantum picture could be worth a thousand *secure* words.

In Chapter 5 an algorithm for extreme low-light level imaging with a correlated photon source was developed. By using a correlated light source with a probability of 25% for the photons of the pair to arrive in adjacent pixels, and by using a pair detection algorithm, the contrast was improved by a factor of ×1.94 compared to the raw data of the uncorrelated photon source. The SNR was improved by a factor of ×3.1, while SBR of the recorded image was enhanced by a factor of ×3.3. Further improvements of the contrast, SNR and SBR might be possible by using a low noise camera. For future experiments using a single-photon sensitive camera with a smaller pixel size and a reduced amount of noise might make sub-Rayleigh imaging at the single photon level possible [6.17, 6.18], when a modified pair detection algorithm covering a larger region of interest is used.

6.1 References

[6.1] A. C. Dada, J. Leach, G. S. Buller, M. J. Padgett and E. Andersson. 'Experimental high-dimensional two-photon entanglement and violations of generalized Bell inequalities'. Nat. Phys., Vol. 7, (2011), pp. 677–680 (cited on page: 182).

[6.2] D. S. Tasca, R. M. Gomes, F. Toscano, P. H. Souto Ribeiro and S. P. Walborn. 'Continuous-variable quantum computation with spatial degrees of freedom of photons'. Phys. Rev. A, Vol. 83, (2011), p. 052325 (cited on page: 182).

[6.3] J. C. Howell, R. S. Bennink, S. J. Bentley and R. W. Boyd. 'Realization of the Einstein-Podolsky-Rosen paradox using momentum- and position-entangled photons from spontaneous parametric down conversion'. Phys. Rev. Lett., Vol. 92, (2004), p. 210403 (cited on page: 182).

[6.4] M. D'Angelo, Y.-H. Kim, S. P. Kulik and Y. Shih. 'Identifying entanglement using quantum ghost interference and imaging'. Phys. Rev. Lett., Vol. 92, (2004), p. 233601 (cited on page: 182).

[6.5] S. P. Walborn, D. S. Lemelle, D. S. Tasca and P. H. Souto Ribeiro. 'Schemes for quantum key distribution with higher-order alphabets using single-photon fractional Fourier optics'. Phys. Rev. A, Vol. 77, (2008), p. 062323 (cited on page: 182).

[6.6] S. P. Walborn, D. S. Lemelle, M. P. Almeida and P. H. Souto Ribeiro. 'Quantum key distribution with higher-order alphabets using spatially encoded qudits'. Phys. Rev. Lett., Vol. 96, (2006), p. 090501 (cited on page: 182).

[6.7] S. P. Walborn, D. S. Ether, R. L. de Matos Filho and N. Zagury. 'Quantum teleportation of the angular spectrum of a single-photon field'. Phys. Rev. A, Vol. 76, (2007), p. 033801 (cited on page: 182).

[6.8] T. Brougham and S. M. Barnett. 'Information communicated by entangled photon pairs'. Phys. Rev. A, Vol. 85, (2012), p. 032322 (cited on page: 182).

[6.9] A. Martin, F. Kaiser, A. Vernier, A. Beveratos, V. Scarani and S. Tanzilli. 'Cross time-bin photonic entanglement for quantum key distribution'. Phys. Rev. A, Vol. 87, (2013), p. 020301 (cited on page: 182).

[6.10] G. Gibson, J. Courtial, M. J. Padgett, M. Vasnetsov, V. Pas'ko, S. M. Barnett and S. Franke-Arnold. 'Free-space information transfer using light beams carrying

orbital angular momentum'. Opt. Express, Vol. 12, (2004), pp. 5448–5456 (cited on page: 183).

[6.11] A. M. Yao and M. J. Padgett. 'Orbital angular momentum: origins, behavior and applications'. Advances in Optics and Photonics, Vol. 3, (2011), pp. 161–204 (cited on page: 183).

[6.12] *ProEM+ Performance | Precision | Peace of Mind*. online, last accessed 2013-02-11. Princeton Instruments, (2012). URL: http://www.princetoninstruments.com (cited on page: 183).

[6.13] Nüvü Cameras. *EMCCD Tutorial - Understanding underlying principles | Nüvü Cameras*. online, last accessed 2013-02-13. URL: http://www.nuvucameras.com/emccd-tutorial/ (cited on page: 183).

[6.14] D. Durini. *Ultrasensitive photon hunter*. Press release, online, last accessed 2013-03-22. (2013). URL: http://www.mikroelektronik.fraunhofer.de/en/press-media/microelectronics-news/article/ultrasensitive-photon-hunter.html (cited on page: 184).

[6.15] D. Durini and F. Zappa. *Advances in time-of-flight and time-correlated single-photon-counting devices*. online, last accessed 2013-04-23. (2013). URL: http://spie.org/x93517.xml (cited on page: 184).

[6.16] A. K. Ekert. 'Quantum cryptography based on Bell's theorem'. Phys. Rev. Lett., Vol. 67, (1991), pp. 661–663 (cited on page: 184).

[6.17] F. Guerrieri, L. Maccone, F. N. C. Wong, J. H. Shapiro, S. Tisa and F. Zappa. 'Sub-Rayleigh imaging via N-photon detection'. Phys. Rev. Lett., Vol. 15, (2010), p. 163602 (cited on page: 184).

[6.18] S. Mouradian, F. N. C. Wong and J. H. Shapiro. 'Achieving sub-Rayleigh resolution via thresholding'. Opt. Express, Vol. 19, (2011), pp. 5480–5488 (cited on page: 184).